
ACTIVE AND PASSIVE
MICRORHEOLOGY OF
F-ACTIN MEMBRANE COMPOSITES
– FROM MINIMAL CORTEX MODEL SYSTEMS TO LIVING CELLS –

DISSERTATION

for the award of the degree
“Doctor rerum naturalium”
of the Georg-August-Universität Göttingen

Within the doctoral program “International Max Planck Research School”
“Physics of Biological and Complex Systems”
of the “Georg-August-University School of Science” (GAUSS)

submitted by
Helen Nöding
from Heidelberg/Germany

Göttingen, 2017

MEMBERS OF THE THESIS COMMITTEE

Prof. Dr. Andreas Janshoff,
Institut für Physikalische Chemie,
Georg-August-Universität Göttingen

Dr. Florian Rehfeldt,
Fakultät für Physik, III. Physikalisches Institut – Biophysik / Komplexe Systeme,
Georg-August-Universität Göttingen

Prof. Dr. Jörg Enderlein,
Fakultät für Physik, III. Physikalisches Institut - Biophysik / Komplexe Systeme,
Georg-August-Universität Göttingen

MEMBERS OF THE EXAMINATION BOARD

Prof. Dr. Andreas Janshoff (Reviewer),
Institut für Physikalische Chemie,
Georg-August-Universität Göttingen

Dr. Florian Rehfeldt (Reviewer),
Fakultät für Physik, III. Physikalisches Institut – Biophysik/ Komplexe Systeme,
Georg-August-Universität Göttingen

Prof. Dr. Jörg Enderlein,
Fakultät für Physik, III. Physikalisches Institut – Biophysik/ Komplexe Systeme,
Georg-August-Universität Göttingen

Prof. Dr. Sarah Köster,
Fakultät für Physik, Institut für Röntgenphysik,
Georg-August-Universität Göttingen

Prof. Dr. Michael Meinecke
Abteilung Biochemie II - Zelluläre Biochemie
Universitätsmedizin Göttingen

Prof. Dr. Silvio O. Rizzoli
Abteilung für Neuro- und Sinnesphysiologie
Universitätsmedizin Göttingen

DATE OF ORAL EXAMINATION:

October 20th, 2017

DECLARATION

I, Helen Nöding, hereby certify that my doctoral thesis “Active and Passive Microrheology of F-Actin Membrane Composites – From Minimal Cortex Model Systems to Living Cells” has been written independently and with no other sources and aids than quoted.

Göttingen, 2017

Helen Nöding

“What a good way to begin a science course! Take apart the toy; see how it works. See the cleverness of the gears; see the ratchets. Learn something about the toy, the way the toy is put together, the ingenuity of people devising the ratchets and other things.”

RICHARD FEYNMAN

ABSTRACT. The complex mechanical properties of a living cell are not only a function of its structural components but also of the organizational super-structure and the dynamic interconnection of filaments, proteins and the plasma membrane. Especially, the F-actin cortex plays a central role in cell adhesion, migration, division, growth and differentiation. Abnormalities in these essential cellular processes are tightly connected to diseases such as cancer and malaria. It is thus of pivotal interest to study the determinants of cellular mechanics.

The main part of this thesis is dedicated to the investigation of a minimal cortex model of the F-actin cortex. A pre-polymerized network of semi-flexible F-actin polymers is attached to a lipid bilayer by the physiological cross-linker ezrin. A pseudo-phosphorylated mutant of ezrin, T567D, is used to study the impact of transient membrane linkage on the frequency dependent viscoelastic properties. Here, passive as well as active microrheological measurements are established on these thin composite materials and frequency spectra ranging from 10^{-3} - 10^2 Hz are measured. In an intermediate frequency regime (10^{-2} - 10^1 Hz) the elastic properties dominate the force response of the model system. The stiffness of the system is dominated by the mesh size of the self-organized model cortex, which is in turn a function of the availability of pinning-points in the membrane. These findings suggest the formation of an affine network. The low frequency regime (10^{-3} - 10^{-2} Hz) of the shear modulus is dominated by the transient binding kinetic of the membrane cross-link ezrin. An apparent unbinding rate constant is determined from the microrheological data and the transient nature of the membrane attachment is supported by a low energy barrier for the unbinding. For the high frequency regime (10^1 - 10^2 Hz) deviations from the typically found power law scaling of $\frac{3}{4}$ are observed and discussed in the context of increased inertia upon F-actin attachment to a solid supported model membrane. The minimal actin cortex model is compared to entangled networks of the semi-dilute F-actin filament as well as F-actin membrane composites isolated from the apical cortex of living cells by the sandwich cleavage method.

In the second part of this thesis, the focus is set on mechanotransduction and rigidity sensing in epithelial monolayers. Cell mechanics in response to surface elasticity are studied by active atomic force microscopy based microrheology and interpreted in terms of (active) soft glassy rheology. Epithelial cells from the kidney (MDCK II) and mammary gland (MCF-10A) are studied as a function of substrate elasticity ($E=1$ -100 kPa). Cells cultured on soft substrates (1 kPa) exhibit similar frequency dependent viscoelastic properties as cells, which are F-actin depleted by latrunculin A. Both cell lines behave stiffer when cultured on surfaces of higher elasticity. Above a certain threshold of substrate stiffness no further changes can be observed upon increase in surface stiffness. This final cortical stiffness can only be increased for a short time by the F-actin reinforcing drug jasplakinolide. Additionally, the impact of cell size on the frequency dependent viscoelastic properties is elucidated.

Altogether, the essential contribution of the membrane linkage to the viscoelastic properties of the F-actin cortex is shown in a minimal model system and the importance of extracellular mechanical cues, such as substrate elasticity, on the organization and mechanics of the F-actin cytoskeleton in living cells is emphasized.

Contents

1.	Introduction	1
2.	Theory	4
2.1.	Soft Condensed Matter	4
2.2.	Viscoelasticity and Rheology	4
2.2.1.	Basic Definitions	4
2.2.2.	Rheometry and Rheology	6
2.3.	F-Actin as a Semi-Flexible Polymer Network	11
3.	Biological Background	16
3.1.	Introduction to the F-Actin Cytoskeleton	16
3.1.1.	Cellular Architecture and Cell Mechanics	16
3.1.2.	F-Actin is Sculpturing Different Cellular Compartments	16
3.1.3.	The F-Actin Cytoskeleton on Protein Level	18
3.1.4.	Ezrin: Membrane Anchorage of the F-Actin Cytoskeleton	19
3.2.	Mechanical Cortex Model Systems – Bottom-Up Approaches	21
3.2.1.	Cross-Linked F-Actin Networks	21
3.2.2.	Membrane Coupled F-Actin Networks as Minimal Actin Cortices	28
3.3.	Mechanical Cortex Model Systems – Top-Down Approaches	31
3.3.1.	Functional Networks	31
3.3.2.	Viscoelastic Properties of Living Cells	33
4.	Methods and Experimental Procedure	35
4.1.	Methods and Experimental Procedures to Study Cortex Model Systems	35
4.1.1.	Preparation of Artificial Model Systems	35
4.1.2.	Network Analysis of the Self-Assembled Minimal Actin Cortex (MAC)	39
4.1.3.	Force Spectroscopy Methods to Study the Viscoelasticity of MACs	41
4.1.4.	Langevin Equation for the Motion of a Particle in a Viscoelastic Medium	48
4.2.	Methods and Experimental Procedure to Study Living Cells	49

4.2.1.	Polyacrylamide Gels as Cellular Substrates of Different Elasticities	49
4.2.2.	Cell Culture and Sample Preparation.....	51
4.2.3.	Determination of Cellular Topography.....	53
4.2.4.	Preparation of Apical Cellular Membrane Patches.....	53
4.2.5.	Fluorescence Microscopy Methods	54
4.2.6.	Electric Cell-Substrate Impedance Sensing	55
4.2.7.	Force Spectroscopy Methods to Study the Mechanics of Living Cells	57
5.	Results and Discussion.....	60
5.1.	Self-Organization and Viscoelastic Properties of Actin Networks Attached to Lipid Bilayers	60
5.1.1.	Self-Organization and Network Properties of F-Actin Attached to a Lipid Bilayer.....	63
5.1.1.1.	Mesh Sizes of F-Actin Networks Attached to a Lipid Bilayer	64
5.1.1.2.	Single Filament Properties of F-Actin Networks Attached to a Lipid Bilayer	67
5.1.2.	Frequency Dependent Viscoelastic Properties of MACs.....	69
5.1.2.1.	Viscosity of Liquids	69
5.1.2.2.	Mean Squared Displacements of Entangled F-Actin Networks and Networks Attached to Lipid Bilayers.....	71
5.1.2.3.	Frequency Dependent Viscoelastic Properties of Entangled F-Actin Samples	73
5.1.2.4.	Frequency Dependent Viscoelastic Properties of F-Actin Networks Attached to a Lipid Bilayer via the PIP ₂ -Ezrin or the Biotin-Neutravidin Interaction.....	78
5.1.2.5.	Temperature Dependency of the Apparent Unbinding Rate Constant	88
5.1.2.6.	Possible Sources of Error in VPT Based Microrheology on MACs.....	89
5.1.2.7.	Comparison of Different Microrheology Methods.....	94
5.1.3.	Frequency Dependent Viscoelastic Properties of Apical Cellular Membrane Patches.....	99
5.1.4.	Conclusion.....	101
5.2.	Cell Mechanics of Epithelial Cells in Response to Substrate Stiffness	103
5.2.1.	Influence of the F-Actin Cytoskeleton on the Viscoelastic Properties of Epithelial Cells ...	105
5.2.2.	Viscoelasticity of Kidney Epithelial Cells in Response to Matrix Elasticity.....	108
5.2.3.	Impact of Cell Size on the Viscoelastic Properties of Epithelial Cells	113
5.2.3.1.	Influence of Cell Size on the Viscoelasticity of Cells Cultured on Substrates of Different Elasticities	115
5.2.4.	Viscoelasticity of Mammary Gland Cells in Response to Matrix Elasticity.....	117
5.2.5.	Conclusion.....	120
6.	Summary.....	122
7.	References.....	125

Appendix 1: Supplementary Data	a
I. Formation of Confluent Cell Layers as a Function of Seeding Density	a
II. Cell-Cell Contacts as a Function of Seeding Density.....	a
III. Impact of Cell Size and Substrate Properties on the Viscoelastic Parameters obtained from PLSDM.....	b
IV. Table of Parameters Used to Model the Frequency Dependent Viscoelastic Properties..	c
Appendix 2: List of Abbreviations, Symbols, Figures and Tables	d
List of Abbreviations and Symbols	d
List of Figures	g
List of Tables.....	o
Appendix 3: Curriculum Vitae	q
Appendix 4: Acknowledgments	s

1. Introduction

From a physics perspective, living cells are one of the most complex materials. It is astonishing, how a cell can be motile and maintain structural integrity at the same time. Key to these extraordinary properties is the dynamic reorganization of the load bearing cytoskeleton.¹ The cytoskeleton is a hierarchically organized structure of different filaments within the cell, which defines cellular shape and is crucial to many cellular functions such as adhesion, migration, division, growth and differentiation. Additionally, many disease patterns and cellular functions are accompanied by F-actin cytoskeleton reorganization and mechanical alterations on a cellular level. This relation has already been shown in cancer²⁻⁴ and infectious diseases such as malaria⁵⁻⁸ among others. High-throughput mechanical measurements on living cells in suspension recently made it possible to measure the mechanical fingerprint of diseases and primary stem cells on large scales.^{9,10} This mechanical phenotyping developed by Guck, Käs and coworkers emphasizes the role of biophysical properties in many different diseases and enables the clinical application of mechanical measurements as a diagnostic tool.¹¹ The increasing interest in cellular mechanics highlights likewise the importance to understand the interconnections between biochemical alterations in cells and the resulting mechanical properties. Among these cytoskeletal filaments, F-actin is the most resistant to external stresses and thus greatly determines the force response of cells.¹² The F-actin cytoskeleton is spatially organized by cross-linking proteins, so called actin binding proteins. Some of these proteins cross-link, branch or sever the filaments¹³. Active motor proteins like myosin II generate tension and drive the system far from thermodynamic equilibrium¹⁴⁻¹⁸. Others like the so called ERM (ezrin, radixin and moesin) proteins anchor the F-actin cytoskeleton at the plasma membrane¹⁹. This thin²⁰ (≈ 200 nm) shell-like composite of F-actin filaments attached to the plasma membrane is called the cellular cortex. Here, short F-actin filaments²¹ ($< 2 \mu\text{m}$) are highly cross-linked and form dense meshes²². This F-actin membrane composite greatly determines the cytoskeletal tension^{20,23}.

While already the F-actin filament²⁴ and entangled networks of this semi-flexible biopolymer²⁵⁻²⁹ exhibit interesting mechanical properties, the rich viscoelastic properties of the construct of F-actin and the over one hundred actin binding proteins in the cellular cortex are far from being understood. Cross-links stiffen the F-actin cytoskeleton, but at the same time the transient nature^{21,30-33} of these cross-links introduce time scale dependent viscoelastic properties³⁴⁻³⁶. As a result, transiently cross-linked networks show either a stiff elastic response or flow like a liquid depending on the investigated time scale.^{37,38} The interplay of all cross-links in the cytoskeleton, together with actomyosin generated tension, determine the bulk mechanical properties of cells as well as cellular processes like motility and mechanosignaling^{1,39-44}. An exemplary study that provides a link between cortical mechanotransduction and the actin cytoskeleton, especially membrane cross-links, myosin II, dynacortin and filamin, has been published by Luo *et al.*⁴² Adhered cells transmit

environmental cues from their environment into the cell. The role of the mechanosensitive transmembrane proteins integrin and cadherin in integration of mechanical signals into the cell has been reported and is generally referred to as mechanotransduction.^{45–48} Cadherin conveys signals from neighboring cells, while integrin provides a link to the extracellular membrane and allows the cell to respond to stimuli from the underlying substrate. The impact of the substrate in cell culture and the design of implant materials has largely been neglected in the past. Even though the substrate takes a central stage in the differentiation and motility of cells.^{46,49–53} Additionally, the majority of actomyosin generated tension is counterbalanced by the substrate.⁵⁴ In the last decade, the role of chemical as well as mechanical properties of the substrate – density of binding motives, porosity and elasticity – on the F-actin cytoskeleton and cellular mechanics has become of increasing interest.^{55–58} Additionally, the role of integrin mediated mechanotransduction in the progression of cancer has become evident in the last years.^{59–63}

The cellular cortex and the interplay of different proteins in cellular mechanotransduction and other signaling processes are complex. Model systems are thus developed to quantitatively probe the impact of cross-linking proteins, fibrous macromolecules, the plasma membrane and their interconnections, in order to address questions such as what the molecular origin of the rich mechanical properties of living cells is. The reduction to minimal model cortices is important to reveal the impact on viscoelastic behavior of each component involved. Additionally, the quantitative study of living cells in well controlled environments enables conclusions about higher hierarchical structures such as force transmission in cellular layers and tissues. Both, bottom-up^{64–67} as well as top-down^{38,68–70} approaches, have been useful means to study the complex linear^{34,36–38,71–73} and non-linear^{65,66,74,75} viscoelastic properties of living cells. These material properties of living cells and *in vitro* constituted model systems are commonly probed by microrheology because only small sample volumes are needed and broader frequency regimes can be probed than in conventional rheometers. In general, the viscoelastic response behavior to a deformation at different frequencies can either be probed by thermally excited fluctuations of tracer particles⁶⁴ (passive) or by application of external forces (active). The latter is often achieved by oscillatory shear measurements. A broad variety of experimental setups can be used for this kind of measurements ranging from cone and plate rheometers^{65,66}, over atomic force microscopy^{76,77} to optical^{14,78} and magnetic³⁸ tweezer based force spectroscopy.

In this doctoral thesis I focus on two main research questions: (1) What is the impact of transient membrane linkage via ezrin on the frequency dependent viscoelastic properties of F-actin networks? (2) How is the viscoelasticity of epithelial monolayers altered by substrate elasticity? To answer these questions tunable model systems are envisioned (Figure 1) ranging from bottom up to top down approaches. The impact of transient membrane attachment of F-actin networks via the physiological cross-linker ezrin to the frequency dependent viscoelastic properties of F-actin networks is studied in a bottom up minimal cortex model system (5.1.2). Passive video particle tracking microrheology as well as optical tweezer based passive and active microrheology will be used to study the linear viscoelastic properties of these composite materials. In addition, the self-organization of the F-actin membrane composite as well as important network parameters will be studied with the use of imaging techniques such as confocal laser scanning microscopy and atomic force microscopy. Microrheological measurements will also be performed on apical cellular membrane patches (5.1.3), which are isolated from epithelial cells via the sandwich cleavage method in order to bridge the gap between model systems and living cells (5.2). Second, the impact of substrate elasticity on the viscoelastic properties of epithelial monolayers is investigated.

Frequency dependent viscoelastic moduli will be measured via atomic force microscopy based active microrheology. Relevant viscoelastic parameters obtained by the power law structural damping model will be reported and interpreted in terms of (active) soft glassy rheology.

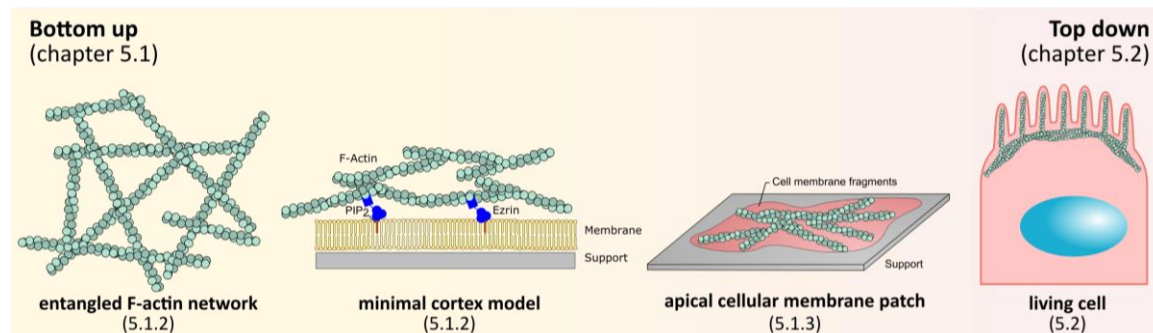


Figure 1: Scheme of mechanical model systems for cellular viscoelasticity investigated in the context of the here presented dissertation. Top down approaches: 3D entangled F-actin networks and 2D F-actin networks transiently cross-linked to a solid supported membrane via the physiological cross-link ezrin. Top down approaches: functional apical membrane patches from epithelial cell cortices and living cells.

2. Theory

2.1. Soft Condensed Matter

Many materials belonging to condensed matter fall into the classical classes of fluids or solids. However, there is a class of materials which cannot fully be attributed to either of them. It was Pierre-Gilles de Gennes who coined the term "soft condensed matter" for this class of materials in his Nobel Prize lecture 1991.⁷⁹ Soft matter comprises a large class of complex materials such as foams, colloidal grains, surfactants, liquid crystals and polymers. While solids like steel can be described by the elastic modulus with moduli on the order of GPa, soft condensed matter exhibits elastic moduli of about ten to thirteen orders of magnitude lower. Additionally, these materials often display rich viscoelastic behavior depending on the time scales probed.⁸⁰ Practically all biological material is "soft" and has been studied in the past years in the context of soft matter. Interesting examples are lipid membranes, micelles and wormlike micellar solutions^{81–83}, biopolymers and networks like DNA, neurofilaments, spider silk⁸⁴, mucus⁸⁵ as well as scleroproteins¹² like collagen⁸⁶ and actin^{12,29} among other hydrogels⁸⁷. But also more complex systems of higher order like single cells^{15,38}, cell monolayers⁸⁸ and whole biological tissues exhibit interesting mechanical properties. Even the swimming behavior of nematodes like *C. elegans* has been interpreted in terms of soft matter.⁸⁹ Here I am interested in the F-actin cytoskeleton a scleroprotein within the cortex of eukaryotic cells. While already the networks of the semi-flexible biopolymer F-actin exhibit complex mechanical properties, the rich viscoelastic properties of the construct of F-actin and the over 100 actin binding proteins in the cellular cortex is far from being understood. To discuss these complex mechanical properties and their biological implications, knowledge of basic rheology is necessary, which will be introduced in the next chapters.

2.2. Viscoelasticity and Rheology

2.2.1. Basic Definitions

Rheology is the study of deformation and flow of materials in response to applied stress. A detailed overview over mechanics and rheology can be found in many textbooks.^{90–92}

2.2.1.1. Elastic Solid

Elasticity is the characteristic of a material to return to its original shape after being deformed by an external force. There are several ways to probe the deformability of elastic bodies: isotropic lateral deformation, bending and shearing. For experiments performed within this thesis shearing is the dominant deformation. Stress and strain in a material are tensors. However, I am interested in the uniaxial stress strain relationship, this is why only simplified equations are shown.

A force F that is acting on a wire with a cross section A is causing a stress σ ($\sigma = F/A$). The material response in form of relative elongation is the strain ε ($\varepsilon = \Delta l/l_0$). In elastic materials stress and strain are connected by a materials characteristic value, the elastic modulus E :

$$\sigma = E \cdot \varepsilon \quad (1)$$

This equation is equivalent to Hooke's law. When the material is stretched in one direction it will contract in the orthogonal direction. The ratio of stretching in one direction $\Delta l/l_0$ and the contraction in the orthogonal direction $\Delta d/d_0$ is called Poisson ratio ν

$$\nu = -\frac{\Delta d \cdot l_0}{\Delta l \cdot d_0} \quad (2)$$

With the help of the Poisson's ratio the elastic modulus can be easily transformed into the shear modulus G .⁹³

$$G = \frac{E}{2 \cdot (1 + \nu)} \quad (3)$$

Most biological material is largely incompressible since a great percentage is water and water is nearly incompressible at forces generally exerted in biology. Thus, for cells and F-actin networks a Poisson's ratio of 0.5 is assumed.

2.2.1.2. Viscous Fluid

The simplest case of a viscous fluid is a Newtonian fluid like water, which can be fully characterized by one characteristic material value, the viscosity η . In these fluids the stress under laminar flow conditions is proportional to the shear rate $\dot{\varepsilon}$:

$$\sigma = \eta \cdot \dot{\varepsilon} \quad (4)$$

Another helpful quantity to describe Newtonian fluids is the mass diffusivity D , which is connected to the viscosity by the Stokes-Einstein equation. For a spherical particle the diffusion in a Newtonian fluid is described by the Stokes-Einstein equation as follows:

$$D = \frac{k_B T}{6\pi\eta r} \quad (5)$$

where k_B is the Boltzmann constant, T the temperature and r the radius of the particle.

2.2.1.3. Linear Viscoelasticity

Many other materials like polymers and cells show a so-called viscoelastic behavior. Here, the material shows both elastic and viscous properties. Time dependent dissipation of elastically stored energy is a key property of viscoelastic materials. This characteristic appears in stress-strain curves as a hysteresis between extension and retraction. In step experiments with constant strain, a stress relaxation and in step experiments with constant stress an increase of strain with time, called creep, can be observed. For example, the stress and the shear modulus for a stress relaxation following a strain step $\delta\varepsilon$ in the linear viscoelastic regime are time dependent functions:

$$\sigma(t) = G(t) \cdot \delta\varepsilon \quad (6)$$

This equation is only true for small strain steps, typically $\delta\varepsilon \leq 0.05$. For larger strains the shear modulus and the shear stress are dependent on the strain and materials might be either shear thinning or shear thickening. At very large strains plastic deformation can be reached.

According to the Boltzmann Superposition Principle, the stress that results for multiple strain steps $\delta\varepsilon_i$ at time points t_i is simply additive:

$$\sigma(t) = \sum_{i=1}^N G(t - t_i) \cdot \delta\varepsilon_i \quad (7)$$

Or written as integral over all past times t' :

$$\sigma(t) = \int_{-\infty}^t G(t - t') \cdot \dot{\varepsilon}(t') dt' \quad (8)$$

Equation (8) is a commonly used description for viscoelastic behavior and will be used in the following in respective equation of motions.

Most commonly, the viscoelastic behavior of a material is quantified by the shear modulus. The shear modulus in a viscoelastic medium is a complex number G^* with a real part G' reflecting the elastic contribution, the so called storage modulus, and an imaginary part G'' , reflecting the viscous dissipation in the medium, called loss modulus. The storage and loss modulus are not independent:

$$G^* = G' + iG'' \quad (9)$$

The loss tangent, which is the ratio of loss to storage modulus, is another important measure in rheology. If the loss tangent $\delta = G''/G' > 1$ the medium behaves more like a viscous fluid, while for $\delta < 1$ the elastic part dominates and the medium resembles an elastic solid.

The two simplest and most prominent models for linear viscoelastic materials are the Maxwell model and the Kelvin-Voigt model. A simple way to visualize these models is to use mechanical equivalent circuits. The elastic contribution is modeled with a Hooke's spring with an elastic modulus E and the viscous contribution with a dashpot of viscosity η . The Maxwell model is essentially a serial combination of the two elements (Figure 2 A), whereas in the Kelvin-Voigt model the two elements are in parallel (Figure 2 B). While the Kelvin-Voigt model captures the high frequency creep recovery of networks of semi flexible polymers better, the Maxwell model is able to describe the stress relaxation of elastically stored energy at low frequencies. Combinations of both are able to approximately capture the essential mechanical properties of F-actin networks. In the case of the equivalent circuit pictured in Figure 2 C the series connection within the parallel-series connection determines the short response time of the system, whereas the second spring determines the plateau region and the second dashpot represents viscous dissipation to the shear modulus at long times. However, these models are not well suited to model the weak power law rheology that living cells exhibit, since large numbers of elements are necessary. For this purpose, other descriptions as described in chapter 3.3.2 are commonly used.

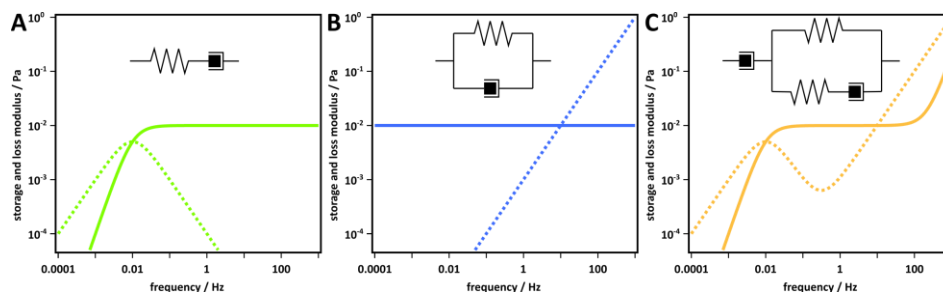


Figure 2: Equivalent circuits and shear modulus of viscoelastic models. A: Maxwell model. B: Kelvin-Voigt model. C: A more elaborate model capturing most of the rheological properties of F-actin networks. Solid lines: Storage modulus. Dotted lines: loss modulus.

2.2.2. Rheometry and Rheology

To test the viscoelastic properties of materials many experiments have been developed. As mentioned above, creep and stress relaxation experiments as well as experiments in which the hysteresis of a stress strain curve is probed can be performed. Additionally, it is common to access the frequency dependent viscoelastic properties by applying active oscillations to the material and measuring its response behavior. The setup used for the measurement of rheological properties is adapted to the conditions of the sample. For large quantities of material and high stiffness bulk measurements, like drag flow measurements (sliding plate or cone and plate rheometry) or pressure flow measurements (capillary flow measurements) and falling ball experiments can be used.^{90,94} However, for soft samples with low elastic moduli and especially for samples of only few microliters microrheology measurements are required. There are two ways to perform microrheological measurements. Either by active oscillation similar to the bulk measurements or

by observing the thermally activated motion of a tracer particle in the viscoelastic medium. Active microrheology measurements can be performed by magnetic tweezers, optical tweezers and atomic force spectroscopy. Passive measurements can be performed by video particle tracking (single and multiple particle) as well as with optical tweezer, dynamic light scattering and diffusing wave spectroscopy. The range of viscoelastic moduli and frequency that can be probed by the methods used in this study are summarized in Table 1.

Table 1: Overview of microrheology methods and their measuring ranges.

microrheology method	approximate range of viscoelastic moduli / Pa	approximate range of frequency / Hz
video particle tracking	10^{-6} - 10^0	10^{-3} - 10^2
passive MR optical tweezer	10^{-6} - 10^1	10^{-3} - 10^3
active MR optical tweezer	10^{-4} - 10^2	10^{-3} - 10^4
active MR atomic force spectroscopy	10^{-2} - 10^5	10^{-2} - 10^4

A comprehensive comparison of the micro- and macrorheological properties of isotropically cross-linked F-actin networks was published by Luan, Bausch and co-workers.⁹⁵ In their study they show that the frequency dependent properties are essentially captured in both methods. However, some deviations occurred. The minimum in the loss modulus was shifted towards lower frequencies and seemed to be more pronounced in microrheological experiments. Other working groups have found perfect agreement of these techniques in different model systems.⁹⁶ Within the passive microrheological measurements it is possible to perform single and multiple particle measurements. Liu *et al.*²⁵ showed that results obtained from two-particle measurements correspond better to macroscopic measurements than one-particle measurements do. Additionally, the authors stated that two-particle measurements would probe fluctuations on larger length scales ($>5 \mu\text{m}$) whereas one-point microrheology would probe the direct environment of the tracer particle on the order of the mesh size. Multiple particle tracking techniques are also used to probe special heterogeneities.⁹⁷ Moreover, when particle tracking methods are used, the choice of tracer particles is important. Apart from tracking the motion of microspheres, single filaments or nanotubes can be used as tracer particles in order to obtain rheological information about the system.^{98,99} Depending on their size and geometry different properties of materials can be probed when the viscoelastic response is length scale dependent. Additionally, the highly adhesive surface properties can alter the measured viscoelastic response.¹⁰⁰

2.2.2.1. Microrheology Methods

2.2.2.1.1. Active Microrheology

Equivalently to the classical bulk rheometrical measurements small amplitude oscillatory stresses or strains can be applied in microrheology to probe the rheological properties of viscoelastic samples. When a viscoelastic material is deformed by an oscillatory strain with the frequency ω and an amplitude of ε_0 , the resulting stress will be shifted in phase $\varphi(\omega)$ in respect to strain and the stress amplitude σ_0 will be damped in respect to the strain amplitude. Amplitude damping and phase shift are the two observables in active microrheology. Based on the equation of motion of a probe in the viscoelastic medium, the frequency dependency of the stress and strain can be written as:

$$G^*(\omega) \propto \frac{\hat{\sigma}(\omega)}{\hat{\varepsilon}(\omega)} = \frac{\sigma_0}{\varepsilon_0} \cdot \exp(i \cdot \varphi(\omega)), \quad (10)$$

where $\hat{\sigma}(\omega)$ and $\hat{\varepsilon}(\omega)$ are the Fourier transforms of stress and strain at ω respectively. An ideal Newtonian fluid will give a phase shift of 90° whereas a fully elastic body will exhibit a phase shift of 0° . Viscoelastic materials show phase shifts between 0° and 90° . The specific analysis for each active microrheological experiment depends on the method and can be derived from the equation

of motion of the testing probe. For the methods used here the resulting specific analysis is shown in the respective methods chapter (4.1.3.3 and 4.2.7.1).

2.2.2.1.2. Passive Microrheology

In the absence of active motions it is also possible to perform passive microrheological measurements to assess the microrheological properties of soft biological properties. In contrast to active microrheological measurements no external strain is applied, but the thermal motion of a tracer particle embedded in a viscoelastic medium is analyzed. This is possible since in such systems the fluctuation-dissipation theorem can be applied. It states that in equilibrium the response of a system to a small external disturbance is the same as the response of the system to a spontaneous fluctuation. In particular that means that the dissipative response (like friction) is proportional to spontaneous fluctuations:

$$2 \cdot k_B T \cdot \zeta(t) \cdot \delta(t - t') = \langle f_R(0) f_R(t) \rangle \quad (11)$$

where $k_B T$ is the thermal energy, $\delta(t - t')$ an infinitesimal time lag, $\zeta(t)$ the time dependent memory function or friction coefficient of the material and $\langle f_R(0) f_R(t) \rangle$ the autocorrelation of a fluctuating force that counteracts the viscous dissipation.

The measuring principle of passive methods is quite easy, the motion of a tracer particle is recorded and tracked. This trajectory of a bead can be transformed into the mean squared displacement, a helpful quantity, which enables the analysis of the bead motion. One result from Einstein's theory is that the mean squared displacement MSD or $\langle \Delta x^2(\tau) \rangle$ of a bead in a Newtonian fluid is proportional to the time lag τ . Generalized for other materials this gives:

$$\langle \Delta x^2(\tau) \rangle = 2 \cdot N \cdot D \cdot \tau^\alpha, \quad (12)$$

where N is the dimensionality and D the diffusion coefficient. When the mean squared displacement follows a power law $\alpha = 1$ then the particle diffuses normally. When $\alpha < 1$ the motion of the particle is hindered and the type of diffusion is called sub-diffusion, whereas $\alpha > 1$ refers to super-diffusion.

According to the equipartition theorem, the mean squared displacement can be either calculated from one particle trajectory as a time average:

$$\langle \Delta x^2(\tau) \rangle = \frac{1}{N} \cdot \sum_i (x_i(t + \tau) - x_i(t))^2, \quad (13)$$

or from an ensemble of N particles, or both. However, when taking the time average the general assumption that the physical properties do not evolve with time has to be valid. τ is the elapsed time and i the index of the time.

In the context of video particle tracking the generalized Stokes-Einstein equation is used, which is based on a generalized Langevin equation as follows:^{101,102}

$$m \frac{d^2 x}{dt^2} = f_R(t) - \int_0^t \zeta(t - t') \cdot \frac{dx(t')}{dt} dt', \quad (14)$$

The Langevin equation states that the motion of a particle is a sum over all forces acting on a particle counterbalanced by the inertia force where m is the mass of the particle: the integral term is the restoring force due to viscoelastic damping of the medium where ζ is a time dependent memory function, $f_R(t)$ are random forces acting on the particle due to inter-particle and stochastic thermal Brownian forces. Equation (14) can be related to the velocity autocorrelation applying Laplace transform and simplifications with the following assumptions: (i) the stochastic thermal force is uncorrelated with the velocity of probe, (ii) the equipartition theorem $m \cdot \langle v^2(0) \rangle = N \cdot k_B T$ applies and (iii) the assumption that inertia can be neglected for the investigated frequency regime $\tilde{\zeta}(s) > m \cdot s$, giving:

$$\langle \tilde{v}(s) \cdot v(0) \rangle = \frac{N \cdot k_B T}{\tilde{\zeta}(s)} \quad (15)$$

s represents the frequency parameter in the Laplace domain ($s \hat{=} i\omega$ in Fourier domain). Based on this velocity correlation, which depends on the time dependent memory function $\tilde{\zeta}(s)$, the mean squared displacement $\langle \Delta \tilde{x}^2(s) \rangle$ can be expressed as a function of the complex viscosity $\tilde{\eta}(s)$ using the proportional relation of the memory function with the complex viscosity $\tilde{\eta}(s)$.

$$\tilde{\zeta}(s) = 6\pi r \cdot \tilde{\eta}(s). \quad (16)$$

This equation is exact for purely viscous media and a widely accepted assumption for viscoelastic fluids.¹⁰¹ This procedure results in the generalized Stokes-Einstein equation:

$$\langle \Delta \tilde{x}^2(s) \rangle = \frac{N \cdot k_B T}{3\pi r \cdot s^2 \cdot \tilde{\eta}(s)} \quad (17)$$

which together with the relation of the complex viscosity and the shear modulus $\tilde{G}(s)$:

$$\tilde{G}(s) = \tilde{\eta}(s) \cdot s \quad (18)$$

gives a relation between the mean squared displacement and the complex shear modulus:

$$\tilde{G}(s) = \frac{N \cdot k_B T}{3\pi r \cdot s \cdot \langle \Delta \tilde{x}^2(s) \rangle} \text{ or in Fourier space:} \quad (19)$$

$$G^*(\omega) = \frac{N \cdot k_B T}{3\pi r \cdot i\omega \cdot \langle \Delta \hat{x}^2(\omega) \rangle}, \quad (20)$$

where N is the number of dimensions, k_B is the Boltzmann constant, T the temperature, r the radius of the tracer particle, and $\langle \Delta \hat{x}^2(\omega) \rangle$ the Fourier transform of the mean squared displacement.

In principle equation (20) depicts a simple relation between the complex shear modulus and the observed particle trajectory, however the evaluation of the Fourier transforms is non-trivial due to the finite set of data points recorded during the measurement and due to the non-convergence of the Fourier integral. Different methods have been proposed to circumvent artefacts arising from this obstacle.^{103,78}

Fit to Mean Squared Displacement after Mason *et al.* and Dasgupta *et al.*

For the video particle tracking based passive microrheology measurements (chapter 5.1.2) I calculate the viscoelastic moduli, the complex shear modulus $G^*(\omega)$, the storage modulus $G'(\omega)$ and the loss modulus $G''(\omega)$, using an alternative form of the generalized Stokes-Einstein equation derived by Dasgupta *et al.*¹⁰³, which is a modification of a method introduced by Mason *et al.*:¹⁰⁴

$$G^*(\omega) = \frac{N \cdot k_B T}{3\pi r \cdot \Gamma[1+\alpha(\omega)] \left[1+\frac{\beta(\omega)}{2}\right]} \cdot \frac{1}{\langle \Delta x^2(1/\omega) \rangle} = \frac{A}{\langle \Delta x^2(1/\omega) \rangle} \quad (21)$$

$$G'(\omega) = G^*(\omega) \left\{ \frac{1}{1+\beta'(\omega)} \right\} \cdot \cos \left[\frac{\pi\alpha'(\omega)}{2} - \beta'(\omega)\alpha'(\omega) \left(\frac{\pi}{2} - 1 \right) \right] = G^*(\omega) \cdot B \quad (22)$$

$$G''(\omega) = G^*(\omega) \left\{ \frac{1}{1+\beta'(\omega)} \right\} \cdot \sin \left[\frac{\pi\alpha'(\omega)}{2} - \beta'(\omega)[1 - \alpha'(\omega)] \left(\frac{\pi}{2} - 1 \right) \right] = G^*(\omega) \cdot C \quad (23)$$

α and β are the 1st and 2nd order log-time derivative of a local polynomial fit function to the mean squared displacement vs. time lags, α' and β' are the 1st and 2nd order log-time derivative of a local polynomial fit function to the shear modulus $G^*(\omega)$ vs. frequency. Truncation errors by the Fourier transform are avoided by using the local power law, in form of the local first log-time derivative, of the mean squared displacement to describe the curve progression of the shear modulus. The additional dependency on the second derivative was introduced based on empirical observations¹⁰³, in order to accomplish more reliable shear moduli in highly curved regions. While this method works well and has been widely used¹⁰³⁻¹⁰⁶ it masks experimental uncertainty since the data has to be smoothed for this procedure.

Direct Conversion of the Compliance after Evans *et al.*

A method that avoids fitting and smoothing procedures to obtain the viscoelastic moduli from the mean squared displacement has been reported by Evans *et al.*¹⁰⁷ They use a direct conversion method of the creep compliance ($J(t) = 1/G(t)$) into the Fourier domain. In their method they use the observation that for most materials the compliance approaches linear behavior at long times (steady state viscosity). Thus, its second derivative vanishes for long times and they were able to find a convergent Fourier integral. They refrained from fitting the data, instead they use a piecewise linear function to describe the data:

$$\begin{aligned} \frac{i\omega}{G^*(\omega)} = & i\omega J(0) + (1 - \exp(-i\omega t_1)) \cdot \frac{[J_1 - J(0)]}{t_1} + \frac{\exp(-i\omega t_N)}{\eta} \\ & + \sum_{k=2}^N \left(\frac{J_k - J_{k-1}}{t_k - t_{k-1}} \right) (\exp(-i\omega t_{k-1}) - \exp(-i\omega t_k)) \end{aligned} \quad (24)$$

The steady state viscosity η and the compliance at time zero $J(0)$ can be obtained from a plot of the compliance versus time. This is a general method and has been applied on microrheological and bulk rheology data, here it is used on data obtained from video particle tracking and optical tweezer based microrheology (5.1.2.7).

2.3. F-Actin as a Semi-Flexible Polymer Network

In the following, the most important predictions from polymer theory for mechanical properties of networks of semi-flexible polymers, like the here investigated F-actin, are briefly summarized. Already the single F-actin filament exhibits interesting mechanical features. A discussion of the force extension behavior of the F-actin filament is provided by De La Cruz *et al.*²⁴ Full descriptions of F-actin polymer networks can be found elsewhere.^{24,108–112}

Polymers can be categorized in stiff or flexible by their end-to-end distance, which is related to the persistence length l_p . F-actin is a semi-flexible filament. Semi-flexible filaments behave neither like stiff rods (microtubules) nor like flexible polymers (intermediate filaments). In several single filament assays, the persistence length of F-actin has been determined to be about 15.6–17.7 μm .^{113–115} It can be expressed in terms of bending modulus κ_B :

$$l_p = \frac{\kappa_B}{k_B T} \quad (25)$$

The persistence length is the average length over which the angular correlation is lost. At length scales below the persistence length, the polymer is stiff like a rod. At length scales much longer than the persistence length the polymer is flexible. This length scale dependency of bending stiffness is also important in compressional situations of F-actin filaments, which is usually considered as negligible since the force needed for Euler buckling F_B is anti-proportional to the second power of the length of a filament l_c :

$$F_B = \frac{\pi^2 \cdot \kappa_B}{l_c^2}. \quad (26)$$

For a typical *in vitro* length of an actin filament ($\approx 20 \mu\text{m}$) the buckling force would be about 0.001 pN, however, for short filaments this enthalpic contribution might also play a significant role ($\approx 0.4 \text{ pN}$).^{77,116} In biological processes, for example when the leading edge of a migrating cell needs to be pushed forward by actin filaments, the network is highly branched and consists of short filaments. This might be a necessity to enhance bending rigidity. Networks of F-actin, however, display a great variety of mechanical properties not only depending on single filament mechanics but rather network morphology. Viscoelasticity in melts is often described as a function of molar mass. In hydrogels such as F-actin, it is convenient to use concentration or density of filaments ρ and contour length l_c for the description of network properties. Depending on these two parameters different phases can form (see Figure 3).

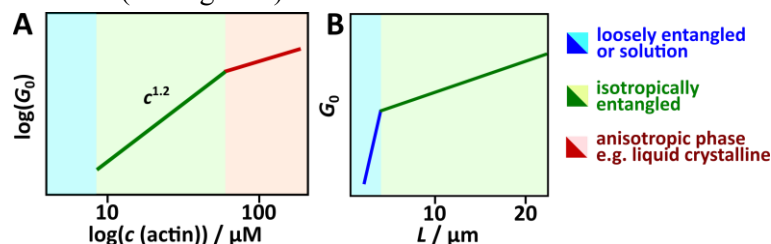


Figure 3: Phase diagrams of entangled F-actin filaments. A: Dependency of the stiffness (G_0) on the concentration of G-actin. Isotropically entangled F-actin networks can be obtained at concentrations in the range of 5–50 μM G-actin (green). Below a concentration of 5 μM , solutions of polymers or loosely entangled networks are formed (blue). At higher concentrations anisotropic phases are forming (red). B: Stiffness (G_0) as a function of filament contour length, illustrating the phase transition from loosely entangled filaments to isotropically entangled filaments dependent on the filament contour length. Adapted from Palmer *et al.*¹¹⁷ and Hinner *et al.*²⁸.

Below a certain filament density or average contour length no network will form (blue area: solution). In an intermediate regime, loosely entangled networks are formed, crossing the line from solvated polymers to loosely entangled networks. In *in vitro* experiments, stable networks under a concentration of 5 μM cannot be achieved. Only at higher density and higher polymer length

sterically entangled networks will form. Within the entangled phase F-actin can be isotropically disordered (green area: isotropically entangled) or anisotropically ordered (red area: anisotropic phase) at higher concentrations.¹¹⁸ Palmer *et al.*¹¹⁷ and others¹¹⁹ found a transition from the isotropic to a possible ordered crystalline phase at about 48-64 μM , associated with a change in network mechanics (see Figure 3 A).

In this study I am interested in semi-dilute actin networks in the isotropically disordered phase (green range in Figure 3). In this phase, actin is sterically entangled since the average contour length $l_c \approx 20 \mu\text{m}$ of a typical actin filament is longer than the average mesh size $\xi \approx 500 \text{ nm}$ (see Figure 4 A). The length distribution of *in vitro* polymerized F-actin filaments ranges from a few micrometers to around 50 μm with the most probable length around 12-30 μm .^{99,120} The schematic drawing of an isotropically entangled polymer network (Figure 4 A) illustrates the most important parameters and conceptual ideas in polymer theory. Filaments of a contour length l_c and a diameter of d form an entangled mesh with mesh sizes of ξ . The average distance between two entanglement points is called entanglement length l_e . The steric hindrance originating in the proximity of other filaments leads to a confinement of the filament to a space between the entanglement positions, which is described as a tube (according to the tube model from de Gennes and Doi Edwards) in which the filament is able to move (Figure 4 A inset). This tube and the entanglement positions greatly determine the elastic properties. On intermediate time scales these entanglement points act similar to a cross-link since the polymer cannot relax from its original position fast enough, hence the system responds rather elastically. The mechanical properties of the network in the entangled regime are entropic in nature since, via the topological constraints of the filaments, the degrees of freedom in the conformation of the filaments is reduced. Essential dynamics of the polymer that contribute to the frequency dependent viscoelastic properties are bending movements and so called reptation (Figure 4 A red indications). Reptation is the long-time diffusion of the polymer along the previously described tube, which leads to relaxation of internal stresses.

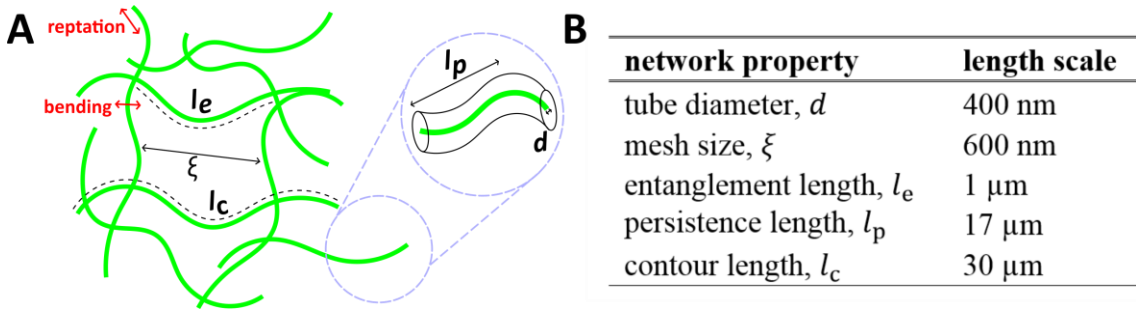


Figure 4: Schematic drawing of an entangled network (A) and respective length scales (B) of F-actin networks. A: Green lines: Polymer contours. Most important parameters describing the polymer network are indicated. ξ : Average distance between filaments = mesh size. l_e : Average length between to entanglements = entanglement length. l_c : Average length of a polymer along its contour = contour length. l_p : Persistence length. d : diameter of the filament. Inset displays also the tube which is formed by the entanglements. The two basic movements of a polymer in a tube are indicated in red: high frequency bending movements and long time diffusion along tube (reptation). B: Important length scales in F-actin networks after Isambert and Maggs.¹²¹

With the exception of the filament diameter all mentioned network parameters are averages for the broad distribution of polymer length, mesh size and entanglement length in a network. For mechanical experiments it is thus preferable to work under isotropic conditions, hence in the concentration regime between 5-50 μM , to reduce inhomogeneity. In this concentration regime the contour length of the filament is much larger than any other length scale in the system, followed by the persistence length. Both are much longer than the mesh size or the entanglement length.

Isambert and Maggs¹²¹, who gave the first description of semi-flexible polymers, reported the approximate length scales shown in Figure 4 B for the description of networks of F-actin.

As described above, network topography and its mechanical properties are strongly associated with each other. In the following, the most important predictions from polymer theory about the scaling of the shear modulus of semi-flexible filament networks are reviewed. Extensive descriptions of semi-flexible polymer theory describing the scaling behavior in a broad frequency regime were developed by Morse as well as Gittes and MacKintosh in 1998.^{110,111,122} In general it is argued that the elastic response of isotropically entangled F-actin networks to an applied strain arises from the stretching of F-actin filaments, which can be considered as an entropic spring. Figure 5 shows exemplary frequency dependent viscoelastic properties of semi-flexible biopolymer networks such as F-actin, notably the storage and the loss modulus. It is convenient to distinguish three different frequency regimes in the viscoelastic behavior of purely entangled networks. The high frequency regime, which is dominated by the bending fluctuations of the filaments (I: green area). The plateau region which is dominated by filament entanglement (II: blue region) and the low frequency/long time translational diffusion of filaments (III: yellow area). These frequency regimes are explained in more detail in the following sections.

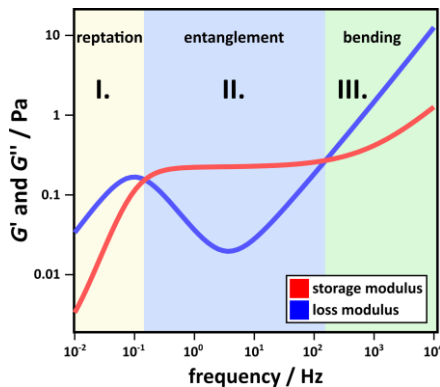


Figure 5: Schematic illustration of the frequency dependent viscoelastic properties of F-actin networks.
Red line: Storage modulus G' . **Blue line:** Loss modulus G'' . **I:** High frequency bending modes. **II:** Plateau regime, which is dominated by entanglements. **III:** Low frequency regime, reptation movement of filaments.

I. High frequency scaling: single filament relaxation modes

Above a certain frequency or below a certain time τ_{ent} the shear modulus of networks of semiflexible polymers is dominated by the bending modes of single filaments. This entanglement time is greatly dependent on the entanglement length since it is the largest possible length scale of transversal fluctuations:

$$\tau_{\text{ent}} = \frac{l_e^4 \cdot 4\pi \cdot \eta}{l_p \cdot k_B T \cdot \ln(\frac{\xi}{d})} \propto l_e^4 \quad (27)$$

The expression $(4\pi \cdot \eta)/\ln(\xi/d)$ is the transverse friction coefficient of the polymers with ξ the mesh size, d the filament diameter and η the solvent viscosity. Below this entanglement time or above this entanglement frequency the storage and loss modulus show a characteristic $3/4$ scaling with increasing frequency (see Figure 5; I. green area). This unique $3/4$ power law scaling has been observed for F-actin in many experiments^{67,117,123,124}. This frequency scaling arises from single filament bending motions. In general, upon shear strain, filaments in different parts in the network are extended or compressed. On single filament level, tension leads to a reduction of chain conformations. Due to the surrounding solvent, the undulations of the polymer within the tube are able to relax in a time dependent manner. To illustrate this time dependency we picture small deformation oscillations. The force response to these small deformation oscillations of filaments is

stiff on timescales where the bending modes are not able to relax since the filament is not able to extend. The higher the frequency, the higher the modulus since only short wavelength undulation modes are able to relax on the respective time scale and can thus contribute to extensibility. With higher frequency less bending modes can equilibrate and thus the system reacts stiffer. Hence, the high frequency scaling of the shear modulus is frequency dependent. After Morse¹¹¹ the shear modulus $G^*(\omega)$ well above the entanglement τ_{ent} is given by:

$$\lim_{\omega \gg \tau_{\text{ent}}^{-1}} G^*(\omega) \cong \frac{1}{15} \frac{k_B T}{l_p \cdot \xi^2} \cdot \left(\frac{2i \cdot 4\pi \cdot \eta \cdot l_p^3}{k_B T \cdot \ln\left(\frac{\xi}{d}\right)} \omega \right)^{3/4}. \quad (28)$$

II. Plateau region: elastic behavior due to filament entanglement

Large amplitude bending fluctuations, which would also contribute to the previously described frequency regime, are prohibited due to the restriction of the filament to its tube. Entanglements of the polymer dominate a wide range of frequencies (see Figure 5: 10^{-1} - 10^1 Hz), as described above entanglements act similar to cross-links on these time scales and the system reacts mostly elastically to external deformation. The loss tangent is smaller than one ($G''/G' \ll 1$), which means that the elastic properties of the material dominate and it behaves rather like an elastic solid. A measure of the stiffness of the system is the plateau modulus G_0 , which is the storage modulus measured in the intermediate frequency regime at the frequency, where the loss modulus exhibits a minimum. Isambert and Maggs¹²¹ as well as Morse¹¹¹ predict a reciprocal scaling behavior of the plateau modulus with the volume of a mesh, which is in agreement with the result from flexible chains:

$$G_0 = \frac{7}{5} \cdot \frac{k_B T}{\xi^2 \cdot l_e} \approx \frac{k_B T}{\xi^3} \propto \frac{1}{\xi^3}. \quad (29)$$

A better approximation¹¹⁰ would be $l_e \approx \xi^{3/4} \cdot l_p^{1/5}$. Janmey and coworkers²⁷ and Gittes and MacKintosh¹²² however propose a reciprocal scaling behavior of the plateau modulus with the fifth power of the mesh size:

$$G_0 = \frac{6 \cdot k_B T \cdot l_p^2}{\xi^2 \cdot l_e^3} \propto \frac{1}{\xi^5} \quad (30)$$

Gittes and MacKintosh's description differs especially in the scaling behavior in the plateau region (equation (31) first term) and in the loss modulus, where an additional term describes the solvent viscosity (equation (32) last term). Here the plateau region is also dependent on the persistence length l_p and the solvent viscosity of the surrounding medium contributes to the viscous dissipation. The expressions for the storage and loss modulus are:

$$G'(\omega) = \frac{6 \cdot k_B T \cdot l_p^2}{\xi^5} + \frac{k_B T \cdot l_p^2}{15 \cdot \xi^2} \cdot \sin\left(\frac{\pi}{8}\right) \cdot \left(\frac{8\pi\eta}{k_B T \cdot l_p \cdot \ln\left(\frac{\xi}{d}\right)} \cdot \omega \right)^{3/4} \quad (31)$$

and

$$G''(\omega) = \frac{k_B T \cdot l_p^2}{15 \cdot \xi^2} \cdot \cos\left(\frac{\pi}{8}\right) \cdot \left(\frac{8\pi\eta}{k_B T \cdot l_p \cdot \ln\left(\frac{\xi}{d}\right)} \cdot \omega \right)^{3/4} + \omega\eta, \quad (32)$$

respectively. Another approximate scaling behavior was introduced by Schmidt *et al.*¹²⁵ according to them the mesh size of isotropically entangled filaments in semi-dilute actin networks depends on the concentration of G-actin in the polymerization mixture $c_A [\text{mg} \cdot \text{mL}^{-1}]$ as follows:

$$\xi \approx \frac{0.3 \mu\text{m}}{\sqrt{c_A [\text{mg} \cdot \text{mL}^{-1}]}} \quad (33)$$

III. Low frequency regime: translational diffusion of filaments

Translational diffusion due to Brownian motion of the polymer along its own contour is called reptation. The time where the filament is able to diffuse from its original tube is the time where the networks goes from mostly elastic behavior to a viscous state. In this time scale stresses are able to relax since the polymer is able to liberate itself from the steric constraints. This disentanglement or reptation time is mostly dependent on the contour length of the polymer:

$$\tau_{\text{rep}} = \frac{l_c^3 \cdot 2 \cdot \eta}{\pi \cdot k_B T \cdot \ln\left(\frac{\xi}{d}\right)} \propto l_c^3. \quad (34)$$

Here the expression $(2\pi \cdot \eta) / \ln(\xi/d)$ is the longitudinal friction coefficient, which differs from the transverse by a factor of two (*vide supra*). While in theory (equation (34)) the reptation time for an actin filament of a contour length of 15 μm should be around 130 s, it was experimentally shown to be rather on the order of 1500 s.⁹⁹ An overview over reported reptation times from various techniques is given in Table 2. The shear modulus obtained from video particle tracking microscopy in entangled F-actin solutions will be discussed in chapter 5.1.2.3.

Table 2: Reported reptation times τ_{rep} for F-actin filaments in entangled networks.

$\tau_{\text{rep}} / \text{s}$	source	method
over 5000	Palmer <i>et al.</i> ¹¹⁷ (extrapolated, not observed in data)	diffusing wave spectroscopy
over 1000	Mason <i>et al.</i> ²⁶ (extrapolated, not observed in data)	diffusing wave spectroscopy
1680	Käs <i>et al.</i> ⁹⁹	direct observation
1000	Tempel, Sackmann ¹²⁶	zero shear viscosity
200	Keller <i>et al.</i> ¹²⁷	magnetic tweezer
130	Morse ¹¹¹	theoretical value
65	Sackmann ¹²⁶	magnetic tweezer
10	Apgar <i>et al.</i> ⁹⁷	multi-particle tracking

3. Biological Background

3.1. Introduction to the F-Actin Cytoskeleton

3.1.1. Cellular Architecture and Cell Mechanics

Eukaryotic cells are self-contained structures surrounded by the plasma membrane composed of different phospholipids mingled with proteins, carbohydrates and cholesterol. Only about half of the interior of the cell is water in which other cell organelles, like the nucleus, the ribosomes, the rough endoplasmic reticulum and the mitochondria to name only a few are floating along with many globular proteins. Additionally, large filaments like microtubules span the cell while others like F-actin form dense and highly structured networks providing shape and stability to the cell alongside with structuring its interior building a cytoskeleton for the cell. However, these cytoskeletal filaments do not only have a mechanical-structural role in the cell but they can also serve as scaffold for motor proteins which actively transport cargo from one part of the cell to another. Other motor proteins like myosin II generate tension between filaments driving the system far from thermal equilibrium. Additionally, hundreds of proteins interconnect and regulate the cytoskeletal proteins in a dynamic manner. On a biomolecular basis, the viscoelastic properties of living cells originate from the sum and the interplay of the above mentioned components of the cell and their mechanical properties. The membrane's major contribution originates in its incompressibility and bending rigidity. The molecular crowding in the cytosol¹²⁸ leads to increased complex viscosity in the cell. The networks formed by the biopolymers introduce strong length scale dependence of the diffusion to the mechanical properties since larger protein complexes and organelles are hindered in motion while small globular proteins can diffuse through the meshes. Additionally, the mechanical properties of cytoskeletal filaments and their networks dominate the frequency dependent viscoelastic response. In the context of this thesis the frequency dependent viscoelastic properties of the cortex of living epithelial cells and artificial model systems is investigated. Hence in the following focus is solely set on the F-actin cytoskeleton.

3.1.2. F-Actin is Sculpturing Different Cellular Compartments

There are three different types of cytoskeletal filaments, notably F-actin, intermediate filaments and microtubules. They are found in different locations in the cell and have distinct mechanical properties. While the rather stiff microtubules ($l_p \gg l_c$) spread from the nuclear region to the cell periphery, the semi-flexible biopolymer F-actin ($l_p \approx l_c$) lines the cortex of the cell and is highly interconnected with the plasma membrane and the flexible intermediate filaments ($l_p \ll l_c$) can be found in between. In an *in vitro* frequency dependent mechanical analysis Janmey *et al.*¹² found that F-actin forms the networks of highest rigidity among the cytoskeletal filaments and shows strain stiffening already at 10 % strain. A mechanism that prevents large deformations which would eventually threaten the structural integrity of a cell. F-actin was shown to deform at most about

20 % under stresses as high as 0.4 Pa before finally rupturing. The occurrence of almost exclusively F-actin in the shear stress bearing shell of cells together with its strain preventing properties makes it reasonable to presume that F-actin is the major structural protein contributing to the rheological properties of a cell and is thus major subject of discussion in cell mechanics. Figure 6 shows a schematic representation of the F-actin cytoskeleton in a migrating cell and a contact inhibited polarized cell in a confluent monolayer. Upon adhesion of cells to a surface, focal adhesions and stress fibers are formed. The former isotropy of the cellular cortex is lost and a highly organized architecture of F-actin is sculpted with different substructures serving different purposes. Stress-fibers are large and highly bundled structures cross-linked via myosin, which generate tension between focal adhesions and to produce a directed motion.^{129,130} The leading edge of a cell during migration, where focal contacts are dynamically formed, consists of lamellipodia and filopodia. Filopodia are finger-like extensions filled with parallel bundles of F-actin, whereas lamellipodia are flat protrusion of the cell where the F-actin cytoskeleton is highly branched and dynamically rebuilt.

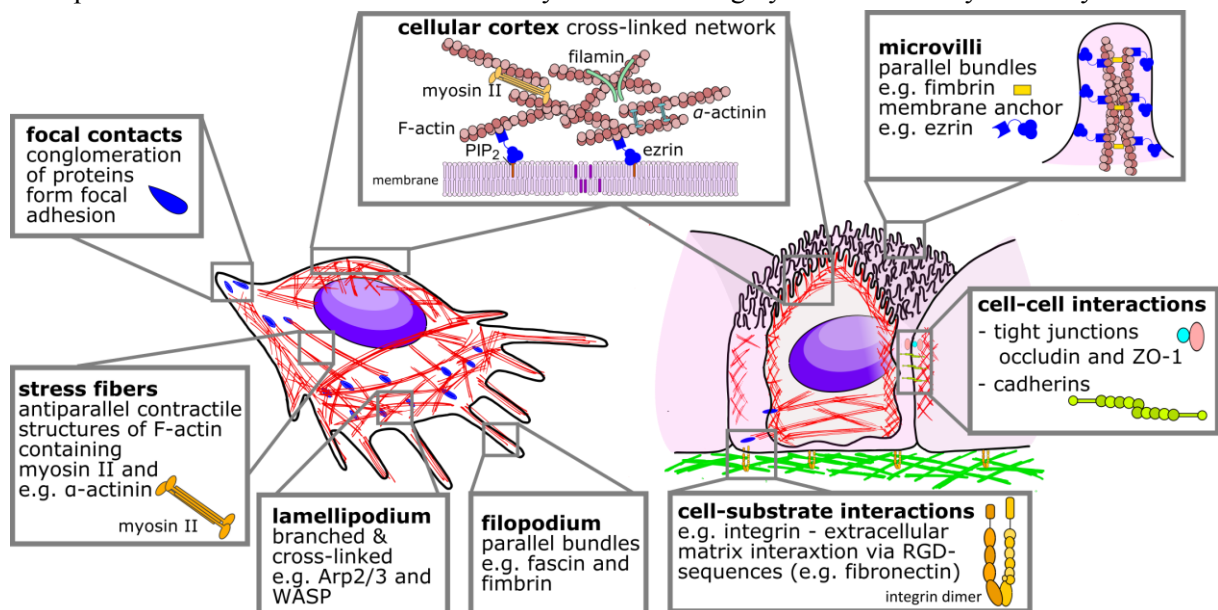


Figure 6: Overview of the architecture of the F-actin cytoskeleton on the basis of a scheme of a migrating cell (left) and a polarized epithelial cell in a confluent layer (right). For detailed explanation see text (Figure partly designed after Blanchoin *et al.*¹³).

The apical F-actin cortex of a cell is a thin shell of a thickness of approximately 200-300 nm lining the cytosolic side of the plasma membrane.^{131,132} Compared to other compartments of the cell the F-actin cytoskeleton in the cortex is homogeneously cross-linked by bundling, cross-linking and branching filaments. About 170 actin binding proteins were found in isolated blebs from HeLa cell cortices among them many cross-linkers, myosin motor proteins and membrane linkers.¹³³ It is thus a highly contractile structure in the cell, whose tension is maintained via motor proteins. The resulting mesh sizes in living cells was measured to be roughly 50-200 nm.²² The composition, thickness and mesh size of cells depends of course on the cell line, stage in cell cycle and other important factors. Upon contact with neighboring cells, intercellular contacts are formed and mechanical tension is maintained via the interconnection of the actin cytoskeleton throughout the cell layer. Alongside with the closure of the intercellular space upon forming cell-cell contacts and adhesion signaling, the cell develops a polarization leading to a strong differentiation between apical and basal part of the cell.¹³⁴ In epithelial monolayers microvilli, membrane protrusions, will form on the apical part of the cell. Below these membrane protrusions, the highly cross-linked cortex maintains tension homeostasis. In the case of MDCKII cells a contractile ring forms at the apical side of the cell layer along with the position of the adherens junctions.¹³⁵

3.1.3. The F-Actin Cytoskeleton on Protein Level

The architecture, dynamics and mechanics of the F-actin cytoskeleton have been covered in recent reviews.^{13,136} Filamentous actin (F-actin) consists of 42 kDa subunits (≈ 375 amino acids) of globular actin (G-actin). The G-actin monomer is U-shaped containing 4 subunits and has an ATP binding cleft between the two levers. The side of the hinge between these subunits is called the barbed end, the opposite side pointed end. Three isoforms (α -, β - and γ -isoform) exist, which can be distinguished by their isoelectric point. In general, the abundance of α -actin is dominant in muscle cells, whereas β - and γ - can be found in non-muscle cells. Globular actin concentration in cells can be as high as several hundreds of micromole per liter. High concentrations are needed to induce polymerization. The nucleation step, where two to three monomers have to react, is the energetically least favorable step in the polymerization process. Above a critical concentration of $0.1 \mu\text{M}$ G-actin elongation occurs at both ends of the F-actin filament but with different rates until a steady state is reached. Polymerization is favored at the barbed end (about $10 \mu\text{M}^{-1}\cdot\text{s}^{-1}$), the polymerization at the pointed end is about 10-fold slower. At the same time depolymerization takes place, which leads to a pseudo movement of the filament, called treadmilling. In the polymerization process ATP is hydrolyzed and phosphate dissociates. F-actin filament length distribution in *in vitro* experiments⁹⁹ showed a substantially broadened distribution to higher contour length with the most probable contour length being around $12 \mu\text{m}$. *In vivo* length distribution of F-actin is hard to obtain and strongly depends on the cross-links present in the respective compartment of the cell. *In vitro* length distributions are dependent on the buffer conditions, since the general net charge of actin at neutral pH is negative, thus bivalent ions such as Ca^{2+} and Mg^{2+} increase assembly dynamics in actin polymerization. Easier to obtain is the cortical mesh size which was shown to be about several hundreds of nanometers in diameter in fibroblast cells.²² The actin filament is a right handed double stranded helical biopolymer of a diameter of about 7 nm and a full helical pitch of 72 nm (2.77 nm rise per subunit).¹³⁷⁻¹³⁹ These actin filaments in the cell are interconnected by over one hundred different types of actin binding proteins (ABPs)^{136,140,141}, each serving a specialized function. Capping and severing proteins, like those from the gelsolin family, decrease the length of F-actin filaments by capping the barbed end at the filament or severing it into smaller filaments, while at the same time nucleating new filaments. In the case of gelsolin this process is activated by calcium ions and can be inhibited by PIP_2 .¹⁴² Other capping and severing proteins like cofilin have a high affinity to ADP actin and thus increase the rate of depolymerization at the pointed end. Together with the monomer sequestering protein profilin, which has a high affinity towards ATP actin, cofilin increases the treadmilling and hence the filament turnover manifold. Profilin induces nucleotide exchange and facilitates addition of ATP actin to the barbed end, whereas cofilin dissociates ADP actin from the pointed end. Proteins like formins promote the nucleation at the barbed end of the filament by increasing the local concentrations of G-actin. In the lamellipodium branch-forming proteins like Arp2/3 together with WASP shape the actin cytoskeleton and contribute to the mobility of the cell by contributing more nucleation sites. In other compartments of the cell actin binding proteins like α -actinin, fascin and fimbrin lead to parallel bundle formation as for example in microvilli and filopodia. Whereas in anti-parallel organized actin stress-fibers elevated concentrations of α -actinin and non-muscle myosin II are found.¹²⁹ An extensively studied cross-linking protein, which generates junctions between two filaments and is said to contribute strongly to mechanical signaling in cells is filamin.^{39,42,43} Other actin binding proteins as spectrin and plectrin interconnect the actin cytoskeleton with other cytoskeletal filaments. The ezrin, radixin, moesin (ERM)-family proteins anchor the F-actin cytoskeleton to the plasma membrane of the cell.^{23,143} The impact of these cross-links on the frequency dependent viscoelastic properties is object of this

work and special focus is drawn on ezrin in chapter 3.1.4. The F-actin cytoskeleton of neighboring cells is interconnected by cell-cell contacts such as adherens or tight junctions. Adherens junctions initiate adhesion to neighboring cells via the transmembrane protein cadherin and are connected to the F-actin cytoskeleton via catenins. Tight junctions regulate the transepithelial flow for example of ions. The respective transmembrane proteins here are occluding and claudin. The cytoplasmic scaffolding proteins, the zonula occludens proteins (ZO-1, ZO-2, ZO-3), interconnect the occludins and claudins to the F-actin cytoskeleton. At the basal side of the cell the cytoskeleton is interconnected to the extracellular matrix via cell-substrate interactions, for example mediated by integrins.^{144–146} Integrins are able to bind motives like the well-studied RGD-sequences (Arg-Gly-Asp) on extracellular matrix proteins like the glycoprotein fibronectin.

3.1.4. Ezrin: Membrane Anchorage of the F-Actin Cytoskeleton

The plasma membrane is an important reaction space in the cell. Many signals are transmitted into the cell via transmembrane proteins organized and brought in contact in specialized membrane regions. However, signaling proteins need to be tethered towards the plasma membrane. During many important cellular functions such as migration, cell division and endocytosis, to name only a few, the interconnection between the plasma membrane and the actin cytoskeleton is an important structural component coordinating processes at the membrane interface thereby orchestrating cell shape changes and contributing to e.g. tension homeostasis.¹⁴⁷ The ERM (ezrin, radixin and moesin) protein family provides such crucial linkage to the plasma membrane for cytoskeletal filaments especially for F-actin. On one hand ERM proteins are able to interact with various transmembrane proteins and special phospholipids in plasma membranes, while on the other hand ERM proteins possess many different binding sides for cytoplasmic proteins and cytoskeletal filaments such as F-actin and microtubuli.^{148–150} Their well-established functions as interconnectors and organizers of the F-actin cytoskeleton and the plasma membrane provide this protein family with important functions such as in the rise of cell polarity¹⁵¹, in cell division¹⁵¹, apical morphogenesis like microvilli formation¹⁵², activation of T cells¹⁵³, apoptosis¹⁵³, bleb retraction¹⁵⁴, Rho dependent signaling processes^{19,155} and many more. The ERM proteins share about 85 % sequence homology and similar structural features. Accordingly, ERM proteins possess partially redundant functions. However, in epithelial cells ezrin is predominantly expressed, whereas in endothelial cells moesin is most commonly found. In this study the interest lies thus on ezrin as contributor to tension in epithelial cells. Ezrin has three major domains (see Figure 7 A, PDB 4RM9¹⁵⁶), the C-terminal region called the C-ERMAD (ezrin-radixin-moesin association domain), which presents the F-actin binding side in the last 34 residues¹⁴⁹, a long α -helical domain (about 25 nm) and a highly conserved N-terminal FERM (four-point-one, ERM) domain, comprising three clover-leaf shaped subdomains (F1, F2 and F3, binding site \approx 6 nm in diameter), where binding to PIP₂ occurs. The interaction of the FERM domain with the plasma membrane can be manifold (e.g. CD44 or ICAM)¹⁹. One important binding partner is the phospholipid phosphatidylinositol 4,5-bisphosphate (PIP₂), which makes up for about 1 % of the phospholipids in the plasma membrane^{157,158}. In the cytosolic (dormant) state self-association masks the F-actin association side on the C-ERMAD (ezrin-radixin-moesin association domain).¹⁵⁹ Activation by conformational change¹⁶⁰ (see Figure 7 B) is believed to originate in the binding of PIP₂ at the FERM domain and phosphorylation by serine/threonine-protein kinases, at the conserved regulatory threonine residue T567, which is located at the interface between C-terminus and FERM domains in the dormant conformation.

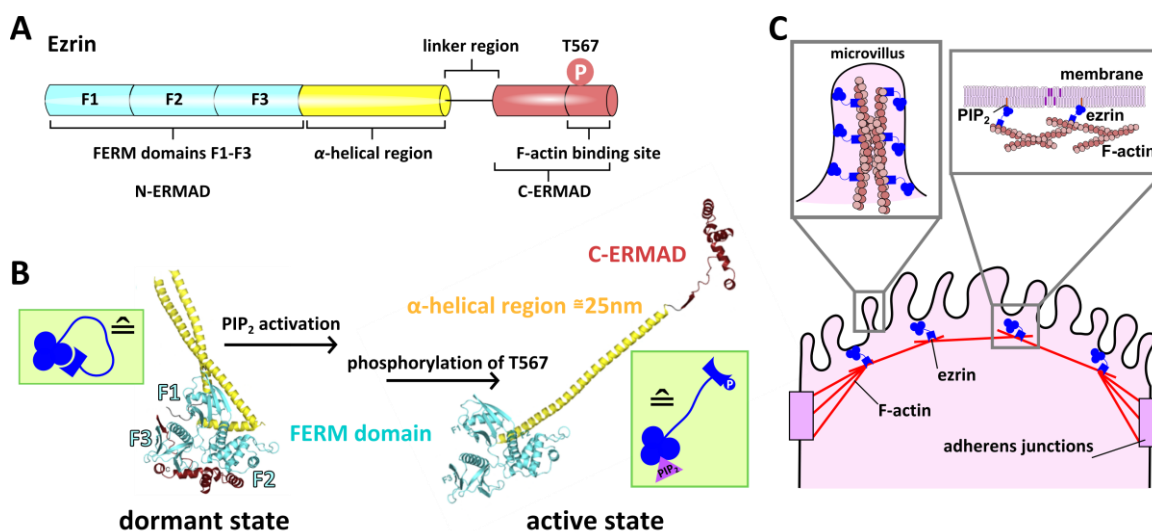


Figure 7: Structure and activation of ezrin. **A:** The different domains of ezrin. **Light blue:** FERM domain; **Yellow:** α -helical domain; **Red:** C-ERMAD with the F-actin binding site and the location of the threonine567 phosphorylation site. **B:** Cytosolic ezrin in a self-associated dormant state and in an activated state. Activation occurs upon PIP₂ binding and phosphorylation at threonine567. The homologous structure of moesin is shown (PDB 2I1J¹⁶¹). A crystal structure of the FERM domain of ezrin and its complex with the C-terminal region can be found at PDB 4RM9 and has been discussed by Phang *et al.*¹⁵⁶ Inset: Simplified scheme of ezrin used throughout the document. **C:** Scheme of the role of ezrin in epithelial cells.

However, there are implications that the process of ezrin activation might occur in a successive manner and that PIP₂ activation might be the first initial step.^{23,151,162} Activity of ERM is regulated by a multitude of signal transduction pathways mirrored in its contributions to many cellular processes. They provide the structural and biochemical link between membrane bound receptors and cytosolic signaling proteins. For example ERM proteins were shown to interact with the Rho signaling pathway, thereby interfering with the actomyosin network in the cortical actin cytoskeleton.^{19,155} Moesin was also shown to play an important role in the signaling pathway of the protein hedgehog during cell differentiation. Additionally, the role of ezrin in malignant transformation of tumor cells especially early stages of metastasis has been investigated in the past decade.^{163,164} In this context Hoskin *et al.* suggested that ezrin promotes breast cancer cell invasion via a possible mechanism of interaction with focal adhesions and invadopodia dynamics.¹⁶⁵ Li, Yu and coworkers recently published a systematic review about the prognostic value of ezrin in various cancers.¹⁶⁶ They show that ezrin expression is significantly associated with poor survival in cancer patients. There are also recent cancer treatment options targeting ezrin.¹⁶⁷ The role of ezrin in the generation of membrane tension in epithelial cell layers¹⁶⁸ and non-adherent oocytes¹⁶⁹ in different mitotic stages has already been investigated in cell mechanical studies.

3.2. Mechanical Cortex Model Systems – Bottom-Up Approaches

Obviously, time scales of signaling and molecular mechanisms of mechanosensing⁴² are highly dependent on the structure and dynamics¹⁷⁰ of cytoskeletal components on different hierarchical levels from single molecule force sensing to interaction kinetics, network properties and many more.^{30,41,171,172} Aspects of these processes as for example the outstanding role of the actin binding proteins ezrin^{163,165,173}, myosin^{14,40} and filamin^{39,43} in mechanotransduction can be studied in suitable minimal model systems under defined conditions. An overview over such model systems is given in this chapter. Bottom-up approaches have been reviewed by Schwille and coworkers.^{174,175}

3.2.1. Cross-Linked F-Actin Networks

By far the most extensively studied system is the entangled F-actin network without cross-links. The formation of isotropically entangled networks depends on the length of the filaments and the concentration of G-actin used.^{28,117} G-actin concentrations between 5 and 48 μM solutions lead to isotropically entangled networks. Mechanical properties of F-actin filaments and the 3D-organization of entangled networks are highly sensitive to buffer conditions especially salt concentrations.^{176–179} Counter ion condensation might lead to bundling transformations and to aster formation in entangled F-actin networks. The theory of the mechanics of entangled F-actin networks was discussed extensively in chapter 2.3.

In general, the effect of cross-linking proteins on the viscoelastic properties of F-actin filaments is quite diverse since every cross-linking protein interacts differently with the F-actin filament. For example α -actinin bundles filaments, whereas filamin forms V-shaped intersections between filaments. An overview is given in chapter 3.1.2. The restructuring of the network induced by cross-links has to be considered in the mechanical analysis.^{180,181} Self-organization and mechanical properties always have to be viewed in conjunction. Additionally, it has to be considered that cross-links might be compliant and may contribute to viscoelastic properties and that they are not permanent but transient in nature.

Network self-organization

The network structures obtained by different cross-links and concentrations are vast. Even F-actin networks without cross-links underlie such a structural polymorphism as discussed above (chapter 2.3). The network is best characterized by the formed mesh sizes, entanglement length, distance between two cross-links and the persistence length, which can be altered upon bundling cross-links such as fascin and α -actinin. In an attempt to generalize the bundling transitions and to obtain a master phase diagram of actin cross-linking proteins Bausch and coworkers suggested that the network self-organization upon cross-link introduction was mainly a function of cross-linker concentration and type of the cross-link (Figure 8).^{180,182} Upon changes in the concentration of cross-links, different phases could be obtained for all investigated cross-links. Leading from quasi purely entangled over weakly cross-linked and isotropically cross-linked networks to composite networks, where bundles are present, bundled networks and finally clusters of bundles. The type of the cross-link determined the occurrence of the different phases. However, all cross-links formed weakly cross-linked networks at low concentrations. Additionally, the size of the cross-link had a weaker impact on the structural organization of F-actin networks than the binding affinity and the type of the cross-link. A reproduction from their review is shown in Figure 8. However, these are general trends and it is pivotal to study the self-organization of the networks in conjunction with mechanical experiments since a broad variety of influences determine their architecture.

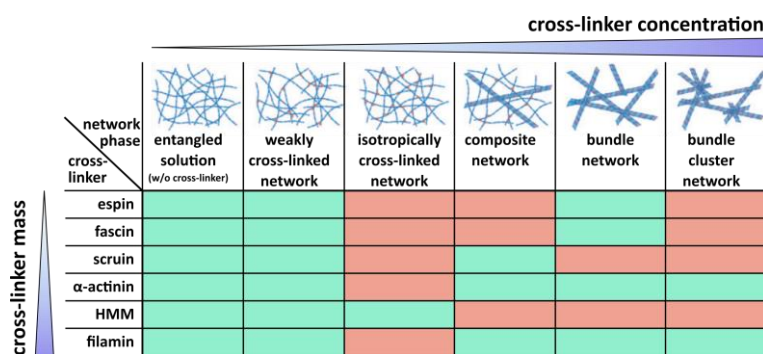


Figure 8: Overview over the structural polymorphism in cross-linked F-actin networks. Phase diagram depending on the cross-linker concentration, type of cross-link and cross-linker mass. **Green:** Phase was observed. **Red:** Phase was not observed. Reproduced from Bausch and coworkers.¹⁸⁰

Linear and non-linear viscoelasticity of cross-linked F-actin networks

In general, the three frequency regimes reviewed in chapter 2.3 are discussed separately in the literature for cross-linking proteins as well. Most of the research focusses on the changes in stiffness (elastic plateau modulus), whereas less is known about the frequency scaling of these networks. An exemplary study was published by Gardel, Weitz and coworkers.⁶⁵ Their study on a rigid (= almost non-compliant) cross-link, which is able to bundle and to cross-link filaments, showed that above a threshold concentration of the cross-link, linear elastic properties are a function of both, the relative cross-linker concentration $R = c_C/c_A$ (here $G_0(\text{scruin}) \propto R^2$) and G-actin concentration, c_A (here $G_0 \propto c_A^{2.5}$). Moreover, they defined two distinct regimes depending on the scaling behavior of the plateau modulus with the concentration of actin and the ratio of cross-link to actin, an affine entropic and a non-affine regime. The non-affine regime corresponds to the situation in a loosely entangled filament network. There, the filaments are only sterically entangled (not directly coupled to each other) and the response to a deformation might involve filament sliding out of its tube.¹⁸³ There is however also evidence of an affine model for entangled networks^{27,183}. In affine networks the filaments are either densely packed or cross-linked so that an applied force to the network will transmit the force through the network via the entanglement points or cross-links and straighten out the filaments. Here, the filaments will be straightened out upon deformation, which leads to an entropic restoring force originating from the reduced bending fluctuations of each filament (affine entropic), similar to the situation in the loosely entangled network. This behavior of cross-linked networks had already been found in simulations by Head *et al.*¹⁸⁴ Head, Levine and MacKintosh also showed that for very high densities and polymer length, the network will become affine enthalpic, stretching-out the thermal fluctuations in the network, thus under a certain force the network will rarely deform and the force response is bending dominated.

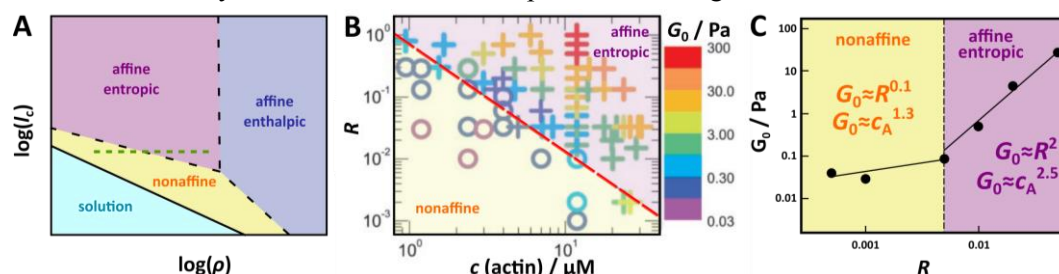


Figure 9: Approximate phase transition and scaling behavior of the plateau modulus for cross-linked semi-flexible biopolymers. A: Phase diagram depending on density of filaments ρ (compares to density of cross-links) and contour length l_c . Green dotted line shows a possible range of operation for the successive figures B+C. B and C: dependency of the plateau modulus (G_0) on relative cross-link concentration to G-actin R and G-actin concentration, c_A . Color code throughout the graphic: **Blue:** solution; **Yellow:** nonaffine; **Pink:** affine entropic; **Violet:** affine enthalpic. Adapted from Head *et al.* (simulation)¹⁸⁴, Gardel *et al.* (study on scruin)⁶⁵ and Lieleg *et al.* (study on fascin and review)^{180,185}.

Later Lieleg *et al.*¹⁸⁰ attributed this scaling behavior to cross-linking proteins in general, stating that a scaling of about $G_0 \approx R^2$ is found in the affine entropic phase, where the network is a composite of filaments and bundles. In the non-affine phase a scaling of $G_0 \propto R^{0.1}$ on the cross-link concentration and a scaling of $G_0 \propto c_A^{1.3}$ was found as reported in entangled networks.¹⁸⁵ Enthalpic and entropic stretching both contribute to the single filament force extension²⁴ and also contribute to the stress stiffening of F-actin filaments in the affine regime depending on the cross-linking density and filament density (Figure 10).^{65,186} The entropic nature can be found in most cross-linked F-actin networks, there an expected strain stiffening for a single chain of $G/G_0 \propto (\sigma/\sigma_0)^{3/2}$ is observed. However, the stress stiffening of networks cross-linked with an inactive form of the motor protein myosin (rigor-HMM) differed strongly from this scaling behavior, with a strong dependency on cross-linker concentration. Also, networks cross-linked by filamin exhibit less strain stiffening at larger stresses ($G/G_0 \propto (\sigma/\sigma_0)^{1/2}$). Zagar *et al.* attributed the latter scaling of $1/2$ to the reorientation of the filaments along the stress path. Interestingly, networks cross-linked with both filamin and myosin show a stress stiffening of $G/G_0 \propto (\sigma/\sigma_0)^1$. Nonlinear response has also been observed in tightly entangled actin networks, suggesting that entanglements might act similar to transient cross-links.¹⁸⁷

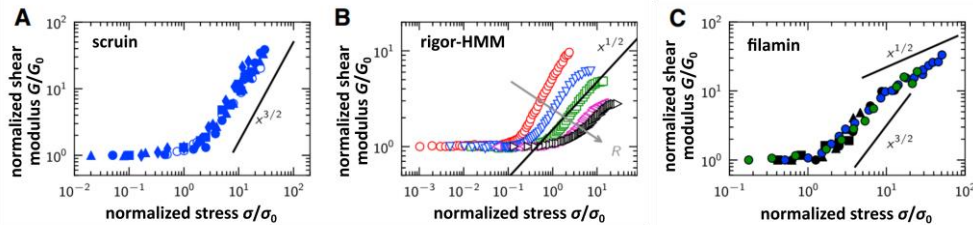


Figure 10: Stress stiffening of affine cross-linked networks. A: F-actin/sruin; B: F-actin/rigor-HMM; C: F-actin/filamin. Reproduced from Zagar *et al.*¹⁸⁶

Kamm and co-workers¹⁸⁸ took a different approach to assess the role of cross-links in the strain softening of cross-linked F-actin networks. In experiments with increasing oscillation amplitude they found strain stiffening in cross-linked networks, at a certain threshold strain softening was observed, whereas in entangled networks only strain softening was observed. They attributed this behavior to a possible mechanism of force induced unbinding of actin binding proteins from actin at large strains or unfolding of internal domains. The dependency of the bond lifetime of important signaling proteins, like integrin, filamin and myosin, on the applied force has long been discussed in the context of catch bonds and is of importance in the context of this work.^{42,46,170,189} The dependency of the crossover from strain hardening to strain softening has also been associated with the cross-linker kinetics by Maier, Lieleg and co-workers.¹⁹⁰

Transient F-actin cross-linking proteins and viscoelastic behavior at low frequencies

Apart from the scaling of the plateau modulus upon cross-linker concentration the impact of transiently bound cross-links to the low frequency regime in linear viscoelastic measurements and the implication for their function in cell signaling is of major interest. During cellular motion the morphology of the cell changes, driven by forces exerted by the dynamics of the cytoskeleton, especially the actin cytoskeleton. This highlights the importance of time scales of cytoskeletal reorganization, which also play an important role in cellular signalling.^{30,171} In other words, the actin network inside a living cell constantly needs to rearrange.³⁰ One important dynamic mechanism in the F-actin cytoskeleton is the constant polymerization and depolymerization, the treadmilling, facilitated by proteins such as profilin and cofilin as discussed previously. Moreover, the high flexibility of the actin cytoskeleton is maintained by so called transient cross-links actin binding

proteins, which bind actin only for a short period of time. Most of the above mentioned actin binding proteins are transient in nature (as highlighted in Table 3). Lieleg, Bausch and coworkers defined transiently cross-linking proteins as actin binding proteins with typical unbinding rate constants of $k_{\text{off}} \approx 10^{-3} - 1\text{Hz}$.^{34,35} However, binding and unbinding rate constants of protein complexes can strongly differ between isoforms (see Table 3 category myosin) and is also dependent on the used buffer³¹. The energy barrier for the unbinding of a transient cross-links is so low that even thermal activation at room temperature can lead to unbinding of the binding complex at time scales of minutes or seconds (see scheme in Figure 11 A). To give an idea about this low activation energy Marston found for the dissociation of F-actin and a sub-fragment of myosin an activation energy of $35\text{ kJ}\cdot\text{mol}^{-1}$.³¹ The dynamics in the cross-linking interaction leads to a cross-over in the viscoelastic moduli in the low frequency regime towards more fluid like behavior, on time scales of the unbinding rate constant (see red area Figure 11 B).³⁴

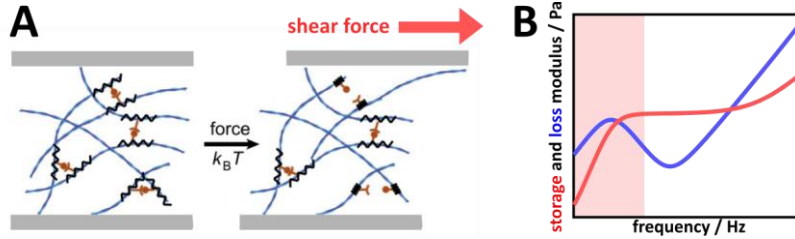


Figure 11: Scheme depicting the implications of transient actin binding proteins to F-actin networks. **A:** Transient cross-links stabilize networks and provide stability under shear conditions. However, due to thermal activation transient cross-links eventually dissociate already at room temperature. **B:** This process leads to relaxation of the network, which determines the viscoelastic response (red: storage modulus, blue: loss modulus) on intermediate to low frequencies (highlighted in red). Adapted from Lieleg *et al.*³⁵

Based on binding kinetics of actin binding proteins between actin filaments Bausch and coworkers introduced a semi-phenomenological model to describe these frequency dependent viscoelastic properties on a macromolecular basis.³⁴ This model assumes a well-known curve progression of the frequency f dependent storage $G'(f)$ and loss modulus $G''(f)$ with a power law p (usually around 0.75 for actin filaments) in the high frequency regime,¹²² with an offset G_0 accounting for the absolute stiffness of the system. Where b and d are pre-factors and f_0 is the time scale of the fluctuation of a single filament set to 1 Hz:

$$G'(f) = G_0 + b \cdot \left(\frac{f}{f_0}\right)^p \quad (35)$$

$$G''(f) = d \cdot \left(\frac{f}{f_0}\right)^p. \quad (36)$$

These terms describe the high frequency fluctuations of the filaments and the elastic behavior due to entanglement phenomenologically. To obtain an expression for the time dependency of the stress relaxation process they assumed it to be a first order decomposition of the binding complex, where the number of closed bonds N_0 decays exponentially depending on the unbinding rate constant k_{off} .

$$N(t) = N_0 \cdot \exp(-k_{\text{off}} \cdot t). \quad (37)$$

To obtain an expression in the frequency domain equation (37) is Fourier transformed:

$$\hat{N}(f) = \frac{N \cdot k_{\text{off}}}{\left(\frac{k_{\text{off}}}{2\pi}\right)^2 + f^2} - i \cdot \frac{N \cdot f}{\left(\frac{k_{\text{off}}}{2\pi}\right)^2 + f^2}. \quad (38)$$

It should be noted that this expression for the stress relaxation due to bond opening is similar to the long time relaxation in the Maxwell model (2.2.1.3). Furthermore, it was presumed that the plateau modulus is proportional to the number of bonds, $G_0 \propto N$. This assumption is valid for isotropically cross-linked semi-flexible networks.³⁴ Thus, this stress relaxation processes can be considered in the storage and loss modulus, giving the following overall equations:

$$G'(f) = G_0 - \frac{a \cdot N \cdot k_{\text{off}}}{\left(\frac{k_{\text{off}}}{2\pi}\right)^2 + f^2} + b \cdot \left(\frac{f}{f_0}\right)^p \quad (39)$$

$$G''(f) = \frac{c \cdot N \cdot f}{\left(\frac{k_{\text{off}}}{2\pi}\right)^2 + f^2} + d \cdot \left(\frac{f}{f_0}\right)^p. \quad (40)$$

The pre-factors a and c were added to account for the remaining dependencies of G_0 . These pre-factors are a measure of the dissipated elastic energy during the process of cross-linker unbinding. Bausch and coworkers interpreted the low frequency regime in microrheological data as cross-linker unbinding with a single relaxation rate comparable to the Maxwell model. However, MacKintosh and coworkers found evidence that transient cross-links might provoke multiple relaxation rates due to unbinding.^{36,191} They propose a resulting power law scaling of $\omega^{1/2}$ for the low frequency regime of the shear modulus.

Even in living cells a cross-over of the moduli in this frequency regime can be observed, however it is unclear if this relaxation process originates in the same underlying mechanism.³⁷ In well controlled polymer assays it has already been shown that non-covalent interaction forces such as hydrogen bonds and electrostatic interactions lead to liquid like behavior of these systems on intermediate time scales.^{192,193}

Table 3: Transient F-actin binding proteins and their respective unbinding rate constant k_{off} from F-actin.

actin binding protein	$k_{\text{off}} / \text{s}^{-1}$	reference
ezrin	1.3	Braunger <i>et al.</i> ²³ (complex of actin, ezrin and PIP ₂)
	1.63	Fritzschke <i>et al.</i> ³³ (complex of actin, ezrin and PIP ₂)
	1.43	Fritzschke <i>et al.</i> ³³ (ezrin actin interaction)
skeletal muscle myosin	500	Trybus <i>et al.</i> (taken from Stam <i>et al.</i> ¹⁹⁴)
	22	Trybus <i>et al.</i> (taken from Stam <i>et al.</i> ¹⁹⁴)
smooth muscle myosin	7	Veigel <i>et al.</i> ¹⁸⁹ (10 μM ATP)
	48	Veigel <i>et al.</i> ¹⁸⁹ (100 μM ATP)
non-muscle myosinIIA	1.72	Kovacs <i>et al.</i> ¹⁹⁵
non-muscle myosinIIB	0.35	Wang <i>et al.</i> ¹⁹⁶
myosin subfragment-1	0.024	Marston ³¹ (without ATP)
	3.4	Marston ³¹ (with ATP)
	0.3	Lieleg <i>et al.</i> ³⁴
heavy meromyosin (HMM)	0.0013	Marston ³¹ (without ATP)
	1.7	Marston ³¹ (with ATP)
α -actinin	0.066	Ferrer <i>et al.</i> ³²
	0.05	Miyata <i>et al.</i> ¹⁹⁷
	0.4	Goldmann <i>et al.</i> ¹⁹⁸
	0.67	Taken from Spiros <i>et al.</i> ¹⁹⁹
	6.3	Volker Watd <i>et al.</i> ²⁰⁰
	9.6	Kuhlman <i>et al.</i> ²⁰¹
filamin	0.087	Ferrer <i>et al.</i> ³²
	0.6	Goldmann <i>et al.</i> ¹⁹⁸
fascin	0.12	Aratyn <i>et al.</i> ²⁰²

Scaling behavior of the linear viscoelastic properties at high frequency

As discussed above the high frequency scaling of the viscoelastic moduli are determined by the bending fluctuations of the single filaments. Accordingly, one would assume that increasing the persistence length by altering the diameter of the fiber ($l_p \propto (d/2)^4$) would lead to a shift in frequency but to the same frequency scaling of $\omega^{3/4}$. However, Müller *et al.* found an altered scaling behavior in the high frequency regime of bundled networks in simulations and argued that the bending modulus of bundled filaments is scale dependent.¹⁹¹ In their model they were also able to retrieve a fitting parameter, which is related to the degree of bundling in the network. Purely

cross-linking not bundled proteins should however mainly contribute to the onset of the high frequency cross-over (entanglement frequency) in linear viscoelastic studies.

The effect of active motor proteins on F-actin networks

Motor proteins in F-actin networks like myosin II produce tension in the network by a power stroke between two anti-parallel F-actin filaments (see Figure 13 A). Myosin II is found in smooth muscle and non-muscle cells in the contractile machinery of the F-actin cytoskeleton.¹⁷ The typical step size of the motor movement was shown to be about 5 nm and the typical force of a power stroke is on the order of 1 pN per myosin head. However, myosin II, in contrast to myosin V, has a very short duty ratio (single filament is non-processive) and is hence only bound to F-actin for about 5 % of the time during the ATP consuming process.²⁰³ Single myosin II motors would thus diffuse from the F-actin filament after the first power stroke. While the high dynamic of myosin II is necessary for fast contraction processes in the cell, large myosin II filament bundles of about 300 myosin molecules have to form in order to produce tension between two F-actin filaments. Myosin filaments can contract the F-actin cytoskeleton at a high rate and can produce substantial forces in cells. However, there is evidence that additional cross-links have to be present in *in vitro* F-actin networks in order to contract. The interplay of network connectivity and concentration of motor-proteins in the formation of different phases of contracting networks in bulk solutions has been studied by Alvarado *et al.* (see Figure 12).¹⁸ They showed in experiment and simulations that a marginal connectivity between the filaments is crucial to achieve contractility. Increasing the ratio of motor proteins only increased local contraction (see Figure 12 A+B). Contractile networks without global rearrangement, so called critically connected actin/myosin networks, can be achieved in experiment above a certain connectivity by cross-links and interestingly with a quite high amount of motor proteins. In their simulations similar mesh formation is found, when forced unbinding of the cross-link is considered, which is supported by the above mentioned findings.

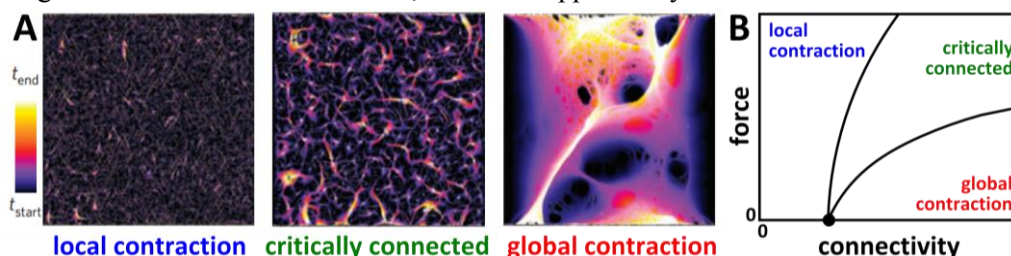


Figure 12: Three phases of active F-actin/myosin networks. A: Phases of actively contracting F-actin/myosin networks shown as time overlays. Left: Local contraction; Middle: critically connected; Right: Global contraction. B: Proposed phase diagram in space of connectivity (=cross-linker concentration) and force (=motor protein concentration). Black dot denotes the marginal connectivity needed to produce contraction. Reproduced from Alvarado *et al.*¹⁸

Transient binding of myosin is especially dependent not only on the isoform (see Table 3) but also on the adenosine triphosphate (ATP) concentration and load applied, which was shown in a study by Veigel *et al.*^{189,204} The scaling dependency of the plateau modulus with the amount of passive myosin (rigor heavy meromyosin, $G_0 \propto R^{1.2}$, where R is the relative cross-linker concentration) has been investigated by Tharmann *et al.*⁷⁴ For this system an unbinding rate was determined from linear viscoelastic data to be $k_{\text{off}} = 0.3 \text{ s}^{-1}$.³⁵

The ATP dependent contractility drives the system far from equilibrium, which leads to the violation of fluctuation dissipation theorem. Mizuno, Schmidt and co-workers capitalized on this, by using passive microrheology, which is based on the fluctuation dissipation theorem (see chapter 2.2.2.1.2), and comparing it to active microrheology. Thus, they were able to isolate the contribution of the active component.^{14,205} The model system they investigated provided connectivity by biotin-

neutravidin cross-links and myosin II motors were used to contract F-actin filaments. Interestingly, they saw no active contribution in the measured rheological spectra upon 5 h after ATP addition (Figure 13 B). After 6.8 h they could observe differences in passive and active measurements (Figure 13 C). 9.3 h after the addition they were able to show a stiffening of the networks and a reduction of the $\frac{3}{4}$ power law scaling at high frequencies to a scaling behavior of $\frac{1}{2}$ of the response function with the frequency, which could be explained by introducing tensed filaments into their model. For the sake of comparison it is helpful to note that the response function α^* corresponds to the Fourier transformed mean squared displacement and is connected to the shear modulus by the generalized Stokes Einstein equation, thus $G^* \propto 1/\alpha^*$.

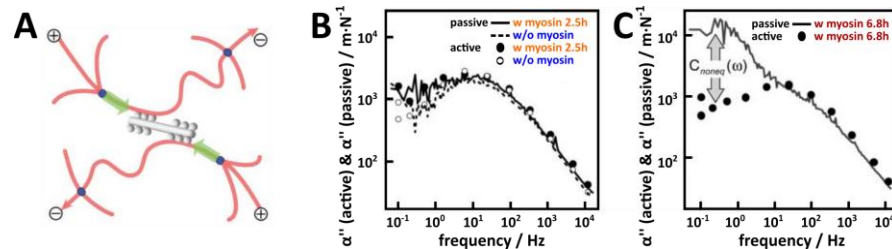


Figure 13: Impact of myosin II on the frequency dependent viscoelastic response of F-actin networks. A: Scheme of the myosin induced tension on F-actin filaments. Red: F-actin filaments; White: Myosin; Green arrows: force. Plus and minus end of the filaments are marked to show the necessity of anti-parallel orientation for the power stroke. B: Imaginary part of the response function (α'') from active and passive measurements are shown for samples without myosin and with myosin (3.5 mM) after 2.5 h. C: Comparable spectrum as in B is shown for a sample containing myosin after 5 h. The non-equilibrium contribution is indicated by an arrow. Myosin activity acts on the frequency regime between 10^{-1} - 10^1 Hz. Reproduced from Mizuno, Schmidt *et al.*¹⁴

Other rheological studies for example by Koenderink *et al.* have also shown network stiffening by more than two orders of magnitude in active F-actin networks cross-linked with myosin and filamin A ($G_0(\text{myo}\&\text{FLNa}) \propto R_{\text{myo}}^2 \propto R_{\text{FLNa}}^{0.8}$).⁶⁶ While Mizuno *et al.* and Koenderink *et al.* observed a stiffening upon myosin activity in cross-linked networks, Käs and coworkers found active fluidization for non-cross-linked networks upon myosin activity (36 μM skeletal F-actin, 0.14 μM skeletal muscle myosin, 500 μM ATP).²⁰⁶ The addition of inactive myosin II to F-actin networks resulted in substantial stiffening (5x) of the network.

Passive cross-linkers in *in vitro* studies

Many elaborate studies on the frequency dependent viscoelastic and nonlinear mechanical properties of cross-linked F-actin networks exist especially for α -actinin, filamin, fascin and myosin. α -actinin and rigor-HMM networks have shown to be especially useful to study cross-linker kinetics.^{34,36} For α -actinin studies exist, which address different mutants.^{200,207} The impact of the length of bundling cross-linkers on the linear viscoelasticity has been published by Wagner *et al.*¹⁸² In point mutations studies of the actin binding domain of fascin Maier *et al.*¹⁹⁰ studied the impact of binding kinetics on the transition from strain-hardening to strain-weakening of cross-linked F-actin networks. For the filamin dimer it was shown that it affects the linear viscoelasticity only weakly, while acting markedly on the nonlinear viscoelastic behavior.²⁰⁸⁻²¹⁰ A seminal study, which directly relates mechanical deformations of actin networks to the differential binding of filamin A to either a subdomain of β -integrin or FilGAP has been published by Ehrlicher *et al.*⁴³ This study provided a crucial link between mechanosensitivity of cross-linkers and chemical signaling, thus elucidating mechanotransduction processes. Non-transiently cross-linked networks, e.g. with a biotin-neutravidin cross-link have served as control in some studies.²¹¹

3.2.2. Membrane Coupled F-Actin Networks as Minimal Actin Cortices

Bundling, cross-linking and capping proteins of different sizes and affinities as well as active motor proteins have been studied extensively in three-dimensional networks. Insights into the role of these cross-links for the self-organization and mechanics of F-actin networks could be gathered. However, space-filling 3D models do not capture the physiological situation, since the cortex is only a few hundred nanometers thick.^{131,132} Additionally, membrane cross-linking might significantly act on the viscoelastic properties of bound F-actin networks and membrane anchorage plays an essential role in tension maintenance in the cellular cortex (see above). Thus, in order to bring these model systems closer to the natural situation in a cellular cortex, membrane linkage is of pivotal interest. Tension generation and symmetry breaking in actively contracting F-actin plasma membrane associates are best studied in liposomes as artificial model systems. Thus, the next higher order of complexity of mechanical model systems includes physiological membrane interaction and geometry. Related studies beginning with supported lipid bilayers and further capturing liposomes as artificial cortex models will be reviewed in this section.

2D model systems

The design of so called minimal actin cortices (MACs) has been reviewed by Vogel, Schwille and co-workers as well as Tanaka and Sackmann.^{174,212,213} Lipid bilayers can either be prepared on solid supports as for example glass, mica and silicon wafer, or on soft polymer cushions or lipopolymer 'tethers'. Surface properties of a solid support can determine the spreading process of liposomes, favor mono- or bilayers and can alter the diffusivity of membranes. Porous materials can also be used as solid supports providing free standing lipid bilayers which might capture the physiological conditions more closely. Moreover, they provide the possibility to perform atomic force measurements on the membrane-cortex ensemble. Vesicles (small or giant unilamellar vesicles) composed of phospholipids and respective pinning-points for F-actin filaments or cross-linking proteins are subsequently spread on these surfaces (see Figure 14 A). Typical membrane anchorage strategies can be pure electrostatic interactions either via bivalent ions that bind to the negatively charged F-actin or the utilization of positively charged membranes. Stable and reproducible results can be achieved by pinning the F-actin network to the membrane by the interaction of streptavidin recognizing biotinylated lipids and G-actin. In addition to these artificial cross-links, the employment of physiological cross-links has been studied but not to the same extent. Some studies on the transmembrane protein ponticulin have shown strong interactions with F-actin filaments^{214,215} and Merkel *et al.* succeeded to reconstitute the membrane anchorage protein complex spectrin/ankyrin in giant unilamellar vesicles.²¹⁶ For physiological cross-linking proteins it is crucial to investigate if they are active under the experimental conditions. For example activation of ezrin is said to be dependent on PIP₂ activation and phosphorylation. Consequently, most recent studies on membrane bound actomyosin networks have been performed with either biotin-streptavidin anchorage or Ni-functionalized lipids and His-tagged proteins as for example fimbrin and ezrin (see Figure 14 B).²¹⁷⁻²²⁰ Others use methylcellulose to confine F-actin networks in proximity to a lipid bilayer.^{221,222} However, substantial progress has been made in accomplishing reliable and controllable minimal actin cortices with physiological membrane cross-links.^{223,224} Their utilization to study self-organization processes, dynamics and mechanics in these more physiological model systems now seems feasible. In membrane network composites with strong artificial interaction it has already been shown that lateral membrane diffusion is altered and that the single components of the construct are less motile.^{219,225} Furthermore, the role of the anchorage in lipid phase separation has been discussed.²²⁵ In systems containing actomyosin it has been shown that already disordered F-actin networks are able to contract cooperatively²²¹ even though the

antiparallel geometry should favor contractility²²⁶. It has also been shown that the underlying mechanism of active in plane contraction is filament sliding.²²² Filament fragmentation upon actively forced buckling has been observed.^{217,220} Many studies focus on the organization of such systems but viscoelastic properties are less studied.

In actively contracting 2D networks boundary conditions are of great importance since global contraction by mere activation of the network via ATP would result in less defined contraction and larger inhomogeneity. A notable technique has been reported, where myosin II motors were inhibited by blebbistatin during the preparation. Blebbistatin can be destroyed upon radiation with blue laser light, thus contraction can locally be switched on (Figure 14 C+D).^{221,227}

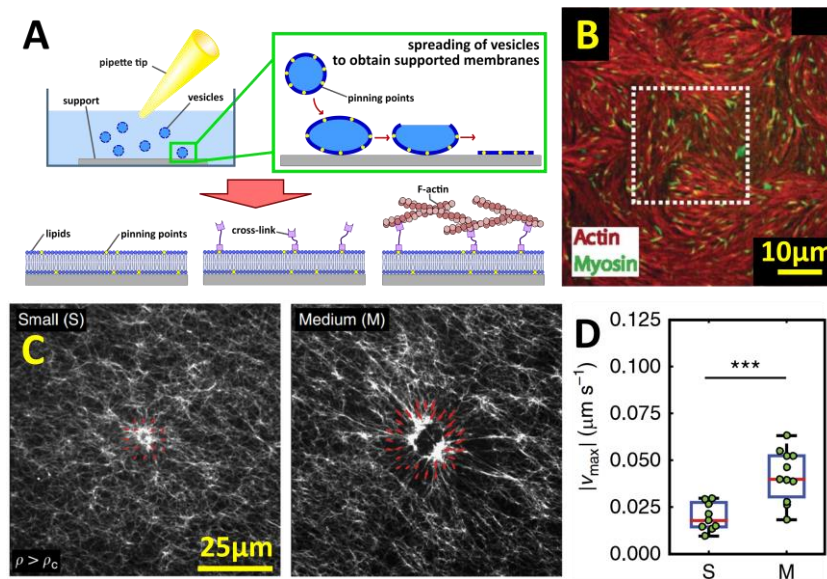


Figure 14: 2D minimal actin cortices. **A:** Schematic drawing of the preparation of quasi 2D minimal actin cortices on solid supported membranes or other substrates. Membrane bilayers are obtained from vesicle spreading. Pinning-points and cross-links provide membrane anchorage for pre-polymerized F-actin. **B:** Static membrane bound actomyosin model cortex reported by Gardel and coworkers.²¹⁷ Red: F-actin filaments; Green: Myosin micro-filaments. **C:** Contraction and restructuring of a 2D confined actomyosin network (methylcellulose) upon local myosin activation (inhibition of blebbistatin) on different length scales. **D:** Respective contractile velocities at the boundary reported by Gardel and coworkers.²²¹

3D model systems

In spherical 3D model systems, where the actomyosin network is organized in a thin shell at the inner or outer leaflet of a lipid structure, the boundary condition is periodic and hence, the tension is uniformly distributed over the surface.

Basically five different approaches can be made in the design of three-dimensional minimal cortex model systems (see Figure 15). First, similar to solid supported systems on flat surfaces, the pinning-point containing membrane can be organized around a microsphere. Sykes and coworkers used such a model system to study the possible force that ActA induced actin polymerization can provoke on a bacterial cell wall.²²⁸ Bussonnier *et al.*²²⁹ optically trapped such a model system and performed elastic measurements as well as creep measurements on the surrounding actin shell. Another quite reproducible way to obtain shell like cortices is to use either ‘water in oil’ or ‘oil in water’ droplets. A water in oil assay was used by Shah and Keren²³⁰ to study the spontaneous symmetry breaking by myosin induced actin flows, a process relevant in cell division. Van der Gucht and coworkers⁶⁴ used oil in water emulsion droplets to study the mechanics of actomyosin networks in shell like structures. Using particle tracking microrheology they were able to show that the amount of membrane-actin cross-link determined the overall stiffness of the system and that active stiffening of the cortex by myosin resulted in further stiffening (see Figure 16).

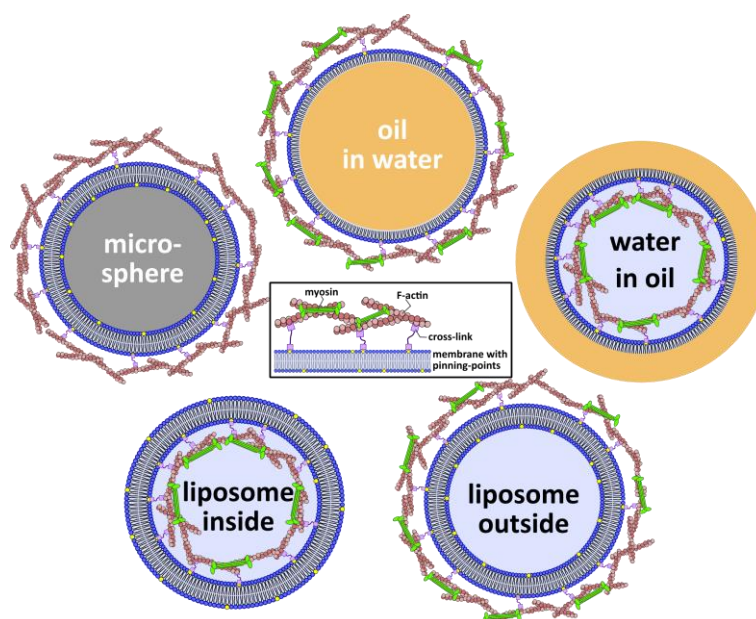


Figure 15: Overview about the different 3D minimal actin cortex models. The interface of F-actin and membrane is of central importance (sketched in the box in the middle). Above: Structurally supported mono- or bilayers using microspheres or oil interfaces to determine the shape of the model system. Below: Liposome based strategies: either F-actin networks are bound to the outer (right) or inner (left) leaflet of the vesicles.

These model systems comprise the geometry of cellular cortices. However, the interaction with bead surfaces and oil interfaces does not provide the structural flexibility inherent to plasma membranes. In the past years free-standing liposome based model systems have been invented. In an early study Häckl, Bärmann and Sackmann²³¹ were able to observe shape changes such as cone-shaped protrusions of giant vesicles filled with F-actin. Here again, the F-actin cortex can be organized at the outer or inner leaflet of the bilayer, where the connection to the inner leaflet captures the situation in the cell better whereas the outer leaflet is more easily accessible. In a mechanical study on the latter system, Caorsi, Sykes and coworkers²³² managed to measure the increase in tension induced by actomyosin contractility. They were able to show that following a 1.3-fold increase the tension can be maintained throughout the artificial cortex. Above a 2-fold increase in tension the minimal cortex ruptures. Actomyosin networks bound to the inner leaflet of a liposome are the gold standard for such model systems. Guevorkian, Sykes and coworkers²³³ reinforced the mechanical importance of the correlation between the length of pulled membrane tethers and F-actin-membrane interaction in a respective assay.

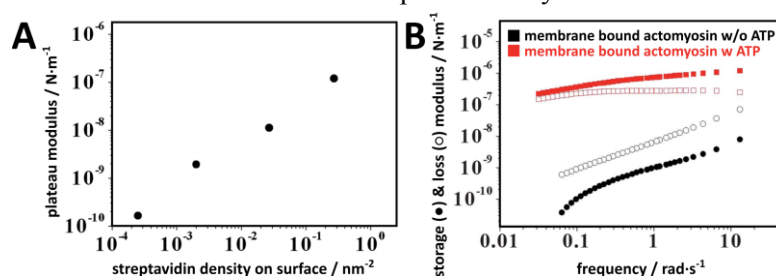


Figure 16: Frequency dependent viscoelastic properties of an actomyosin network bound to a lipid interface via streptavidin in a 3D oil in water approach. **A:** The scaling of the plateau modulus with the surface density of streptavidin is shown (w/o myosin). **B:** The storage (filled symbols) and the loss (open symbols) modulus of a membrane bound actomyosin network is shown in absence (**black**) and presence (**red**) of ATP.

Similar to a study of Bausch and coworkers who used actively driven rod-like microtubules to shape the form of vesicles²³⁴, Tsai and Koenderink²³⁵ used bundled F-actin filaments without motor proteins to induce biomimetic shape changes of vesicles. By changing the osmotic pressure they

showed that the shape changes originate in an interplay between bending rigidity of the membrane and F-actin bundles. Loiseau, Bausch and coworkers²³⁶ generated actively contracting vesicles. Due to the increased pressure, the system started to produce blebs and tether-like protrusions.

Until now, little is known about the frequency dependent properties of F-actin membrane composites. Additionally, the above mentioned systems use artificial (biotin-streptavidin) or at least semi-artificial (physiological cross-links to the F-actin network pin-point to the membrane via Ni-Hist-tag interactions) linkage to the plasma membrane. Altered time scales of binding of the natural membrane linkage might lead to differences in the mechanical properties of these systems.

3.3. Mechanical Cortex Model Systems – Top-Down Approaches

While the afore-mentioned bottom-up approaches provide a good understanding of the role of single actin binding proteins, top-down approaches are commonly used to study more complex assemblies of cellular components. In the following so-called functional networks (3.3.1) and scaling principles found in living cells (3.3.2) will be reviewed.

3.3.1. Functional Networks

The term functional network, as used here, stands for F-actin networks which were isolated from living organisms and where the metabolic machinery is absent. These model systems are especially suitable to investigate mechanical properties of the bare F-actin cytoskeleton including all actin binding properties as present in the living organism. In special model systems even the architecture of the actin cytoskeleton and its interconnection to the membrane is maintained and interesting questions can be addressed regarding the respective substructure of the cell. Thus, these functional networks represent interesting interim stages between artificial model systems and living cells.

One interesting experimental technique to obtain all components of an *in vivo* actin cytoskeleton is the extraction of cytoplasmic extract of oocytes from the South African clawed toad *Xenopus laevis*. In an experiment, Fletcher and coworkers⁷⁷ used these extracts for *in vitro* polymerization of an actin network between an AFM cantilever and a surface to further perform oscillatory microrheology experiments (Figure 17 A). Interestingly, these networks showed quite similar frequency dependent linear viscoelastic properties as found in living cells. Especially, the power law scaling of the shear modulus with frequency $G^*(\omega) \propto \omega^\alpha$ was found to be $\alpha = 0.12$, which is similar to the one found in living cells (about 0.2). The overall stiffness of the system was also comparable with the one found in cells (around 800 Pa). However, the thickness of the actin droplet studied here was much larger than a typical cortex thickness. Additionally, results were obtained from non-linear measurements. Not only did the system show the expected stress stiffening but also stress softening above a critical stress. They hypothesized that the underlying mechanism for this stress softening was induced buckling of short and highly cross-linked filaments orthogonal to the direction of stress in the network, leading to a softening in the direction of stress. In bottom-up model systems stress stiffening is found in many cross-linked F-actin networks (see Figure 10). However, these systems usually break irreversibly at high applied stresses and do not show reversible stress softening. This finding suggests that the non-linear response of F-actin filaments *in vivo* might also be of enthalpic nature not only entropic as suggested for *in vitro* model systems. The difference lies in the contour length and connectivity of the networks. In dendritic networks, observed in the leading edge during cell migration, or here in highly cross-linked networks with a high amount of nucleation promotion factor, actin filaments are much shorter than in *in vitro* systems ($< 3 \mu\text{m}$ for cells²¹ and about $20 \mu\text{m}$ in *in vitro* preparations⁹⁹). The bending rigidity is thus

much higher and they are able to resist compression. Above a certain stress however the filaments orthogonal to the direction of stress are bend resulting in a softening in stress direction. In dendritic F-actin networks such as in the lamellipodium on the leading edge of a migrating cell this increased bending rigidity, coming from shorter filament length, might be essential to push the membrane forwards.

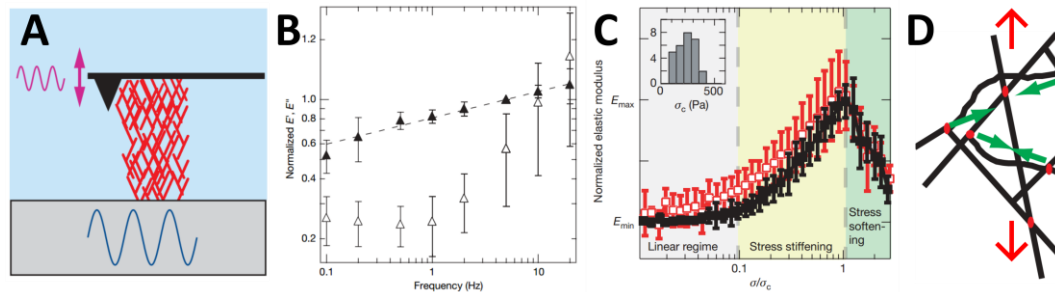


Figure 17: Dendritic actin networks from *Xenopus laevis* egg extracts. **A:** The dendritic F-actin network (red) was polymerized between a surface and a cantilever. Atomic force microscopy based microrheology was performed. **B:** Linear viscoelastic measurements typical weak power law scaling with frequency and a rather high elastic modulus was found ($E(@1\text{Hz}) \approx 800 \text{ Pa}$). **C:** Non-linear viscoelastic measurements. Interestingly, not only stress stiffening (yellow region) but also stress softening (green region) was found. **D:** Hypothesis for the underlying stress softening, induced buckling (green arrows) of short and highly cross-linked filaments, orthogonal to the direction of stress (red arrows) in the network lead to a softening in the direction of stress. Figures reproduced from Chaudhuri, Parekh and Fletcher.⁷⁷

Others have used the *Xenopus laevis* extract to reconstruct model systems similar to the above described 3D minimal actin cortex models.²³⁷ The natural mix of proteins produced a homogen shell in a water in oil emulsion assay showing random myosin driven fluctuations. Another way to isolate the cortex of living cells is to isolate cortex material from blebbing cells.¹³³ An interesting functional network to study force induced mechanosignaling was introduced by Sawada and Sheetz.²³⁸ In their study they seeded cells on elastic gels and washed away all soluble components of the cell with a detergent called Triton-X. The elastic gels allowed stretching of the bare cytoskeletons of 10%. In this assay they tested stretch dependent binding of focal adhesion proteins to these Triton-X cytoskeletons. They found that paxillin, focal adhesion kinase and p130Cas showed increased binding in stretched cytoskeletons, whereas binding of vinculin was unchanged and binding of actin was decreased. In another assay isolated apical membrane or cortex patches can be studied, when the apical membrane-cortex associates are removed from living cells in a controlled manner. These cell cortex fragments can be obtained by pressing a sticky surface to the apical part of a cell layer and subsequently taking it off. Beforehand the cytoskeleton is weakened by osmotic swelling of the cell. If porous substrates are used to attach the apical surface of cells atomic force microscopy experiments can be performed on the free standing part spanning the pores. Using cortex patches Fine, Janshoff and coworkers¹⁶⁸ have already provided evidence that the cellular membrane provides an essential contribution to the mechanical response of cells. Nehls and Janshoff²³⁹ developed a model to assess the area compressibility of such cortical patches and showed that enzymatic activity by proteases and cross-link fixation can alter the area compressibility modulus.

3.3.2. Viscoelastic Properties of Living Cells

The study of cellular mechanics has strongly evolved in the last decades and has become a broad field including many different measuring techniques and tools to assess different characteristic mechanical parameters. These techniques differ in their range of sensitivity, loading rates and length scale they probe.^{240–242} In general, the description of whole cell mechanics can either view the cell as a bulk structure or as a liquid droplet with an isotropic tension in the shell. Even though continuum models describe bulk properties and thus inherently do not provide information about molecular origins of the mechanical properties, the biological origin of the obtained force responses can be assessed with different techniques such as (bio)chemical manipulation of the cells (inhibition or reinforcement of structural proteins). Elaborate methods have been developed to attribute the overall tension to specific contributions such as the incompressibility of the membrane, the cortical tension and the membrane tension.^{143,168} It is evident that different mechanical assays probe the force response of different sections and structural complexes of the cell. Force indentation experiments by atomic force spectroscopy for example probe the apical cellular cortex. Dependent on the indentation depth, the force response may originate in either membrane tension or area compressibility of the membrane or upon large indentation even contributions from the nucleus and other cellular components. In contrast tracer particles injected to a cell probe their local environment, hence length scales on the order of their diameter.²⁴³

In microrheology studies of living cells, where the linear viscoelastic properties of cells are probed, a weak power law scaling of the viscoelastic moduli with the frequency is typically found (Figure 18 A).^{38,68,244,245} Higher scaling behavior is only sparsely reported.^{68,73} A comprehensive review about the rheological properties of living cells was published by Kollmannsberger and Fabry.²⁴¹ The observed weak power law behavior of living cells conforms closely to an empirical law called the power law structural damping model, which was introduced by Fabry *et al.* for the description of cells:³⁸

$$G^*(\omega) = G_0 \cdot \Gamma(1 - \alpha) \cdot \cos\left(\frac{\pi}{2}\alpha\right) \cdot \left(1 + i \cdot \tan\left(\frac{\alpha\pi}{2}\right)\right) \cdot \left(\frac{\omega}{\omega_0}\right)^\alpha + i\omega\eta \quad (41)$$

The parameter G_0 is the scaling factor of the stiffness, α is the power law coefficient, η the viscosity of the sample and Γ the gamma function. Using power law fits to describe the rheology of cells is common since cells exhibit a weak power law rheology ($\alpha \approx 0.2$) over a broad range of frequencies (for frequencies between 1-1000 Hz⁶⁸). Power laws found in this context can be interpreted in terms of soft glassy rheology²⁴⁶ or active soft glassy rheology¹⁵. Essentially the (active) soft glassy rheology model connects the structural disorder of soft material and its meta-stability to the rheological behavior. Key properties of glassy materials are that they are not in thermodynamic equilibrium below the glass transition state and that their physical properties change with time, a process called ageing (reviewed in Mandadapu *et al.*²⁴⁷). Fabry *et al.* attributed the power law rheology of cells to the remodeling of the cortex due to active contractile forces of motor proteins such as myosin filaments. In this model, the rheology of a cell is described by many disordered elements, which interact via attractive and repulsive interactions and are temporarily stationary as they are trapped in energy wells. However, the activation energy to cross the barrier eventually can be overcome by active contributions of myosin and other motor proteins which rise the so-called “effective temperature”. Once in another energy well the system is stressed and needs to deform. The power law exponent in this framework can be interpreted as the agitation energy of myosin in the cell relative to the average binding energy between actin and myosin. If the power law coefficient, hence the myosin activity, is high the cell is able to flow. Otherwise, if the activation energy is not high enough to overcome the energy barriers, the power law coefficient approaches

zero and the cell is quasi elastic. Kollmannsberger, Fabry *et al.*^{75,241} also assessed the stress stiffening behavior of living cells. By performing force steps on living cells they found stress stiffening in all probed cells. They observed that stiffer cells showed less stress stiffening with externally applied stress than softer cells. Assuming a linear behavior of the differential elastic modulus ($K' = d\sigma/d\varepsilon$, measured at fixed frequency) with the sum of the external stress σ_e and the internal pre-stress σ_p , resulting from contractility within the cell:

$$K'(\sigma) = K'_0 + m \cdot (\sigma_e + \sigma_p), \quad (42)$$

they were able to describe the data from cells with different pre-stress well. Where K'_0 is the linear stiffness with no force applied and m a parameter that describes the dependency of the stiffness on the stress. Plotting the obtained pre-stress against the differential modulus they found a universal scaling of the differential stiffness with the pre-stress ($K'(\sigma) \propto \sigma_p$ Figure 18 B). These observations also suggest that the applied external stress is smaller than the internal pre-stress. Together with the observation that the weak power-law scaling with frequency is not independent from the elastic modulus, they proposed a dependency of the power law coefficient α with the pre-stress σ_p :

$$\alpha(\sigma_p) = \frac{\ln(J_0 \cdot (K'_0 + m\sigma_p))}{\ln(\tau_0)}. \quad (43)$$

With J_0 the compliance at time τ_0 . Thus, they proposed a dependency of the power law scaling with the stress that is rising from the active contractility of the cells and hence, myosin II activity. Accordingly, this weak power law scaling does not rise from bending fluctuations and does not show a 3/4 scaling. Recently a power law scaling of $\alpha \approx 0.9$ was found in a high frequency (1 kHz-100 kHz) AFM study⁶⁸ on fibroblasts, which might be comparable to the bending dominated frequency regime found in in model systems.

At higher applied stresses or strains than reported above, non-linear stress stiffening has also been observed by some working groups.²⁴¹ Interestingly, the differential modulus exhibits the same scaling behavior ($K'(\sigma) \propto \sigma^1$) as found in linear viscoelastic measurements with pre-stressed cells.

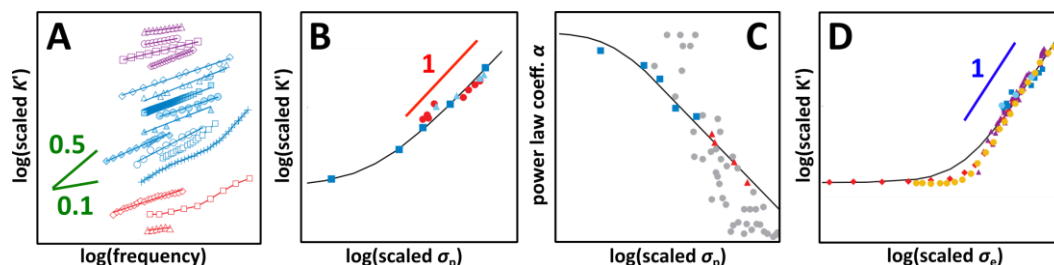


Figure 18: Scaling behavior of living cells after Kollmannsberger and Fabry. A-C: Linear viscoelasticity. A: Weak power law scaling of the scaled elastic modulus with the frequency (0.1-0.5). **Blue:** Cells; **Violet:** Cell layers and tissue; **Red:** Actin networks cross-linked with different proteins. B: Scaling of the scaled elastic modulus with pre-stress. C: Scaling of the power law coefficient with pre-stress. D: Non-linear viscoelasticity, stress stiffening in dependency of externally applied stress. Reproduced from Kollmannsberger and Fabry.²⁴¹

In general, well-studied immortalized cell lines are used in fundamental research rather than primary cultures to provide well controlled model systems which can be compared throughout the literature. Among the immortalized cell lines some from the same origin possess different metastatic potential and can be used in comparative assays.⁵⁹ Additionally, biochemical methods such as knock-down studies of specific proteins can be compared to wild type cell lines. Signaling cascades can be activated in order to activate the tensile stress stiffening. Moreover, a broad variety of cytoskeletal drugs is known that can be used to interfere with the actin cytoskeleton as for example blebbistatin, cytochalasin D, jasplakinolide, latrunculin A and unspecific cross-linking like GDA and PFA.^{38,69} The effect of material properties such as porosity or elasticity of surfaces on the mechanical properties of cells can as well be studied in cell culture assays.

4. Methods and Experimental Procedure

4.1. Methods and Experimental Procedures to Study Cortex Model Systems

4.1.1. Preparation of Artificial Model Systems

Ezrin (T567D mutant) expression in *Escherichia coli* cells and purification as well as preparation of membrane bound artificial model systems (4.1.1.1, 4.1.1.2 and 4.1.1.6) was performed by Markus Schön (Institute of Organic and Biomolecular Chemistry, Georg-August-Universität, Göttingen, Germany).

4.1.1.1. Production of Small Unilamellar Vesicles

Lipid films ($0.8 \text{ mg}\cdot\text{mL}^{-1}$) were produced by solving the desired amount of phospholipids and fluorescence labeled phospholipids in chloroform followed by removal of the chloroform with the help of a water bath ($30 \text{ }^\circ\text{C}$) and a gentle nitrogen steam. Afterwards the lipid films were dried in a vacuum oven at $40 \text{ }^\circ\text{C}$ over night. The formed lipid films were stored at 4°C . 1-palmitoyl-2-oleoyl-*sn*-glycero-3-phosphocholine (POPC), 1,2-dioleoyl-*sn*-glycero-3-phosphocholine (DOPC), phosphatidylinositol 4,5-bisphosphate (PIP_2) and 1,2-dioleoyl-*sn*-glycero-3-phosphoethanolamine-N-(cap biotiny) (Biotin-DOPE) were purchased from Avanti Polar Lipids, Alabaster, Alabama, United States. ATTO 390 labeled 1,2-dioleoyl-*sn*-glycero-3-phosphoethanolamine (Atto390DOPE) was purchased from ATTO-TEC, Siegen, Germany.

Table 4: Overview of lipid film compositions used in this study.

sample name	matrix lipid / mol%	PIP_2 / mol%	Biotin-DOPE / mol%	Atto390DOPE / mol%
PIP_2 3 mol%	POPC 96	3	-	1
PIP_2 5 mol%	POPC 94	5	-	1
Biotin-DOPE 1 mol%	DOPC 98	-	1	1
Biotin-DOPE 3 mol%	DOPC 96	-	3	1

Small unilamellar vesicles (SUVs) were obtained by dissolving the lipid films in $500 \mu\text{L}$ spreading buffer at room temperature for 30 min. Afterwards the solution was mixed with a vortex mixer (3 x 30 s) and sonicated for 30 min (cycle 4, 60 %, Bandelin sonoplus with UW2070, Bandelin electronics, Berlin, Germany), which leads to formation of SUVs.

Table 5: Overview of spreading buffer composition.

spreading buffer	composition
citrate buffer for lipid membranes containing PIP ₂	20 mM natrium citrate 50 mM KCl 0.1 mM EDTA 0.1 mM NaN ₃ pH 4.8
phosphate buffered saline (PBS) for lipid membranes containing biotinylated DOPE	136.9 mM NaCl 2.7 mM KCl 8.1 mM Na ₂ HPO ₄ 1.5 mM KH ₂ PO ₄ pH 7.4

4.1.1.2. Preparation of Hydrophilized Solid Supports

Silicon wafer with a 100 nm siliconoxide layer on top (Silicon Materials, Kaufering, Germany) were cut to fit into a home built sample holder (waver surface: 1.0 x 2.0 cm²) using a glass cutting device. The wafer surface was hydrophilized in an aqueous solution of hydrogenperoxid and ammonia (1:1:5 H₂O₂/NH₃/H₂O) for 20 min at 70 °C. Subsequently the waver was rinsed in ultrapure H₂O (< 20 mΩ·cm), dried in a gentle nitrogen steam, mounted on a Teflon sample chamber and covered with the spreading buffer (see Table 5).

For optical tweezer measurements as well as temperature dependent measurements sterile glass bottom petri dishes (Ibidi, Martinsried, Germany) were used instead of silicon dioxide wavers. The surface of the glass bottom petri dishes was treated as described above.

4.1.1.3. Bead Stock Solutions for Video Particle Tracking and Optical Tweezer Experiments

Stock solutions of microspheres for the microrheological measurements were prepared in aqueous solutions of 0.8 % solids. Stock solutions were stored at 4 °C.

Table 6: Overview over beads used in this study.

beads	properties	manufacturer
4.95 μm (4.8-5.2 μm)	fluorescence red $\lambda_{ex} \approx 660$ nm, $\lambda_{em} \approx 690$ nm carboxylate-modified polystyrene	Bangs Laboratories, Indiana, United States
2 μm (1.9-2.1 μm)	fluorescence red $\lambda_{ex} \approx 575$ nm, $\lambda_{em} \approx 610$ nm carboxylate-modified polystyrene	Sigma-Aldrich, St. Louis, Missouri, United States
2.01 μm (1.8-2.2 μm)	non-fluorescent silica particles plain	Bangs Laboratories, Indiana, United States
300 nm n/a	fluorescent red silica particles plain	Kisker, Steinfurt, Germany

To probe the local viscoelastic properties of artificial model systems of the actin cortex by video particle tracking, mainly fluorescent carboxylate-modified polystyrene latex beads with a diameter of 2 μm were used. For comparison measurements with larger (4.95 μm) and smaller (300 nm) beads were performed. Non-fluorescent beads were used to show the bead incorporation into the network (see Figure 22). For optical tweezer measurements the fluorescent carboxylate-modified polystyrene latex beads with a diameter of 2 μm were used.

4.1.1.4. F-Actin Polymerization

The lyophilized powder of non-muscle G-actin (Cytoskeleton, Denver, Colorado, United States) was solved in ice-cold ultrapure H₂O (< 20 mΩ·cm) to give a stock solution with a concentration of 10 mg·mL⁻¹. Aliquots (à 10 μL) of this stock solution were flash-frozen in liquid nitrogen and stored at -80 °C. Before usage of G-actin G-buffer (see below) was added to give different concentrations between 0.36 - 1.5 mg·mL⁻¹. Afterwards, aqueous solutions of dithiothreitol (DTT, final concentration 0.5 mM) and adenosine 5'-triphosphate (ATP, final concentration 0.2 mM) were added. The solution was stored on ice for 1 h and centrifuged afterwards for 20 min (17,000 g at 4 °C) to remove potential oligomers by precipitation. For samples in which the F-actin polymer networks were attached to the lipid membranes via neutravidin, a mixture of biotinylated G-actin (Cytoskeleton, Denver, Colorado, USA) and G-actin (1:5) was used. For microrheology measurements, approximately 1 μL of the respective bead solution (see 4.1.1.3) was added and the suspension was thoroughly mixed with a vortex mixer before polymerization was induced by adding 10 % (v/v) of a high salt polymerization buffer (see below). The polymers were allowed to grow for at least 30 min. Afterwards, AlexaFluor488-phalloidin (0.01 mol% compared to G-actin monomers, Thermo Fischer Scientific, Waltham, Massachusetts, United States) was added to fluorescently label the actin filaments. For staining, the sample was incubated for at least 60 min with the labeled-phalloidin.

Table 7: Buffer compositions for preparation of pre-polymerized F-actin filaments used in this study.

buffer	composition
G-buffer	5 mM Tris/HCl 0.2 mM CaCl ₂ 0.77 mM NaN ₃ pH 7.4 (NaOH)
polymerization buffer	500 mM KCl 20 mM MgCl ₂ 20 mM ATP pH 7.4 (NaOH)

4.1.1.5. Entangled 3D F-Actin Samples as Basic Model System

For the basic model system, entangled F-actin networks in different concentrations (about 20 μL; preparation described in the previous chapter) were pipetted into self-made measuring chambers consisting of two optical glass cover slips (No. 1, 0.13-0.16 mm, Carl Roth, Karlsruhe, Germany) glued together by double-faced adhesive tape. The chambers were sealed with Parafilm, stored at 7 °C and used the day after. F-actin networks in concentrations of 8-36 μM showed isotropically entangled morphology (Figure 19 A-B), whereas in lower concentrations no entangled network was formed and in higher concentrations nematic phases (Figure 19 C) and aster formation (Figure 19 D) occurred.^{108,118,184,248}

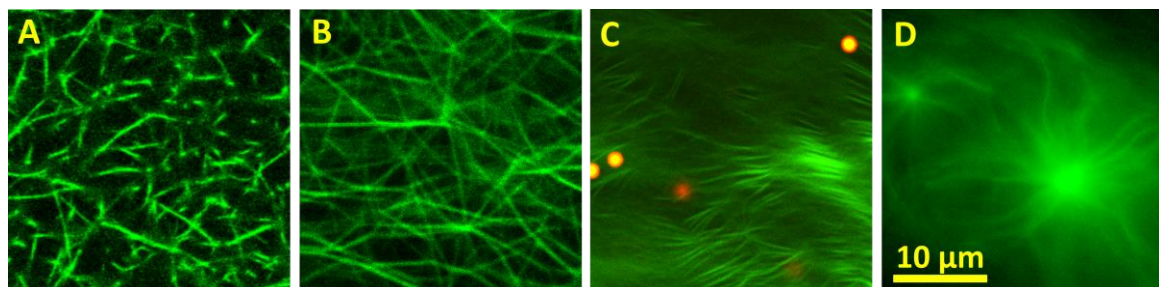


Figure 19: F-actin networks at different concentrations. Confocal images (A-C) and epi-fluorescence image (D) of actin networks made from different G-actin concentrations. **A:** 23 μM; **B:** 36 μM; **C+D:** 40-46 μM. F-actin was stained with AlexaFluoPhalloidin488. Red structures in (C) are tracer particles (2 μm carboxylate).

4.1.1.6. Preparation of F-Actin Networks Attached to Solid-Supported Lipid Membranes

The freshly hydrophilized substrates (4.1.1.2) were immediately incubated with the respective SUV suspension (4.1.1.1) for 1 h. A homogenous membrane including the receptor lipid was achieved as demonstrated in Figure 20 B1 showing homogenous fluorescence of the lipid bilayer and a defect in the upper right corner. To remove excess vesicles from the surface the sample was rinsed with spreading buffer. Subsequently, the buffer system was exchanged towards the ezrin protein buffer or PBS if neutravidin was used for linking the membrane to the actin network. Afterwards, either the protein ezrin T567D (isolated from recombinant expression in *Escherichia coli*²⁴⁹) or neutravidin (Thermo Fischer, Waltham, Massachusetts, United States) was added to the solid supported membrane and the system was incubated at a concentration of around 1 μM at 4 $^{\circ}\text{C}$ over night. A schematic overview of the preparation of F-actin networks attached to solid-supported membranes is shown in Figure 20 A1-3.

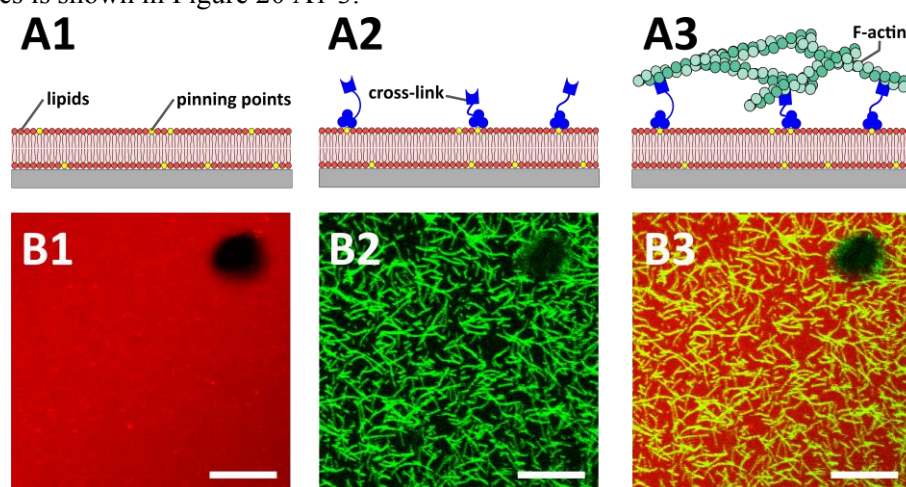


Figure 20: Preparation and self-organization of membrane bound artificial model systems of the actin cortex. **A1-3:** Schematic representation of the preparation process of artificial model systems of the actin cortex. A solid supported lipid bilayer (red) containing receptor lipid (yellow) is incubated with the protein ezrin T567D (blue). Afterwards a pre-polymerized F-actin network (green) is attached to the bilayer. **B1-3:** fluorescence images confirm successfully spread lipid bilayer doped with TexasRed (**B1**) and attachment of the actin network doped with AlexaFluor488-phalloidin (**B2**) and overlay (**B3**). Scale bar: 10 μm . (parts of figure by Markus Schön)

Excess protein was removed by rinsing with the respective protein buffer. Afterwards the buffer system was exchanged towards actin buffer and pre-polymerized actin filaments (8 μM , see 4.1.1.4) were incubated for 4.5 h at room temperature. Finally, unbound filaments were removed from the sample by rinsing with actin buffer. Quasi 2D actin networks attached to the lipid membrane by ezrin or neutravidin, respectively, were achieved (Figure 20 B2-B3).

Table 8: Overview over the protein buffers used in this study. All buffers were used at pH 7.4.

buffer	composition
ezrin buffer	50 mM KCl
	20 mM Tris
	0.1 mM EDTA
	0.1 mM NaN ₃
PBS (for neutravidin studies)	136.9 mM NaCl
	2.7 mM KCl
	8.1 mM Na ₂ HPO ₄
	1.5 mM KH ₂ PO ₄
actin buffer	50 mM KCl
	20 mM Tris
	2 mM MgCl ₂
	0.1 mM NaN ₃

4.1.2. Network Analysis of the Self-Assembled Minimal Actin Cortex (MAC)

4.1.2.1. Network Analysis of MACs by Optical Microscopy

4.1.2.1.1. Confocal Fluorescence Microscopy

Readymade solid supported actin networks attached to lipid membranes (4.1.1.6) or entangled actin networks (4.1.1.5) were imaged by confocal laser scanning microscopy (CLSM). An upright confocal laser scanning microscope (Olympus, FV 1200; Olympus, Hamburg, Germany) equipped with a 405 nm diode laser (50 mW), a 488 nm diode laser (50 mW) and a diode pumped solid state LASER emitting at 561 nm (20 mW) was used. For most measurements a water immersion objective (60 x, LPUMPlanN, NA = 1.0, Olympus) was used. The membrane associated fluorophore Atto390DOPE was excited at 405 nm and detected at 425-475 nm. The AlexaFluor488-phalloidin labeled F-actin was excited at 488 nm and detected at 500-545 nm. For excitation of the tracker particles an excitation wavelength of 561 nm was used and the fluorescence emission was detected at 575-675 nm.

4.1.2.1.2. Network Analysis from CLSM Images

The network analysis was mainly performed by Markus Schön and Ingo Mey (Institute of Organic and Biomolecular Chemistry, Georg-August-Universität, Göttingen, Germany).

In a first step the confocal sections of confocal laser scanning microscopy images were treated with a Fast Fourier Transformation (FFT) filter to increase the signal-to-noise ratio. Subsequently, the filaments were analyzed with an open source software tool called SOAX, which finds single (F-actin) filaments in fluorescence images and therefore is able to compute the length and position of filaments.²⁵⁰ The key element in this software is the initialization and evolution of so-called multiple stretching open active contours (SOACs).²⁵¹ This parametric curve is first initiated along regions in which good contrast and fluorescence intensity allow recognition of filaments, therefore a ridge threshold parameter is used. Afterwards, the curve evolves by elongation according local intensity maxima and stops when it comes into contact with a filament tip, hence, merging filament fragments. The computed filament is drawn to the centerline of the filament. Additionally, the algorithm reconfigures all junctions in the end so that the drawn filaments do not end or bend sharply at filament junctions. The obtained binary images from the computed filament positions are used for further analysis.

The mesh size of the F-actin polymer network was analyzed by a so-called bubble analysis in which the largest sphere (3D) or circle (2D) which fits into the porous zones of a network is determined.²⁵² First an Euclidian distance map (EDM) of the filament network was calculated, displaying the straight-line distance between two points in Euclidean space in form of height information, here the distance of a pixel in a polymer mesh and the surrounding filament. Thus, in this representation a local maximum in the EDM represents the balance point of a mesh, therefore the center of the largest circle which can be fit into the mesh. Subsequently, overlapping circles were compared among each other and only the largest was kept. A MATLAB based open source code written by Münster and Fabry was modified and used for the computation of the EDM, the determination of the local maxima and the comparison of overlapping bubbles.²⁵³ We use the diameter of the resulting bubbles to quantify the mesh size.

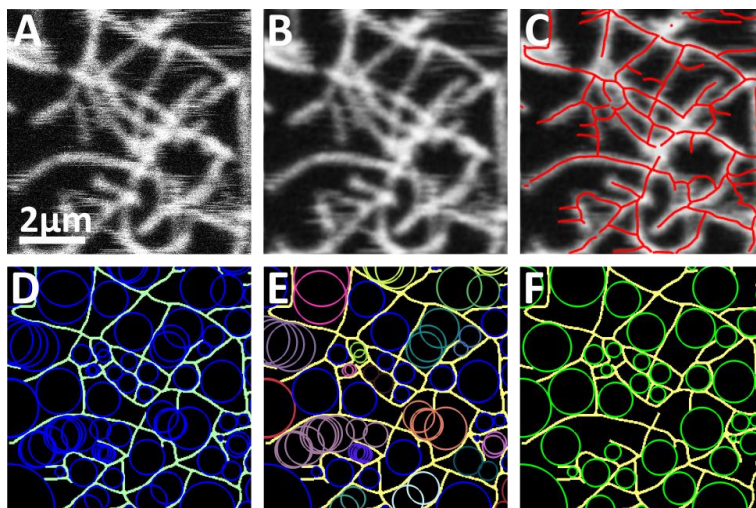


Figure 21: F-actin filament network analysis. A: Confocal fluorescence images of F-actin filament networks were recorded. B: The images were enhanced in signal-to-noise ratio by using a fast Fourier transform filter. C: The open source software tool SOAX was used to detect filaments using multiple stretching open active contours.^{250,251} D: Local maxima in an Euclidian distance map between the computed filaments served as center points for circles inside a network pocket. E: Overlapping circles were compared to avoid multiple responses of one mesh. F: Solely the largest of the overlapping circles was taken as mesh size of one specific pocket. The method was described before.^{252,253} (Figure was gratefully received from Markus Schön)

4.1.2.2. F-Actin Fiber Height Analysis by Atomic Force Microscopy

4.1.2.2.1. Sample Preparation

Clean and flat glass surfaces (35 mm, No. 1.5, MatTek, Ashland, USA) were incubated over night with poly-D-lysine ($0.1 \text{ mg}\cdot\text{mL}^{-1}$; Sigma-Aldrich, St. Louis, MO, United States). Upon rinsing the glass surface with actin buffer (see 4.1.1.6) $10 \mu\text{L}$ of pre-polymerized actin filaments ($8 \mu\text{M}$; 4.1.1.5) were incubated on the sample for 3.5 h (total buffer volume on sample about 1 mL). After further rinsing with actin buffer the sample could be imaged using the atomic force microscope.

4.1.2.2.2. Atomic Force Microscopy Measurements

Atomic force microscopy (AFM) images in quantitative imaging mode ($\approx 100 \text{ nm}\cdot\text{pixel}^{-1}$) were recorded using a JPK NanoWizard4 atomic force microscope (JPK Instruments, Berlin, Germany). Cantilevers with a sharp tip ($r_{\text{nom}} = 2 \text{ nm}$) and high sensitivity (MSNL-10, $k_{\text{nom}} = 100 \text{ pN}\cdot\text{nm}^{-1}$; Bruker AFM Probes, Camarillo, USA) were used for the measurements.

4.1.2.2.3. Fiber Height Analysis

AFM images were analyzed to determine the diameter and the diameter distribution of the pre-polymerized filaments. The height of the filaments was analyzed from line plots with the help of the scientific software tool Gwyddion²⁵⁴ (software version 2.47). The diameter of the fibers could be determined from the measured height of the fibers. In an image with high density of filaments the distribution of filament height was analyzed. Therefore the image was divided in 7×7 quadrants and each filament height was counted once per quadrant. It was necessary to treat the data this way since the beginning and end of one filament is in most cases not easy to analyze due to descending, intersections and branching. Thus, the determined filament distribution is rather a filament per area distribution. For our purposes it might even be more correct to look at this number since a longer filament contributes more to the mechanical properties than a short filament.

4.1.3. Force Spectroscopy Methods to Study the Viscoelasticity of MACs

In this chapter microrheological force spectroscopy methods are described which were used to probe the viscoelastic properties of model systems. Video particle tracking and passive and active microrheology with an optical tweezer are used. The methods differ in the frequency range and range of stiffness they are able to probe (see 2.2.2). Video particle tracking and optical tweezer based microrheology have been used in many artificial model systems of entangled and cross-linked F-actin networks as well as in living cells to record the frequency dependent viscoelastic properties of these systems. Here artificial minimal actin cortices will be studied using these tools.

4.1.3.1. Passive Microrheology Measurements by Video Particle Tracking

4.1.3.1.1. Experimental Procedure

To probe the local viscoelastic properties of artificial model systems of the actin cortex fluorescent carboxylate-modified polystyrene latex beads with a diameter of 2 μm were used if not stated otherwise (see chapter 4.1.1.3). Carboxylate-modified beads were shown to bind non-specifically yet provide stable interaction with the polymer network.¹⁰⁰ Confirmation of the tracer particle incorporation in the actin network is shown in Figure 22. The influence of the bead size on the frequency dependent viscoelastic properties is discussed in chapter 5.1.2.6.

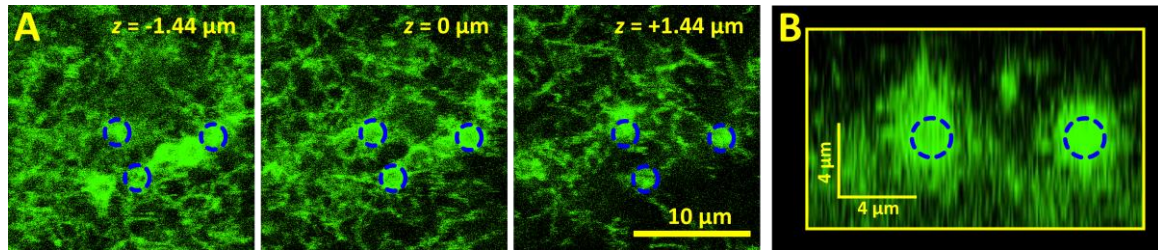


Figure 22: Incorporation of the tracer particles in the F-actin filament network. Confocal fluorescence images of actin networks attached to a lipid membrane containing 3 mol% PIP₂ via ezrin are shown. Tracer particles: size $d = 2 \mu\text{m}$, non-fluorescent silica (Bangs Laboratories, Indiana, United States). **A:** xy -planes at three different z -positions, at the plane of the tracer particles ($z = 0 \mu\text{m}$), two planes below ($z = -1.44 \mu\text{m}$) and two planes above ($z = +1.44 \mu\text{m}$). **B:** An xz -plane is shown. Non-fluorescent beads were used, the F-actin polymers organize around the silica surface. Estimated bead positions are marked with blue dotted lines. F-actin was fluorescently labeled with AlexaFluor488-phalloidin (Life Technologies, Carlsbad, USA).

Before the measurement samples were allowed to equilibrate with room temperature for at least 2 h. Time series of at least 100,000 images were recorded using a sCMOS camera (Zyla-5.5-CL-10, Andor Oxford Instruments, Belfast, UK) mounted on a fluorescence microscope (Olympus, FV 1200; Olympus, Hamburg, Germany) equipped with a 60x Objective (LPUMPlan N, NA = 1.0, Olympus, Hamburg, Germany) with a frame rate of at least 50 fps and an exposure time of about 10 ms. The total magnification was about 108 nm per camera pixel. About 1-10 beads could be recorded in each video frame with subpixel resolution using an algorithm described in the next chapter (Figure 25 A).

Temperature dependent measurements were performed using a home built Peltier element setup (Johannes Schumacher, Institute of Organic and Biomolecular Chemistry, Georg-August-Universität, Göttingen, Germany) adapted to the above described setup. A PID controller helped to control the temperature within less than a tenth of a degree Celsius.

4.1.3.1.2. Data Processing

Tracking, calculation of the time averaged mean squared displacements (MSDs) and determination of the complex shear moduli was accomplished by a MATLAB code written by Maria Kilfoil²⁵⁵ and coworkers based on a tracking algorithm by John Crocker and theory by Weitz and coworkers¹⁰³. Raw data in the form of particle trajectories and time averaged mean squared displacements is shown in Figure 25 B and C. Subpixel resolution of about 3 nm could be achieved. Additionally to the rather high time average (at least 50,000) and average over x - and y -direction, the MSDs for one data set were ensemble averaged (2-9). Accordingly, the reported data points contain a total average of $N = 2 \cdot 10^5 - 2 \cdot 10^6$. Sources of error of this method are discussed specifically for each sample in results and discussion (chapter 5.1.2.6). Each Trajectory was checked before further analysis. Examples of trajectories are shown in Figure 23. Bead trajectories, which showed similar variation (Figure 23 B1 & B2) and were stationary (Figure 23 A1 & A2) over the time of measurement were taken into account, whereas trajectories with sudden jumps or strong changes in position over times were rejected. In such trajectories, ergodicity is not given and it cannot be assumed that time average results in the same mean squared displacement as ensemble average. Additionally, beads with obvious artefacts were sorted out. Two examples are shown in (Figure 23 A3 & A4). In Figure 23 A3 the x - y -projection of a trajectory reveals that the bead has a high probability to be found at the borders of its mean position. Furthermore, the bead spontaneously changes positions from one rim to another. In a plot of particle position *vs.* time these processes show as sudden jumps in position (Figure 23 B3 & B4). This trajectory was recorded in a 3D actin network and it is likely that the beads trajectory is determined by the interaction with the surrounding filament cage. Figure 23 A4 shows another example of a rejected bead. Here again, the probability of the location of the bead is highest on the outer area of the trajectory. This trajectory was recorded in a sample where actin was attached to a model membrane via electrostatic interactions. The bead is most likely not incorporated in the network but sits on top and performs a propeller-like movement, which was observed quite often for this kind of sample.

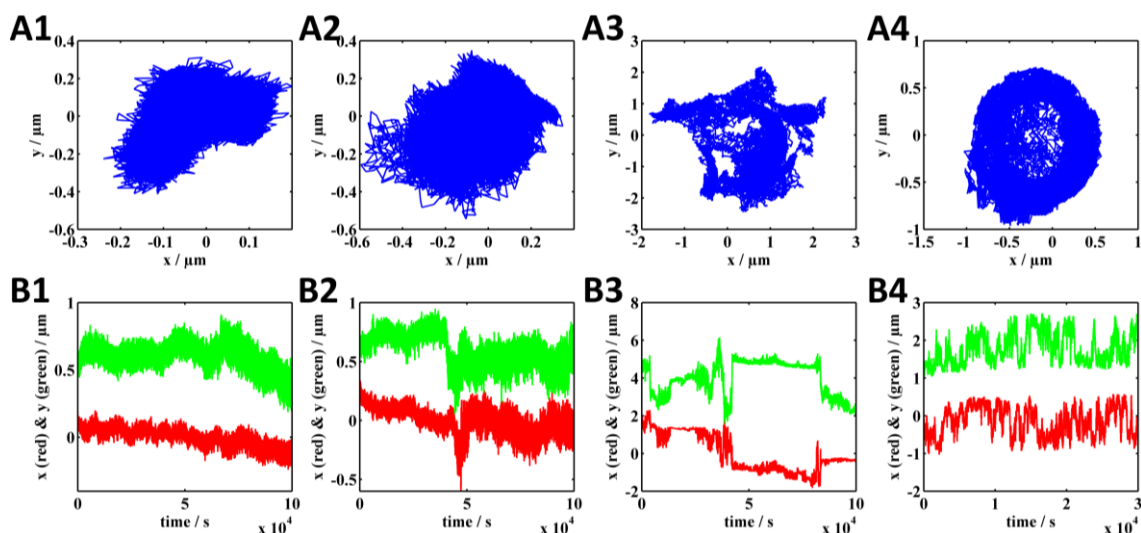


Figure 23: Selection of trajectories. Raw data in the form of bead trajectories is shown. **A:** Trajectories in x - y -representation. **B:** x - and y -position as a function of time. **A+B1:** Trajectory without artefacts, no drift and similar variation in position over a long period of time. **A+B2:** Trajectory with minor artefacts, no drift and only a slight change in position variation. **A+B3:** Trajectory with a major artefact, bead is sticking to the surrounding cage. **A+B4:** Trajectory with a major artefact, bead is moving on a circle. Flickering in the time course between the different positions can be observed. The bead is most likely not incorporated in the network but sits on top and performs a propeller-like movement.

In general these kind of artefacts can be easily detected when plotting histograms of the trajectories. Artefact free trajectories should have a normal distribution around the mean value. Example histograms of bead position in y -position from the trajectories in A1 and A4 are shown in C1 and C2. Beads that showed merely normal diffusion or the same or very similar mean squared displacement than immobile beads (no viscoelastic properties) were rejected as well.

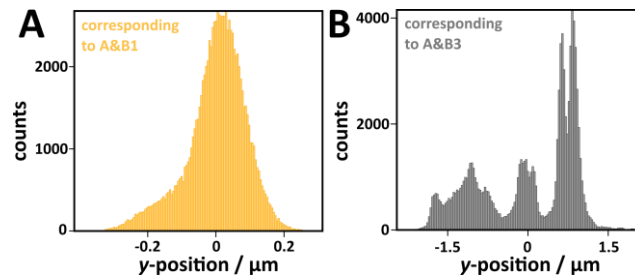


Figure 24: Two example histograms of the y -position. A: Particle 1 from Figure 23 A&B1. B: Particle 3 from Figure 23 A&B3.

If not otherwise stated (see data presentation in results and discussion, PIP₂ 5 % and actin 36 μM) all other data was included in the analysis. Treating the data this way lead to a selection of about 10 % of the recorded trajectories, varying slightly for different samples. Only in samples where the F-actin network was attached to lipid membranes via electrostatic interactions the rate of approval was significantly lower than 10%. The data was thus not included in the here presented dataset.

In order to obtain smooth mean squared displacements as well as first and second derivatives, the data was fitted locally with a second degree polynomial. The viscoelastic moduli are calculated according to equations (23)-(35)). Examples of storage and loss moduli are provided in Figure 25 D. To interpret the frequency dependent viscoelastic moduli in terms of binding kinetics of the actin binding proteins we used a semi-phenomenological model described by Bausch and coworkers to fit the microrheological data.³⁴ The model was modified for our purposes as described in chapter 4.1.3.4.

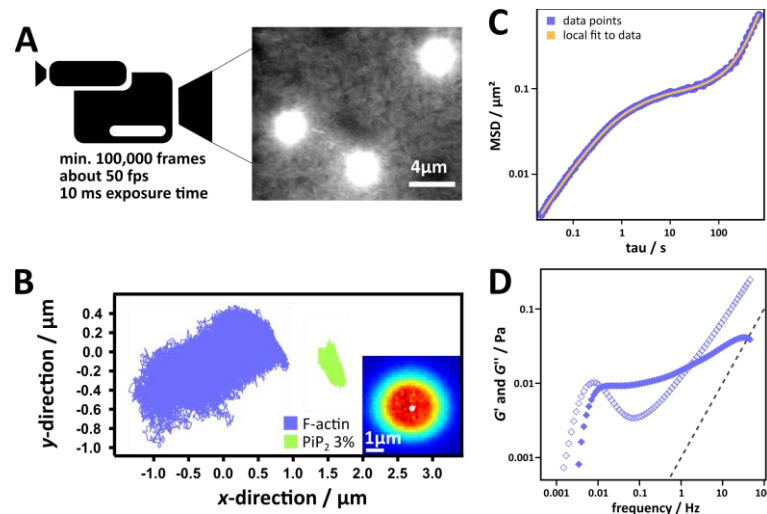


Figure 25: Overview Video Particle Tracking. A: Schematic representation of the method. Videos of at least 100,000 images where recorded on a sCMOS camera with a frame rate of about 50 fps and an exposure time of about 10 ms. B: Examples of trajectories of tracer particles in different viscoelastic media are displayed. Inset: Bead trajectory of a tracer particle in a 2D actin network coupled to a planar membrane via transient ezrin/PIP₂ linkage in comparison to the bead size. C: Mean squared displacement (blue) and respective locally fitted curve (orange). D: Viscoelastic moduli, the storage modulus (closed symbols) and the loss modulus (open symbols). Blue: Shear modulus of entangled F-actin networks. Dotted grey line: Theoretical loss modulus of water.

4.1.3.2. Passive Microrheology Measurements by Optical Tweezer

Optical tweezers are able to manipulate tracer particles, the underlying physical principle is to trap a particle in a highly focused LASER beam on the basis of conservation of momentum. Once trapped, the particle can be moved on pre-defined trajectories through the surrounding medium. Many different experiments are conceivable, here we use the optical tweezer either to track the motion of a particle (passive MR this chapter) or to perform small amplitude oscillations (active MR 4.1.3.3) inside the viscoelastic medium in order to probe its viscoelastic response.

4.1.3.2.1. Theoretical Background

The passive microrheology experiment on the optical tweezer is based on the same theory as the video particle tracking experiment. A comprehensive overview is given by Tassieri *et al.*⁷⁸ Basic concepts are shown here. Solely the tracking of the bead position is recorded by the change of signal on the quadrant photodiode (Figure 27 A and B), allowing a higher band width of frequencies to be analyzed. Following the same derivation as shown before for the video particle tracking in chapter 2.2.2.1.2, the Stokes-Einstein equation is used in this context. However, the restoring force of the trap acting on the tracer particle has to be included in the Langevin equation:

$$m \frac{d^2x}{dt^2} = f_R(t) - \int_0^t \zeta(t - \tau) \cdot \frac{dx(\tau)}{dt} d\tau - \kappa \cdot x(t), \quad (44)$$

where κ is the stiffness of the trap. Using the same assumptions (i)-(iii) as discussed in (2.2.2.1.2) equation (44) can be rewritten in terms of the normalized position autocorrelation $A(\tau)$ ²⁵⁶⁻²⁵⁹:

$$A(\tau) = \frac{\langle x(t_0)x(t_0 + \tau) \rangle}{\langle x^2(t_0) \rangle}, \quad (45)$$

giving

$$\tilde{\zeta}(s) = \kappa \cdot \frac{\tilde{A}(s)}{[1 - s \cdot \tilde{A}(s)]}. \quad (46)$$

The normalized position autocorrelation function (Figure 27 C) is related to the normalized mean squared displacement nMSD(τ) (Figure 27 D) by:²⁵⁷

$$A(\tau) + \text{nMSD}(\tau) = 1 \quad (47)$$

Applying equations (16) and (18) as shown previously the following expression for the shear modulus in Fourier domain is obtained (Figure 27 E):²⁵⁶⁻²⁵⁹

$$G^*(\omega) = \frac{\kappa}{6\pi r} \cdot \frac{i\omega \cdot \hat{A}(\omega)}{[1 - i\omega \cdot \hat{A}(\omega)]}. \quad (48)$$

$\hat{A}(\omega)$ is the Fourier transform of the position autocorrelation function.

Simple evaluation of the Fourier transforms in equation (48) would lead to artefacts in the frequency range of interest due to the limited set of data points collected in the measurements. The two major problems in passive microrheological methods, which have been identified by Tassieri *et al.*, are (i) interpolation artefacts and (ii) noise at long time lags. They approached these problems by virtual oversampling performed as interpolation of the time averaged functions of the normalized mean squared displacement or autocorrelation function, and reducing the data density at long time lags to increase the signal-to-noise ratio. Finally, the adjusted data was used to calculate the viscoelastic moduli after equation (24).

4.1.3.2.2. Experimental Procedure

All samples were prepared on optical glass slides (No. 1.5, 0.165-0.175 mm, μ -Dish^{35mm, high} Glass Bottom, Ibidi, Martinsried, Germany) for optical tweezer measurements and allowed to equilibrate at room temperature for at least 2 h before measurement. The passive microrheological measurements were performed on a NanoTracker 2 optical tweezer (JPK Instruments, Berlin, Germany) build on an inverted Zeiss microscope equipped with a 5 W 1064 nm LASER and a water

immersion objective (63 x, C-Apochromat, NA = 1.2, Carl Zeiss, Jena, Germany) for trapping (see Figure 26).

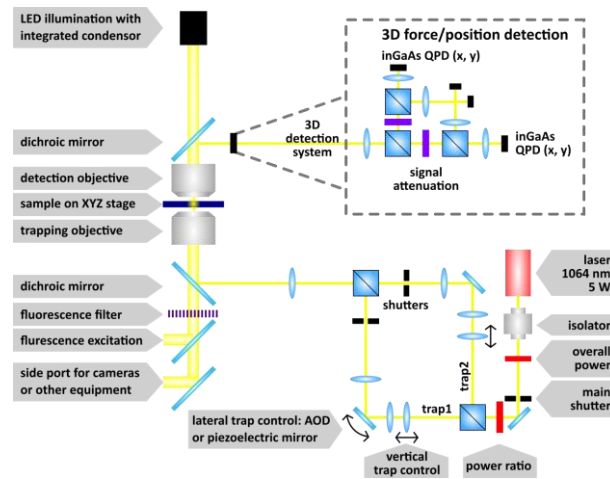


Figure 26: Schematic representation of the optical tweezer setup and beam bath. The NanoTracker 2 optical tweezer (JPK Instruments, Berlin, Germany) build on an inverted Zeiss microscope equipped with a 5 W 1064 nm LASER and a water immersion objective (63 x, C-Apochromat, NA = 1.2, Carl Zeiss, Jena, Germany). The LASER beam is split into two light paths. Trap 1 can be stirred by a piezo electric mirror, trap 2 by an acousto-optic deflector (AOD). Detection of the signal is carried out by quadrant photodiodes.

Polystyrene particles (2 μm , Sigma-Aldrich, St. Louis, Missouri, United States) were used as colloidal probes. Laser power was set to 500 mW and reduced to about 10 % for the measurement. The trap stiffness and detector's sensitivity to particle displacements from the trap center were calibrated on at least 3 tracer particles in ultrapure water before the measurement (typical trap stiffness: $\kappa \approx 0.0007 \text{ pN} \cdot \text{nm}^{-1}$) using a power spectral analysis (see Figure 29 B1-B2).²⁶⁰ Motion of the tracer particle was recorded on a quadrant photodiode with 1000 Hz for at least 20 min.

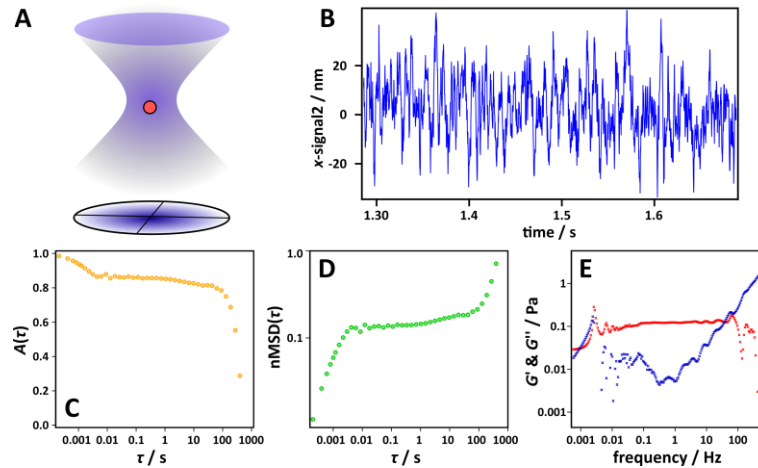


Figure 27: Overview of passive microrheology measurements by optical tweezer. A: Schematic representation of the setup. A tracer particle (red circle) is trapped in a polymer network (not shown). An optical trap of low trap stiffness (blue) records the particle movement. The motion of the tracer particle is recorded by a quadrant photodiode. B: Example of particle movement in x -direction of a tracer particle in a viscoelastic medium (raw signal). C: Example of normalized position autocorrelation function $A(\tau)$ (orange) of the tracer particle position. D: Example of normalized mean squared displacement $n\text{MSD}(\tau)$ (green) of the tracer particle position. E: Example of viscoelastic moduli, storage (red) and loss (blue).

4.1.3.2.3. Data Processing

For data analysis the open access LabVIEW executable MOT written by Manlio Tassieri was used.^{78,261} This program is based on the method described above. The obtained data was corrected by the trap stiffness experimentally determined in water.

4.1.3.3. Active Microrheology Measurements Using an Optical Tweezer

4.1.3.3.1. Theoretical Background

The active microrheological measurement was performed with a tracer particle trapped in a relatively strong optical trap, which was actively oscillated. The motion of the bead was recorded with a second weaker trap. A schematic representation of the setup is shown in Figure 28 A. Forces acting on the tracer particle are displayed in Figure 28 B. The one dimensional equation of motion of a tracer particle embedded in a viscoelastic material and excited to oscillatory movement with a relatively strong optical trap ($k_1 \cdot (A \cdot \exp(i\omega t) - x)$) is shown in equation (49). The motion of the tracer particle is recorded by a second weaker trap ($k_2 x$). The viscoelastic response is modelled as a complex drag force $6\pi r \eta^*(\omega) \cdot \dot{x}$. Additionally, the inertia force $m\ddot{x}$ of the tracer particle and statistical random forces $f_R(t)$ act on the bead:

$$m \frac{d^2x}{dt^2} = -6\pi r \eta^*(\omega) \cdot \frac{dx}{dt} + k_1 \cdot (A \cdot \exp(i\omega t)) - k_1 x - k_2 x + f_R(t) \quad (49)$$

With the ansatz for the resulting motion:

$$x(t) = D(\omega) \cdot \exp(i(\omega t - \varphi(\omega))), \quad (50)$$

and taking $G^*(\omega) = \eta^*(\omega) \cdot i\omega$ an expression for the shear modulus can be found. Here $D(\omega)$ and $\varphi(\omega)$ are the resulting damped amplitude and the phase shift, respectively (Figure 28 C inset). The inertial term and the stochastic thermal forces are neglected, giving:

$$G^*(\omega) = \frac{k_1}{6\pi r} \left(\frac{A}{D(\omega)} \cdot (\cos(\omega) + i \cdot \sin(\omega)) - 1 - \frac{k_2}{k_1} \right) \quad (51)$$

Where the real and imaginary part are:

$$G'(\omega) = \frac{k_1}{6\pi r} \left(\frac{A}{D(\omega)} \cdot \cos(\omega) - 1 - \frac{k_2}{k_1} \right) \text{ and} \quad (52)$$

$$G''(\omega) = \frac{k_1}{6\pi r} \left(\frac{A}{D(\omega)} \cdot \sin(\omega) \right) \quad (53)$$

An exemplary spectrum is shown in (Figure 28 C).

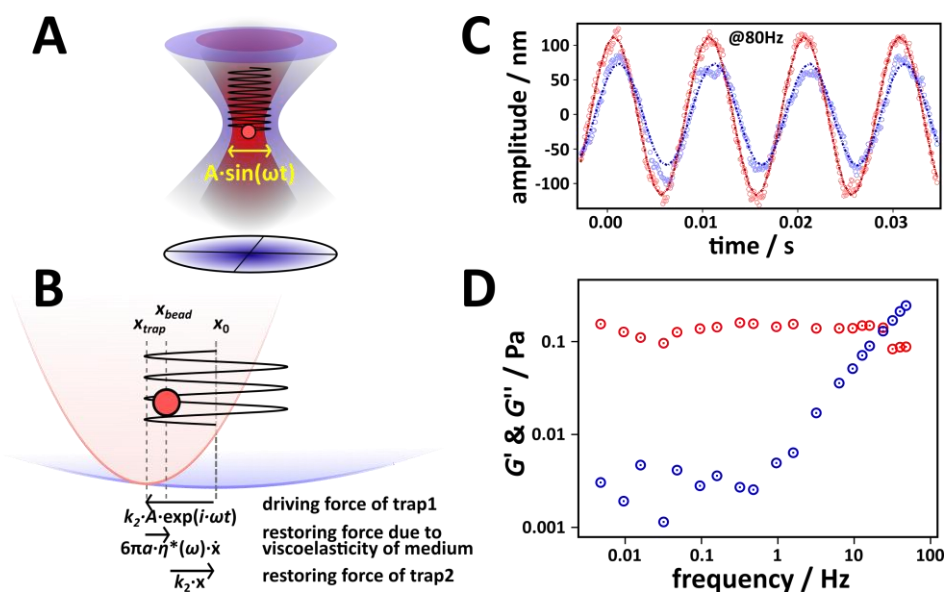


Figure 28: Active microrheology measured by optical tweezer. **A:** Schematic representation of the setup. A tracer particle (red circle) is trapped in a polymer network (not shown), an optical trap of low trap stiffness (blue) records the particle movement, while another optical trap of higher trap stiffness (red) excites oscillatory movement of different frequencies and low amplitude ($2 \cdot A = 80 - 200$ nm, peak to peak). The motion of the tracer particle is recorded by a quadrant photodiode. **B:** Forces acting on the tracer particle (red circle). Harmonic potentials of the traps (trap 1 (red) & trap 2 (blue)). **C:** Detected signals at 80 Hz, response signal (blue) is damped in amplitude and phase shifted compared to the input signal (red). **D:** Exemplary spectrum of the viscoelastic moduli versus frequency. Red: Storage modulus; Blue: Loss modulus.

4.1.3.3.2. Experimental Procedure

Samples were prepared equivalently and measured on the same setup as described in 4.1.3.2. The Laser power was set to 500 mW with approximately 90 % of the power entering the beam path of trap 1 and about 10 % the beam path of trap 2. The trap stiffness and detector's sensitivities to particle displacements from the trap center were calibrated on at least 3 tracer particles in ultrapure water before the measurement (typically: $k_1 \approx 0.04 \text{ pN} \cdot \text{nm}^{-1}$ and $k_2 \approx 0.0007 \text{ pN} \cdot \text{nm}^{-1}$) using a power spectrum analysis.²⁶⁰ The trap stiffness k was calculated from the corner frequency $f_c = k/12\pi^2\eta r$ (see Figure 29 B 1 and 2), where η is the viscosity of the medium and r the radius of the bead. Trap positions were calibrated before each measurement to ensure that both traps lie on top of each other (Figure 29 A). Motion of the tracer particle was recorded on a quadrant photodiode. Trap one was used to oscillate the tracer particle in order to get absolute values for the shear modulus since the true motion of the mirror and hence the LASER beam could be measured by a strain gauge strip. Mirror movement was calibrated several times giving a sensitivity of 33 nm/mV. Oscillation protocols with oscillation frequencies ranging from 0.001 to 200 Hz at small amplitudes ($2 \cdot A = 80 - 200 \text{ nm}$, peak to peak) were used to probe the viscoelastic properties.

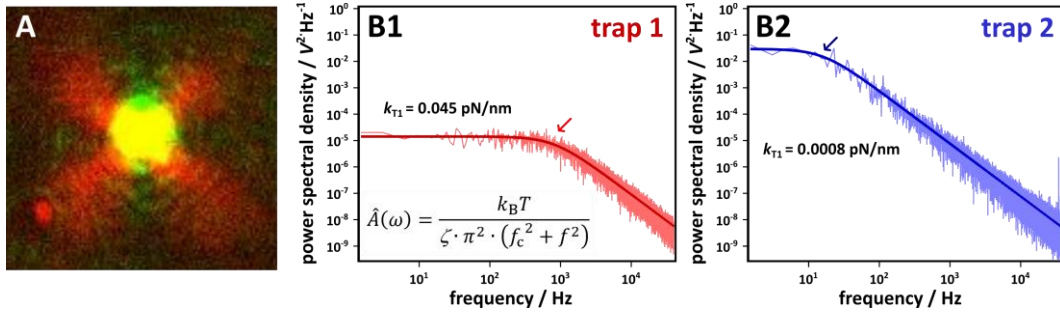


Figure 29: Overview optical tweezer calibration. A: Trap position calibration, trap 1 (red) and trap 2 (green) lie on top of each other. B: Example of a power spectra of both traps with respective fit (equation shown in B1). B1: Trap 1. B2: Trap 2. $\hat{A}(\omega)$: Power spectral density (Fourier transform of the position autocorrelation); ζ : hydrodynamic drag coefficient; f_c : the corner frequency.

4.1.3.3.3. Data Processing

Signals were fitted with a sinus fit (simplex algorithm) and moduli were calculated after equations (51)-(53) using a self-written MATLAB script.

4.1.3.3.4. Semi-Phenomenological Model to Interpret the Frequency Dependent Viscoelastic Data in Terms of Binding Kinetics of Transient Cross-Links

In order to interpret the collected frequency dependent viscoelastic data in terms of binding kinetics of transient cross-links, a semi-phenomenological model introduced by Bausch and co-workers (see 3.2.1) is used.³⁴ I modified this model to account for more than one independent relaxation process i at low frequencies in the network originating for example in cross-linker unbinding or filament reptation. The following dependencies of the storage $G'(f)$ and loss modulus $G''(f)$ on the frequency f are obtained:

$$G'(f) = G_0 + b \cdot \left(\frac{f}{f_0}\right)^p - \sum_i \frac{a_i N_i k_{\text{off}}^i}{\left(\frac{k_{\text{off}}^i}{2\pi}\right)^2 + f^2} \quad (54)$$

$$G''(f) = d \cdot \left(\frac{f}{f_0}\right)^p + \sum_i \frac{c_i N_i f}{\left(\frac{k_{\text{off}}^i}{2\pi}\right)^2 + f^2} \quad (55)$$

Where, N is the number of bonds, $a - d$ are pre-factors and f_0 is 1 Hz (as described in 3.2.1). The full set of parameters for each sample is presented in Appendix 1 IV.

4.1.4. Langevin Equation for the Motion of a Particle in a Viscoelastic Medium

4.1.4.1. Theoretical Background

In order to simulate the motion of a tracer particle in a viscoelastic medium we use a similar generalized Langevin equation as applied by Mason and Weitz²⁶² and described above (equation (16)), adding an additional term for the force of a harmonic potential ($-kx$) of a cage of filaments acting on the particle:

$$m \frac{d^2x}{dt^2} = -kx - \beta \int_0^t \tilde{\zeta}_{\text{Maxwell}}(t - \tau) \cdot \frac{dx}{dt} \Big|_{\tau} d\tau + f_R(t), \quad (56)$$

where m is the mass of the tracer particle, x the position of the tracer particle, k the trap stiffness of a harmonic potential, $\tilde{\zeta}_{\text{Maxwell}}$ the memory function, dt the time lag between two positions, β is a pre-factor $[\beta] = \text{N} \cdot \text{m}^{-1}$ and $f_R(t)$ a fluctuating force. This force is correlated to the friction coefficient ζ as expressed by the fluctuation dissipation theorem (equation (13)). In our simulations we use an exponential decay to describe the memory function ζ , similar to the relaxation function obtained from the canonical Maxwell model, and via the fluctuation dissipation theorem also the correlation of the noise term.

$$\tilde{\zeta}_{\text{Maxwell}} = \exp\left(-\frac{|t|}{K}\right), \quad (57)$$

where K is the correlation time at which the time dependent memory function $\tilde{\zeta}_{\text{Maxwell}}$ decays to $1/e$ of its original value. The above Langevin equation (56) can be rewritten in order to obtain the position x_i at each index of time i . Additionally we introduce a term for the long time diffusion of the entanglement cage with the diffusion coefficient D_{cage} :

$$x_i = \frac{-\frac{m}{\Delta t^2}(x_{i-2} - 2x_{i-1}) + \beta \cdot x_{i-1} - \beta \sum_{j=0}^{i-1} \zeta_{i-j} \cdot (x_j - x_{j-1}) - \beta \cdot 2 \cdot k_B T \cdot \frac{v_i}{\sqrt{\Delta t}}}{\frac{m}{\Delta t^2} + k + \beta} + \sqrt{2D_{\text{cage}}\Delta t} \cdot \omega_i, \quad (58)$$

where i is the index of time and j is the index of time lag and Δt is the time lag between two positions. ω_i is an uncorrelated white noise and v_i a correlated Gaussian noise.

4.1.4.2. Proceeding

Particle trajectories in complex viscoelastic media were simulated by an in house python script 'Generalized Langevin Equation Simulator Version 5 (2017-02-16)' via equation (58). Example of such simulations with varying parameters are shown in Figure 30. For comparison the resulting trajectories were treated like data from video particle measurement, hence the mean squared displacement and the moduli were calculated as described in 4.1.3.1.

Initial parameter set:

- mass $m = 1 \cdot 10^{-4}$ kg
- time between two positions $\Delta t = 0.01$ s
- spring constant of the harmonic potential $k = 5$ a. u.
- diffusion coefficient of the cage $D_{\text{cage}} = 0.5 \cdot 10^{-16} \text{ m}^2 \cdot \text{s}^{-1}$
- correlation time $K = 1$ s
- temperature $T = 1 \text{ k}_B T$

An increase of the spring constant shifts the plateau region and the MSD in the low time lag region to lower magnitudes as expected (Figure 30 A). Alterations in the diffusion coefficient of the cage act on the long time diffusion of the simulated particle while the mean squared displacement on short time lags is not altered (Figure 30 B). Changing the Kernel parameter determines the power law scaling of the MSD in the short time lag regime, without affecting other time lag regimes (Figure 30 C). The temperature acts on all time regimes (Figure 30 D) as all processes are dependent

on the temperature. The transition from the short time lag regime to the plateau regime is determined by the Kernel parameter and the stiffness of the trap. The transition from the plateau region to the cage diffusion is determined by the diffusion coefficient of the cage and the trap stiffness.

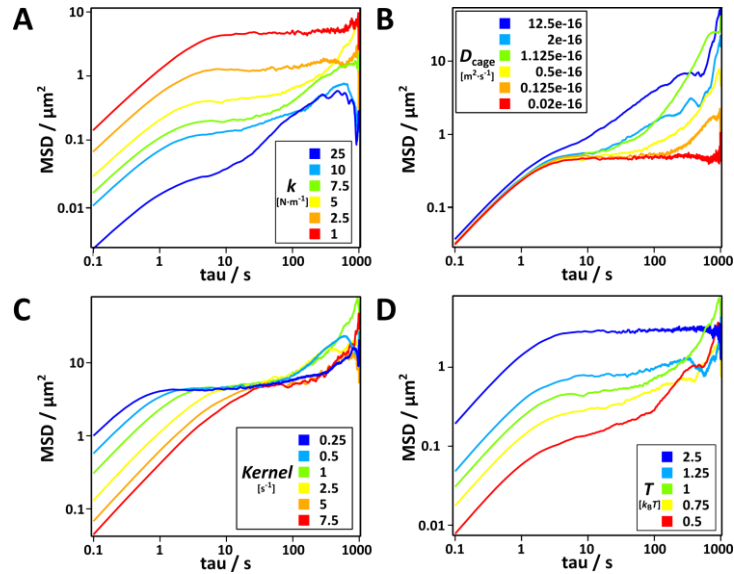


Figure 30: Evaluation of the model to simulate the motion of a tracer particle in a viscoelastic medium. Graphs display the mean squared displacement over time lag. **A:** Variation of the spring constant of the harmonic potential k . **B:** Variation of the diffusion coefficient D_{cage} of the cage. **C:** Variation of the correlation time K at which the time dependent memory function decays to decays to $1/e$ of its original value. **D:** Variation of the temperature T . Other parameters were kept constant: mass $m = 1 \cdot 10^{-15}$ kg, time between two positions $\Delta t = 0.01$ s and total number of positions calculated $L = 100,000$.

4.2. Methods and Experimental Procedure to Study Living Cells

4.2.1. Polyacrylamide Gels as Cellular Substrates of Different Elasticities

4.2.1.1. Fabrication of Polyacrylamide Gels

To produce substrates of different elasticity collagen coated polyacrylamide gels with different degrees of cross-links were produced after a modified protocol from Pelham and Wang²⁶³.

4.2.1.1.1. Preparation of Surface Treated Coverslips

Silanized bottom coverslips: Coverslips (square, 20 mm, Thermo Fisher Scientific, Gerhard Menzel B.V. & Co. KG, Braunschweig, Germany) were treated with argon plasma for 15 min (Diener electronic, Plasma Surface Technology, Ebhausen, Germany) and treated in an ultrasonic bath at 60 °C in ethanol ($\geq 99.8\%$ (GC), Sigma-Aldrich, St. Louis, Missouri, United States) for 5 min. Coverslips were dried in a gentle nitrogen steam and covered with NaOH (0.1 M) for 5 min. After removal of the NaOH the substrate was covered with ((3-aminopropyl)triethoxysilane) (APTES, Sigma-Aldrich, St. Louis, Missouri, United States) for 3 min to silanize the surface. The coverslips were rinsed in ultrapure water (< 20 m Ω -cm) several times, dried in a gentle steam of nitrogen and placed at a petri dish with the silanized side facing upwards. The substrate was treated with an aqueous glutaric dialdehyde solution (GDA 0.5 %, Acros Organics, Geel, Belgium) for 30 min, rinsed with ultrapure water (< 20 m Ω -cm) several times and dried in a gentle steam of nitrogen. This silanization process and additional functionalization with glutaric dialdehyde is important to covalently bind the polyacrylamide gels to the coverslip.

Surfasil treated coverslip: Coverslips (round, 25mm, Thermo Fisher Scientific, Gerhard Menzel B.V. & Co. KG, Braunschweig, Germany) were cleaned in an ultrasonic bath at 60 °C in ethanol ($\geq 99.8\%$ (GC), Sigma-Aldrich, St. Louis, Missouri, United States) for 5 min and subsequent

drying in a gentle nitrogen steam. The coverslips were treated with a hydrocarbon siliconizing fluid solution (10 %, Thermo Fisher Scientific, Waltham, Massachusetts, United States) in chloroform for 10 min to render the surface hydrophobic. The reaction takes place by a covalent reaction between the hydroxyl groups on the surface and the silicon. After the removal of the surfasil solution the coverslips were dried and stored at room temperature.

4.2.1.1.2. Polymerization of Polyacrylamide

Different ratios of acrylamide (Sigma-Aldrich, 01696, St. Louis, Missouri, United States) and *N,N*-methylenebis(acrylamide) (Sigma-Aldrich, M7279, St. Louis, Missouri, United States) were mixed for the preparation of the acrylamide stock solutions (Table 9). To 500 μL of this mixture the radical starter ammoniumperoxodisulfat (APS, 5 μL 1:100) and the catalyst *N,N,N,N*-tetramethylethan-1,2-diamin (TEMED 0.5 μL of 1:1000, Carl Roth, 2367, Karlsruhe, Germany) were added to initiate the polymerization. The silanized and GDA treated bottom coverslips were placed on the bench facing the top with the silanized side. The mixture was added to the coverslip immediately after the addition of APS and TEMED. A surfasil treated coverslip was then placed on the droplet. Polymerization was complete after 45 min and resulted in polyacrylamide gels of about one millimeter in height. After removal of the coverslip the gel was washed in phosphate buffered saline (PBS) and stored for 2 days at 7 $^{\circ}\text{C}$ in PBS before usage to allow swelling. Gels of *E*-moduli ranging from 0.2 to 100 kPa were obtained.

4.2.1.1.3. Collagen Coating of Polyacrylamide Gels

The polyacrylamide gels were covalently coated with collagen to provide RGD-sequences (Arg-Gly-Asp) to mediate cellular adhesion. Therefore, gels were washed with HEPES buffer (50 mM, 5 min) and treated with UV-light ($\lambda = 365$ nm) for 10 min. Afterwards, an aqueous solution of sulfosuccinimidyl 6-(4'-azido-2'-nitrophenylamino)hexanoate (Sulfo-SANPAH, 1 $\text{mg}\cdot\text{mL}^{-1}$, Thermo Fisher Scientific, Waltham, Massachusetts, United States) was brought into contact with the polyacrylamide gel for 15 min and the reaction between the azide and the amide group was triggered by a irradiation with UV-light ($\lambda = 365$ nm) for 10 min. The gels were rinsed at least 5 times with HEPES (50 mM) for 5 min before incubating with a solution of bovine collagen I (50 $\mu\text{g}\cdot\text{mL}^{-1}$, Thermo Fisher Scientific, Waltham, Massachusetts, United States) in acetic acid (0.02 M) over night at 7 $^{\circ}\text{C}$. Before usage the excess collagen was removed by rinsing with PBS.

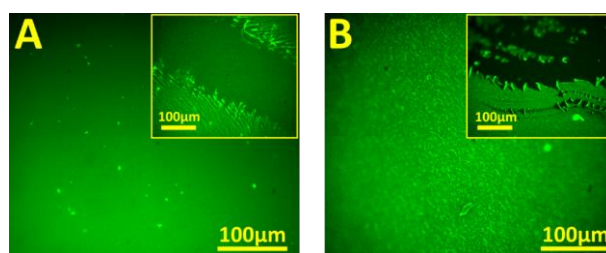


Figure 31: Fluorescence staining of collagen I coated polyacrylamide gels. A: 8 kPa gel. B: 30 kPa Gel. Insets are deliberately produced defects to illustrate the difference between coated and uncoated locations. Collagen I was fluorescently labeled as described in 1.2.4 (Fluorescence images were produced during the Bachelor thesis of Franziska Ries (2016), Institute of Physical Chemistry, Georg-August-Universität, Göttingen, Germany).

4.2.1.2. Determination of the *E*-Modulus with AFM

The *E*-modulus of each gel was confirmed before cell culture by fitting Hertzian contact mechanics to force distance curves²⁶⁴ using an atomic force microscope (MFP3D Standalone, Asylum Research) equipped with silicon nitride cantilevers (Bruker AFM Probes, Camarillo, United States). The spring constant of each cantilever was determined using the thermal noise method.²⁶⁵ At least 200 force distance curves were collected on three different positions on the sample. For the stiffer

gels of a Young's modulus of 30-100 kPa the F-lever ($k_{\text{nom}} = 500 \text{ pN}\cdot\text{nm}^{-1}$) was used, for gels with expected E -moduli with 1-10 kPa the D-lever ($k_{\text{nom}} = 100 \text{ pN}\cdot\text{nm}^{-1}$) and for the gel with an expected E -modulus of 0.2 kPa the C-lever ($k_{\text{nom}} = 10 \text{ pN}\cdot\text{nm}^{-1}$) was used. The force distance curves were base line corrected and the contact point was set manually. Analysis of the E -moduli was performed by an in house code 'FDC_loader' (version 05.03.2015) written by Andreas Janshoff and Ingo Mey in Matlab (Version 2014a, MathWorks Inc., Massachusetts, United States), based on Hertzian contact mechanics (see equation (59))^{266,267}. The measured E -moduli are listed in Table 9. Collagen coating did not alter the elastic properties significantly.

Table 9: Volume ratio of acrylamide (AA) and bis-acrylamide (bis-AA) in stock solutions and the resulting E -modulus (mean \pm std) after polymerization measured by atomic force microscopy. (Measured E -moduli were partially produced during the Bachelor thesis of Franziska Ries (2016) and Christine Franke (2014), Institute of Physical Chemistry, Georg-August-Universität, Göttingen, Germany).

expected E -modulus / kPa	AA / % (v/v)	bis-AA / % (v/v)	measured E -modulus / kPa
0.2	3	0.03	0.040 ± 0.011 ($N = 60$)
1.0	3	0.14	1.05 ± 0.37 ($N = 2777$)
8.0	8	0.05	6.33 ± 1.34 ($N = 748$)
30	10	0.1	23.3 ± 9.34 ($N = 1501$)
100	10	0.75	90.4 ± 33.5 ($N = 1572$)

4.2.2. Cell Culture and Sample Preparation

Cells were cultured and prepared for measurement by Angela Rübeling and Anja Herdlichke (Institute of Organic and Biomolecular Chemistry, Georg-August-Universität, Göttingen, Germany).

4.2.2.1. Cell Culture

All cell lines were cultured in cell culture flasks (TPP, Transachingen, Switzerland). The cells (overview of all cell lines in Table 10) were cultured in the respective cell culture medium in a humidified incubator (Heracell 1510, Thermo Scientific) under the indicated environmental conditions (see Table 11). For cell passage, confluent grown cells were released from the surface by incubation with trypsin/EDTA (0.05 % / 0.02 %; Biochrom, Berlin, Germany) for 3-5 min. Re-suspended cells were added into a stop solution containing culture medium and fetal calf serum (1:1) and centrifuged for 3 min (1200 rpm). After centrifugation the supernatant was removed, the cell pellet was re-suspended in 1 mL culture medium and the density of cells was determined using a disposable counting chamber (C-Chip, Digital Bio, Seoul, Korea). Depending on the cell line about 1 million cells were used for further cell culture whereas the rest was used for sample preparation.

Table 10: Cell lines used in this study.

cell line	information	origin
MDCK-II	Madin-Darby canine kidney epithelial cell line	purchased from the Health Protection Agency (Salisbury, UK)
MCF-10A	benign epithelial cell line from mammary gland	thankfully received from oncology department
MCF-7	adenocarcinoma cell line from mammary gland (epithelial)	Universitätsmedizin Göttingen, Georg-August-Universität, Göttingen
MDA-MB-231	adenocarcinoma cell line from mammary gland (epithelial)	

Table 11: Composition of the cell culture media for the different cell lines used in this study.

cell line	composition of cell culture medium	culture Conditions
MDCK-II	MEM with Eagle's salts +10 % FCS +4 mM L-glutamine	37°C 5 % CO ₂
MCF-10A	DMEM:F12 +5 % FCS + 4 mM L-glutamine + 5 µg·mL ⁻¹ insulin + 100 ng·mL ⁻¹ cholera toxin + 20 ng·mL ⁻¹ EGF	37 °C 7.5 % CO ₂
MCF7	DMEM:F12 +10 % FCS +4 mM L-glutamine	37 °C 7.5 % CO ₂
MDA-MB-231	DMEM:F12 +10 % FCS +4 mM L-glutamine	37 °C 7.5 % CO ₂

Table 12: List of ingredients of the cell culture media.

ingredient	manufacturer information
PBS phosphate buffered saline w/o Ca ²⁺ /Mg ²⁺	Biochrom, Berlin, Germany
MEM minimum essential medium with Eagle's salts with 2.2 g·L ⁻¹ NaHCO ₃	Lonza, Basel Switzerland
DMEM:F12 mixture (1:1) of Dulbecco's modified minimum essential medium with Eagle's salts and Ham's F12	Lonza, Basel Switzerland
FCS Fetal Calf Serum	BioWest, Nuaille, France
L-glutamine	Lonza, Basel Switzerland
Bovine insulin in PBS (10 mg·mL ⁻¹)	Biochrom, Berlin, Germany
Cholera toxin from <i>Vibrio cholerae</i>	Sigma-Aldrich, St. Louis, Missouri, United States
Human EGF human epidermal growth factor	Peptotech, Rocky Hill, New Jersey, United States

4.2.2.2. Cell Sample Preparation for Mechanical Measurements

For experiments, substrates (either glass substrates or polyacrylamide gels of different elasticity, coated with collagen (4.2.1.1.3)) were rinsed three times with PBS and subsequently placed in the respective cell culture medium for 30 min. The substrates were placed into a Petri dish (2.5 cm, TPP, Transachingen, Switzerland) and cells were seeded in a density of $0.5 \cdot 10^6$ (MDCK-II) or $0.75\text{--}1.5 \cdot 10^6$ (MCF-10A, MCF-7, MDA-MB-231) cells per substrate and incubated for 2 days at 37 °C and 5 % CO₂ in a humidified incubator.

Experiments with living cells were carried out in the respective medium (see Table 11) supplemented with penicillin/streptomycin ($0.2 \text{ mg} \cdot \text{mL}^{-1}$, GE Healthcare, SV30010, Logan, Utah), amphotericin B ($0.5 \text{ mg} \cdot \text{mL}^{-1}$ Biochrom, A2612, Berlin, Germany) and HEPES (15 µM, Biochrom, Berlin, Germany).

For subsequent fluorescence labeling or measurement of topography the cells were fixed by incubation of the cell-sample with paraformaldehyde solution (4 %, Fluka, Switzerland) in phosphate buffered saline for 20 min at room temperature.

4.2.3. Determination of Cellular Topography

In order to determine the shape of the cellular caps, contact images measured by atomic force microscopy were collected at the sample position the microrheological measurements were performed. Additionally, cellular cap topography was examined on PFA fixed cell samples. Two orthogonal diameters (length and width) and the height of each cell were obtained from the height profile of the contact images. One diameter was taken in the direction the cell was elongated the most, the other in approximately 90° to the first one. The approximate cell spreading area $A = \pi \cdot \left(\frac{\text{length}}{2}\right) \cdot \left(\frac{\text{width}}{2}\right)$ was obtained by assuming an elliptic form.

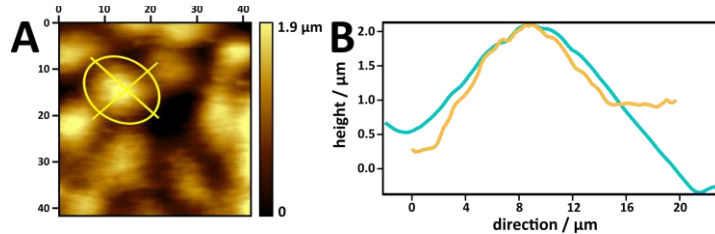


Figure 32: determination of cell topography. AFM images (contact mode) of cells were evaluated. Two orthogonal diameters (length and width) and the height of each cell were obtained from the height profile of the contact images. Spreading area was calculated assuming an elliptic form.

4.2.4. Preparation of Apical Cellular Membrane Patches

Preparation of apical cellular membrane patches was performed by Stefan Nehls (Institute of Physical Chemistry, Georg-August-Universität, Göttingen, Germany).

Preparation of apical cellular membrane patches was performed as described before by a method called sandwich-cleavage (Figure 33 A).^{168,268} Briefly, MDCK II cells were cultivated on a poly-D-lysine coated glass surface (1 mg·mL⁻¹, 2 h, Sigma Aldrich, St. Louis, Missouri, United States) as described in chapter 4.2.2.1 and cells were grown to confluence. Then, the cell monolayer was washed with PBS and was subsequently exposed to an osmotic pressure with ultrapure water for 2 min before another poly-D-lysine coated glass surface was gently pressed to the apical surface of the cell layer for 30 min to form a conformal surface contact. When the upper glass substrate was taken off, cellular patches were transferred to the surface of the second cover glass, with the cytoskeleton remains facing up (Figure 33 B1-3). For microrheological experiments, tracer particles (see chapter 4.1.1.3) were incubated for at least 3 h.

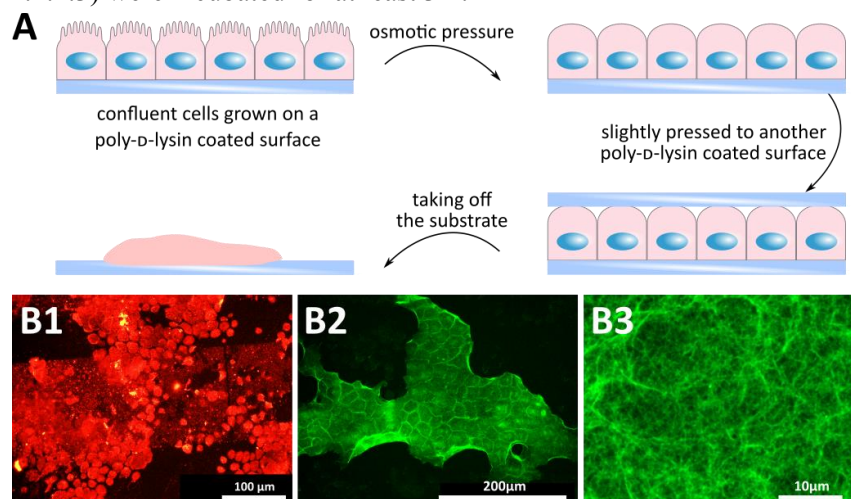


Figure 33: Overview preparation of cellular patches with the sandwich-cleavage method. **A:** Schematic overview over the experimental procedure.¹⁶⁸ MDCK II cells are cultivated on a poly-D-lysine coated surface and exposed to osmotic pressure with ultrapure water before another poly-D-lysine coated surface was slightly pressed to the cell layer. When the substrate was taken off, apical cellular membrane patches could be identified on the surface of the second coverslip. **B1:** Epi fluorescence images of the plasma membrane of a cellular patch stained with CellMask Orange plasma membrane stain (Life Technologies GmbH, C10045, Eugene, Oregon, United States) on a porous substrate (fluXXion, Netherland; pore diameter 1.2 μm, gold coated) substrate; **B2+B3:** Epi fluorescence images of F-actin staining of a cellular patch with AlexaFluoPhalloidin488 in different magnifications. (Images B1-B3 were gratefully received from Stefan Nehls)

4.2.5. Fluorescence Microscopy Methods

4.2.5.1. Fluorescence Staining

Fluorescence staining was used to analyze changes in the actin cytoskeleton upon different environmental conditions as well as to control of the surface coverage of collagen I on polyacrylamide gels of different elasticities. Buffers conditions are specified in Table 13 and usage of the respective fluorescence marker in Table 14.

Samples were washed with PBS and cells were fixed with paraformaldehyde (4 % in PBS, FLUKA, Switzerland) for 15 min at room temperature and washed two times with PBS. Prior to fluorescence staining unspecific binding was blocked by incubating the sample with a blocking buffer at room temperature for 45 min. Subsequently, different proteins were labeled either with primary and secondary antibodies or by the usage of a coupled antibody and fluorophore. Between the individual staining treatments the sample was washed two times with washing buffer on a rocking shaker (80 rpm, GFL, Burgwedel, Germany) for 5 min.

Primary and secondary antibodies. Primary antibodies were diluted to the concentrations specified below with dilution buffer. The sample was incubated for 1 h at room temperature with the respective solution. Afterwards a secondary antibody diluted with dilution buffer to the desired concentration was incubated on the sample for 1 h at room temperature.

Fluorophore coupled antibody. The sample was incubated for 1 h at room temperature with the respective fluorophore coupled antibody diluted in dilution buffer.

Nuclear acid staining. DNA was stained using 4',6-diamidino-2-phenylindole (DAPI) in PBS incubating for 15 min at room temperature.

Finally, samples were washed two times with PBS for 5 min. The samples were analyzed within 3 days.

Table 13: Composition of the different buffers used in this study for fluorescence staining. The globular protein bovine serum albumin and the nonionic surfactant Triton X-100 were purchased at Sigma Aldrich, St. Louis, Missouri, United States. Buffers were sterile filtered after preparation and used under sterile conditions.

buffer	ingredients
blocking buffer	5 % (w/v) BSA 0.3 % (w/v) Triton X-100 in PBS
dilution buffer	1 % (w/v) BSA 0.3 % (w/v) Triton X-100
washing buffer	0.1 % (w/v) BSA in PBS

Table 14: Overview of fluorescence markers used in the cell studies.

fluorescence marker	manufacturer	dilution and final concentration
monoclonal mouse anti-collagen I IgG ₁ (primary antibody)	Sigma Aldrich, St. Louis, Missouri, United States	9.4 $\mu\text{g}\cdot\text{mL}^{-1}$
monoclonal mouse anti-ezrin IgG ₁ (primary antibody)	BD Biosciences, San Jose, California, United States	2.5 $\mu\text{g}\cdot\text{mL}^{-1}$
monoclonal mouse anti E-cadherin, Clone 36 IgG _{2a} (primary antibody)	BD Biosciences, San Jose, California, United States	5 $\mu\text{g}\cdot\text{mL}^{-1}$
secondary Antibody, Alexa Fluor 488 or 546 goat Anti-mouse IgG (secondary antibody)	Life Technologies, Carlsbad, Germany	2.5 $\mu\text{g}\cdot\text{mL}^{-1}$
monoclonal mouse anti-ZO-1-1A12, AlexaFluor488 (combined)	Fisher Scientific, Waltham, Massachusetts, United States	5 $\mu\text{g}\cdot\text{mL}^{-1}$
AlexaFluor546 or 488-labeled phalloidin (combined)	Invitrogen, Germany	60 $\text{nmol}\cdot\text{L}^{-1}$
4',6-diamidino-2-phenylindole (DAPI)	Life Technologies, Carlsbad, Germany	25 $\text{ng}\cdot\text{mL}^{-1}$

4.2.5.2. CLSM Imaging

No more than three proteins or two proteins and nuclear acid were fluorescently labeled in one cell sample. Each structure was labeled with a dye emitting in a separate range of wave-length to allow good distinction between the different signals. Fluorescence labeled cells on polyacrylamide gels were imaged by confocal laser scanning microscopy (CLSM). An upright confocal laser scanning microscope (Olympus, FV 1200; Olympus, Tokyo, Japan) equipped with a 405 nm diode laser (50 mW), a 488 nm diode laser (50 mW) and a diode pumped solid state laser emitting at 561 nm (20 mW) was used. For most measurements a water immersion objective (60 x, LPUMPlanN, NA = 1.0, Olympus) was used.

4.2.6. Electric Cell-Substrate Impedance Sensing

To investigate the impact of different seeding densities on cell-cell and cell-substrate contacts electric cell-substrate impedance sensing (ECIS) experiments were carried out. ECIS data were collected during the Bachelor thesis of Franziska Ries (2016), Institute of Physical Chemistry, Georg-August-Universität, Göttingen, Germany.

4.2.6.1. Theoretical Background

Electric cell-substrate impedance sensing is a non-invasive technique to analyze the attachment, spreading and cell proliferation of cells^{269–271}. The characteristics of the cell-cell connections and the cell-substrate distance can be studied. Additionally, ECIS is widely used in migration essays such as studies of the metastatic process of cancer cells, and cell toxicity tests.

The complex impedance $|Z|$ of a system exposed to an alternating current AC , applied between two electrodes is measured (Figure 34 A). The AC current is applied through a 1 M Ω resistor to obtain an approximately constant current source. The amplitude and phase of the voltage is measured by a lock-in amplifier. The impedance is altered by every material covering the electrode e.g. cells. Especially tightly interconnected confluent monolayers alter the impedance signal. The complex impedance is a function of frequency and time after the addition of cells. In a plot of the complex impedance over time at a given frequency (for MDCKII @ ≈ 4 kHz) three stages can be distinguished (Figure 34 C). First, the signal of the uncovered electrode can be observed. Second,

cell attachment and spreading on the electrode as well as cell proliferation alter the complex impedance and finally cellular motion in the confluent monolayer leads to fluctuations in the plateau of the complex impedance. The frequency spectrum of $|Z|$ of a cell covered electrode is determined by the following parameters (see Figure 34 B&D): (i) constant phase element (CPE) describing the capacitance of the electrode, (ii) bulk resistance of the medium R_{bulk} , (iii) the barrier resistance R_b which is determined by the cell layer permeability hence the cellular junctions, (iv) the membrane capacitance C_m and (v) γ which is proportional to the square root of the resistivity of cell culture medium ρ and inversely proportional to the square root of the cell-substrate distance h .

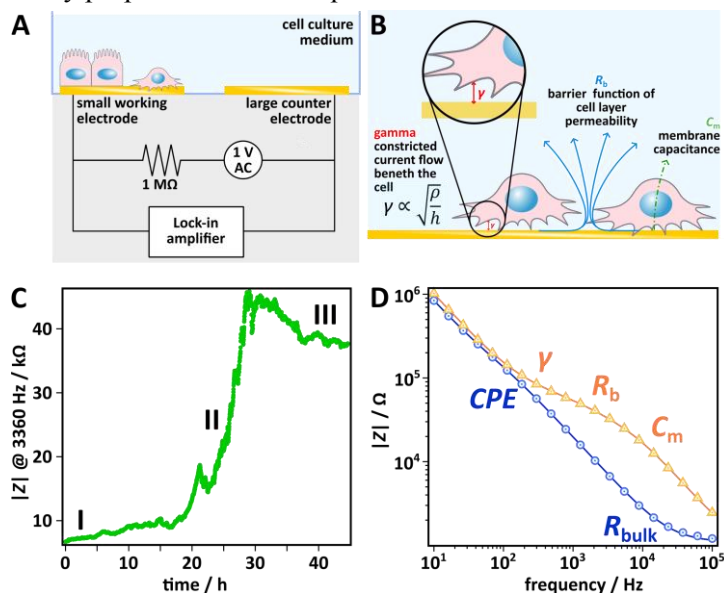


Figure 34: Overview electric cell-substrate impedance sensing (ECIS). **A:** Schematic representation of the ECIS experiment. Attachment of cells and state of confluency of the cellular monolayer are observed by impedance measurements. *AC* current is applied through a $1 \text{ M}\Omega$ resistor to obtain an approximately constant current source. The amplitude and phase of the voltage is measured by a lock-in amplifier (adapted from²⁷²). **B:** Schematic representation of the three parameters the measured complex impedance is a function of, the barrier resistance R_b , the membrane capacitance C_m and γ which is dependent on the distance between cell and substrate (adapted from <http://biophysics.com/ecismodel.php> (access 10.05.2017, 15:15)). **C:** Complex impedance over time at a frequency of 3360 Hz (green). Three stages can be distinguished. **I:** Empty electrode; **II:** Cell spreading on the electrode and cell proliferation; **III:** Cellular motion in the confluent monolayer. **D:** Complex impedance over frequency. **Blue:** Data (circles) and fit (line) for an empty electrode are shown. **Orange:** Data (triangles) and fit (line) for a confluent monolayer are shown. Inset: Equivalent circuit for a cell covered electrode. For description see text.

4.2.6.2. Experimental Procedure

Electric cell-substrate impedance sensing (ECIS) experiments were carried out on a homebuilt setup described previously.²⁷³ For measurements an 8-well-1-electrode array (8W1E PET ECIS culture ware, Ibidi, Munich, Germany) was placed in a 5 % CO_2 humidified incubator set to 37 °C. The electrodes were incubated with 200 μL cell culture medium for 0.5 h before adding different numbers of cells (see Table 15) suspended in 300 μL cell culture medium into each well and incubating for approximately 45 hours. Impedance was measured at 20 logarithmically spaced frequencies between 10 and 100,000 Hz in this time.

Table 15: Seeding densities of cells in ECIS experiments used in this study.

cell number in ECIS well (0.8 cm^2)	equivalent cell number in petri dish (9.2 cm^2)
21,720	250,000
43,500	500,000
65,220	750,000
87,000	1,000,000

4.2.6.3. Data Processing and Cell-Electrode Model

An empty electrode can be modelled by an Ohmic resistor R_{bulk} and a constant phase element CPE in series (Figure 34 D). Frequency dependent impedance spectra of living cells can be interpreted in terms of cell-electrode models to yield the barrier resistance R_b , the membrane capacitance C_m and γ (Figure 34 D). Models have been described by Giaever and Keese²⁷² and Lo and Ferrier²⁷⁴. In this study we use the model of Lo and Ferrier in which the cells are considered to be flat rectangular boxes with a half disk on each end as opposed to the earlier model which assumes the cells to be circular disks and that the electric currents flow radially beneath the cell surface and through the intercellular space.

4.2.7. Force Spectroscopy Methods to Study the Mechanics of Living Cells

Atomic force microscopy (AFM) is a versatile tool in biomechanics. Its applications range from mapping of the topology of biological surfaces, over single cell or molecule applications to quantitative force manipulations in a relevant force regime to measure cell mechanics (nN forces). Here we use the AFM for two different purposes: (i) for force manipulation on cell monolayers, especially for microrheological measurements (for description see chapter 2.2.2.1.1) and (ii) to map the topography of the apical side of the cell monolayer before starting the measurement.

4.2.7.1. Active Microrheology Measurements by Atomic Force Microscopy

4.2.7.1.1. Theoretical Background

AFM oscillatory experiments to probe cellular viscoelasticity go back to Shroff *et al.* and were refined by Alcaraz *et al.*^{76,244,275} A detailed description of the method can be found in the work of Alcaraz and coworkers. The most important steps are revised here. In force-indentation experiments with the AFM the contact geometry between the indenting probe and the sample has to be considered in the linear relation between the force and the Young's modulus. Hertzian and related contact mechanics yield:^{266,276}

$$F = C \cdot E \cdot \delta^n \text{ for a pyramidal tip geometry } F = \frac{3 \cdot E \cdot \tan(\theta_{\text{half}})}{4(1-\nu^2)} \cdot \delta^2 \quad (59)$$

where, F is the force acting on the cantilever, C is a pre-factor and n an exponent depending on the tip geometry, E is the Young modulus, δ the indentation depth, θ_{half} denotes the half opening angle of a pyramidal cantilever tip and ν the Poisson's ratio of the viscoelastic medium. After linearization for small amplitudes after Mahaffy *et al.*, transformation in frequency space and using equation (3), the following expression was obtained:²⁷⁷

$$G^*(\omega) = \frac{(1-\nu)}{3\delta_0 \cdot \tan(\theta_{\text{half}})} \cdot \frac{F(\omega)}{\delta(\omega)}, \quad (60)$$

where ω is the angular frequency, δ_0 denotes the indentation depth at which the oscillation was excited and $F(\omega)/\delta(\omega)$ is the term for amplitude damping and phase shift in the Fourier space after equation (10):

$$\frac{F(\omega)}{\delta(\omega)} = \frac{A}{D(\omega)} \cdot \exp(i(\varphi(\omega))), \quad (61)$$

with A the amplitude of the excitation amplitude, $D(\omega)$ the amplitude of the response amplitude and $\varphi(\omega)$ the phase shift. Additionally, Alcaraz *et al.* corrected the response of the viscoelastic medium for hydrodynamic drag force $i\omega \cdot b(h_0)$ acting on the cantilever from the surrounding medium at the cell surface:²⁷⁸

$$G^*(\omega) = G'(\omega) + i \cdot G''(\omega) = \frac{1-\nu}{3 \cdot \delta_0 \cdot \tan(\theta_{\text{half}})} \cdot \left[\frac{F(\omega)}{\delta(\omega)} - i\omega \cdot b(h_0) \right] \quad (62)$$

4.2.7.1.2. Experimental Procedure

Atomic force microscopy (AFM) experiments were carried out using a MFP-3D (Asylum Research, Santa Barbara, CA, USA) set-up equipped with a BioHeater mounted on an inverted Olympus IX 51 microscope (Olympus, Tokyo, Japan). MLCT cantilevers (C-lever, nominal spring constant $10 \text{ pN}\cdot\text{nm}^{-1}$, length 200 mm , tip height 8 mm , Bruker, Camarillo, CA, USA) with a pyramidal tip ($\theta_{\text{half}} \approx 17.5^\circ$) were used for imaging and force spectroscopic experiments. All experiments were performed at 37°C in buffered cell culture medium. The spring constant and the hydrodynamic drag force acting on the cantilever in different distances from the surface were determined prior to each experiment on a stiff substrate such as glass. For the calibration of the spring constant the thermal noise method was used.^{265,279} After the calibration the sample was mounted to the measuring cell and thermally equilibrated. Surface topography images ($60 \times 60 \mu\text{m}^2$, $256 \times 256 \text{ px}^2$) were collected using the contact mode (sampling frequency = 0.3 Hz). Following the topography images Force Maps of 32×32 force distance curves were collected at the same sample position. The force spectroscopy experiments were performed with a cantilever velocity towards the cell surface of $3 \mu\text{m}\cdot\text{s}^{-1}$. As soon as the cantilever reached a deflection corresponding to a force of 500 pN the cantilever was held in this indented position for 0.5 s before starting an oscillation protocol with oscillation frequencies ranging from 5 to 100 Hz at small amplitudes ($2 \cdot A = 40 \text{ nm}$, peak to peak) after another 0.5 s without oscillation the cantilever was retracted from the cell.

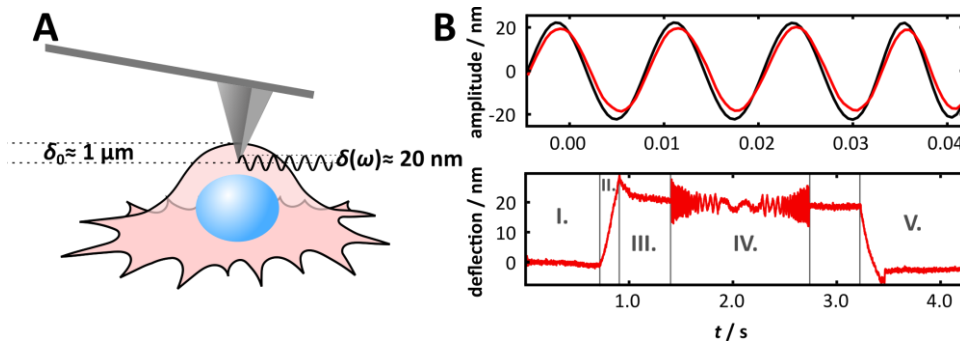


Figure 35: Measuring principle of the active microrheological measurement with AFM. **A:** Schematic representation of the measurement. **A** Cantilever with a pyramidal tip was indented approximately $\delta_0 \approx 1 \mu\text{m}$ into a cell before an oscillation protocol was performed to probe the viscoelastic properties of the cell. **B:** Measuring signal. **Above:** Amplitude diminution and phase shift between excitation and response signal (black and red curve respectively). **Below:** Deflection signal of the cantilever vs. time. Different regimes can be seen. **I:** Approach; **II:** Indentation; **III:** Creep; **IV:** Oscillation; **V:** Retraction.

4.2.7.1.3. Data Processing

From the overall 1024 force-indentation curves only those obtained from the center of the cell were chosen for further mechanical analysis to avoid artefacts from the cell boundaries. Force-distance curves showing mechanical instabilities or artefacts were disregarded as well.^{244,280} Contact point was identified by a sudden change in force. The hydrodynamic coefficient $b(h_0)$ was extrapolated from a plot of the hydrodynamic drag force versus the distance to the sample²⁷⁸. The shear modulus was evaluated after equation (64) using an in house code 'ShearFM' (version 14.07.2015) written by Jan Rother including subroutines by Ingo Mey and Andreas Janshoff in Matlab (Version 2014a, MathWorks Inc., Massachusetts, United States).

4.2.7.2. AFM Force Spectroscopy on Living Cells by Force Indentation Curves

Force indentation experiments on living cells measured with AFM allow not only to probe the viscoelastic properties of a cell but also to access other mechanical parameters. Mechanical parameters notably the sum of the cortical and the membrane tension T_0 and the apparent area compressibility $\bar{\kappa}_A$ in this context were determined by fitting a mechanical model to the contact

area of a force distance curve, called the *liquid droplet model* introduced by Discher and co-workers²⁸¹, which describes the contact of a cone-like indenter with a spherically modeled cap of a cell. A suitable model for confluent monolayers of cells was developed by Pietuch *et al.*¹⁶⁸ Prior to mechanical analysis the cap of the cell needs to be modeled in order to obtain the restoring force as a function of the indentation depth. In order to determine the shape of the cell caps, contact images were collected at the sample position the measurements was taken. From these measurements the averaged radius of the contact zone and the wetting angle could be obtained from which the cell cap was modeled. It is important to note that the model assumes constant volume and curvature during the indentation process. The model assumes the tension to dominate the force on the cantilever in the first few hundred nanometers of indentation. Upon further indentation the force does no longer scale linearly but quadratic, which is attributed to area dilatation. The isotropic tension T is given by the sum of the cortical tension and the membrane tension T_0 as well as a term describing the area dilatation of the membrane:

$$T = T_0 + \kappa_A \cdot \frac{\Delta A}{A_0} \quad (63)$$

where ΔA marks the change in surface area and A_0 the initial area of the computed cell. κ_A denotes the area compressibility modulus which is dominated by the incompressible lipid bilayer rather than the underlying actin mesh. The real surface area in an epithelial cell is much larger than the geometrical area A_0 due to protrusions and invaginations. Thus, the area compressibility modulus κ_A needs to be corrected for this excess area A_{ex} . The apparent area compressibility modulus $\tilde{\kappa}_A$ replaces κ_A .

$$\tilde{\kappa}_A = \kappa_A \cdot \frac{A_0}{A_0 + A_{ex}} \quad (64)$$

The overall tension can be itemized in two parts the cortical T_c and the membrane tension T_t

$$T_0 = T_c + T_t \quad (65)$$

The former originates e.g. in myosin II contractility. The membrane tension is dominated by attachment sites (about 80 %) and in plane tension (about 20 %)¹⁴³ and can be determined experimentally from the tether force F_t (Figure 36), neglecting minor viscous contributions:

$$T_t = \frac{1}{2 \cdot \kappa_B} \cdot \left(\frac{F_t}{2\pi} \right)^2 \quad (66)$$

κ_B is the bending module of a lipid bilayer, which we chose to be $\kappa_B = 2.7 \cdot 10^{-19} \text{J}$.²⁸²

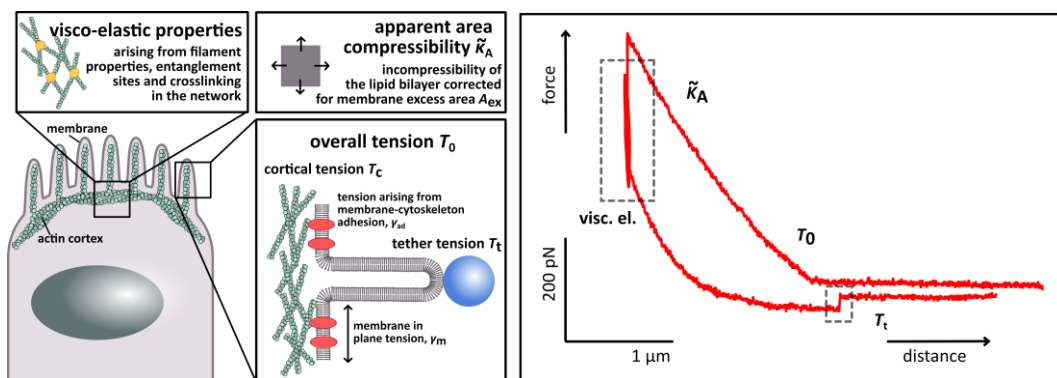


Figure 36: Schematic overview of mechanical parameters, which can be probed by AFM force indentation experiments. **Left:** Relation of the cellular cortex components and the mechanical parameters probed by AFM indentation measurements. Microrheology measurements probe the viscoelasticity of the cellular cortex hence the F-actin cytoskeleton and its cross-links. Apparent area compressibility modulus dominated by the incompressibility of the lipid bilayer and the tension rising from either active contractility of the actin cytoskeleton or the interconnection of the membrane and the cytoskeleton. **Right:** Example of force distance curve measured on with an AFM. Regions are dominated by different mechanical properties of the cell. The trace of the contact regime is dominated by the overall tension and the area compressibility. The hysteresis between the trace and the retrace curve is a measure of the viscoelasticity of the cell. Sudden jumps in the retrace following a long plateau in force originate in the pulling of so called tethers.

5. Results and Discussion

5.1. Self-Organization and Viscoelastic Properties of Actin Networks Attached to Lipid Bilayers

*“C'est l'inconnu qui m'attire.
Quand je vois un écheveau bien enchevêtré,
je me dis qu'il serait bien de trouver un fil conducteur.”*
- PIERRE GILLES DE GENNES (1991)²⁸³

The mechanical properties of a living cell are predominantly determined by its cortex.^{12,69,284} The cortex of eukaryotic cells consists of a thin layer of actomyosin filament network, interconnected with the cell-encapsulating plasma membrane. The architecture of this thin network layer is regulated by a large variety of actin binding proteins, among them bundling, branching and cross-linking proteins like fascin, filamin, ARP 2/3 and α -actinin as well as active motor proteins such as myosin (see chapter 3.1.3).¹³ Myosin contractility together with actin cortex architecture mostly determines the cortical tension in living cells.^{20,285} Though, another contribution to cellular tension originates in the linkage of the actomyosin cortex to the plasma membrane.²⁷³ Cortical tension, which is transmitted by actin-membrane linkages can also drive cellular shape changes.^{19,286} Thus, cortical tension is of utmost importance in many cellular functions such as resistance to external stresses, migration and cell division.^{151,287,288} Additionally, reorganization in the cortical actin layer is associated with different phenotypes of diseases such as cancer and malaria.^{2,3,5-7,244} It is thus important to understand the complex interplay between the different components present in the cellular cortex and their structural-mechanical role.

Conventional model systems (see chapter 3.2 and 3.3) are only partially suitable to model the mechanical properties of the cortex of living cells. Possible reasons for these mechanical differences are manifold and fall into three categories. First, the cellular cortex typically self-assembles into a thin layer which is only a few hundred nanometers thick.¹³¹ Recently it was shown that thinner as well as thicker network architecture are associated with decreased tension in the cellular cortex, suggesting an important role of spatial organization for mechanical properties.²⁰ Second, the complex composition of the F-actin cortex leads to a great diversity in the network architecture in living cells, which is used to regulate structure and mechanics according to the cellular function. Third, membrane anchorage plays an essential role in tension maintenance in the cellular cortex and thus acts on the mechanical properties.^{143,273} Potent cross-linkers between the plasma membrane and the F-actin cytoskeleton are the proteins from the ezrin, radixin, moesin (ERM)-family. Their importance in the rise of cell polarity, cell division, microvilli formation, bleb retraction as well as signaling processes in living cells has been described previously (see chapter 3.1.4).^{19,151,152,154} A significant difference between these natural actin-membrane cross-links and commonly used

artificial cross-links is the life time of the interaction. While artificial actin-membrane cross-links like the avidin-biotin interaction at solid-liquid interfaces has a half-life of about 32 hours²⁸⁹, there is evidence that the ERM proteins unbind more rapidly and are thus transient in nature^{23,33}. This difference in the time scale of remodeling might be essential for biological functions such as motility, since the apical cortex needs to be remodeled on time scales of these biological processes.²⁸⁶ Therefore, the actin cortex constantly needs to rearrange. The nature of the membrane cross-link to the plasma membrane might thus be crucial to mimic the cortex properties of living cells more closely and alter the frequency dependent viscoelastic properties of minimal actin cortices essentially.³⁴ Dysfunction of the membrane-actin connection is also associated with diseases. Most widely discussed is the role of ezrin in onset of metastasis in cancer progression.^{164,166}

Here, I examine the microrheology and the self-organization of minimal actin cortices, which are designed to mimic the physiologically relevant membrane interconnection. The complexity of the cellular cortex is reduced to the most important components: the plasma membrane, a transient cross-link between pinning-points in the membrane and pre-polymerized F-actin filaments. The focus of this study lies on the characterization of the membrane-actin interaction and is a first necessary step towards a model system containing actively contracting motor proteins. For the preparation of the minimal cortex model systems, the lipid bilayer is spread on a silicon substrate to generate a solid supported membrane.²⁹⁰ The 2D confinement is essential to enable good characterization since it is easily accessible to in-plane imaging as well as scanning probe techniques. Additionally, in 2D environments the reaction layer is easily accessible for the addition of components and washing steps. The plasma membrane is mimicked by the use of 1-palmitoyl-2-oleoyl-*sn*-glycero-3-phosphocholine (POPC) as matrix membrane lipid, since phosphatidylcholines are the major component in the plasma membrane of living cells in mammals.¹⁵⁷ In contrast to previous studies, the membrane cross-link ezrin is not tethered to the membrane by an artificial polyhistidine-tag²¹⁸, but rather bound and activated by the natural pinning-point phosphatidylinositol-4,5-bisphosphate (PIP₂)²⁹⁰. In mammalian cells the plasma membrane contains about 5 % phosphatidylinositols and about 1 % PIP₂.^{157,291} Ezrin, in its cytosolic state is conformationally self-inhibited. Two steps are proposed to be necessary for the activation of ezrin.²⁹² Binding of PIP₂ to the FERM (four-point-one, ERM) domain and additional phosphorylation of the threonine residue T567 located at the C-terminal ERM association domain (C-ERMAD) (see chapter 3.1.4). Here, a pseudo-phosphorylated mutant of ezrin, ezrinT567D, where the regulatory threonine is replaced by a negatively charged aspartate, is used. This mutant has already been shown to possess binding activity towards F-actin in *in vitro*^{223,290} as well as in *in vivo* models²⁹³. After the incubation of ezrin, pre-polymerized F-actin filaments (non-muscle) are incubated on these lipid membranes to obtain self-assembled minimal actin cortices. For comparison a similar model system is analyzed, where the F-actin network is attached to the lipid membrane via biotin-neutravidin cross-links. The deglycosylated neutravidin was used instead of streptavidin or avidin since it exhibits less nonspecific adsorption to surfaces. This bond is one of the strongest known non-covalent bonds.^{294,295}

From a rheological point of view, these F-actin membrane composite materials are interesting since they are arranged in thin shells at the interface between a bulk medium and a lipid membrane on a solid support. So far frequency dependent viscoelastic of comparable materials have only sparsely been reported⁶⁴ and no data exists on model systems using the physiological cross-link ezrin. As argued above the transient nature of ezrin might alter the frequency dependent viscoelastic

properties of such model systems.³⁴ Therefore, to study these (linear) frequency dependent viscoelastic properties, active as well as passive tracer particle based micromechanical force measurements^{26,78,103,106,107,205} will be established. For such thin ($<1\ \mu\text{m}$) layers particle-based rheology are the best choice for viscoelastic measurements. Even though setups for thin film microrheology are by now able to measure bulk samples in gap separations of 100 nm - 2000 nm²⁹⁶, there are striking experimental disadvantages such as the influence of dust particles and the need for a bulk medium as well as hydrodynamic effects. While passive particle tracking methods are well suited to probe 'soft' samples up to a shear modulus of about 1 Pa (depending on the tracking accuracy), active optical tweezer based microrheology methods cover stiffness ranges from about 1 mPa to 100 Pa (see chapter 2.2.2). Moreover, the combined use of passive and active microrheological measurements can reveal the contribution of motor proteins in networks^{14,205} (see chapter 3.2.1, Figure 13).

In the following chapters I will first analyze the self-organization and other network parameters relevant for network mechanics (see chapter 2.3) of F-actin networks on membranes containing different concentrations of pinning-points and cross-links. Second, I will carry out microrheological measurements on Newtonian liquids and entangled F-actin networks, before studying the frequency dependent viscoelastic properties of the described minimal cortex model systems. Furthermore, I aim to interpret these spectra in terms of semi-flexible polymers and binding kinetics of transient cross-links. Simulations are used to estimate the error of the unbinding rate obtained from microrheological measurements.

5.1.1. Self-Organization and Network Properties of F-Actin Attached to a Lipid Bilayer

The following chapters comprise data from a cooperation with Prof. Dr. Claudia Steinem and Markus Schön (Institute of Organic and Biomolecular Chemistry, Georg-August-Universität, Göttingen, Germany). Most of the experiments have been performed in cooperation, while my main focus has been to establish microrheological measurements and Markus Schön mainly focused on the analysis of the self-organization of the network. Data that has not been produced by myself is indicated in the figure captions.

In this chapter the self-organization of pre-polymerized F-actin filaments on solid supported lipid bilayers with different concentrations of pinning-points is presented. Important network parameters such as the mesh size and the average filament diameter will be evaluated. Furthermore, reasonable assumptions about other filament and network parameters are briefly discussed.

Bottom up minimal cortex model systems were prepared with different concentrations of pinning-points in the lipid bilayer as described in chapter 4.1.1. The pseudophosphorylated mutant of ezrin T567D as well as the pre-polymerized F-actin filaments were added in excess and incubated for a sufficiently long time, before the respective unbound protein was washed away in several rinsing processes. Conducting the experiments this way ensured that samples with different pinning-point densities and cross-link densities could be obtained. For the cross-linking protein ezrin (see Figure 37 A), pinning-point densities, respectively molar ratios of phosphatidylinositol-4,5-bisphosphate (PIP₂) in the lipid bilayer, between 1 and 6 mol% were used since previous results²⁹⁷ showed that surface coverage of ezrin reached saturation at around 6 mol% PIP₂ in the lipid membrane. Major changes in surface coverage of ezrin could be achieved between 2 and 5 mol%.

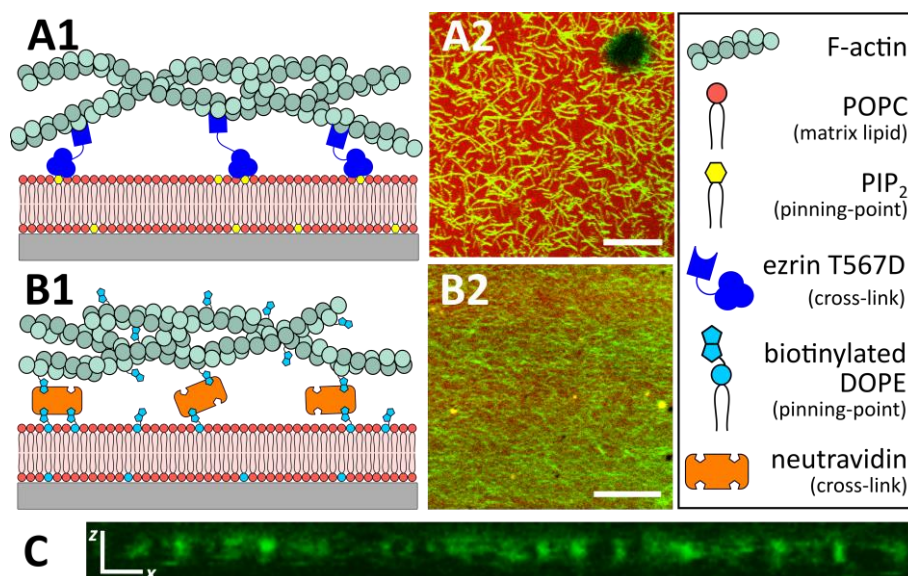


Figure 37: Overview of the two different minimal actin cortex models. **A1:** Scheme of a minimal actin cortex using physiological combination of pinning-point and cross-link, PIP₂-ezrinT567D-actin. **B1:** The artificial combination of pinning-point and cross-link, biotinylated DOPE-neutravidin-biotinylated-actin. The two cross-links differ in binding ratio and binding affinity. **A2 & B2:** Confocal fluorescence images of the membrane F-actin composite. Membrane is shown in red (A2: membrane was doped with TexasRed; B2: membrane was doped with Atto390DOPE) and F-actin is shown in green (stained with low amounts of AlexaFluor 488 phalloidin). Bar is 5 μm . **C:** Orthogonal view of the network (x - z -direction). Total height of the image is 4 μm (Figure adapted from Markus Schön)

For samples, where neutravidin provided linkage to the membrane, lower concentrations of pinning-points were used since the cross-link neutravidin is able to bind up to three additional biotin

molecules (4 binding sites in total) hence it provides more cross-links per pinning-point in the membrane (illustrated in Figure 37 B1). Here, samples with pinning-point concentrations between 0.5 and 3 mol% were analysed. Pre-polymerized non-muscular F-actin filaments were subsequently attached to either of the membrane and cross-link composites and unbound filaments were removed. In both preparations filamentous actin networks could be verified on continuously spread lipid bilayers using confocal LASER scanning microscopy (for examples see Figure 37 A & B2). Figure 37 A2 additionally shows that there is no unspecific binding between the network and the solid support as no actin is observed on a location where a membrane defect can be observed (right upper corner). From confocal image stacks, the height of the network can also be estimated (see Figure 37 C). However, the height of the self-organized network in all sample preparations, independent of pinning-point density or cross-link used, was below the resolution limit in z-direction. For a fluorescent dye excited with a wave length of 488 nm and a numerical aperture of the objective of 1.0 this is about 950 nm.²⁹⁸ Thus, we can assume that the thickness of the minimal cortex is well below 1 μm . Despite the fact that this is a rough estimation, a height below 1 μm agrees well with the cortical thickness found in living cells where a thickness of approximately 200 nm could be observed.¹³¹

Nomenclature: Throughout this document the samples will be named after the pinning-point and the molar ratio of the pinning-point. For example, ‘PIP₂ 3 mol%’ or ‘PIP₂ 3%’ will be the nomenclature for the model system with a molar ratio of 3 mol% PIP₂ in the lipid membrane and ‘biotin 3%’ for the respective lipid membrane containing a molar ratio of 3 mol% biotin-DOPE.ⁱ

5.1.1.1. Mesh Sizes of F-Actin Networks Attached to a Lipid Bilayer

The mesh size ξ is an important parameter to describe the elastic properties of F-actin filament networks. A strong anti-proportional correlation of the mesh size with the plateau modulus ($G_0 \propto \xi^{-5}$) has been predicted by many working groups (see chapter 2.3).^{27,111,121,122} Here, I want to address the question if and to what extend differences in the pinning-point concentration alter the mesh size of the resulting minimal cortex model. Examples of confocal images of F-actin networks attached to lipid bilayers via the cross-linking protein ezrin as a function of pinning-point density are shown in Figure 38.

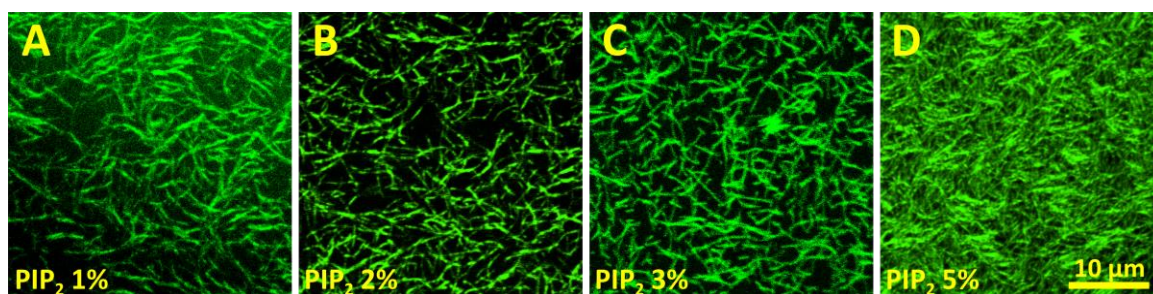


Figure 38: Examples of confocal fluorescence images of F-actin bound to solid supported lipid membranes via the cross-linking protein ezrin T567D containing different molar ratios of PIP₂. A: PIP₂ 1 mol%; B: PIP₂ 2 mol%; C: PIP₂ 3 mol% and D: PIP₂ 5 mol%. (Data obtained from Markus Schön)

Visual differences in the ratio of filament surface coverage can be observed in the different images. In order to quantify these visual differences, which are correlated to the mesh size, we use a straight

ⁱ It would be more intuitive to name the samples after the used cross-link, since we investigate the differences in frequency dependent viscoelastic properties due to their binding affinities, however, the absolute amount of surface coverage of ezrin or neutravidin cannot be determined and depends on the binding mechanism and strength of each cross-link.

forward strategy known from literature²⁵³, where the mesh size is assumed to be the diameter of the biggest circle which can be drawn into a mesh (for detailed description see chapter 4.1.2). Overlapping circles are then compared among each other and only the largest is kept. Before performing this analysis the signal-to-noise ratio in the images needs to be increased and filament positions need to be assigned. For this purpose we use a software tool called SOAX (see chapter 4.1.2.1.2).²⁵⁰ An example image overlain by the identified filaments and mesh sizes is shown in Figure 39 A. Figure 39 B shows box plots of the mesh size distribution in dependency of different molar ratio of PIP₂. Mesh sizes of $\xi(\text{PIP}_2 \text{ 1 mol\%}) = (1210 \pm 542) \text{ nm}$ (median \pm sem) for a molar ratio of pinning-points of 1 mol% are observed. Doubling the molar ratio of PIP₂ to 2 mol% leads to a slight decrease in the mesh size $\xi(\text{PIP}_2 \text{ 2 mol\%}) = (1140 \pm 560) \text{ nm}$. Increasing the pinning-point density further to 3 mol% and 5 mol% leads to significant decrease in the mesh size to $\xi(\text{PIP}_2 \text{ 3 mol\%}) = (1024 \pm 546) \text{ nm}$ and $\xi(\text{PIP}_2 \text{ 5 mol\%}) = (641 \pm 293) \text{ nm}$ respectively. Large distributions of mesh sizes are observed in one population, hence a large sample size of mesh sizes are evaluated (at least $N=1143$). The significance of the differences in the observed medians of each sample are confirmed by two-sample tests with a minimum of 95 % confidence level.

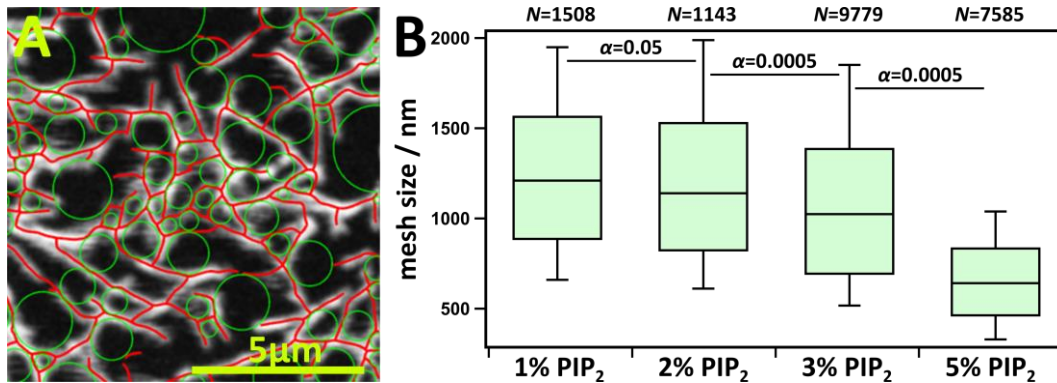


Figure 39: Mesh size analysis of actin networks attached to a lipid membrane containing different pinning-point densities. **A:** A typical filament analysis for a network attached to a lipid membrane containing 3 mol% PIP₂. Confocal fluorescence image (black and white image) with the multiple Stretching Open Active Contours (SOACs) algorithm of the software SOAX (see chapter 4.1.2).²⁵⁰ In **red** the identified filaments are shown. Meshes were identified by drawing circles originating in local maxima in an Euclidian distance map and subsequently removing all overlapping circles but the largest.²⁵³ The mesh size was interpreted as the diameter of these circles. In **green** the resulting meshes are depicted. **B:** Distribution of the mesh sizes ξ observed on samples with different pinning-point density in the lipid bilayer ranging from 1 mol% to 5 mol% PIP₂ in the solid supported membrane. Data is provided in form of box plots. Box plots extend from the 25th to the 75th percentile, whiskers from the 10th to the 90th. The number of analyzed meshes is provided on top of the graph. A Wilcoxon rank test indicated that the median of $\xi(\text{PIP}_2 \text{ 5 mol\%}) = 641 \text{ nm}$ ($M=33$) is significantly lower than the median of $\xi(\text{PIP}_2 \text{ 3 mol\%}) = 1024 \text{ nm}$ ($M=12$), $\alpha < 0.0005$, while a t -test was used to show that the median of $\xi(\text{PIP}_2 \text{ 3 mol\%})$ is significantly lower than the median of $\xi(\text{PIP}_2 \text{ 2 mol\%}) = 1140 \text{ nm}$ ($M=2$), $\alpha < 0.0005$, and that the median of $\xi(\text{PIP}_2 \text{ 2 mol\%})$ is significantly lower than the median of $\xi(\text{PIP}_2 \text{ 1 mol\%}) = 1210 \text{ nm}$ ($M=5$), $\alpha < 0.05$. M is the number of images analyzed, α is the confidence level. (Data by M. Schön)

An approximate relationship between the concentration of G-actin and the resulting mesh size has been reported and experimentally confirmed earlier for entangled F-actin networks by Schmidt *et al.* (see chapter 2.3).²⁹⁹ According to their derivation the mesh size depends on the square root of the concentration c_A of G-actin $\xi[\mu\text{m}] \approx 0.3/\sqrt{c_A[\text{mg} \cdot \text{mL}^{-1}]}$. For concentrations usually used in our experiments this approximation would give a mesh size of 514 nm. In our experiments we found mesh sizes ranging from about 650 to 1250 nm, which is in the same range but deviates mostly for low pinning-point concentrations. The underlying assumption of this approximation is that the mesh size is solely determined by the entanglements in the network and is thus not well applicable to a quasi 2D situation where the influence of pinning-points might play a crucial role. Moreover, mesh sizes observed in 3D F-actin networks of comparable concentrations were much larger than the

expected 514 nm (for comparison consult chapter 4.1.1.5). However, from this comparison it can be concluded that confinement of F-actin networks to a pinning-point containing membrane reduces the mesh size. These findings suggest the abundance of a dynamic network, which is prone to establish more bonds towards the membrane to reduce free energy.

Additionally, it has to be noted that the term mesh size as used in the description for polymers is rather the edge length of the three dimensional mesh formed by the filaments. For acute angles between the filaments our assumption of spherical meshes is poor since the diameter of a circle drawn in an elongated mesh, for example an ellipse, is always the shorter minor diameter of an ellipse. Thus, our data is on the one hand biased towards lower mesh sizes. On the other hand, all overlapping circles but the largest are removed in our approach, sorting out many smaller circles. A reasonable quality factor for the accuracy of the method or the anisotropy of the meshes is how much of area in the image is described by circles. Furthermore, anisotropy in z-direction is not taken into account in our analysis of 2D images. A more accurate value for the description of the mesh size would be to track filaments in 3D images and reconstruct the filament network. Meshes would then be defined as the volume between filaments (polyhedron instead of sphere). The side walls between filaments could be found by minimization of surface area and minimize the surface area between neighboring filament intersections. A similar procedure in 2D has been tried, the challenge in this analysis however is the treatment of loose filaments. Open meshes will introduce large errors in this method. Such an analysis exceeded the scope of this thesis but would be interesting to do in a separate project.

In living normal rat kidney fibroblasts Morone *et al.*²² determined the mesh size of the cytoskeleton located directly at the apical plasma membrane interface by electron tomography. They interpreted the mesh size as the square root of the area between the filaments. For normal rat kidney fibroblasts they found mesh sizes of about 200 nm. Even smaller mesh sizes (about 50 nm) were found for fetal rat skin keratinocytes. The mesh sizes found here are approximately 4 to 24 times larger. Disregarding the differences in the analysis of the mesh size, the most important difference between the here presented model system and the apical cortex of a living cell is the absence of regulatory proteins. Cross-linking proteins introduce additional intersections between filaments. Additionally, capping and branching actin binding proteins shorten the average length of F-actin filaments. Thus, in living cells F-actin filaments are substantially shorter ($< 2 \mu\text{m}$ according to Fritzsche *et al.*²¹) than *in vitro* polymerized F-actin filaments (around 10-20 μm according to Käs *et al.*⁹⁹). Shorter filaments need to be more densely packed in order to build affine networks. This could be an additional explanation why mesh sizes *in vivo* are smaller than the mesh sizes found here and in other *in vitro* studies.^{125,300}

5.1.1.2. Single Filament Properties of F-Actin Networks Attached to a Lipid Bilayer

Next to the mesh size, the persistence l_p and the contour length l_c are important characteristic parameters determining the mechanics of actin polymer networks. Actin as a semi-flexible biopolymer has been shown to exhibit a persistence length in the same range as its contour length $l_p \approx l_c$. For actin filaments other working groups reported a persistence length between 15.6 and 17.7 μm .^{113–115,301} However, the persistence length is highly sensitive to the diameter of the filament ($l_p \propto d^4$). Since depending on the polymerization conditions the percentage of spontaneous bundling (= variation in diameter) and thus the persistence length might vary^{176,178,179}, we studied the fiber diameter of F-actin obtained via our polymerization protocol by means of atomic force microscopy in order to estimate the distribution of filament diameter in our samples. Therefore, F-actin filaments were pre-polymerized according to the standard protocol and attached to a poly-D-lysine coated surface in a high dilution to ensure thin layers of filaments (see chapter 4.1.2.2). Height sensitive quantitative imaging atomic force microscopy images were performed (see Figure 40).

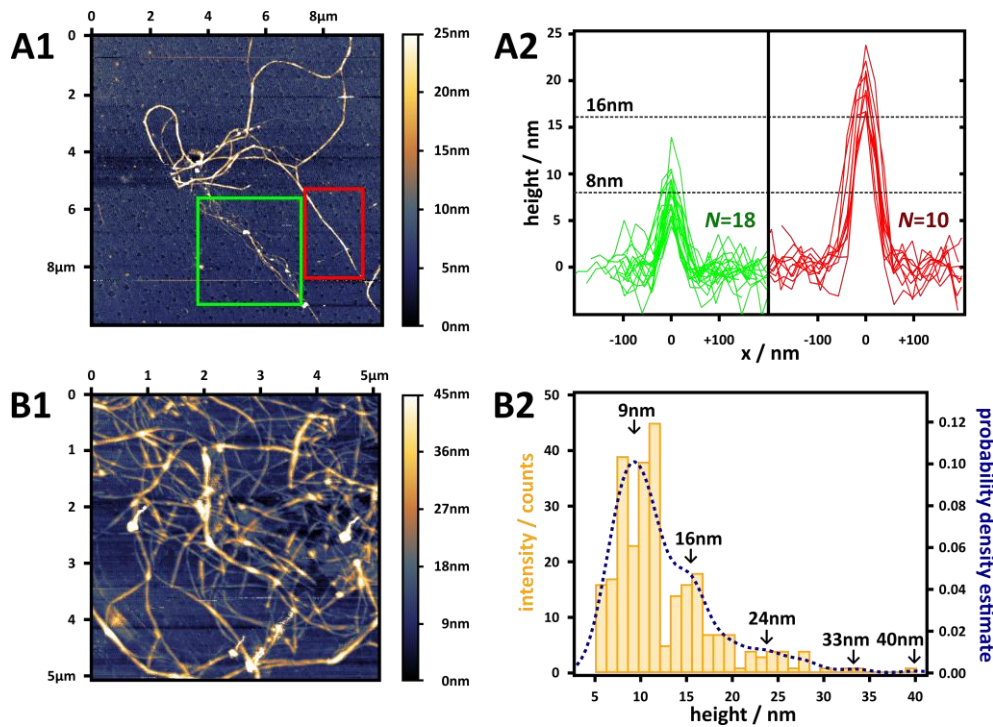


Figure 40: Analysis of the actin filament diameter. Atomic force microscopy images of pre-polymerized F-actin filaments attached to a surface via poly-D-lysine were analyzed to determine the diameter (A1-2) and the diameter distribution (B1-2) of the pre-polymerized filaments. Both images (A1 and B1) were recorded in quantitative imaging mode to ensure high precision in z -direction. The height of the filaments was analyzed from line plots. **A:** The height of filaments (A2, **green**) and small bundles (A2, **red**) was determined. The green and red boxes (A1) mark the respective regions where the filament diameter was analyzed. Filaments diameters of $d(\text{filament}) = (7.9 \pm 2.4) \text{ nm}$ (A2, green; $N=18$) and bundle diameters of $d(\text{bundle}) = (19.1 \pm 2.6) \text{ nm}$ (A2, red; $N=10$) could be determined. **B:** In an image with medium density of actin the distribution of filament diameters was analyzed. The distribution of the height of the actin fibers ($N=277$) is shown in a histogram (B2), the blue curve represents a Kernel probability density estimate. Peaks in the histogram are marked by black arrows.

The height of the filaments was analyzed from line plots in an image in which the filament density was sparse (Figure 40 A1&A2). This ensured that no filaments were lying on top of each other and that height profiles provided a smooth base line. The height of filaments (A2, green) and small bundles (A2, red) was determined. The green and red boxes (A1) mark the respective regions where the filament diameter was analyzed. Filaments diameters of $d(\text{filament}) = (7.9 \pm 2.4) \text{ nm}$ (A2,

green; $N=18$) and bundle diameters of $d(\text{bundle}) = (19.1 \pm 2.6)$ nm (A2, red; $N=10$) with a background noise of maximal 3 nm could be determined. These findings are in good agreement with the thickness of about 7 nm for the F-actin filament reported in literature^{13,137–139} and an approximately doubled diameter for the smallest possible bundle. In an image with medium density of actin the distribution of filament diameters was analyzed (Figure 40 B1 & B2). Similar to the network analysis in confocal fluorescence images the difficulty in this analysis is to determine where one filament ends and another begins, intersections and branching of the filaments foster this complexity. To circumvent this problem a filament per area distribution was analyzed (as described in chapter 4.1.2.2). For our purposes (determine the average bending rigidity) it might even be more correct to look at this number since a longer filament contributes more to the mechanical properties of the composite material than a short filament. The distribution of the height of the actin fibers is shown in a histogram (B2). About 64 % of the analyzed fibers have the diameter of a single actin filament ≈ 8 nm, 27 % two times the diameter of a filament ≈ 16 nm (=small bundles), only 9 % thicker bundles were found. Thus, in the following analysis we assume the persistence length to be $17 \mu\text{m}$ and the bending modulus $\kappa = l_p \cdot k_B T \approx 7 \cdot 10^{-26} \text{ N} \cdot \text{m}^2$ as reported for single filaments. Even though both, confocal fluorescence images and AFM images, show filaments which are bend on length scales below $17 \mu\text{m}$.

In principle the contour length l_c of the F-actin filaments should be derivable from the above reported confocal fluorescence images or atomic force microscopy images. However, as pictured above the contour of a filament is not easy to determine in networks. Additionally to the optical method, the contour length can also be derived from mechanical data (see chapter 2.3) using the polymer theory by Morse.¹¹¹ According to this theory the average contour length is estimated from a frequency dependent shear modulus of entangled actin networks (Figure 43 A):

$$l_c = \sqrt[3]{\frac{\tau_{\text{rep}} \cdot \pi \cdot k_B T \cdot \ln\left(\frac{\xi}{d}\right)}{2 \cdot \eta}}, \quad (67)$$

where ξ is the mesh size, d the filament diameter, η the solvent viscosity and τ_{rep} the reptation frequency (see chapter 5.1.2.3). For entangled 3D F-actin networks of concentrations between 8–23 μM we find $l_c \approx 14 \mu\text{m}$ for the polymerization conditions used here. However, it is possible that the filament length is affected by the reorganization on the membrane interface. Thus, contour length analysis in the actual samples would be advantageous. When this estimation is compared to the confocal images shown in Figure 38 it can be stated that a contour length of $14 \mu\text{m}$ might be a fair assumption. As argued above filament length in the cortex are much shorter $< 2 \mu\text{m}$ according to Fritzsche *et al.*²¹, due to the presence of a multiplicity of regulatory proteins.

Overall, it could be shown that the self-organization of the model cortex shows similar structural properties compared to F-actin cortices in living cells, regarding the thickness of the composite, the mesh size and the random organization of the filaments.

5.1.2. Frequency Dependent Viscoelastic Properties of MACs

5.1.2.1. Viscosity of Liquids

In order to measure frequency dependent viscoelastic properties of the above described minimal actin cortex models, three microrheological measurement techniques were established: (1) video particle tracking based passive microrheology (VPT), (2) passive microrheology using optical tweezers (PMR OT) and (3) active microrheology measured with an optical tweezer (AMR OT).

In a first experiment, the frequency dependent viscous properties of two well studied Newtonian fluids with different density properties, water and an aqueous solution of glycerol (1:1 (v/v)), were tested, in order to establish quantitative measurements with these microrheological methods. Figure 41 shows the imaginary part of the shear modulus, the loss modulus, as a function of the frequency for tracer particles in water (A) and in an aqueous solution of glycerol (B) measured with the different microrheological techniques. For Newtonian fluids the shear modulus scales with frequency as follows $G(\omega)^* = i\omega \cdot \eta$, where η is the dynamic viscosity of the fluid. The loss modulus in all measurements follows a power law behavior over at least three orders of magnitude (0.1-100 Hz).

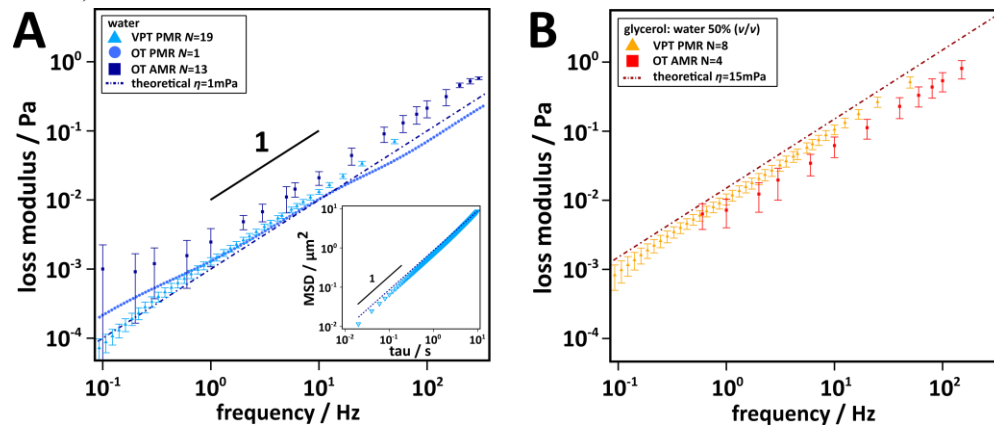


Figure 41: Measured viscosity of liquids. The scaling of the loss modulus with the frequency for samples of different viscosity is shown. **A:** water and **B:** aqueous solutions of glycerol (1:1 (v/v)). Three different methods were employed. \blacktriangle : Video particle tracking microrheology; \bullet : Passive microrheology measured an optical tweezer. \blacksquare : Active microrheology measured an optical tweezer. **Dotted lines:** expected scaling of the loss modulus with the frequency for different viscosities of the medium η (water 20 °C = 1 mPa · s) and η (glycerol: water 1: 1 (v/v), 20 °C \approx 15 mPa · s). Inset in A shows the mean squared displacement obtained from video particle tracking measurements (open triangles) and the theoretical curve progression for 22 °C (dotted line).

According to literature, the dynamic viscosity of water at 20 °C is η (water 20°C = 1.0 mPa · s)³⁰² and the dynamic viscosity of an aqueous solution (65 % (w/w) closely corresponding to 50 % (v/v)) of glycerol at 20 °C is η (glycerol: water 65 % (w/w), 20 °C \approx 15.2 mPa · s).³⁰³ The theoretical loss modulus calculated with these viscosities are shown as dashed lines in Figure 41. The dynamic viscosity from the presented data is listed in Table 16.

Table 16: Dynamic viscosities measured by different microrheology methods. Passive microrheology methods (PMR) and active microrheology methods (AMR), by video particle tracking and by optical tweezer (OT). The dynamic viscosities were obtained by a fit ($G''(\omega) = -i\omega\eta$) to the data shown in Figure 41.

method	η (water, PMR VPT) / mPa · s	η (glycerol: water 1: 1 (v/v)) / mPa · s
theoretical	1.0 (20 °C)	15.2 (20 °C)
PMR VPT	1.4 (N = 19)	10.4 (N = 8)
PMR OT	0.65 (N = 1)	n/a
AMR OT	2.1 (N = 13)	5.4 (N = 4)

With all measuring techniques, significant differences between the water and the glycerol/water samples could be observed. While the measured viscosities obtained from passive microrheology measurements showed good agreement with the data from literature, more pronounced deviations were found for the active measurements obtained on an optical tweezer. However, no clear trend to over- or underestimation of the viscosity could be determined. Fitting equation (12) to the mean squared displacement obtained from video particle tracking data ($\alpha = 1$) resulted in roughly the same values as determined from a fit to the shear modulus (see Table 16 $\eta(\text{water, PMR VPT from MSD}) = 1.24 \text{ Pa} \cdot \text{s}$ vs. $\eta(\text{water, PMR VPT from } G^*) = 1.4 \text{ Pa} \cdot \text{s}$). Thus, no major errors are introduced by the method to calculate the Fourier transform equation (21)-(23). However, $\alpha = 1$ is not truly given for the dataset of PMR OT ($\alpha = 0.88$). Ambient temperature during the measurements was about 22 °C. Thus, we expect small deviations between the measured data and the dashed lines in Figure 41: Deviations towards lower dynamic viscosities could be observed in some of the measurements (see Table 16) but not systematically throughout all measurements. The observation that active optical tweezer based microrheology measurements show the highest variation in the data meets our expectations since the active optical tweezer measurement is dependent on several calibration factors, while for example the video particle tracking data underlies only a constant conversion factor depending on the camera sensor size and magnification in the light path. Force measurements with an optical tweezer generally require the calibration of the trap stiffness and sensitivity of each trap, which depends on each individual bead. Active experiments with an optical tweezer as conducted here require several additional calibrations (see description of the method 4.1.3.3.2). The calibration of the trap stiffness of the actively oscillating trap and the relative positioning of the traps has the largest influence on the measured loss modulus. In passive measurements the measured loss modulus is solely dependent on the trap stiffness of the trap recording the bead movement. Thus, the largest uncertainties are expected for the active experiment. In general, the low frequency regime is experimentally hard to access with all methods since it takes much time to measure data points at low frequencies. At the same time the duration of the experiment cannot be infinitely long since the sample may change its physical properties on such long time scales. Consequently, less data points are collected, leading to a worse statistic. In video particle tracking based microrheology, setup drift and background noise can also affect the signal in the low frequency regime. In water and glycerol these effects could not be measured since tracer particles are not locally stationary for such a long time span (especially in z -direction).

Altogether, significant differences in the dynamic viscosities between the two samples could be observed with all three methods and quantitative measurements could be accomplished. I found that errors resulting from the measuring method should be negligible compared to the influence of inhomogeneity in the samples where F-actin is present. Most of the data presented in the following chapters has been produced with video particle tracking microscopy, comparison to the other methods will be discussed in chapter 5.1.2.7.

5.1.2.2. Mean Squared Displacements of Entangled F-Actin Networks and Networks Attached to Lipid Bilayers

Bead trajectories are recorded (see chapter 4.1.3.1.1) for video particle tracking based microrheology measurements. From these trajectories mean squared displacements are calculated which are subsequently transformed into shear moduli. In this chapter the time averaged mean squared displacement (MSD) in x - y -direction is shown, which was additionally averaged over a small ensemble of tracer particles. In the following I use the term mean squared displacement to describe the data obtained by this *modus operandi*.

Figure 42 shows the mean squared displacement of tracer particles embedded in either entangled F-actin networks or F-actin networks attached to lipid bilayer with different cross-linking proteins (see above). In general the mean squared displacement can be described as $\langle \Delta x^2(\tau) \rangle = 2 \cdot N \cdot D \cdot \tau^\alpha$, where N is the dimensionality and D the diffusion coefficient and α a power law coefficient. If $\alpha \neq 1$ then the particle diffusion is anomalous. In contrast to purely viscous samples (theoretical curve progression for water: Figure 42 A dotted red line) all actin containing MSDs show a plateau at medium time lag and sub-diffusive behavior over the whole range of time lags ($\alpha < 1$). In the plateau regime the tracer particle is only able to move an average of about 300 nm in the entangled F-actin network and 40-80 nm in actin networks attached to lipid membranes.

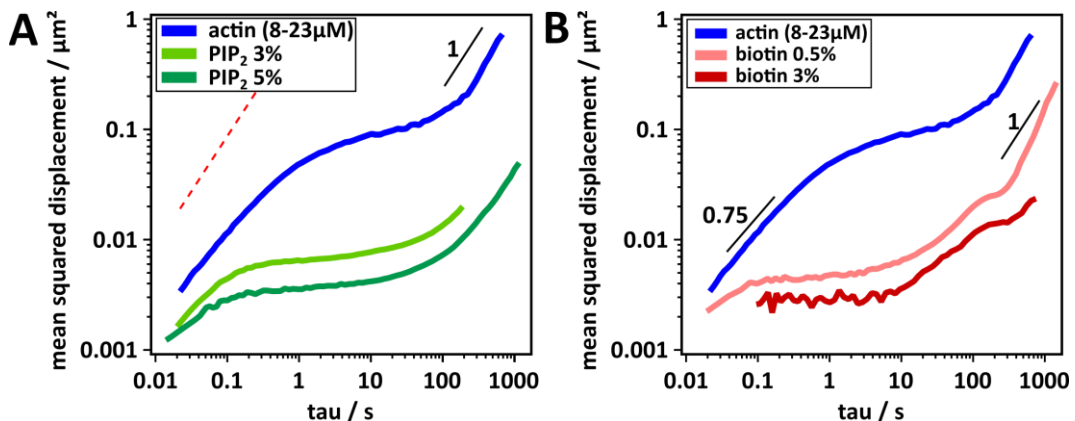


Figure 42: Mean squared displacements of F-actin model systems. Shown is the time and ensemble averaged MSD of different samples. **A:** Physiological linker ezrin, which transiently links the membrane phospholipid PIP₂ and actin and **B:** Interaction *via* neutravidin, biotinylated lipids and biotinylated actin. **Blue:** Entangled actin network without connection to a membrane (8-23 μm , $N=5$). **Light green:** Actin attached to a lipid membrane via ezrin containing 3 mol% PIP₂ ($N=6$). **Dark green:** Actin attached to a lipid membrane containing 5 mol% PIP₂ via ezrin ($N=9$). **Dark red:** Actin attached to a lipid membrane containing 3 mol% biotinylated-DOPE via neutravidin (biotin 3 mol%, $N=2$). **Light red:** Actin attached to a lipid membrane containing 0.5 mol% biotinylated-DOPE via neutravidin (biotin 0.5 mol%, $N=1$). Red dotted line shows the theoretical MSD for water at 22 °C and similar bead size. For better comparison some scaling behaviors are shown in the plot (straight black lines).

For sufficiently short time lags the mean squared displacements of all samples fall on the same line in the double logarithmic plot for all samples. The frequency range of this scaling is most pronounced for entangled F-actin networks. Here, a power law scaling of 0.76 at time lags between 0.02 and 0.3 Hz is found. This scaling behavior agrees well with a scaling behavior of 0.75 expected for semi-flexible polymers.^{67,111,122,304} In the regime of long time lags, pronounced differences in power law scaling and absolute values can be observed. In most samples, however, the mean squared displacement approaches a power law scaling of about one, attributed to normal diffusion (with higher diffusion coefficient than for water). An exception is the frequency scaling of the biotin 0.5 mol% sample at long time lags. Here, the mean squared displacement shows a super-

diffusive behavior $\alpha = 1.5$. Super diffusive behavior in absence of active processes, like motor protein activity, has not been reported and is probably an artefact.

So far the data is consistent with the hypothesis, that the time regime of low time lags is dependent on the high frequency bending modes of the semi-flexible filaments (see chapter 2.3) and that the tracer particles 'feel' the constriction of the surrounding filaments in form of a cage that hinders the motions of the particles on medium time scales. In most samples the assumption that at long time lags the particle is able to escape its cage and diffuses freely ($\alpha = 1$) seems eligible.

The plateau region of these networks exhibits the largest variances (see Figure 53) among the frequency regimes probed. This is anticipated since, as mentioned before, the largest source of error is the inhomogeneity of the composite material in terms of network self-organization and bead incorporation. Neither the scaling behavior in the high nor low frequency regime should be affected by this contribution since they are mostly determined by the persistence length and solvent viscosity as well as the long-time diffusion coefficient in the medium, respectively. The plateau modulus in contrast greatly depends on these local inhomogeneity. In fact, large ensemble averages would be beneficial for such samples. Nonetheless, I prioritize high time averages since I aim to access the low frequency regime and carefully exclude artefact-containing trajectories from our analysis. An error estimation for the statistical ensemble is provided in 5.1.2.6. Reported values for the plateau in the mean squared displacement range from $5 \cdot 10^{-3}$ to $10^{-2} \mu\text{m}^2$ for entangled F-actin networks with concentration of about $23 \mu\text{M}$ ($1 \text{ mg} \cdot \text{mL}$).^{25,26,29,117} For averaged mean squared displacements of $8\text{-}23 \mu\text{M}$ concentration a value of $0.09 \mu\text{m}^2$ was found for the plateau region. The deviation towards higher mean squared displacements in the plateau region can be explained by the differences in average F-actin concentration. For model systems, where the F-actin network was attached to a lipid bilayer, mean squared displacements as low as about $0.002 \mu\text{m}^2$ were observed for the plateau region. However, in comparison to living cells ($\text{MSD}_0(\text{cell}) \approx 10^{-4} \mu\text{m}^2$)²⁴³ all model systems show higher mean squared displacements.

5.1.2.3. Frequency Dependent Viscoelastic Properties of Entangled F-Actin Samples

First, the frequency dependent viscoelastic properties in dependency of the G-actin concentration used for polymerization are studied. Second, the effect of filament length on the cross-over in the low frequency regime is investigated. The data will be discussed in context of the polymer theory for semi-flexible polymer solutions, which has been reviewed in chapter 2.3.

Viscoelastic properties are usually described by the elastic contribution to the shear modulus $G^*(f)$, the storage modulus $G'(f)$, and the viscous contribution to the shear modulus, the loss modulus $G''(f)$ (see 2.2.2). Figure 43 A+B show these frequency dependent material properties for two entangled F-actin samples of different concentration and a semi-phenomenological model fit by Bausch and co-workers (equation (69)+(70)).³⁴ In general, the applied fit describes the data well. However, deviations in scaling behavior could be observed especially in the low and high frequency regime. Fit coefficients are reported in Appendix 1 IV. These samples were analyzed as a control for the F-actin network properties without the influence of a membrane and for comparison with the literature. Due to the different relaxation timescales in networks of semi-flexible biopolymers already the rheological properties of entangled F-actin networks are intricate, exhibiting several frequency regimes with different power law behavior and strong dependence on the organization of the polymer network. Similar to the respective regimes in the mean squared displacement (see chapter 5.1.2.2) the storage and loss modulus of F-actin samples exhibit three distinct frequency regimes, which can be sub-divided by changes in the loss tangent $\delta = G''/G'$, (see chapter 2.2.2). At intermediate frequencies the elastic contributions are larger than the viscous contributions ($G'' < G'$ thus $\delta < 1$) in both samples. In this frequency regime the sample behaves mostly like an elastic solid. At higher or lower frequencies the viscous contribution is larger than the elastic contribution ($G'' > G'$), hence, the network rather behaves like a viscous fluid at these time scales ($\delta > 1$). The three frequency regimes will be discussed independently in the following. The general characteristics of an F-actin sample of concentration 8-23 μM (Figure 43 A) are first discussed before alterations with regard to the F-actin concentration or filament contour length are described.

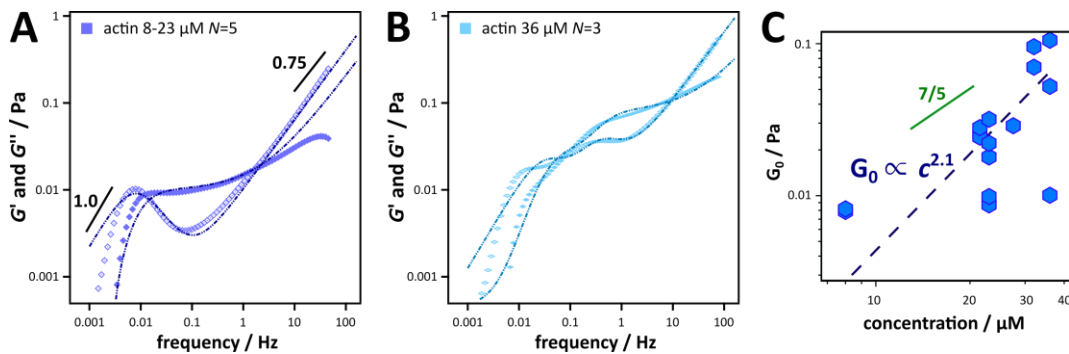


Figure 43: Frequency dependent viscoelastic properties of entangled F-actin networks of different concentrations. Shown are the storage modulus G' (filled symbols), the loss modulus G'' (open symbols) and a respective fit according to equation (69)+(70) (dashed line, for full set of parameters see Appendix IV).³⁴ **A:** Entangled F-actin network of concentration 8-23 μM (dark blue, $N=5$). **B:** F-actin networks at higher concentration without connection to a membrane (light blue, 36 μM , $N=3$). The data represents not all data collected for this concentration, other data showed a similar frequency dependency as in (A). **C:** The dependency of the plateau modulus G_0 on the G-actin concentration is shown. A power law fit to the data showed a scaling with the concentration as $G_0 \propto c^{2.1 \pm 0.8}$. Additionally, for comparison important scaling behaviors are shown in (A) + (C). (Data was partially collected in the Master thesis of Katharina Silbersdorff (2015))

High frequency regime. In the high frequency regime ($f > 1$ Hz) bending mode relaxations along the filament contribute to the viscoelastic response usually resulting in a power law with an exponent of approximately $p=0.75$ (see chapter 2.3).^{111,122} In our experiments we generally find

high frequency power law scaling of the shear modulus ($G^*(f) = G'(f) + i \cdot G''(f)$) between $p=0.60$ and $p=0.84$, while the power law scaling of only the real part in most cases is substantially lower. For example the scaling of the real part of the shear modulus for the entangled F-actin network shown in Figure 43 is found to be $p(G'(\text{actin}, 8 - 23 \mu\text{M})) = 0.40$, while the power law scaling of the imaginary part is $p(G''(\text{actin}, 8 - 23 \mu\text{M})) = 0.84$. In literature a $3/4$ power law scaling in both storage and loss modulus is reported for entangled F-actin networks.^{25,26,67} The persistence length is the network parameter that most strongly affects this high frequency regime of the shear modulus. As shown in Figure 40 B2 the filament networks analyzed here do not solely consist of filaments, about 27 % of the fibers in the network are small bundles. Müller *et al.*¹⁹¹ studied the frequency scaling of bundled F-actin networks in simulations and found an altered high frequency scaling with a higher frequency scaling in the loss modulus and a lower frequency scaling in the storage modulus. It is hence possible that the observed sub-population of actin bundles affects the frequency scaling in the described way. Another plausible explanation for the lower power law exponent of the storage modulus is that inertia might act on the response of the system as discussed later (see Figure 51 A).³⁰⁵ While the mass of the tracer particle is rather small, inertia of the local environment might have an influence. Inertia might also explain the descent in the storage modulus at frequencies of 30 Hz. This effect on the storage modulus increases with increased inertia acting on the tracer particle and decreases with increased stiffness of the system. Accordingly, we don't observe this effect in stiffer entangled F-actin samples (Figure 43 B).

Another important parameter in the high frequency regime is the entanglement frequency. As discussed in chapter 2.3 the entanglement frequency strongly depends on the entanglement length since bending modes are only able to equilibrate up to this length. In entangled F-actin networks of 8-23 μM we find an entanglement frequency of 1.5 Hz. In literature entanglement frequencies between 1 and 10 Hz have been reported for similar preparations.^{25,26,29,67,127} For the here presented higher F-actin concentration a 7-fold increase of the entanglement frequency is found (Figure 43 B). Since higher concentrations of F-actin result in smaller mesh sizes this trend is expected (mesh size and entanglement length are strongly related parameters and often $\xi \approx l_e$ is assumed see 2.3).

Intermediate frequency regime. At intermediate frequencies between 0.01 Hz and 1-10 Hz entangled actin samples behave like elastic solids ($G'(f) > G''(f)$) due to entanglement between the biopolymers (see 2.3). In this regime the storage modulus ($G'(f)$) exhibits a plateau. I picture that the polymers form a cage for the tracer particle and thereby hinder its motion. The magnitude of this plateau modulus G_0 reports on the stiffness of the system. The plateau modulus G_0 in entangled F-actin samples is mainly a function of entanglement of the semi-flexible biopolymers and thus, a function of the mesh size formed by the biopolymers (see 2.3).¹²¹ In Figure 43 C the plateau modulus G_0 as a function of G-actin concentration c is shown. In entangled 3D actin samples the plateau modulus $G_0(\text{actin})$ is found to be well below 0.1 Pa for all studied concentrations, c . A plateau modulus of $G_0(\text{actin}, 23 \mu\text{M}) = 0.017 \text{ Pa}$ (mean, $N = 6$) is found. The observed value is about 20-times lower than the absolute stiffness found by Gardel *et al.* ($G_0(\text{actin}, 23 \mu\text{M}) \approx 0.3 \text{ Pa}$)²⁹ and Mason *et al.* ($G_0(\text{actin}, 29 \mu\text{M}) \approx 0.5 \text{ Pa}$), about six times lower than found by Gardel and co-workers²⁵ and Hinner *et al.* ($G_0(\text{actin}, 23 \mu\text{M}) \approx 0.1 \text{ Pa}$)²⁸, while Palmer *et al.* reported substantially higher plateau moduli ($G_0(\text{actin}, 23 \mu\text{M}) \approx 1.5 \text{ Pa}$).¹¹⁷

The concentration dependency of the plateau modulus $G_0 \propto c^{2.1 \pm 0.8}$, however, agrees reasonably well with predictions by MacKintosh *et al.* ($G_0 \propto c^{2.2}$)²⁷ as well as experiments by Gardel *et al.* ($G_0 \propto c^{1.8 \pm 0.4}$)²⁹, while others found slightly lower dependencies of the plateau modulus on the

concentration (Palmer *et al* ($G_0 \propto c^{1.2 \pm 0.2}$).¹¹⁷, Hinner *et al.* ($G_0 \propto c^{1.4}$)²⁸ and Gurmessa *et al* ($G_0 \propto c^{1.4}$)¹⁸³). There are two opposing theories for the plateau regime of entangled F-actin networks¹⁸³. An "affine model" introduced by MacKintosh, Käs and Janmey²⁷, which predicts a $c^{11/5}$ scaling of the plateau values and an absolute stiffness of about 10 Pa. A "non-affine" model, based on the tube model introduced by Isambert and Maggs¹²¹, predicts a concentration dependency of $c^{7/5}$ and lower absolute stiffness²⁸. Based on the data I cannot discriminate between those two models. While the fit to the concentration dependency of the plateau modulus suggests an 11/5 scaling, the observed distribution in the plateau moduli is too broad to discriminate between these two models. Also, the observed absolute stiffness is well below what has been predicted by MacKintosh *et al.*²⁷

Valentine *et al.*¹⁰⁰ showed that the measured absolute stiffness of F-actin networks weakly depends on the surface chemistry of the tracer particle. They showed that carboxylated beads exhibit a two times stiffer response than BSA coated beads. In our experiments we did not observe strong alterations (within the accuracy of the method) between carboxylated and BSA coated tracer particles. We used BSA coated beads in entangled F-actin networks and carboxylated beads without further treatment in F-actin networks on lipid membranes, since the electrostatic interaction might support the incorporation of the beads in the F-actin network on these samples.

Low frequency regime. In the low frequency regime of the shear modulus long time relaxation processes of the filaments in the network can be observed. In the case of entangled actin polymers (see 2.3) this relaxation might be due to translational movement of the filaments out of its restricting tube, a movement which is called reptation. For entangled networks (Figure 43 A) I observe a crossover of the storage and loss modulus in the low frequency regime at $f = 0.012$ Hz and a local maximum in the loss modulus at 0.007 Hz (see Figure 43 A). Fitting the parameters of the semi-phenomenological model (equations (69)+(70)) to the viscoelastic spectrum yielded an unbinding rate constant of $k_{\text{off}}^{\text{app}}$ (actin entanglement) = 0.05 s^{-1} . In such a simple model system the unbinding rate constant can also be obtained by $k_{\text{off}}^{\text{app}} = 2\pi \cdot f_{\text{rep}}$, which results in a similar value. Polymer models for semi-flexible polymers¹¹¹ (see chapter 2.3) predict a peak in the loss modulus in the low frequency regime at about $f_{\text{rep}} = 0.008$ Hz for un-shortened entangled F-actin filaments resulting from reptation according to:

$$f_{\text{rep}} = \frac{\pi \cdot k_{\text{B}} T \cdot \ln\left(\frac{\xi}{d}\right)}{l_c^3 \cdot 2 \cdot \eta_s}, \quad (68)$$

with a solvent viscosity $\eta_s = 10^{-3} \text{ Pa} \cdot \text{s}$, a temperature $T = 298 \text{ K}$, a mesh size $\xi \approx 1600 \text{ nm}$ and a filament diameter $d = 8 \text{ nm}$. While the time scale observed in our experiments agrees well with the theoretical time scale of the reptation movement, several experimental data provided in the literature suggest much longer time scales for this process. The reported experimental time scales for the reptation process range from 10 to over 5000 s (see Table 2). In frequency dependent moduli obtained by microrheology a peak in loss modulus is only rarely observed^{97,126,127}. Others report spectra that might show an onset of a rising peak in the loss modulus, which was, however, not included in the frequency range probed^{26,117}, while again others don't observe a low frequency rise of the loss modulus at all.²⁵ One explanation for this diversity of results is that this process is dependent on the contour length (see equation (68)) of the filament, hence different preparations might lead to variations in the reptation frequency. Additionally, in entangled F-actin solutions the contour length exhibits a broad distribution in *in vitro* polymerizations⁹⁹, thus the entanglement frequency is expected to vary at different locations in the sample.

We carefully checked trajectories for indications of drift and camera noise in order to rule out measuring artefacts that could affect the low frequency regime. However, we did not find any effects that might cause this peak in the loss modulus other than reptation. An additional setup related query for video particle tracking based techniques was published by Golde *et al.*³⁰⁶ They showed softening of F-actin networks, which contained fluorescent polystyrene beads, when irradiated with fluorescent light and interpreted these results as degradation of the network. Even though no statement regarding the reptation frequency is made in this study, impairment of the network structure as suggested by softening of the network, would also increase the reptation frequency. However, in a later chapter (5.1.2.7) I show frequency dependent viscoelastic data measured with an optical tweezer on the same model systems, which should not be subject to this possible effect and which, nevertheless, show similar behavior in the low frequency regime. Still, the width of the peak in the loss modulus found here is steeper than expected. A frequency scaling of the loss modulus with a power law coefficient of one and a frequency scaling of the storage modulus with a power law coefficient of two is expected (see Figure 2 C)³⁶ for a single relaxation rate from the Maxwell model. Applying de-drifting tools to the recorded trajectories lead to lowered power law scaling in this regime, however I refrained from using de-drifting tools.

Briefly, the low frequency regime is experimentally hard to access, especially in entangled F-actin networks where the low frequency regime is not dominated by one specific cross-linker unbinding frequency. Accordingly, a great variety of different observations exist in literature. However, we have reasons to believe that the observed peak in the loss modulus rises from reptation movement of the filament out of its restricting tube: (1) shortening the filaments with gelsolin showed the anticipated shift of the reptation frequency (Figure 44), (2) a long time diffusion-like frequency regime can already be observed in the mean squared displacement (Figure 42), hence it is no artefact from the analysis and (3) the noise introduced by the setup is several orders of magnitude lower than the observed mean squared displacement of the bead (Figure 56). Thus, we assign the reported low frequency peak in the loss modulus ($k_{\text{off}}(\text{actin entanglement}) = 0.05 \text{ s}^{-1}$) to the filament reptation.

Effect of anisotropy in the networks due to higher F-actin concentration. Some of the microrheology data recorded in entangled F-actin networks of higher concentrations show two apparent relaxation time scales in the low frequency regime (Figure 43 B). One at $f_1 \approx 0.012 \text{ s}^{-1}$ and another at $f_2 \approx 0.2 \text{ s}^{-1}$. The first relaxation frequency is close to the reptation frequency observed in isotropically cross-linked actin networks (Figure 43 A). The other appears at a frequency about one decade higher. This phenomenon might occur due to a nematic orientation of filaments at higher concentrations since there is always one spatial direction in which the tracer particle can diffuse quicker than in another, other than in isotropically entangled networks. Above $48 \mu\text{M}$ actin reportedly occurs in different phases e.g. liquid crystalline¹¹⁹ or in aster like structures. In confocal microscopy images I also occasionally observed nematic phases in samples of $36 \mu\text{M}$ (see Figure 19 in chapter 4.1.1.5), while other regions in the sample looked isotropically entangled.

Effect of shorter filament contour length on the viscoelastic properties of F-actin networks. As a verification that filament reptation is observed in the low frequency regime of video particle tracking based microrheology F-actin, filaments were shortened by polymerizing the filaments in presence of gelsolin, a known actin capping and severing protein.³⁰⁷ Two different ratios of F-actin to gelsolin were used (700:1 and 2500:1) to obtain two filament contour lengths in addition to the initial filament length (unshortened, Figure 43). Frequency dependent viscoelastic properties of these networks are shown in Figure 44 A&B. The length of the filaments can be estimated from the

stoichiometric ratio of actin and gelsolin (370 monomers correspond to $1 \mu\text{m}$).³⁰⁷ A filament contour length for actin:gelsolin ratios of 750 and 2500 of $2 \mu\text{m}$ and $6.8 \mu\text{m}$, respectively, can be obtained. For the sample without gelsolin l_c was estimated from the reptation frequency ($l_c(\text{actin}, 8 - 23 \mu\text{M}) \sim 13 \mu\text{m}$).¹¹¹ A clear shift of the low frequency peak of the loss modulus towards higher frequencies can be observed.ⁱⁱ

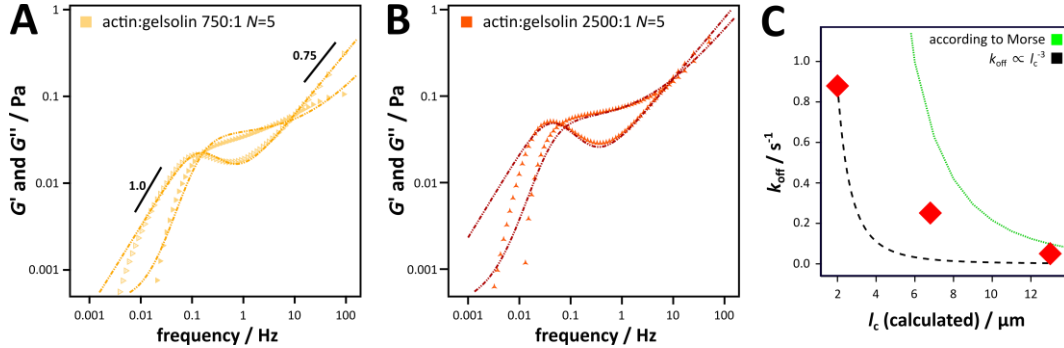


Figure 44: Frequency dependent viscoelastic properties of entangled F-actin networks adjusted to different polymer contour length by gelsolin. Shown are the storage modulus G' (filled symbols), the loss modulus G'' (open symbols) and a respective fit according to equation (69)+(70) (dashed line, for full set of parameters see Appendix 1 IV).³⁴ **A:** Entangled F-actin network consisting of actin filaments shortened by gelsolin ($26 \mu\text{m}$; actin:gelsolin, 750:1; $N=5$). **B:** Entangled F-actin network consisting of actin filaments shortened by gelsolin ($23 \mu\text{m}$; actin:gelsolin, 2500:1; $N=5$). **C:** The apparent unbinding rate constant $k_{\text{off}} = 2\pi \cdot f_{\text{rep}}$ from entangled F-actin networks as a function of the mean filament contour length, l_c . The length of the filaments can be estimated from the stoichiometric ratio of actin and gelsolin for the gelsolin containing samples.³⁰⁷ For the sample without gelsolin l_c was estimated from the reptation frequency.¹¹¹ Data was compared to a predicted scaling behavior (equation (34))¹¹¹ (green line) and fitted with a function $k_{\text{off}}(l_c) = a \cdot l_c^{-3}$ (black dashed line). (Data was partially collected in the Master thesis of Katharina Silbersdorff (2015) especially data in (A))

The model for semi-flexible polymers introduced by Morse¹¹¹ as shown in equation (59) predicts a dependency of the reptation frequency on the filament contour length. The predicted trend according to this model is shown in Figure 44 C (green line; the following parameters were used: $\xi \approx 1600 \text{ nm}$, $T = 298 \text{ K}$, $d = 8 \text{ nm}$, $\eta_s = 10^{-3} \text{ Pa} \cdot \text{s}$). Since the predicted absolute values did not confirm well with the obtained data I also fitted with a general function of $k_{\text{off}}(l_c) = a \cdot l_c^{-3}$ to the data (black dashed line, $a = 7 \mu\text{m}^3 \cdot \text{s}^{-1}$ was obtained). This scaling behavior describes the data reasonably well. Thus, a general scaling of $k_{\text{off}}(l_c) \propto l_c^{-3}$ can be assumed but this calculation is subject to versatile interpretation and has to be treated with caution. This data shows that the peak in the loss modulus at low frequencies, which we interpret as the reptation frequency, can be changed by shortening the average filament length. This finding supports our hypothesis that the rise in stress relaxation behavior at low frequencies results from translational filament motion. Yet more data is needed to draw a solid conclusion.

ⁱⁱ It has to be mentioned that one dataset (corresponding to 3 beads) for the actin:gelsolin ratio of 2500:1 was neglected since the observed plateau modulus was nearly one order of magnitude lower than the expected plateau for this concentration. This dataset showed a very low reptation frequency below 0.001 Hz and stands in contrast to the here presented data.

5.1.2.4. Frequency Dependent Viscoelastic Properties of F-Actin Networks Attached to a Lipid Bilayer via the PIP₂-Ezrin or the Biotin-Neutravidin Interaction

In this chapter the frequency dependent viscoelastic properties of minimal cortex model systems composed of a thin layer of F-actin network, interconnected with a lipid bilayer (as described in Figure 37) are presented. The microrheological data has been collected as described for the 3D F actin networks (see chapter 5.1.2.3). The alterations of the frequency dependent viscoelastic properties due to membrane attachment will be assessed as well as the influence of the cross-linker used to attach the F-actin network to the lipid bilayer.

The frequency dependent viscoelastic properties of F-actin networks self-assembled on lipid membranes containing 3 and 5 mol% PIP₂ and attached via the physiological cross-link ezrin (PIP₂-ezrinT567D-actin) respectively, are shown in Figure 45. In comparison, viscoelastic properties from a similar preparation, where the artificial cross-link neutravidin (biotinylated DOPE-neutravidin-biotinylated-actin) was used to attach the network to the lipid membrane, is shown in Figure 46. Compared to entangled 3D actin networks, all samples in which the network was attached to a lipid membrane showed higher plateau moduli. Additionally, the frequency regime in which the minimal actin cortex behaves like an elastic solid ($\delta < 1$) was broadened. In entangled F-actin networks the storage modulus dominates in frequency regimes between 0.01 Hz and 1 Hz. In contrast, networks attached to lipid membranes exhibit predominantly elastic behavior in frequency regimes between 0.01 Hz and 10 Hz (PIP₂) or ≈ 40 Hz (biotin). Although the absolute stiffness of the two model systems are on the same order of magnitude, essential differences in the frequency dependent viscoelastic properties of the two different model cortices can be observed in the low frequency regime of the biotin 0.5 and 3 mol% samples.

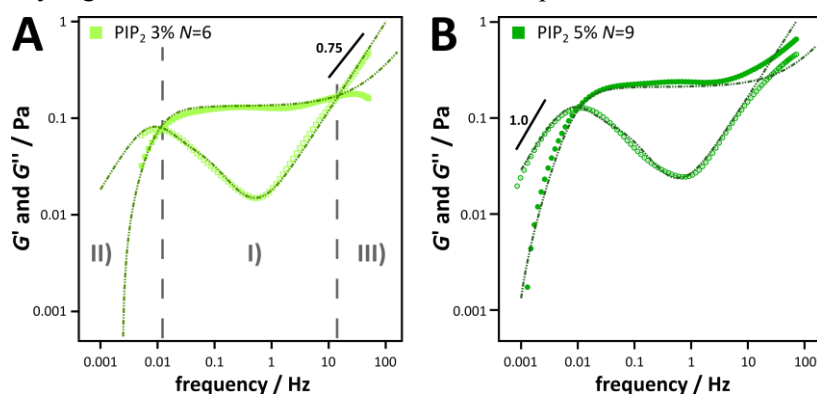


Figure 45: Frequency dependent viscoelastic properties of quasi 2D actin networks coupled to a planar membrane via PIP₂-ezrin linkage. Shown are the storage modulus G' (filled symbols), the loss modulus G'' (open symbols) and a respective fit according to equation (69)+(70) (dashed line, for full set of parameters see Appendix 1 IV).³⁴ **A:** Actin attached to a lipid membrane containing 3 mol% PIP₂ mediated by ezrin, $N=6$. Three characteristic frequency regimes are marked: **(I)** Elastic regime at intermediate frequencies ($f \approx 0.01 - 10$ Hz), **(II)** low frequency regime ($f \approx 0.001 - 0.01$ Hz) and **(III)** high frequency regime ($f \approx 10 - 100$ Hz). **B:** Actin attached to a lipid membrane containing 5 mol% PIP₂ mediated by ezrin, $N=9$. For comparison important scaling behaviors are shown in (A) + (B) (straight line). N is the number of averaged bead trajectories.

In the following, the different frequency regimes (see Figure 45 A) will be discussed separately. First, the elastic regime will be discussed, which can be observed at intermediate frequencies ($f \approx 0.01 - 10$ Hz). Second, differences in the low frequency regime ($f \approx 0.001 - 0.01$ Hz) will be analyzed. Third, the high frequency ($f \approx 10 - 100$ Hz) scaling of the viscoelastic moduli will be examined. In order to describe the full frequency dependent viscoelastic spectra, I modified the semi-phenomenological model by Bausch and co-workers³⁴, to account for more than one independent relaxation process in the low frequency regime (see chapter 4.1.3.4). The full set of parameters used for this fit is shown in Appendix 1 IV.

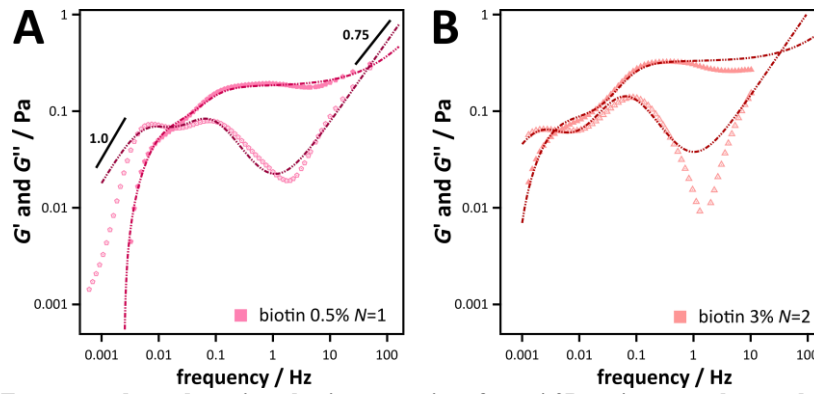


Figure 46: Frequency dependent viscoelastic properties of quasi 2D actin networks coupled to a planar membrane via neutravidin-biotin linkage. Shown are the storage modulus G' (filled symbols), the loss modulus G'' (open symbols) and a respective fit according to equation (54)(69)+(70) (dashed line, for full set of parameters see Appendix 1 IV).³⁴ **A:** Actin attached to a lipid membrane containing 0.5 mol% biotinylated DOPE via neutravidin, $N=1$. **B:** Actin attached to a lipid membrane containing 3 mol% biotinylated DOPE via neutravidin, $N=2$. For comparison important scaling behaviors are shown in (A) (straight line). N is the number of bead trajectories averaged.

D) Intermediate frequency regime ($f \approx 0.01 - 10$ Hz)

The attachment of F-actin polymer networks (low concentration: $G_0(\text{actin}, 8 \mu\text{M}) = 0.008$ Pa) to a lipid membrane generally resulted in significant stiffening of the composite material compared to the purely entangled F-actin network (see Figure 47). Attachment via transient cross-links increased the plateau modulus at least 14-fold upon binding the actin network to a PIP_2 containing lipid membrane mediated by ezrin ($G_0(\text{PIP}_2 3 \text{ mol}\%) = 0.133$ Pa (median)) and even 21-fold upon binding the actin network to a lipid membrane via neutravidin and biotin ($G_0(\text{biotin } 0.5 \text{ mol}\%) = 0.189$ Pa). A mere increase in F-actin density at the surface can hardly explain this magnitude of increase of the plateau modulus. Thus, I hypothesize that by confining the movement of the actin filaments through attachment to a lipid membrane via transient cross-links, the plateau modulus, hence the overall stiffness of the actin cortex model system, rises.

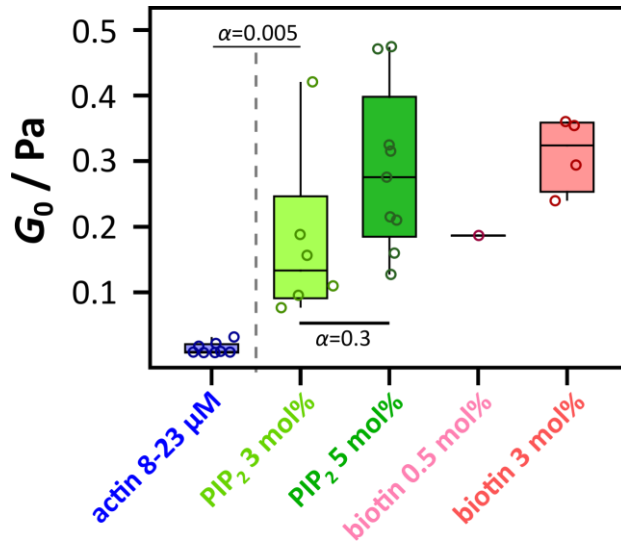


Figure 47: Plateau modulus G_0 as a function pinning-point concentration and cross-linker. **Dark blue:** Entangled actin network ($8-23 \mu\text{M}$, median: 0.009 Pa), $N=8$. **Light green:** Actin attached to a lipid membrane containing 3 mol% PIP_2 via ezrin (median: 0.133 Pa), $N=6$. **Dark green:** Actin attached to a lipid membrane containing 5 mol% PIP_2 via ezrin (median: 0.276 Pa), $N=9$. **Pink:** Actin attached to a lipid membrane containing 0.5 mol% biotinylated DOPE via neutravidin (0.189 Pa), $N=1$. **Red:** Actin attached to a lipid membrane containing 3 mol% biotinylated DOPE via neutravidin (median: 0.324 Pa), $N=4$. A Wilcoxon rank test indicated that the median of $G_0(\text{PIP}_2 5 \text{ mol}\%) = 0.276$ Pa is significantly higher than the median of $G_0(\text{PIP}_2 3 \text{ mol}\%) = 0.133$ Pa, with a confidence level of $\alpha < 0.3$, while the median of $G_0(\text{PIP}_2 3 \text{ mol}\%)$ is significantly higher than the median of $G_0(\text{actin } 8-23 \mu\text{M}) = 0.009$ Pa, $\alpha < 0.005$. Box plots extend from the 25th to the 75th percentile, whiskers from the 10th to the 90th. Individual data points are plotted as circles.

Regardless of how the attachment of the actin networks to the lipid membrane was realized, PIP_2 -ezrin-actin or biotin-neutravidin-biotin, the density of pinning-points in the membrane also had an effect on the plateau modulus of the composite material, exhibiting a higher plateau modulus for a higher number of cross-links ($G_0(\text{PIP}_2 3 \text{ mol}\%) = 0.133$ Pa $<$ $G_0(\text{PIP}_2 5 \text{ mol}\%) = 0.276$ Pa

(median each)). The effectiveness of an actin binding protein in its ability to fortify the resulting networks is usually expressed in a power law scaling of the plateau modulus with the relative cross-linker concentration $R = c_{\text{cross}}/c_{\text{actin}}$ ($G_0 \propto R^x$, $x \approx 2$ for cross-link containing 3D networks) as described by Lieleg *et al.*¹⁸⁰. In the here presented composite cortex model system the equivalent to a cross-link concentration is the pinning-point density in the membrane P (here 3 or 5 mol% in the PIP₂ containing model system). We find $G_0(\text{PIP}_2) \propto P^{1.4}$ for the more physiological model system and $G_0(\text{biotin}) \propto P^{0.3}$ for the model system where neutravidin was used as a cross-link (see Figure 48). It is reasonable that a membrane bound quasi 2D cross-link exhibits a lower scaling of the plateau modulus with the cross-linker density than a cross-link in a 3D F-actin network. A direct comparison of these values with those obtained in 3D model systems is impractical for two reasons: (1) the final amount of F-actin attached to the lipid membrane is not known in the here presented systems, thus R and P might not compare and (2) the differences due to the 2D membrane confinement, mediated by the pinning-points, are difficult to estimate. However, there are two comparable studies where the F-actin network was attached to a lipid interface by a biotin-streptavidin linkage.^{64,308} In both reported model systems a linear relationship $G_0 \propto P^1$ of the plateau modulus with the surface density of streptavidin has been observed for F-actin networks attached to a lipid interface. These studies interpret a scaling of $G_0 \propto P^1$ in the context of the affine deforming networks as reported by Head *et al.*¹⁸⁴ (see chapter 3.2.1) for 3D F-actin networks. The here presented scaling of the plateau modulus with pinning-point density in samples, in which the F-actin network was attached to the lipid bilayer via the PIP₂-erzin linkage, lies within the experimental uncertainty with these observations. The model system in which the biotin-neutravidin linkage was used showed, however, a lower scaling behavior. For these samples, the stiffness of the model system is in the limit of the measuring technique (see chapter 5.1.2.6) thus a bias for the biotin 3 mol% sample towards lower plateau moduli is possible. In chapter 5.1.1.1 we showed that the mesh size scales approximately linear with the pinning-point concentration in the membrane ($\xi \propto P^{-0.9}$). Together with the above reported dependency of the plateau modulus on the pinning-point concentration a scaling behavior of the plateau modulus with the mesh size of $G_0 \propto \xi^{-1.5}$ was found. For entangled 3D F-actin networks a dependency of the plateau modulus with $G_0(3\text{D actin}) \propto \xi^{-3}$ or ξ^{-5} depending on the model (see chapter 2.3) is predicted. Here, a lower dependency of the plateau modulus on the mesh size is found.

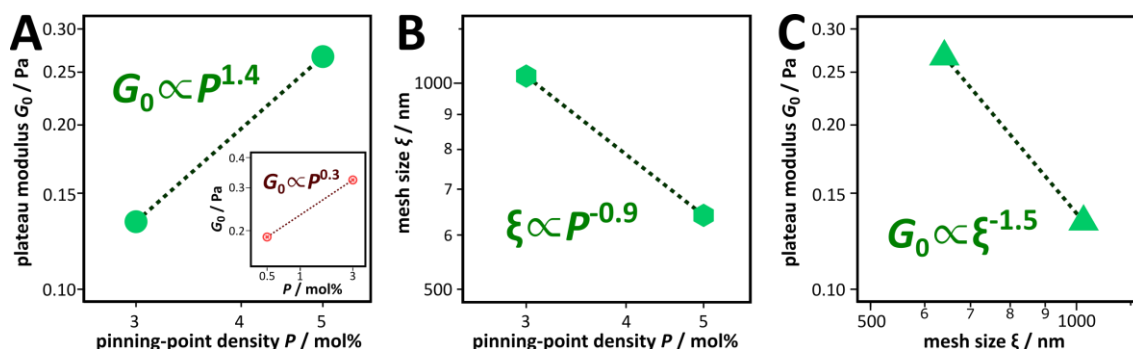


Figure 48: Scaling behavior of the mesh size and the plateau modulus as a function of pinning-point density in the 'PIP₂' minimal actin cortex. A: Scaling of the plateau modulus G_0 with the pinning-point density P ($G_0 \propto P^{1.4}$). Inset shows the scaling of the plateau modulus G_0 with pinning-point density P ($G_0 \propto P^{0.3}$) for the 'biotin' sample. B: Scaling of the mesh size ξ with the pinning-point density P ($\xi \propto P^{-0.9}$). C: Scaling of the plateau modulus G_0 with the mesh size ξ ($G_0 \propto \xi^{-1.5}$). Median values are plotted. Dotted lines show the respective power law fit to the data points.

II) Low frequency regime ($f \approx 0.001 - 0.01$ Hz)

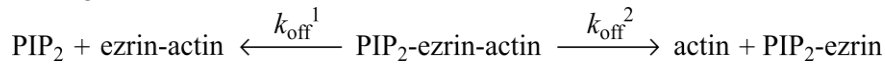
In this part, the impact on the low frequency regime of the viscoelastic properties upon attaching actin networks to a lipid membrane via the cross-links ezrin and neutravidin will be discussed. In the low frequency regime the loss modulus ($G''(f)$) exhibits a local maximum, while the storage modulus ($G'(f)$) drops monotonically with decreasing frequency, similarly as observed for entangled F-actin networks. A local maximum in the loss modulus is associated with an increase of viscous behavior in the system at the respective time scale. Bausch and co-workers attributed this network relaxation to a local stress release arising from thermal cross-link unbinding.³⁴ Additionally, other processes that lead to a relaxation processes of the polymer cage surrounding the probe particle, can also be observed on this time scale (see chapter 5.1.2.3). The polymer network interactions can be either pure entanglement of the filaments or transient intermolecular cross-links between the filaments (e.g. other actin binding proteins such as filamin) or transient cross-links between the filaments and attachment-points to a lipid membrane. Accordingly, more than one peak in the loss modulus at low frequencies is expected for minimal actin cortex models: one resulting from the reptation movement of the filaments and another resulting from dissociation of the binding complex of the cross-link. Two peaks in the low frequency regime of the viscoelastic properties were observed for the biotin 0.5 mol% and 3 mol% samples (Figure 46) and a broadened peak with a soft shoulder at about $f \approx 0.1 \text{ s}^{-1}$ was observed for the PIP₂ 3 mol% and PIP₂ 5 mol% samples (Figure 45). Here, the relaxation time scales of the entanglement and the opening of the binding complex occur at similar frequencies so the second peak cannot be resolved.

Model. The observed peaks in the low frequency loss modulus were interpreted in terms of a semi-phenomenological model (see 4.1.3.4) by Bausch and coworkers³⁴ in order to determine the apparent unbinding rate constants that dictate these processes. Bausch and coworkers used a simple exponential decay to model the unbinding of the cross-linker between two filaments. Transforming this decay into frequency space, they yield a simple model to describe the low frequency regime of the shear modulus, which has the form of a Maxwell model. Additionally, they added an offset and a commonly found high frequency scaling to describe the frequency dependent viscoelastic properties of cross-linked F-actin networks. Here, I altered the model to account for more than one independent relaxation process (for example entanglement relaxation and cross-linker unbinding). The storage and loss modulus can be describe as:

$$G'(f) = G_0 + b \cdot \left(\frac{f}{f_0}\right)^p - \sum_i \frac{a_i N_i k_{\text{off}}^i}{\left(\frac{k_{\text{off}}^i}{2\pi}\right)^2 + f^2} \quad (69)$$

$$G''(f) = d \cdot \left(\frac{f}{f_0}\right)^p + \sum_i \frac{c_i N_i f}{\left(\frac{k_{\text{off}}^i}{2\pi}\right)^2 + f^2} \quad (70)$$

Where, N is the number of bonds, $a - d$ are pre-factors that describe the elastically stored energy that is released upon cross-linker unbinding and f_0 was set to 1 Hz (as described in 3.2.1). In the case that the binding complex between the filaments is composed of three different binding partners, as it is the case in both artificial model cortices here, the binding complex dissociates with two different unbinding rate constants:



The unbinding rate constants in this case are not independent and cannot be distinguished in the fit, since:

$$\begin{aligned} d[\text{actin} - \text{ezrin} - \text{PIP}_2]/dt &= -k_{\text{off}}^1[\text{actin} - \text{ezrin} - \text{PIP}_2] - k_{\text{off}}^2[\text{actin} - \text{ezrin} - \text{PIP}_2] \\ &= -(k_{\text{off}}^1 + k_{\text{off}}^2) \cdot [\text{actin} - \text{ezrin} - \text{PIP}_2] \end{aligned} \quad (71)$$

Hence, the apparent unbinding rate constant $k_{\text{off}}^{\text{app}} = \sum k_{\text{off}}^n$ is a sum of all unbinding rate constants n of the binding complex (under the assumption that k_{on} does not play a role). An overview over the apparent unbinding rate constants obtained by this fit to the ensemble averaged data and to the single curves in an entangled 3D F-actin sample and F-actin networks attached to a lipid membrane is provided in Figure 49 (for full set of parameters see Appendix 1 IV).

As reported above two independent relaxation processes can be observed in the low frequency regime of minimal actin cortex models. So far, I was not able to obtain conclusive evidence to assign one of those peaks to the unbinding of the binding complex. In the following, I discuss one possible assignment of the observed unbinding rate constants to long time relaxation processes in the model systems. I interpret the observed soft shoulder in the PIP₂ 3 mol% and PIP₂ 5 mol% dataset as the relaxation of the entanglement, as it compares well with the first peak at 0.41 s^{-1} in the biotin 3 mol% sample. Accordingly, I use an unbinding rate constant similar to the unbinding rate constant of the entanglement on the biotin 3 mol% sample to fit the PIP₂ curves ($k_{\text{off}} \approx 0.4 \text{ s}^{-1}$ see Appendix 1 IV). Another possible interpretation of the data is discussed later.

Biotin. By fitting the parameters of the model expressed in equations (69)+(70) to the data obtained for the biotin 3 mol% sample, two unbinding rate constants $k_{\text{off}}^1 = 0.41 \text{ s}^{-1}$ and $k_{\text{off}}^2 = 0.014 \text{ s}^{-1}$ could be determined. In comparison, an apparent unbinding rate constant for the entangled actin (8-23 μM) of $k_{\text{off}}(\text{actin entangl.}) = 0.05 \text{ s}^{-1}$ was obtained (see previous chapter). I attribute the first rate constant k_{off}^1 to the unentanglement of the actin filaments and the second k_{off}^2 to the unbinding of the biotin-neutravidin-biotin complex. It is legitimate to assume that the rate constant for the relaxation of the entanglement $k_{\text{off}}^1 = k_{\text{off}}(\text{entangl.}, \text{biotin 3 mol\%}) = 0.41 \text{ s}^{-1}$ is faster for thin layers of actin network on a surface, than in entangled networks $k_{\text{off}}(\text{actin}, 8 - 23 \mu\text{M}) = 0.05 \text{ s}^{-1}$ because there are less entanglement points in the z -direction, hence the system is able to relax in less time. Shorter filaments on the minimal cortex model systems compared to the 3D F-actin networks might also lead to an increase in the rate constant k_{off}^1 similar to the observations from the previous chapter (see Figure 49 actin:gelsolin (orange)). The second unbinding rate constant at 30-times lower frequencies $k_{\text{off}}^2 = 0.014 \text{ s}^{-1}$ was assigned to the unbinding of the membrane-neutravidin-actin interaction. In literature unbinding rate constants of streptavidin³⁰⁹ and avidin²⁸⁹ dissociating from a surface have been reported to be about $k_{\text{off}}(\text{biotin} - (\text{strept})\text{avidin}) \approx 5 \cdot 10^{-6} \text{ s}^{-1}$ in passive measurements. For neutravidin (low surface coverage), however, faster unbinding rate constants of $k_{\text{off}}(\text{biotin} - \text{neutravidin}) \approx 5 \cdot 10^{-4} \text{ s}^{-1}$ have been reported.^{294,295} In the here presented sample the binding complex might, in the simplest case, consists of two biotin molecules binding to neutravidin, thus the unbinding rate constant is estimated to be $k_{\text{off}} \approx 2 \cdot 5 \cdot 10^{-4} \text{ s}^{-1} = 1 \cdot 10^{-3} \text{ s}^{-1}$. This value is 14-times lower than the unbinding rate constant observed for the biotin 3 mol% dataset $k_{\text{off}}(\text{biotin 3 mol\%}) = 0.014 \text{ s}^{-1}$ and 40-times lower than the unbinding rate constant observed for the biotin 0.5 mol% data set $k_{\text{off}}(\text{biotin 0.5 mol\%}) = 0.042 \text{ s}^{-1}$. However, molecular force spectroscopy experiments have reported both, substantially higher unbinding rate constants for the biotin-(strept-)avidin bond $k_{\text{off}} \approx 0.75 \text{ s}^{-1}$ (extrapolated to the force free situation)^{310,311} as well as lower or similar unbinding rate constants $k_{\text{off}} \approx 10^{-5} - 10^{-2} \text{ s}^{-1}$.³¹² Disregarding the very quick unbinding rates measured in force spectroscopy experiments, which might be erroneous, the differences between the measured unbinding rates and those reported in literature hint that the simple binding model used here might not be suitable for the description of this dataset. In general, it might not be useful to describe such a complex composite structure by means of molecular binding kinetics, which might

lead to substantial differences in the unbinding rates. In particular, the model assumes that the balance of the reaction ($\text{actin} + \text{ezrin} + \text{PIP}_2 \rightleftharpoons \text{binding complex}$) is greatly shifted towards the unbinding of the binding complex. However, F-actin filaments that are bound to a lipid membrane are (1) attached to the membrane via multiple bonds, (2) sterically hindered from diffusing away by the surrounding polymers in the network and (3) the binding rate for the biotin-neutravidin is not negligible since the equilibrium of the reaction is shifted towards the bound state. Rebinding might thus contribute to the apparent unbinding rate constant measured here. This effect would, however, lead to an underestimation of the unbinding rate constant. Additionally, neutravidin is able to bind up to four biotin molecules it is also possible that the binding complex consists of neutravidin and additional binding partners that might foster the bond between actin and membrane, leading to lower apparent unbinding constants. Although neutravidin, unlike streptavidin, is uncharged at physiological conditions (pI 6.3) and hence the binding affinity should not be influenced by the pH under physiological conditions it is not unlikely that the unbinding rate constant of neutravidin also depends on the specific buffer conditions and proteins in the sample as well as the orientation of the binding partners.³¹³ Especially, oxidizing agents were shown to have an impact on the binding affinity of the very similar avidin-biotin complex.³¹⁴ Others already reported that special macromolecules can reduce the affinity of avidin and streptavidin towards biotin.^{315,316}

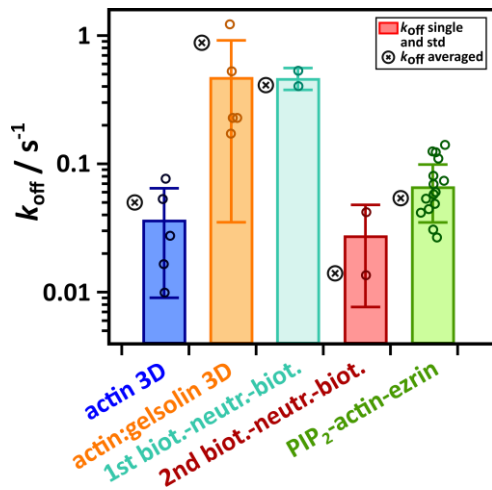


Figure 49: Unbinding rate constants k_{off} from microrheological measurements. Unbinding rate constant k_{off} obtained fitting the parameters of equation (69)+(70) to the viscoelastic spectra. **Dark blue:** Unbinding of entangled 3D actin networks 8-23 μM (mean \pm std: $(0.037 \pm 0.028) \text{ s}^{-1}$, averaged: 0.05 s^{-1} , $N=5$). **Orange:** Unbinding of 3D actin network actin:gelsolin 750:1 ($(0.475 \pm 0.440) \text{ s}^{-1}$, averaged: 0.877 s^{-1} , $N=5$). **Light blue:** First unbinding rate from the biotin samples, here attributed to the entanglement unbinding of quasi 2D actin network attached to lipid membranes ($(0.468 \pm 0.091) \text{ s}^{-1}$, averaged: 0.41 s^{-1} , $N=2$). **Red:** Second unbinding rate from the biotin samples, here attributed to the dissociation of the binding complex biotinylated lipid-neutravidin-biotinylated actin ($(0.028 \pm 0.020) \text{ s}^{-1}$, averaged: 0.014 s^{-1} , $N=2$). **Green:** Unbinding rate constant of the binding complex PIP₂-ezrin-actin ($(0.067 \pm 0.032) \text{ s}^{-1}$, averaged: 0.054 s^{-1} , $N=15$). For the second underlying peak an unbinding rate constant of 0.4 s^{-1} , was assumed in accordance with the second peak in the biotin sample. Bar plot shows the respective mean values of single measurements; error bars represent the standard deviation; crosses depict k_{off} values from fit on shear modulus obtained from averaged MSD curves. (full set of parameters in Appendix 1 IV)

PIP₂. For samples where the actin network was attached to a lipid membrane mediated by ezrin we also expect two peaks in the low frequency regime of the loss modulus similar to the 'biotin' sample. However, only one broad peak centered at about 0.01 Hz is observed. This peak might be an overlap between two unbinding kinetics, the entanglement and the unbinding of the PIP₂-ezrin-actin complex. The broadened peak width supports this presumption. I propose that the two time scales of these relaxation processes are too close together so that the peaks in $G''(f)$ cannot be resolved. In order to fit the parameters of equations (69)+(70) to the microrheology data I needed to fix the relaxation of the un-entanglement peak to $k_{\text{off}}^1(\text{ent angl., PIP}_2 \text{ 3 mol\%}) = 0.40 \text{ s}^{-1}$, assuming that the unentanglement shows the same frequency dependency as in the biotin 3 mol% sample $k_{\text{off}}^1(\text{ent angl., biotin 3 mol\%}) \approx k_{\text{off}}^1(\text{ent angl., PIP}_2 \text{ 3 mol\%}) = 0.40 \text{ s}^{-1}$ (see above). In the here presented interpretation of this peak (entanglement unbinding) this assumption is reasonable since the shift towards higher frequencies is only a function of steric hindrance not a function of

cross-link properties. Theoretically, $k_{\text{off}}^1(\text{ent angl., PIP}_2 \text{ 3 mol\%})$ is weakly dependent on the mesh size, which is altered by the cross-link concentration (see above). However, the differences in mesh size between 3 mol% and 5 mol% PIP₂ in the lipid membrane are not large enough to influence the reptation frequency in a significant way (see chapter 2.3). As a result from this proceeding, the second unbinding rate constant of the PIP₂-ezrin-actin binding complex was found to be $k_{\text{off}}^2(\text{PIP}_2 - \text{ezrin} - \text{actin}) = 0.054 \text{ s}^{-1}$. With this set of unbinding rate constants ($k_{\text{off}}^1(\text{ent angl., PIP}_2 \text{ 3 mol\%}) = 0.40 \text{ s}^{-1}$ and $k_{\text{off}}^2(\text{PIP}_2 - \text{ezrin} - \text{actin}) = 0.054 \text{ s}^{-1}$) we are able to fit the parameters of equations (69)+(70) to the data obtained from measurements with both cross-link concentrations well (PIP₂ 3 mol% and 5 mol%, see Figure 45). The unbinding rate constant of the PIP₂-ezrin-actin complex corresponds to a half-life of $t_{1/2} = \ln(2) / k_{\text{off}} \approx 13 \text{ s}$. To illustrate this quick passive dynamic of F-actin networks bound to a lipid membrane via ezrin I recorded the movement of the filaments in a time series. Figure 50 shows three images from this time series as well as a differential overlay of two images, where positions that showed rearrangement during an observed time interval of 45 s where highlighted in color. Changes in position of the filaments are clearly visible after 45 s.

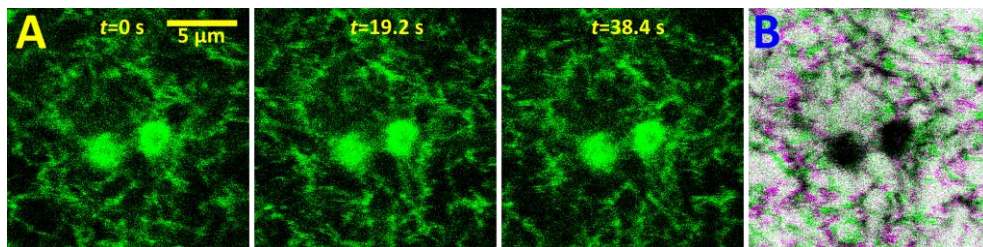


Figure 50: Time lapsed images of the F-actin network bound to a lipid membrane via ezrin. Confocal time lapsed images of F-actin filaments (green, AlexaFluorPhalloidin488 labeled) bound to a lipid membrane containing 3 mol% PIP₂ were recorded in time intervals of 1.6 s. **A:** Three images at $t = 0, 19.2$ and 38.4 s are shown. **B:** Inverted composite image of two images 45 s apart. **Green:** Positions that showed intensity at $t = 0 \text{ s}$ but not at $t = 45 \text{ s}$. **Violet:** Positions that showed intensity at $t = 45 \text{ s}$ but not at $t = 0 \text{ s}$. **Black:** positions no movement was observed. Scale bar is $5 \mu\text{m}$. Similar to the image stacks shown in Figure 22 the green circles (or black in B) of diameter $d = 2 \mu\text{m}$ correspond with the bead position.

The unbinding rate constant determined from microrheology measurements of the binding complex PIP₂-ezrin-actin lies within the previously reported range for transient cross-links (see overview in Table 3).³⁴ Braunger *et al.* determined an unbinding rate constant of $k_{\text{off}}(\text{PIP}_2 - \text{ezrin} - \text{actin}) = 1.3 \text{ s}^{-1}$ for the same ezrin mutant as used here from molecular force spectroscopy experiments *in vitro*.²³ This unbinding rate constant is about 24 times higher than what we found in passive *in vitro* experiments. It is well established that unbinding rate constants obtained from force spectroscopy data, which are extrapolated to the zero force condition, are often erroneous, with a tendency to higher values than in passive measurements.^{310,317–320} *In vivo*, Fritzsche *et al.* determined binding and unbinding rate constants using fluorescence recovery after photo bleaching for the PIP₂-ezrin and the ezrin-actin interaction.³³ An unbinding rate constant for the binding complex of PIP₂, ezrin and actin determined from their measurements suggested an unbinding rate constant of the binding complex $k_{\text{off}}(\text{PIP}_2 - \text{ezrin} - \text{actin}) = 1.63 \text{ s}^{-1}$. This value, despite measured with a passive method, is also substantially higher compared to our findings. Yet, ligand receptor interactions often depend on specific experimental conditions as argued above. Moreover, high molecular crowding, the interaction with other actin binding proteins and especially active processes might lead to diverse effects on the unbinding rate constants.

Nevertheless, it is also possible that the here determined unbinding rate constants are afflicted with errors. The interpretation of the low frequency peak in the loss modulus underlies one important assumption (see above), which is that the binding rate k_{on} does not alter the time scale where the

peak occurs. This assumption does not hold if $k_{\text{on}} > k_{\text{off}}$, which is the case for the biotin-neutravidin bond and might be an issue for the PIP₂-ezrin-actin interaction. Additionally, it might be more useful to describe the data by simulations in the future since molecular binding kinetics might not be suitable to describe the situation here.

As mentioned before no conclusive evidence is presented, which justifies the assignment of the underlying processes to the peaks. The assignment as discussed above follows the assumption that the entanglement peak has to be the peak that is similar in both minimal cortex model systems. However, it is also possible that the peak at 0.054 s^{-1} found in the PIP₂ samples corresponds to the reptation frequency, as the time scale in 3D actin networks is very similar (0.05 s^{-1}). If this was the case, the PIP₂-ezrin-actin interaction would show an even more pronounced transient binding as the corresponding unbinding rate constant would be $k_{\text{off}} \approx 0.4 \text{ s}^{-1}$. I did not follow this line of argument since the probability that the entanglement frequency should not shift in frequency, despite substantial rearrangement and additional cross-links towards the membrane, leading to a restricted movement of the filaments, did not seem plausible to me. However, if the peak in loss modulus should be caused by a different phenomenon such as an underlying drift this interpretation would be more likely.

The problematic of drift for the interpretation of the viscoelastic data in the low frequency regime has already been covered in the previous chapter but plays an equal role in the here presented data. Moreover, in samples where the F-actin network was attached to lipid membranes other slow motions in the systems might influence the low frequency regime. Especially rocking of beads that are not well incorporated into the network causes significant perturbations. Another possibility is a drifting of the lipid bilayer on a thin water film or the diffusion of the pinning-points in the lipids. We checked for these influences by tracking tracer particles settled on and interconnected with the lipid bilayer by weak electrostatic interactions. While the majority of the beads showed no motion some of the tracer particles showed an apparent long time diffusion, which could be interpreted as a slow diffusion or bead rocking, since the particles were essentially stationary over 30 min. In total no major influences of other processes to the low frequency regime could be determined.

III) High frequency regime ($f \approx 10 - 100 \text{ Hz}$)

In the high frequency regime a power law scaling of $\frac{3}{4}$ is expected for semi-flexible polymers in a polymer network (see equation (31)+(32)). Deviation from this relaxation behavior of filaments is only predicted for tensed filaments³²¹ ($G^* \propto \omega^{1/2}$) and very high frequencies in cross-linked networks³²² ($G^* \propto \omega^{7/8}$).¹⁰⁸ In F-actin networks attached to lipid bilayers (see Figure 45 A and Figure 46 A) a scaling behavior of the loss modulus with $G'' \propto f^{0.7-0.8}$ can be observed, which is in good agreement with the predicted $\frac{3}{4}$ scaling. The storage modulus shows a substantially lower power law behavior (< 0.3) for high frequencies with a decrease in power for frequencies above 50 Hz (see Figure 45 A). In most of the measurements the high frequency could not be assessed since the frequency f_{ent} was shifted towards higher frequencies. Compared to entangled F-actin networks, the entanglement frequency was found to be about ten times higher ($f_{\text{ent}}(\text{MAC}) \approx 10 \text{ Hz}$ vs. $f_{\text{ent}}(\text{ent. actin}) \approx 1 \text{ Hz}$). The entanglement frequency is the relaxation time of an undulation mode, which is on the same order as the entanglement length of the polymer. Additional pinning-points that restrict the movement of the filament are expected to lead to higher entanglement frequencies. In the following I will comment on two essential influences on the high frequency regime of the viscoelastic properties of F-actin networks bound to a lipid membrane: inertia effects and an altered effective drag coefficient close to a surface. The observed deviation from the $\frac{3}{4}$ scaling of the storage modulus might be caused by increased inertia as discussed below.

Inertia. Similar to the storage modulus of entangled F-actin networks (8-23 μM see Figure 43 A) the PIP₂ 3 mol% sample shows a decline in the storage modulus in the high frequency regime, which might result from a higher effective inertia acting on the tracer particle. To illustrate this effects I generated artificial frequency spectra of the storage and loss modulus using a model developed by Gittes and MacKintosh (see 2.3) with additional terms describing (1) the stress relaxation in the low frequency regime after Bausch and coworkers (see also 3.2.1) and (2) one additional term to the storage modulus describing the effect of inertia:^{34,122,305}

$$G'(\omega) = -\frac{a \cdot N \cdot k_{\text{off}}}{\left(\frac{k_{\text{off}}}{2\pi}\right)^2 + \omega^2} + \frac{6 \cdot k_{\text{B}}T \cdot l_p^2}{\xi^5} + \frac{k_{\text{B}}T \cdot l_p^2}{15 \cdot \xi^2} \cdot \sin\left(\frac{\pi}{8}\right) \cdot \left(\frac{2\zeta \cdot \omega}{k_{\text{B}}T \cdot l_p}\right)^{3/4} - \frac{2 \cdot \rho \cdot r^2 \cdot \omega^2}{5} \quad (72)$$

$$G''(\omega) = \frac{c \cdot N \cdot f}{\left(\frac{k_{\text{off}}}{2\pi}\right)^2 + \omega^2} + \frac{k_{\text{B}}T \cdot l_p^2}{15 \cdot \xi^2} \cdot \cos\left(\frac{\pi}{8}\right) \cdot \left(\frac{2\zeta \cdot \omega}{k_{\text{B}}T \cdot l_p}\right)^{3/4} + \omega\eta \quad (73)$$

I use the following values for the parameters: persistence length $l_p = 17 \mu\text{m}$, mesh size $\xi = 2 \mu\text{m}$, $k_{\text{B}}T = 4.11 \cdot 10^{-21} \text{ J}$, unbinding rate constant $k_{\text{off}} = 2\pi \cdot 0.01 \text{ Hz}$, number of bonds $N = 330$, prefactors $a = 1.042 \cdot 10^{-4} \text{ Pa} \cdot \text{s}^{-1}$ and $c = 1 \cdot 10^{-4} \text{ Pa} \cdot \text{s}^{-1}$, solvent viscosity $\eta = 0.0891 \text{ mPa} \cdot \text{s}$, lateral drag coefficient $\zeta = 4\pi\eta/\ln(0.6 \cdot \lambda/d)$ with a fixed wavelength of motion $\lambda = 1 \mu\text{m}$ and a filament diameter $d = 8 \text{ nm}$, material density of tracer particle $\rho = 1100 \text{ kg} \cdot \text{m}^{-3}$ (polystyrene, cellular density is similar). To test the effect of inertia I vary the radius of the tracer particle from $r = 1 - 10 \mu\text{m}$ in steps of $\Delta r = 1 \mu\text{m}$, the resulting viscoelastic moduli are shown in Figure 51 A. Upon increasing mass, the storage modulus in the high frequency regime (scaling: $\omega^{3/4}$) exhibits damping by the $-\omega^2$ scaling of the inertia term. Qualitatively the resulting storage modulus shows striking similarities with the observations in the storage modulus in the entangled F-actin sample reported in Figure 43 A and even more pronounced in Figure 45 A. For stiffer samples like the membrane bound F-actin networks a descent in the storage modulus in this frequency regime can only be caused by rather large moments of inertia. However, the complex of tracer particle and its close environment of large macromolecules and a solid supported lipid bilayer might cause such a large effect.

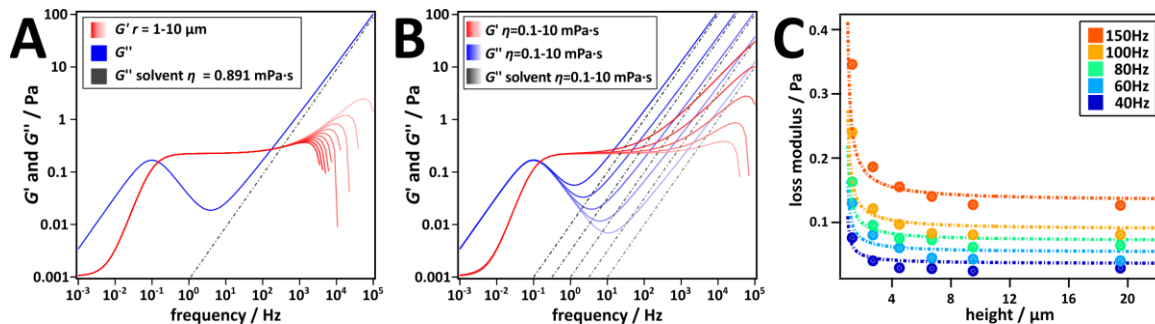


Figure 51: Two different effects acting on the high frequency scaling of F-actin networks bound to a lipid membrane. **A:** The impact of inertia on frequency spectra of viscoelastic properties. Calculated frequency dependent viscoelastic moduli, storage moduli (red shades) and loss moduli (blue shades) calculated by the above mentioned model. The radius r of the tracer particle was varied between 1-10 μm . Grey dotted line: theoretical loss modulus in pure water ($G''(\omega) = -i\omega\eta$, with $\eta = 0.981 \text{ mPa} \cdot \text{s}$). **B:** Calculated frequency dependent viscoelastic moduli, storage moduli (red shades) and loss moduli (blue shades). The solvent viscosity was set to values $\eta = 0.10, 0.32, 1.0, 3.2, 10 \text{ mPa} \cdot \text{s}$, respectively, in order to illustrate the impact of increased viscosity near surfaces on the measured viscoelastic moduli of solid supported actin cortex models. Grey dotted lines: theoretical loss modulus in pure solvent with different viscosities ($G''(\omega) = -i\omega\eta$). Frequency dependent moduli where calculated after equations (72) and (73) by a combined model.^{34,122,305} **C:** Measured loss modulus in water obtained by active microrheological measurements on an optical tweezer at different frequencies and heights above the sample surface (dots) (height was corrected for 0.5 μm) and the predicted dependency of the loss modulus with height and frequency (dashed lines). **Dark blue:** 40 Hz; **Light blue:** 60 Hz, **Green:** 80 Hz; **Orange:** 100 Hz; **Red:** 150 Hz.

Hydrodynamic drag in proximity to a surface. The model shown in equations (72) and (73) can also be used to estimate the impact of altered hydrodynamic properties on the frequency spectra of viscoelastic properties in close vicinity to a surface. From the above mentioned equations, a scaling of the high frequency regime with the solvent viscosity of $G^* \propto \eta^{3/4}$ is expected. The altered hydrodynamic drag acting on the microsphere above a surface is estimated using Faxen's law.³²³ For small velocities v and laminar flow the drag force of a solvent with the viscosity η on a sphere with a radius r is given by the Stokes law ($F = \zeta \cdot v = 6\pi\eta r \cdot v$). Close to a surface the hydrodynamic drag coefficient ζ acting on a moving sphere has to be corrected due to proximity effects. An approximate correction is:³²⁴

$$\zeta_{\text{eff}} = \frac{6\pi\eta r}{\left(1 - \frac{9}{16}\left(\frac{r}{h}\right) + \frac{1}{8}\left(\frac{r}{h}\right)^3 - \frac{45}{256}\left(\frac{r}{h}\right)^4 + \frac{1}{16}\left(\frac{r}{h}\right)^5\right)} \quad (74)$$

Thus, the approximate effective viscosity η_{eff} close to a surface is:

$$\eta_{\text{eff}} = \frac{\eta}{\left(1 - \frac{9}{16}\left(\frac{r}{h}\right) + \frac{1}{8}\left(\frac{r}{h}\right)^3 - \frac{45}{256}\left(\frac{r}{h}\right)^4 + \frac{1}{16}\left(\frac{r}{h}\right)^5\right)} \quad (75)$$

In an example this means that if a bead with the radius $r = 1 \mu\text{m}$ is moving $h = 1 \mu\text{m}$ above the surface (similar to our experimental condition) of the sample the effective solvent viscosity is: $\eta_{\text{eff}} \approx 3 \cdot \eta(\text{water}, 20^\circ\text{C}) \approx 3 \text{ mPa}$. This behavior and the impact on the loss modulus (Figure 51 C) was confirmed by active optical tweezer based microrheological measurements at different frequencies and heights above the sample surface (height was corrected for $0.5 \mu\text{m}$ ⁱⁱⁱ). To illustrate the effect of increased viscosity near a surface on the frequency dependent viscoelastic properties of actin attached to solid supported membranes, I use the same combined model as reported above now varying the viscosity between 0.1 and 10 mPa·s (Figure 51 B). Since both the storage modulus (31) and the loss modulus (32) have one term scaling with $\eta^{3/4}$ and the loss modulus has an additional term scaling with η^1 the high frequency range of the frequency dependent viscoelastic moduli should be strongly influenced by this effect. It is thus likely that the reported data is influenced by this effect in the high frequency regime.

In sum, the high frequency range of the viscoelastic properties of membrane bound F-actin networks underlie several influences from the 2D confinement and an some alterations to the predicted $3/4$ power law scaling are expected. Over all a similar scaling behavior to the predicted $3/4$ scaling can be observed.

ⁱⁱⁱ This is legitimate since only a relative height difference to the Köhler position was available.

5.1.2.5. Temperature Dependency of the Apparent Unbinding Rate Constant

In this subchapter the height of the unbinding energy barrier of the PIP₂-actin-ezrin binding complex is estimated from temperature dependent video particle tracking based microrheology experiments.

We measured the frequency dependent viscoelastic properties of the PIP₂-actin-ezrin model system (Figure 37 A1) at three different temperatures 12, 27 and 36 °C and plotted the resulting unbinding rate constants in a typical Arrhenius plot (Figure 52). Accordingly, we are able to estimate the transition barrier height ΔE_a and a pre-exponential factor A :

$$\ln(k_{\text{off}}) = \ln(A) - \frac{\Delta E_a}{R} \cdot \frac{1}{T} \quad (76)$$

where R is the universal gas constant. We found a transition barrier height of $\Delta E_a = (31.3 \pm 12.4) \text{ kJ} \cdot \text{mol}^{-1} = 12.6 k_B T$ and a pre-exponential factor of $A = (1660 \pm 8299) \text{ s}^{-1}$ for the unbinding of the complex. The rather low transition barrier height emphasizes the transient nature of the binding complex. Hence, already at low temperatures the complex is able to dissociate. The barrier height observed here agrees well with the activation energy for the dissociation of an actin sub-fragment and heavy meromyosin ($\Delta E_a = 35 \text{ kJ} \cdot \text{mol}^{-1}$), another transient cross-link for F-actin networks, found by Marston *et al.*³¹ Another study found no variation of the unbinding rate observed in microrheological measurements in F-actin networks cross-linked with heavy meromyosin.³⁵ Volkmer Ward *et al.* found about three times higher transition barrier heights for networks cross-linked with α -actinin in microrheological studies.²⁰⁰ The measured pre-exponential factor A obtained here is only vaguely determined since solely low changes in temperature could be measured. However, even for the highest value within the error margin, the pre-exponential factor is still several orders of magnitudes lower than in molecular reactions. In unimolecular reactions of small molecules the pre-factor usually is on the order of a vibrational frequency (10^{13} s^{-1}). Proteins are too large to move in such a short time corresponding to only picoseconds. As suggested by Yang and Gruebele protein folding occurs rather on timescales of 10 ns to 100 μs , corresponding to vibrational frequencies of about $10^5 - 10^8 \text{ s}^{-1}$.³²⁵ It is conceivable that the binding complex, which includes a very large filament consisting of several hundreds of proteins reacts on larger timescales leading to even smaller pre-exponential factors.

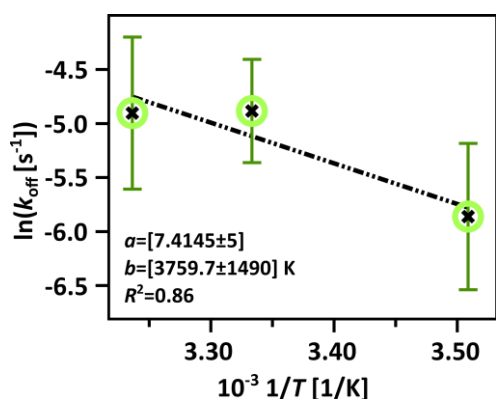


Figure 52: Unbinding rate constant of the PIP₂-ezrin-actin complex in dependency of the temperature. The dependency of $k_{\text{off}}(\text{PIP}_2 - \text{ezrin} - \text{actin})$ on the temperature (12, 27 and 36 °C) obtained from video particle tracking measurements is shown in a typical Arrhenius plot. Data points are mean values ($N=5$); error bars are the respective standard deviation; the dotted line represents an Arrhenius fit. Fit results: activation energy $\Delta E_a = (31.3 \pm 12.4) \text{ kJ} \cdot \text{mol}^{-1} = 12.6 \cdot k_B T$ and pre-exponential factor $A = (1660 \pm 8299) \text{ s}^{-1}$. All unbinding rate constants were determined using equations (69)+(70)(see 4.1.3.4).³⁴

To improve the quality of the determination of Arrhenius parameters a broader range of temperatures could have been measured. However, upon changing the temperature the whole model system undergoes changes including changes in the fluctuation of the filaments, the membrane and in solvent viscosity. Additionally, denaturation of the proteins can occur at higher frequencies, leading to error prone results. Thus, 36°C as physiological condition was chosen as the upper limit to ensure that the model system is still intact. These results support the hypothesis that the local maximum in the loss modulus at low frequencies in the measured microrheological data originates in a transient binding kinetic, which we interpret as the unbinding of the PIP₂-ezrin-actin complex.

5.1.2.6. Possible Sources of Error in VPT Based Microrheology on MACs

In this chapter I intent to discuss possible sources of error for the frequency dependent viscoelastic measurements on minimal actin cortex models performed via video particle tracking. During the course of the experiment and analysis multiple sources of error come into play, ranging from local inhomogeneity in the sample preparation, over static and dynamic errors in the particle tracking to the calculation of the mean squared displacement and the viscoelastic moduli and finally the fit to the data. In the following I will discuss four major sources of error: (1) the inhomogeneity of the samples will be addressed by showing the standard deviation of the ensemble average, (2) the variations in the viscoelastic moduli as a result of low time averages in the low frequency regime will be discussed with the help of simulations, (3) the anisotropy of the bead environment embedded in a thin layer instead of an 3D environment will be discussed and (4) the limitation of video particle tracking based microrheology for the study of minimal actin cortex models will be discussed. Since one of the most interesting property of the physiological cross-link is its transient nature, the low frequency regime of the viscoelastic properties is a major interest.

Error propagation of the standard deviation of the ensemble averaged mean squared displacement. In order to assess the variation of the frequency dependent viscoelastic properties due to local inhomogeneity of the sample, I chose a simple Gaussian error propagation for the standard deviation of the mean squared displacement of the ensemble average.

In principle the relationship of the shear modulus $G^*(\omega)$ and the mean squared displacement $\langle \Delta x^2(\tau) \rangle$ is given by the generalized Stokes-Einstein equation (21)-(22). Neglecting possible errors of the fit, we can calculate the following error estimates for the frequency dependent storage $G'(\omega)$ and loss modulus $G''(\omega)$ from the standard deviation of the ensemble average of the mean squared displacement $\Delta(\langle \Delta x^2(1/\omega) \rangle)$:

$$\Delta(G^*(\omega)) = \frac{A \cdot \Delta(\langle \Delta x^2(1/\omega) \rangle)}{(\langle \Delta x^2(1/\omega) \rangle)^2} \quad (77)$$

$$\Delta G'(\omega) = B \cdot \Delta(G^*(\omega)) \quad (78)$$

$$\Delta G''(\omega) = C \cdot \Delta(G^*(\omega)) \quad (79)$$

Figure 53 shows an example of the standard deviation of the ensemble average of the mean squared displacement (A) and it's propagation of error to the storage and loss modulus (B). The regime of short lime lags in the mean squared displacement, hence the regime of high frequency in the viscoelastic moduli, shows little variation over all locations in the sample. This regime in the data is dominated by single filament bending, therefore it is expected that the viscoelastic properties observed on these time scales show only little variation over different locations in the sample. In the long time regime, where the diffusion after dissociation of transient cross-links can supposedly be observed, the data shows medium variation, whereas the intermediate time or frequency regime exhibits the largest variation. A substantial variation in the intermediate regime was anticipated, since the plateau region is greatly determined by the mesh size (chapter 2.3), which shows a large distribution over different locations in the sample (see Figure 39). Additionally, the incorporation of the tracer particles in the network can be controlled only to a limited extend. Accordingly, the tracer particles can be situated in vicinity to the membrane or in an upper layer where the influence of the attachment is less influencing the motion of the particle. Even though the variations in the long time regime are expected to be largest for samples where the variation is a mere result of the diffusive nature of the underlying process (see below Figure 54), this variation is small compared to the variations observed in the intermediate time regime.

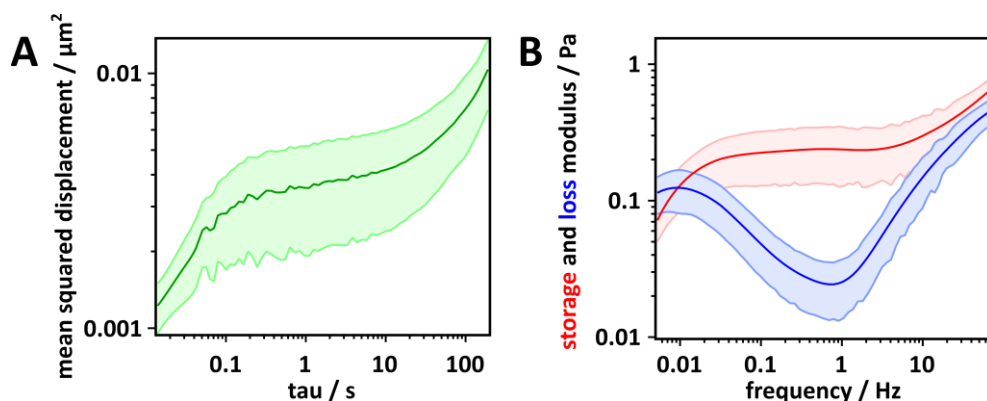


Figure 53: Error analysis and propagation of error of the ensemble average of the mean squared displacement. The standard deviation of the ensemble average of the mean squared displacement (A) and its propagation of error to the storage and loss modulus (B) is shown as an example for the dataset of PIP₂ 5 mol% ($N=9$). **A:** ensemble and time averaged mean squared displacement (solid line) and standard deviation of the ensemble average (light green filled area) of the mean squared displacement. **B:** storage (red) and loss (blue) modulus (solid lines) and the respective propagated error (red and blue filled areas) from an error propagation of the standard deviation of the ensemble average.

Precision of unbinding rate constants at low ensemble averages. As discussed before, the low frequency regime in the viscoelastic data is experimentally hard to access. Owing to long measurement times and low numbers of artefact-free bead trajectories on these time scales, only few ensemble averages can be obtained. Additionally, the time average is lower than in the high frequency regime. However, this frequency regime contains interesting information about the nature of the membrane cross-link. Even in the absence of sample inhomogeneity and other experimental artefacts the viscoelastic sample shows variations due to the stochastic nature of the underlying diffusive processes in the long time regime. Since it is not possible to exclude other contributions in experimentally obtained data, I chose to study this effect in simulations.

A viscoelastic model was used to simulate the data with an additional elastic contribution (chapter 4.1.3.4), which accounts for the filament cage surrounding the tracer particle and a diffusional process acting on long times, where the cage is able to diffuse. In the following I report three datasets, which were simulated using equations (56)-(58). The parameters were adjusted to meet the experimentally obtained viscoelastic properties (see 5.1.2.3 and 5.1.2.4). In the simulation the material properties of the complex viscoelastic medium is contained in the correlation time K at which the time dependent memory function ζ_{Maxwell} decays to decays to $1/e$ of its original value, the trap stiffness k of the harmonic potential of the cage and diffusion coefficient of the cage D_{cage} . The values for these parameters used to simulate the spectra similar to the experimental data are shown in Table 17. All other parameters were kept constant: mass $m = 1 \cdot 10^{-15}$ kg, time between two positions $\Delta t = 0.01$ s and total number of positions calculated $L = 100,000$. 'Set 1' corresponds to the experimental data of entangled F-actin (8-23 μM). 'Set 2' corresponds to the experimental data of actin attached to a lipid membrane containing 3 mol% PIP₂ mediated by ezrin and 'set 3' corresponds to the experimental data of actin attached to a lipid membrane containing 5 mol% PIP₂ mediated by ezrin. Each data set was simulated ten times and the resulting time and ensemble averaged mean squared displacement as well as the standard deviation and the experimental mean squared displacement are shown Figure 54 together with the respective frequency dependent viscoelastic moduli.

In the here presented simulations at long time lags (>100 s) the mean squared displacement of a tracer particle in a viscoelastic medium is determined by the diffusion of the cage D_{cage} surrounding the tracer particle (for verification see Figure 30 B).

Table 17: Parameters used to simulate particle traces by equation (58) in media with similar properties as found in experiments. k is the trap stiffness of the harmonic potential of the cage, D_{cage} is the diffusion coefficient of the cage and K is the correlation time at which the time dependent memory function $\tilde{\zeta}_{\text{Maxwell}}$ decays to half of its original value.

simulation	K / s	$k / \text{a. u.}$	$D_{\text{cage}} / \text{m}^2 \cdot \text{s}^{-1}$
set 1	0.8	13	$2 \cdot 10^{-16}$
set 2	0.05	50	$8 \cdot 10^{-18}$
set 3	0.05	65	$4.5 \cdot 10^{-18}$

In the simulations (set 1) a diffusion coefficient of $D_{\text{cage}}^{\text{sim}}(\text{set 1}) = 2 \cdot 10^{-16} \text{ m}^2 \cdot \text{s}^{-1}$ is used, which is close to what we find in experiments ($D_{\text{cage}}^{\text{exp}}(\text{3D actin}) = 2.6 \cdot 10^{-16} \text{ m}^2 \cdot \text{s}^{-1}$) from a fit to the mean squared displacement in the long time regime. This means that the diffusion coefficients used in the simulation are in good agreement with the experimentally determined. In a medium frequency regime at around 1 Hz the cage stiffness k has the largest impact. As shown in Figure 54 the stiffness used here results in comparable values for the plateau modulus. At the short time limit of the frequency spectrum the correlation time K dominates the viscoelastic properties. As the underlying model (Maxwell model) for the correlation used here can only model the viscoelastic properties to a limited extend (see chapter 2.2.1.3 and Figure 54) no interpretation or comparison of this time regime is done. Since we are interested in the frequency region where the cross-over from the plateau region to the long-time diffusion takes place, using this model is valid.

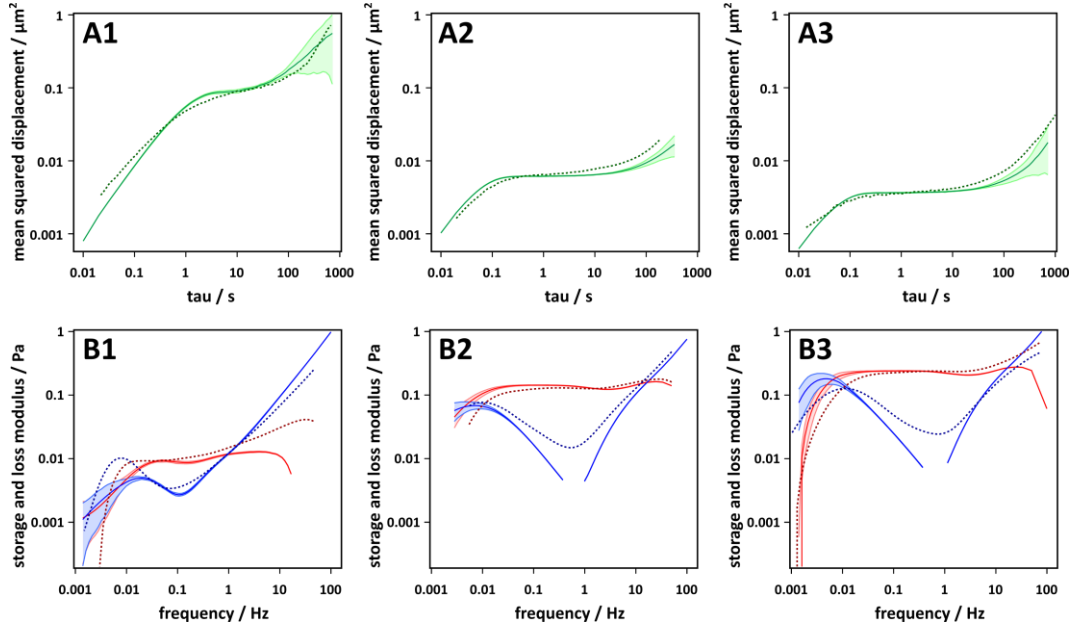


Figure 54: Mean squared displacement and viscoelastic moduli resulting from simulated particle motions in a viscoelastic medium. The trace of the particle in a medium of varying viscoelastic properties was simulated ten times as described in chapter 4.1.4, afterwards the time and ensemble averaged mean squared displacement as well as the viscoelastic moduli were adjusted to resemble the experimental data. **A:** mean squared displacement (green) vs. time. **B:** storage (red) and loss modulus (blue) vs. frequency. **A+B 1:** simulated spectra similar to the experimental data of entangled F-actin (8-23 μM), $N = 10$. **A+B 2:** simulated spectra similar to the experimental data of actin attached to a lipid membrane containing 3 mol% PIP₂ mediated by ezrin, $N = 10$. **A+B 3:** simulated spectra similar to the experimental data of actin attached to a lipid membrane containing 5 mol% PIP₂ mediated by ezrin, $N = 10$. Dark solid line: mean value of the ensemble average. Light areas: standard deviation and error estimation by Gaussian error propagation (see equation (77)). Dotted lines: experimental data. Parameters for the simulation are listed in Table 17.

At long times it can be observed that the mean squared displacement and hence, the viscoelastic moduli in all simulations in Figure 54 show increased scattering. This has two reasons: (1) the lower time average in this regime and (2) the stochastic nature of the underlying diffusional process. Accordingly, the latter results in higher scattering for higher diffusion coefficients. In order to

estimate the variation of the moduli due to this influence for each simulation corresponding to the experiments we can calculate the standard deviation of the unbinding rate constant due to intrinsic distribution of the long-time cage diffusion (at constant k). Therefore, we determined the unbinding rate constant as explained in chapter 4.1.3.4. For the second set of simulations we obtained the following mean unbinding rate constants and standard deviation:

$$k_{\text{off}}(\text{set 2, simulation}) = (0.047 \pm 0.014) \text{ s}^{-1} (N = 6).$$

From the experimental data we obtained (see Figure 49):

$$k_{\text{off}}(\text{PIP}_2 \text{ 3 mol\%, experiment}) = (0.067 \pm 0.032) \text{ s}^{-1} (N = 6).$$

Compared to the standard deviation from the simulated data, the standard deviation of the experimental data is about two times higher. As explained above the unbinding rate constant underlies two sources of error: the stiffness and the diffusion of the cage. In the simulations k was kept constant hence the standard deviation displayed there originates only in the variations of the diffusion of the cage. Whereas the experimental data (for standard deviation see Figure 54) also depends of the local properties of the cage.

Influence of the bead size on the frequency dependent viscoelastic properties. As shown in Figure 22 the tracer particles used here to study thin F-actin layers attached to lipid bilayers have a larger diameter than the thickness of the F-actin layer. As a result the bead stick out of the F-actin layer. It could already be confirmed that the beads are still incorporated in the networks since the F-actin layer organizes around the beads, however, it might be possible that the anisotropy of the bead environment alters the viscoelastic properties. In order to estimate the influence of this effect we increased the bead size 2.5-fold, accordingly artefacts originating from the bead size should increase. In general, the mean squared displacement is proportional to the inverse radius of the tracer particle ($\text{MSD} \propto r^{-1}$). However, in the calculation of the viscoelastic moduli we correct for the $1/r$ dependency from the Stokes-Einstein equation.¹⁰² A resulting spectrum of viscoelastic properties for a sample where the F-actin network was attached to a lipid membrane containing PIP₂ 3 mol%, cross-linked by ezrin, is shown in Figure 55. Some minor differences in the recorded spectra for tracer particle radii of $r = 2.5 \mu\text{m}$ were observed. While the the plateau modulus ($G_0(\text{PIP}_2 \text{ 3 mol\%, } r = 2.5 \mu\text{m}) = 0.092 \text{ Pa}$) lies within the confidence interval ($2\sigma/\sqrt{N} = 0.05 \text{ Pa}$, $N = 6$) compared to samples with tracer particle radii of $r = 1 \mu\text{m}$ ($G_0(\text{PIP}_2 \text{ 3 mol\%, } r = 1 \mu\text{m}) = 0.133 \text{ Pa}$), the deviations in the loss modulus are slightly more pronounced. Notably the unbinding rate constants are shifted towards lower frequencies by a factor of about two: $k_{\text{off}}(\text{entanglement, } r = 2.5 \mu\text{m}) = 0.165 \text{ s}^{-1}$ & $k_{\text{off}}(\text{PIP}_2 \text{ 3 mol\%, } r = 2.5 \mu\text{m}) = 0.027 \text{ s}^{-1}$. Deviations in the high frequency scaling of the storage modulus might be due to increased inertia (see Figure 51). These observations suggest that, although slightly altered, the frequency spectrum contains the same information even though the bead diameter is substantially larger than the F-actin network layer thickness. As illustrated in Figure 22 the bead surface chemistry interacts nonspecifically yet provides a stable interaction with the polymer network resulting in a complete embedding of the tracer particle.¹⁰⁰ Hence, the larger bead size has supposedly a minor influence on the viscoelastic properties of the F-actin membrane composite. Smaller beads with a diameter of 300 nm were also used in experiments. However, these smaller beads were only found in close proximity to the membrane and did not show noticeable motion. This finding supports that the mesh sizes of the F-actin network attached to a lipid membrane are larger than 300 nm in average (compare to 5.1.1.1).

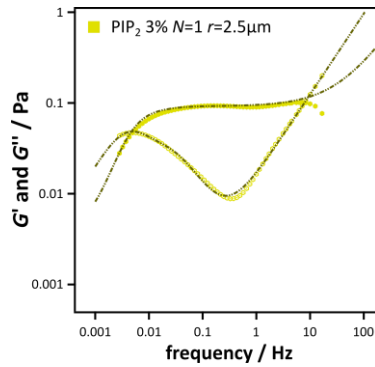


Figure 55: Influence of the bead size on the frequency dependent viscoelastic properties of minimal actin cortex models. Shown are the storage modulus G' (filled symbols), the loss modulus G'' (open symbols) and a respective fit according to equation (69)+(70) (dashed line, for full set of parameters see Appendix 1 IV).³⁴ Actin attached to a lipid membrane containing 3 mol% PIP₂ mediated by ezrin measured with a tracer particle of a 2.5-fold larger radius ($r = 2.5 \mu\text{m}$), $N=1$, compared to the particle radius used in Figure 45.

Limitations of video particle tracking as a method to study artificial model cortices. For some samples (biotin 3 mol% see 5.1.2.4 and apical cellular membrane patches see 5.1.3) the movement of the tracer particles is so small that the mean squared displacement at short and medium time lags becomes nearly the same order of magnitude as the noise signal from the system. As a result the mean squared displacement in the regime of short time lags shows a noise signal, which translates into the viscoelastic moduli as a broadened band peak at about 1 Hz. To illustrate this effect we recorded the movement of particles stuck to a surface (see Figure 25 A, grey curve). The system noise depends on many factors and may vary from day to day. As suggested by Massiera *et al.* this artefact can be removed from the signal via the usage of a notch filter for data processing.²⁴³ Figure 56 A2 and B2 show the effect of a notch filter on the mean squared displacement and the resulting moduli. Although this method results in smooth mean squared displacements and reduced artefacts in the moduli at intermediate frequencies, the regime at very low tau values is also affected in magnitude which is probably a fringe effect of the filter. Hence, I chose to show the untreated data and emphasize that the signal to noise ratio in this case is reduced for the high frequency regime since the tracer particle movement is at the limit of what can be measured.

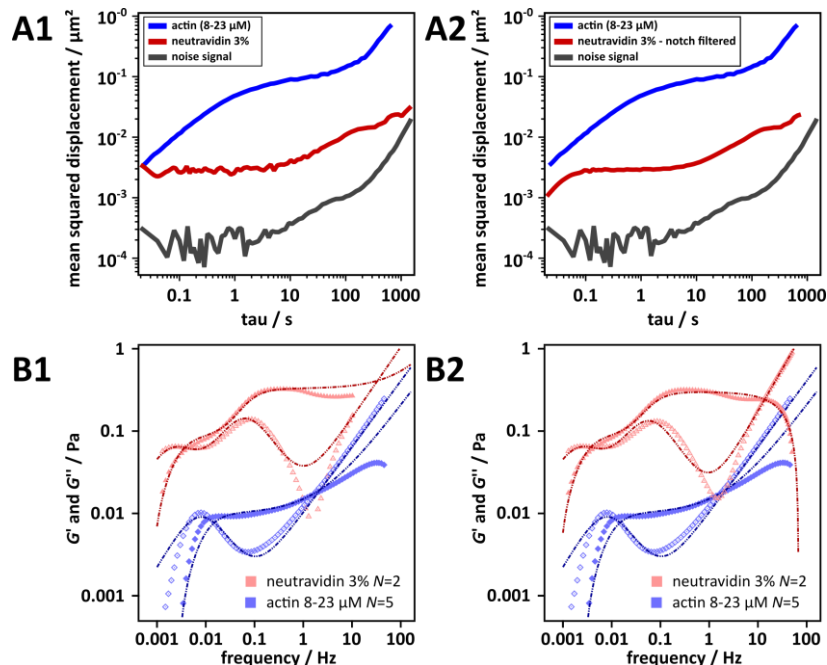


Figure 56: Limitations of video particle tracking as a method to study artificial model cortices. Shown are the mean squared displacements (A1-2) and the respective viscoelastic moduli (B1-2) of a tracer particle embedded in an actin network. A1 and B1 show unfiltered data; A2 and B2 show the same data filtered with a notch filter. **Red:** Actin network attached to a lipid membrane containing 3 mol% biotinylated- DOPE via neutravidin. **Blue:** Entangled actin networks (8-23 μM) are shown for comparison. **Grey:** the mean squared displacement of stuck beads on a surface are shown.

5.1.2.7. Comparison of Different Microrheology Methods

In this chapter results from optical tweezer based microrheology methods and another method to obtain the viscoelastic moduli from mean squared displacements are discussed on a comparative basis with the previously described video particle tracking based microrheology and subsequent calculation of the moduli by fitting the mean squared displacement as described in 2.2.2.1.2.^{103,104}

First, the same data from video particle tracking experiments is evaluated with an additional method to transform the time dependent compliance data into a frequency dependent shear modulus. Figure 57 shows the resulting viscoelastic moduli obtained by this method. The averaged mean squared displacement collected for each model system was either transformed into frequency dependent viscoelastic moduli by a method developed by Mason *et al.* and Dasgupta *et al.*^{103,104} (dashed lines, same as in previous chapters) or by another method developed by Evans *et al.*¹⁰⁷ (storage: closed symbols; loss: open symbols). Both methods have been described in 2.2.2.1.2. While the former uses a weighted fit to the mean squared displacement in order to describe its time dependent behavior by a local power law, the latter transforms the time dependent compliance function directly into the viscoelastic moduli, interpolating the data with a piecewise linear function. Here, the advantage is that additional information about the experimental uncertainty still is contained in the data and not smoothed by a fitting function.

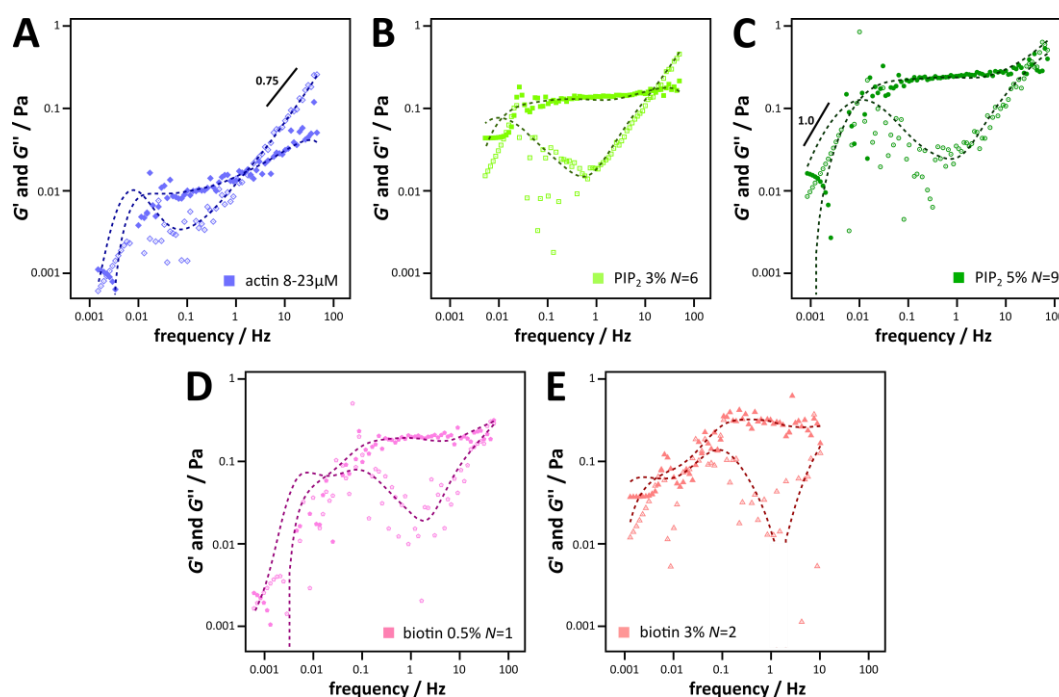


Figure 57: Comparison of two methods to obtain the viscoelastic moduli from mean squared displacements. Mean squared displacements of the previously described model systems measured by video particle tracking were transformed to viscoelastic moduli by a direct conversion method introduced by Evans *et al.* (see chapter 2.2.2.1.2).¹⁰⁷ Storage (closed symbols) and loss modulus (open symbols) obtained by this method are shown. For comparison the moduli calculated after the method introduced by Dasgupta *et al.* (see chapter 2.2.2.1.2)¹⁰³ as shown in the previous chapter are displayed (dashed lines). **A:** Entangled 3D F-actin 8-23 μM ; **B:** PIP₂ 3 mol%; **C:** PIP₂ 5 mol%; **D:** Biotin 0.5 mol%; **E:** Biotin 3 mol%.

In general both methods show similar results in the medium to high frequency regime. In the low frequency regime however, the moduli show substantial variance when not smoothed by a fitting function. Especially in the case of the entangled F-actin network and the biotin 0.5 mol% sample, but also in the other samples, strong deviations between the two methods can be observed for frequencies below the reptation frequency. The low frequency regime in the biotin samples is hard to interpret from the directly converted data. Without the information from the mean squared

displacement, that a small second plateau is observed in this frequency region, the data could not have been interpreted. The method by Evans *et al.* seems, however, to be more robust against the influence from the noise signal contributing to the viscoelastic moduli in the biotin 3 mol% at frequencies above 3 Hz (see Figure 57 E above 1 Hz). In both PIP₂ samples the cross-over in the low frequency regime can still be observed, which is not surprising since an inflexion point can be observed in the mean squared displacement (see chapter 5.1.2.2). Still it is reassuring that the cross-over frequency is not altered as much as in the entangled F-actin sample. Also similar curve progression at frequencies above the cross-over can be observed. The divergence of the results from both methods suggests prudence in the interpretation of the low frequency regime (especially the slope of the curve) below the cross-over at low frequencies and with respect to the biotin samples. The observed differences might be an effect of the weighted fit function. Other than that both methods converge over a broad frequency regime.

Second, microrheological data obtained by active and passive optical tweezer measurements is shown in comparison to the results from the video particle tracking based technique (Figure 58 A-C). Passive optical tweezer measurements (Figure 58 crosses) have been performed as previously described (chapter 4.1.3.2) and were analyzed by the above mentioned method by Evans *et al.*¹⁰⁷ Active optical tweezer based microrheology data is shown in form of large circles in the same figure (storage modulus: closed symbols, loss modulus: open symbols). Data obtained from video particle tracking is displayed for comparison (Figure 58 dashed lines). For better comparison the moduli were scaled in absolute height. Thus, in the following the absolute stiffness is not discussed for the here presented data. For data that has not been altered in absolute stiffness see Figure 60. The data was rescaled so that the loss modulus of each dataset in the high frequency regime fell on the same line. The loss modulus in the high frequency regime has been observed to be a robust part of the spectra values, since almost all data presented in the previous chapters fall on the same line in this regime (see Figure 45 and Figure 53). Active microrheology showed a tendency to slightly elevated values (about a factor of 3-4 for the here presented data). Passive microrheology partially showed strong tendencies to lower values. An additional source of error for optical tweezer measurements are the calibrations of trap stiffness and sensitivity that has been performed on other beads than measured and thus might lead to variance in the actual stiffness and sensitivity. The storage modulus of the active measurements is the modulus that is dependent on the largest number of calibration factors, thus it is the most error prone quantity. Moreover, most of the data was not collected on the same particle and variance to local sample properties also play a role.

A cross-over in the high frequency regime is visible for all samples and applied methods. In some samples this entanglement frequency is slightly shifted depending on the relative magnitude of the storage modulus. The high frequency scaling in entangled F-actin networks showed very similar frequency scaling in the active measurement as obtained from passive video particle tracking microrheology. However, in other measurements on similar samples (not shown) a lower scaling behavior with frequency was found by this method. In the passive measurement obtained from optical tweezer measurements the storage and loss modulus at high frequencies both show a power law scaling with a power law coefficient close to 3/4, similar to what has been predicted and reported by other working groups. The high frequency scaling of the storage modulus in the PIP₂ samples obtained by active and passive methods shows the same decline in magnitude as observed by video particle tracking. This might support the hypothesis that this is an artefact rising from increased inertia effects on the bead.

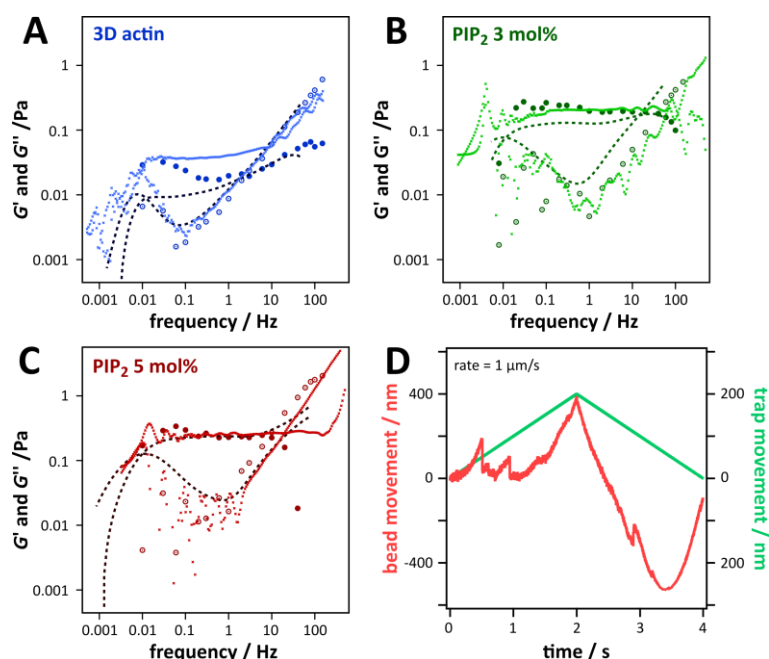


Figure 58: Comparison of three microrheology methods to measure the frequency dependent viscoelastic properties of cortex model systems. Large circles, ●: Active microrheology, optical tweezer. Crosses, x: Passive microrheology, optical tweezer. Dashed lines: Passive, video particle tracking based microrheology. A: Entangled F-actin (VPT: 8-23 μM , PMR OT: 15 μM , AMR OT: 36 μM); B: PIP₂ 3 mol%; C: PIP₂ 5 mol%. For better comparison the moduli were scaled by a factor so that the loss modulus in the high frequency regime agrees approximately throughout the methods. D: Trap (green) and bead movement (red) versus time are shown obtained from a force extension experiment of a bead on a PIP₂ 3 mol% sample. Sudden jumps in the bead movement correspond to a force of about 10 pN.

In the intermediate frequency regime predominantly elastic behavior is observed with all methods for every sample. In the low frequency regime, the cross-over is visible in all samples at similar frequencies compared to those obtained by video particle tracking for both passive microrheology measurements. This observation indicates that it is unlikely that the peak in the loss modulus results from artefacts in the measurement or analysis. Thus, it supports the hypothesis that this local maximum in the loss modulus shows a characteristic time scale of stress relaxation in the network. In active microrheology measurements, this cross-over has not been observed. However, the low frequency regime in the active measurements underlies strong artefacts resulting from the method. Figure 59 shows the same viscoelastic spectrum of water as reported in chapter 5.1.2.1 for a broader frequency range. The standard deviation of the measured loss modulus increases significantly below a frequency of 1 Hz. Additionally, here below 0.3 Hz the loss modulus increases for decreasing frequency, which is not expected for a Newtonian viscosity. These artefacts are most likely a result from a decreased accuracy of the measuring signal (phase separation), since this deviation from the expected behavior increases in magnitude when a smaller amplitude is chosen for the measurement (signal-to-noise ratio is lower). The expected phase separation for commonly applied measuring parameters and studied samples is about 5 ms. One active oscillation at 0.01 Hz takes 100 s. During this time the measuring signal underlies drifts resulting from variations in the LASER output and perturbations by other material pulled into the trap by the trapping force of the optical tweezer leading to jumps in the measuring signal. These perturbations in the measuring signal result in changes in the determined phase separation, the measured variable that determines the loss modulus. These artefacts can be minimized by increasing the signal-to-noise ratio by measuring at lower trap stiffness of the driving trap and applying oscillations with higher amplitudes. Small amplitudes are preferable ($A = 40 \text{ nm}$)²⁰⁵ to ensure that the measured force response is still in the

linear viscoelastic regime. However, I have not observed differences in the plateau modulus up to $A = 200$ nm peak-to-peak. The here presented data is thus measured at $A = 100$ nm peak-to-peak.

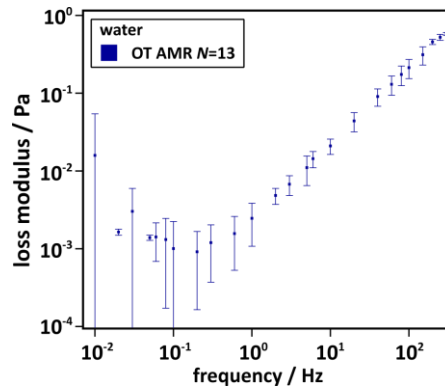


Figure 59: Artefacts in the low frequency regime of the loss modulus in active microrheology measurements. The loss modulus of water obtained by active optical tweezer based microrheology is shown. Error bars are the standard deviation. The spectrum is the same as in chapter 5.1.2.1, a broader frequency regime is shown.

Additionally, force extension experiments of beads embedded in an F-actin network attached to a PIP₂ containing membrane, via the cross-link ezrin, were performed in order to reassure that the beads were embedded in the network. Figure 58 D shows one example of a trap movement (at a rate of $1 \mu\text{m} \cdot \text{s}^{-1}$) and the resulting bead movement versus time. The bead movement shows a characteristic delay and lower amplitude of the bead movement, which is expected for a non-fluid material. Moreover, sudden jumps in the bead movement, corresponding to a force of about 10 pN, suggest the presence and rupturing of a soft material, most likely F-actin.

Third, the influence of altered buffer viscosity on the viscoelastic properties of membrane bound F-actin networks is shown by active microrheology (Figure 60 A). The viscoelastic moduli of an entangled F-actin network, a PIP₂ 2 mol% sample and the same PIP₂ 2 mol% sample with a small percentage of glycerol (below 10 % (v/v)) added to the buffer are shown. Figure 60 B shows the measured loss modulus of water and an aqueous solution of glycerol for comparison. Spectrum interpretation of viscous samples has been discussed in chapter 5.1.2.1. Here, the viscoelastic moduli were not rescaled and mostly measured at the same day and if possible on the same tracer particle to reduce variations in absolute stiffness and calibration errors. The comparison between the entangled F-actin networks and the PIP₂ 2 mol% sample shows an increase in the storage modulus. The absolute values of the loss modulus in the entangled F-actin and the PIP₂ 2 mol% sample are similar in the high frequency regime, which is also observed in video particle tracking results. The measured plateau moduli for the entangled F-actin sample ($G_0(\text{actin } 36 \mu\text{M}, \text{OT AMR}) = 0.077 \text{ Pa}$) and the PIP₂ 2 mol% sample ($G_0(\text{PIP}_2 \text{ 2 mol\%, OT AMR}) = 0.210 \text{ Pa}$) @ 0.1 Hz are comparable to the results from video particle tracking microscopy (see chapter 5.1.2.3 and 5.1.2.4), while the latter is slightly elevated. The low frequency regime shows no cross-over of the moduli for similar reasons as discussed above. Upon addition of glycerol to water the loss modulus of the aqueous solution increases about three-fold (from 0.028 to 0.084 Pa @ 20 Hz), suggesting a three-fold increase in viscosity. Accordingly, adding similar concentrations of glycerol to the buffer in the PIP₂ 2 mol% sample increases the loss modulus (same bead) by a factor of three (from 0.0407 to 0.128 Pa @ 2 Hz), while the storage modulus is only increased by a factor of two (from 0.210 to 0.456 Pa @ 0.1 Hz). These shifts in the moduli lead to a change in the entanglement frequency from about 10 Hz (PIP₂ 2 mol%) to about 6 Hz (PIP₂ 2 mol% + glycerol). A decrease in entanglement upon increase of

solvent viscosity is expected since the entanglement frequency is anti-proportionally connected with the solvent viscosity (see equation (27)). A substantial increase in the storage and loss modulus at high frequencies is also predicted by polymer theory (see equations (31)+(32)). However, the plateau in the real part of the shear modulus should be unaffected by an increase in viscosity (see equation (29)). These experiments show, that the loss modulus can be qualitatively altered by increased viscosity in of the medium as expected from theory, while the storage modulus could be regulated by a change in the stiffness of the model system similar to other measurements. Furthermore, the absolute values of the plateau moduli are similar to those obtained from video particle tracking microscopy based microrheology for the respective model system. Hence, it can be presumed that the measured moduli are determined by the viscoelastic properties of the sample.

In conclusion, preliminary data from other microrheology techniques is reported. It could be shown that almost all important features of the frequency dependent viscoelastic properties could be observed by applying other microrheology methods.

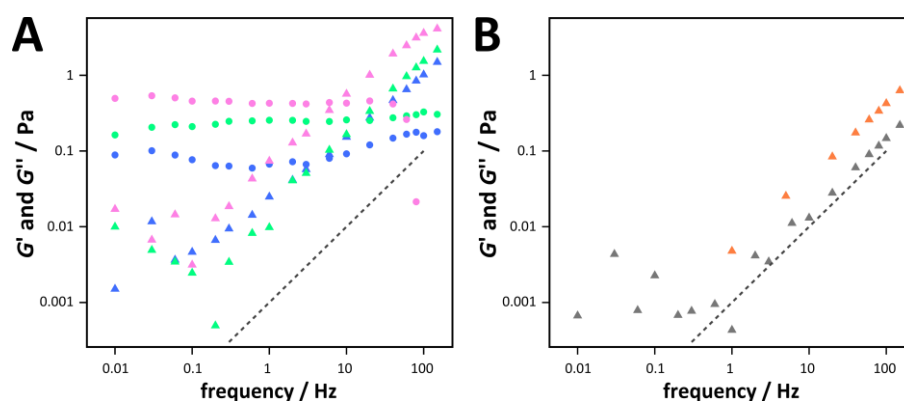


Figure 60: Influence of solvent viscosity on the frequency dependent viscoelastic spectrum of the minimal actin cortex model system measured by active optical tweezer based microrheology. Storage modulus (G' , circles) and loss modulus (G'' , triangles). **A:** Spectrum of entangled F-actin ($36 \mu\text{M}$, blue), PIP₂ 2 mol% under normal buffer condition (green) and PIP₂ 2 mol% in aqueous solution of glycerol (same bead, pink). **B:** Spectrum of water (grey) and an aqueous solution of glycerol (red) are shown for comparison. **Dashed line:** Theoretical loss modulus of water. All data measured on the same day (despite the entangled F-actin sample) to minimize the error due to variation in trap calibration. All data measured with trap stiffness of $k_1 = 0.007 \mu\text{N} \cdot \text{m}^{-1}$ and $k_2 = 0.001 \mu\text{N} \cdot \text{m}^{-1}$, peak-to-peak amplitude was $A = 100 \text{ nm}$.

5.1.3. Frequency Dependent Viscoelastic Properties of Apical Cellular Membrane Patches

In this chapter, the frequency dependent viscoelastic properties of apical cellular membrane patches (ACMP) will be discussed. Apical cellular membrane patches were prepared as described in 4.2.4 and tracer particles for video particle tracking based microrheological measurements were incubated on the ready-made samples for at least 3 h. Video particle tracking microrheological measurements were carried out as described above. Preparation of apical cellular membrane patches was performed by Stefan Nehls (Institute of Physical Chemistry, Georg-August-Universität, Göttingen, Germany).

Figure 61 A shows an F-actin network of an apical cell cortex (MDCKII), which was transferred to a glass substrate by the sandwich-cleavage method (4.2.4), and fluorescent particles, which were used as tracer particles for video particle tracking, attached to this functional network. In Figure 61 B & C the mean squared displacement and the frequency depending viscoelastic properties of these apical cellular membrane patches are shown. A plateau modulus of $G_0(\text{ACMP}) = 0.662 \text{ Pa}$ ($N=2$) was found, which is two to six times higher in value than the plateau modulus found for minimal actin cortices (see chapter 5.1.2.4). Compared to living cells (see chapter 5.2.1) however, this value is still about 300 times softer ($G_0(\text{cell}) \approx 200 \text{ Pa}$). The difference in the absolute stiffness of the system compared to living cells is manifold. First, tension generated by actomyosin contraction is absent in apical cellular membrane patches. Second, in AFM indentation experiments the axis of strain is perpendicular to the membrane, hence counteracting forces originating in the incompressibility of the lipid bilayer and the water filled cell body equally act as restoring forces on the cantilever.

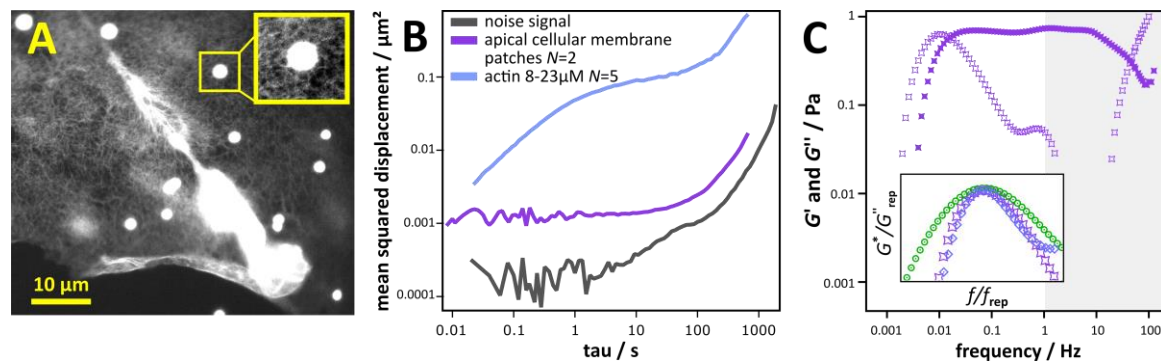


Figure 61: Frequency dependent viscoelastic properties of apical cellular membrane patches. **A:** Fluorescence image of an F-actin cortex attached to glass prepared by the sandwich-cleavage method (see chapter 4.2.4) and fluorescent beads (bright spherical spots, diameter $2 \mu\text{m}$) used for video particle tracking based microrheology measurements. Inset: local actin cortex organization around a bead. **B:** Mean squared displacement of beads attached to apical cellular membrane patches (violet) is shown in comparison to the MSD that corresponds to setup noise (grey) and entangled F-actin networks (blue). **C:** Storage modulus G' (filled symbols) and loss modulus G'' (open symbols) of apical cellular membrane patches. Grey area marks the frequency regime that is disturbed by an artefact caused by a noise signal in samples, where the signal-to-noise ratio (the mean squared displacement) is not high enough. Inset: normalized peaks in the low frequency regime of apical cellular membrane patches (violet) and entangled F-actin networks (blue). Additionally a low frequency maximum of a sample with different band width is shown (green: PIP₂ 5 mol%). (Data has been collected in collaboration with Stefan Nehls)

In the medium to high frequency of the shear modulus (Figure 61 C greyed area) pronounced artefacts are observed. As already discussed for video particle tracking based microrheology measurements on minimal actin cortices with neutravidin as a cross-linker, the mean squared displacement and hence the viscoelastic properties of these samples show substantial artefacts due to a poor signal-to-noise ratio of observed motion to setup noise. Here, we observe the same kind of artefact. In both samples the stiffness of the sample is high and the thermal energy is not sufficient

to induce bead movements that can be easily recorded. Hence, the signal (Figure 61 B violet line) is approximately on the same order of magnitude as the noise signal (Figure 61 B grey line). This causes pronounced artefacts in the medium to low frequency regime of the shear modulus (Figure 61 C greyed area). As described above, this artefact could be removed by a notch filter, which in turn could introduce other artefacts. For higher regimes of stiffness, measurements with active microrheology methods would be preferable (see Table 1).

From the local maximum in the loss modulus at low frequencies (Figure 61 C) an apparent unbinding rate constant of $k_{\text{off}} = 0.066 \text{ s}^{-1}$ can be determined, which is very similar to that obtained in networks of entangled F-actin networks. However, it is highly unlikely that dynamic processes such as cross-link unbinding or long-time filament reptation take place in such highly cross-linked and biochemically inactive systems. Interestingly, the low frequency peak in the loss modulus also exhibits a peak width, which is very similar to that observed in F-actin networks, while cross-link containing samples exhibit much broader peaks in this frequency range³⁶ (see Figure 61 C inset). This observation can also be explained in comparison of the mean squared displacement. While the signal of stuck beads to a surface and mean squared displacements affected by this artefact show an apparent super-diffusion for long time lags (see 5.1.2.2), apparent normal diffusion is found here for the apical cellular membrane patches and entangled F-actin networks in the same frequency regime. However, no striking similarities can be found in these samples that could cause this effect. In the apical cellular membrane patches it is likely that rocking of the beads influences the shear modulus at low frequencies, since the particles were only condensed on top of the functional networks. In 3D F-actin networks however it is unlikely that a bead performs this kind of motion.

Bead attachment, as mentioned above, is a sensible parameter for experiments on this kind of sample, where the tracer particles are not incorporated in the network but are rather condensed on top of the sample. Basically all frequency regimes of the measured shear modulus are affected by a poor incorporation of the tracer particle into the network. Moreover, poor bead incorporation into the network would affect the possible alternative microrheology measurements as well, such as active microrheology measurements carried out on an optical tweezer. Bead incorporation into a functional network after the cleavage of the cell layer is not possible. However, it might be possible to force the uptake of beads in living cells before cleavage of the cell layer. In order to control the bead position in the cell the beads would need to be functionalized with an F-actin affine coating.

In total little can be learned about the frequency scaling especially in the high and low frequency regime from video particle tracking experiments on apical cellular membrane patches. However, the plateau modulus provides an estimate about the absolute stiffness of this system even though this value should be cross-checked by an active microrheology method.

5.1.4. Conclusion

In conclusion, frequency dependent linear viscoelastic properties of a minimal actin cortex model system containing ezrin as a physiological cross-link between an F-actin network and a lipid bilayer, were measured for the first time. Frequency spectra over a wide frequency range (10^{-3} - 10^2 Hz) are reported to provide a more complete picture of the alterations of the viscoelastic properties of F-actin networks upon attachment to a lipid membrane, instead of a reduction of the mechanical properties to the more easily accessible plateau modulus. The composition of the minimal cortex model is based on its physiological counterpart in living eukaryotic cells and reduced in complexity to study the isolated effect of the native membrane cross-link. It was shown that the components of the model system self-organize into a thin F-actin membrane composite layer, with a similar thickness as found for F-actin cortices in a living cell and, thus, mimic the structural characteristics of the cellular cortex well. Important parameters of the biopolymer network bound to the lipid membrane were analyzed, such as the mesh size ($\xi(\text{PIP}_2 \text{ 3 mol\%}) = 1024 \text{ nm}$ and $\xi(\text{PIP}_2 \text{ 5 mol\%}) = 641 \text{ nm}$) and the filament diameter (8 nm: 64 %; 16 nm: 27 %). These results were viewed in conjunction with the resulting linear viscoelastic response of the system. Frequency dependent viscoelastic properties and scaling behaviors similar to those reported in the literature were found for entangled F-actin networks. It could also be shown that attachment of these networks to a lipid membrane introduces alterations throughout a broad regime of frequencies of the viscoelastic moduli. Similar to what has been reported by others^{64,308} a scaling of the plateau modulus with the pinning-point concentration of $G_0(\text{PIP}_2) \propto P^{1.4}$ was found for the membrane associated network. This finding implicates an affine behavior of the membrane-network composite. An approximately anti-proportional dependency of the mesh size on the pinning-point concentration was found, leading to a scaling of the plateau modulus with the mesh size of $G_0 \propto \xi^{-1.5}$, which is about two times lower than expected for entangled 3D F-actin networks in accordance with expectations for 2D systems. While the mesh size and the plateau modulus are largely determined by the number of pinning-points in the membrane, the low frequency regime is controlled by the dynamics of the cross-link. Here, the transient nature of the physiological cross-link ezrin leads to a stress relaxation behavior of the network and the unbinding kinetic of the binding complex between actin filament, cross-link and membrane determines the time scale this process. The obtained unbinding rate constant for this complex was found to be $k_{\text{off}}^{\text{app}}(\text{PIP}_2 - \text{ezrin} - \text{actin}) = 0.054 \text{ s}^{-1}$, which is similar to unbinding rate constants found for other transient cross-linking proteins (see Table 3) and slightly lower than unbinding rate constants obtained for the PIP_2 -ezrin-actin complex by AFM based single molecule force spectroscopy measurements²³. The activation energy of the unbinding process ($E_a \approx 13 k_B T$), which was determined from temperature dependent measurements, conforms well with the assumption that ezrin is a transient cross-link. Additional evidence for rather high rates of unbinding was obtained from time lapsed images of the filaments. Similar time scales have been reported in literature for the ezrin dynamic in living cells.³³ In the high frequency regime a power law scaling of $3/4$ could be found for the shear modulus of entangled F-actin networks. For F-actin membrane composites deviation from this scaling was observed. A description for the influence of the surface proximity and the supposedly altered inertia on the tracer particle was provided to argue that this deviation from the expected scaling behavior is a result of the membrane attachment. The use of other microrheology methods confirmed the findings from video particle tracking microrheology. An artificial cross-link, which was studied in comparison with the physiological ezrin, did show a similar effect on the absolute stiffness, while the low frequency relaxation was altered, but not quite as expected. Additional independent measurements of the unbinding rate constants would be beneficial and could be

accomplished in the future by fluorescence recovery after photo bleaching experiments on the composite material³³ or by tracking the motion of single filaments in the actin layer attached to the lipid bilayer.⁹⁹ Additionally, the viscoelasticity of apical cellular membrane patches were probed. About 4 times higher plateau moduli were found. Whereas the absolute stiffness of living cells is usually found to be about 300 times larger.

Quantitative microrheological measurements could be established on thin composite layers consisting of F-actin network and a lipid membrane. The main interest of this study was to characterize the alterations due to the interconnection of the F-actin network to a lipid membrane. These results are an important basis for further studies with additional actin binding proteins added to the system such as an active motor protein like myosin II, which would be a reasonable next step. In this context active and passive methods have been introduced and established here for future experiments.

Compared to other available minimal cortex model systems reported in literature, the use of the natural and transient cross-linking protein ezrin as interconnection to the membrane might be important for the development of model systems to study mechano-signaling processes, since mechano-signaling and time scales are tightly intertwined. The importance of the ERM proteins in cortical signaling processes has already been described.^{19,173}

5.2. Cell Mechanics of Epithelial Cells in Response to Substrate Stiffness

“[...] the cell is not just an inert playground for a few almighty masterminding molecules, but [...] a hierarchically ordered system, of mutually interdependent species of molecules, molecular groupings, and supramolecular entities; and [...] life [...] depends on the order of their interactions”
- PAUL A. WEISS (1961)³²⁶

Alongside with providing stability and structuring the F-actin cytoskeleton many actin binding proteins are said to contribute to intracellular signaling processes like mechanotransduction. Mechanotransduction describes a universal process in cells in which mechanosensitive proteins respond to mechanical cues and integrate a mechanical signal into the cell eventually translating it into a biological signal or stimulus in order to adapt to mechanical stimuli. Mechanotransduction is important in many cellular processes such as migration, development and cell differentiation.^{52,327} Many different mechanosensitive processes are known today.^{328,62} They reach from stretch activated ion channels, e.g. calcium channels, over the shear flow sensitive glycocalyx in endothelial cells to changes in chromatin conformation in the nucleus upon deformations.^{62,329} As demonstrated before the actin cytoskeleton is a major contributor to the mechanics of a cell. Additionally, it plays an important role in cellular mechanotransduction. Cell-substrate interactions serve as integrator of environmental cues, whereas cell-cell interactions transmit mechanical signals from neighboring cells. Especially proteins at the cadherin and the integrin interface are studied in the context of mechanosensitivity.^{45,46,330} In general, these mechanosensitive transmembrane protein complexes are believed to transmit mechanical stresses into the cell, where conformational changes in mechanosensitive cross-linking proteins can lead to altered binding affinities of signaling proteins. The influence of chemical and physical substrate surface properties^{48,56,280,331–337} and especially the elasticity of surfaces^{44,50–52,55,338} have been attributed a substantial role in the development of cells. Additionally, the malignant transformation of cancer cells as a result of changes in the tissue microenvironment and especially the extracellular matrix (ECM) has been subject of research in the last decade^{60,61,339,340}. In this context integrin mediated mechano-sensing has been studied extensively. In the normal integrin signaling pathway (see Figure 62 A) the heterodimer integrin binds to RGD sequences presented in scleroproteins in the ECM (e.g. collagen, fibronectin or laminin).^{46,341,342} Stretch activated integrin binding proteins like talin³⁴³ and paxilin recruit vinculin and the focal adhesion kinase (FAK) to form adhesion complexes. Vinculin enables linkage to the F-actin cytoskeleton whereas FAK has a major role in orchestrating the organization of the F-actin cytoskeleton either by destabilizing actin stress-fibers by α -actinin phosphorylation and downregulation of Rho signaling proteins or conversely also by activating the Rho signaling pathway.^{47,59} This Rho activation is achieved by phosphorylation of Rho guanine nucleotide-exchange factor p190 RhoGEF. Activation of Rho indirectly leads to increased myosin light chain kinase (MLCK) activity, thus the phosphorylation of the regulatory light chains of myosin II, hence to increased tension in the actin cytoskeleton.¹⁷ There are findings that more rigid matrices as found in tumor tissue and tumor environments activate the Rho/ROCK (Rho-associated kinase) pathway by signaling via integrins, leading to increased myosin activity and hence higher cell contractility and by a positive feedback loop even to higher ECM stiffness (see Figure 62 B).^{59,60,344} In an exemplary study Paszek *et al.*⁵⁹ did not only underline the importance of matrix stiffness for the malignant phenotype in mammary gland cells, they also correlated this to enhanced Rho activated tension generation and an increase in extracellular signal-regulated kinases (ERK) activation, which drives cell proliferation. However, the established hypothesis that increased matrix rigidity leads to the progression and growth of stiff tumor tissue stands in contrast to the need of flexibility of

metastasizing cancer cells.^{345,346} During the process of intravasation and extravasation to and from blood and lymphatic vessels (see Figure 62 C) the cellular cytoskeleton needs to be demounted and reorganized in order to enable enough flexibility to squeeze through tight cell layers surrounding the vessel. Experiments in microfluidic assays support this reasoning^{347,348} and many mechanical measurements on immortalized cell lines lead to the conclusion that cells with a higher metastatic potential are indeed softer than comparable cells of lower metastatic potential^{2,11,244,349,350}. Importantly, metastatic cancer cells additionally lose their ability to sense and to respond to the extracellular matrix stiffness.⁴ Agus *et al.*³⁵⁰ showed that cell proliferation is a function of substrate stiffness in non-tumorigenic MCF-10A cells, whereas proliferation in metastatic MDA-MB-231 remained nearly unaltered.

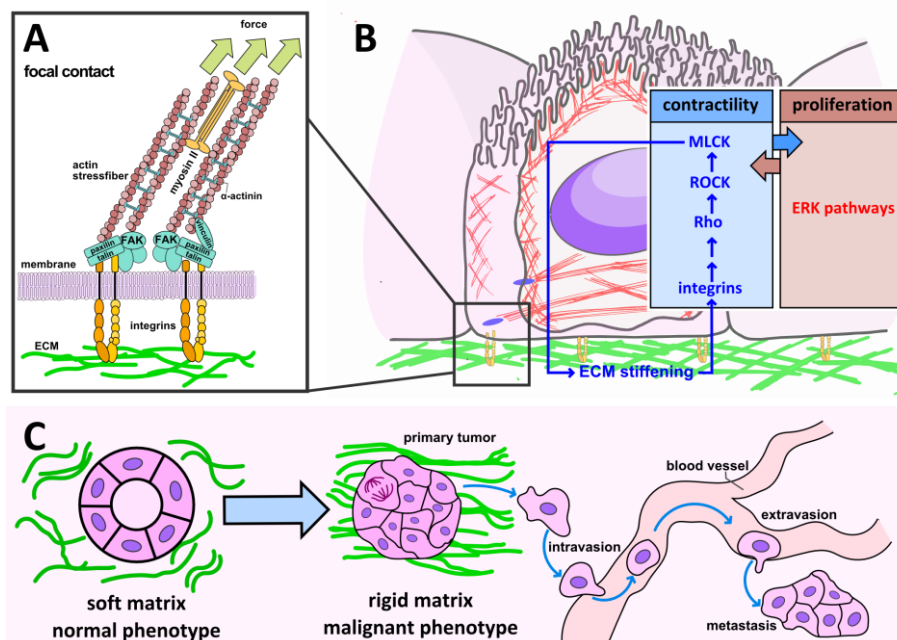


Figure 62: Scheme of the integrin mediated mechanotransduction and its role in cancer. **A:** Structure and important proteins in focal contacts. **B:** Integrin signaling. Especially the Rho mediated tension generation in the actin cytoskeleton and its feedback loop on the stiffness of the extracellular matrix (ECM) leading to a positive feedback in cancer progression. **C:** Malignant transformation as a result of the tissue environment and the metastatic process. Cellular dislocation occurs via transportation in the blood vessels. Cellular flexibility is crucial for intravasation and extravasation. Modified from Mitra *et al.*⁴⁷, Paszek *et al.*⁵⁹ and Huang *et al.*³⁴⁴.

To test if cancer cells still reorganize their actin cytoskeleton in accordance with extracellular matrix stiffness and if there is a dependency on the metastatic potential I want to use a well-established *in vitro* model system of three comparable immortalized cell lines (MCF-10A, MCF-7 and MDA-MB-231) from the mammary gland^{350–353} in conjunction with collagen coated polyacrylamide gels of varying stiffness as substrates. In order to analyze, whether the cell size influences the viscoelasticity of cell monolayers or if the changes in the viscoelastic properties originate solely in the mechanical signaling based on the properties of the substrate, the MDCKII cell line was used.^{280,354,355} The benefit of this cell line is that almost exclusively monolayers are formed and that cells usually grow in brick like patterns reducing the variations from inhomogeneous size distributions. Atomic force microscopy based force spectroscopy methods were used to determine the mechanics of the cells (see chapter 4.2.7).

5.2.1. Influence of the F-Actin Cytoskeleton on the Viscoelastic Properties of Epithelial Cells

In order to provide a linkage between the viscoelastic properties of living cells measured in active microrheology measurements and the F-actin cytoskeleton two well-known F-actin cytoskeleton manipulating drugs, were used to either destabilize or reinforce the F-actin cytoskeleton. The effect of the F-actin cytoskeleton organization on the viscoelastic parameters obtained by the power law structural damping model (PLSDM, see chapter 3.3.2) will be assessed.

Cytoskeletal drugs are frequently used to study the influence of the cytoskeleton on mechanical properties of living cells.^{68,69,356,357} Prominent candidates are the cytochalasins, phalloidin, blebbistatin, latrunculin and jasplakinolide. Latrunculin A and jasplakinolide are used here to assess the impact of F-actin degradation and reinforcement on the frequency dependent viscoelastic properties of living MDCKII cells recorded by atomic force spectroscopy based active microrheology measurements. Latrunculin A destabilized F-actin via interaction with G-actin and thereby preventing polymerization to F-actin. This leads to a shift in the dynamic equilibrium towards depolymerized actin.³⁵⁸ In contrast jasplakinolide is said to catalyze the rate determining nucleation step of the polymerization of F-actin.³⁵⁹ The role of these drugs on the F-actin cytoskeleton and their mechanism of action have been described by many research groups^{358–366} as well as their impact on the mechanical properties of living cells^{69,356,357,367}. Here, I investigate the frequency dependent viscoelastic properties of MDCKII cells exposed to these drugs. The general alterations in the frequency-dependent viscoelastic moduli are depicted in Figure 63.

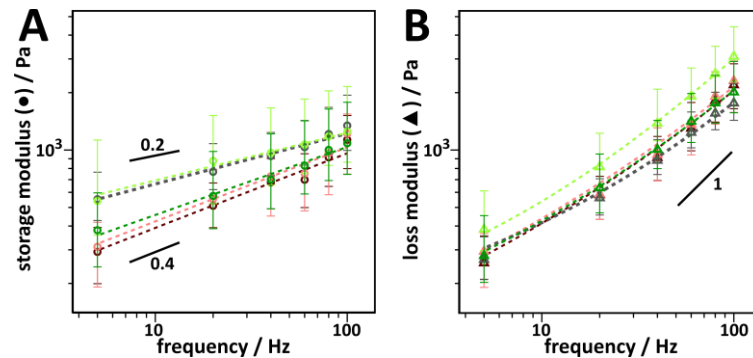


Figure 63: The effect of F-actin cytoskeleton manipulating drugs on the viscoelastic moduli. Confluent layers of MDCKII cells were subjected to latrunculin A (LatA) or jasplakinolide (Jas) ($1\mu\text{M}$) for 30 min (**LatA** & **Jas**) and 60 min (**LatA** & **Jas**) respectively. Data obtained from active atomic force microscopy based microrheology measurements (see 4.2.7.1) (data points: median value; error bars: 25th and 75th percentile) were fitted by the power law structural damping model (equation (41), dashed lines). **A:** Storage modulus (\bullet); **B:** Loss modulus (\blacktriangle). Important power law scaling are indicated in the figures (solid lines).

For the unmodified MDCKII cells similar viscoelastic properties were found as reported before^{168,244,280,355}: a stiffness offset of the viscoelastic moduli $G_0 = (189 \pm 16)$ Pa (median \pm sem), a power law coefficient $\alpha = 0.27 \pm 0.003$ and a viscosity of $\eta = (1.97 \pm 0.25)$ Pa \cdot s ($N = 408$). For cells with an impaired cytoskeleton, provoked by latrunculin A, the storage modulus $G'(\omega)$ drops to lower absolute values, suggesting that the cells loose stiffness, whereas the loss modulus $G''(\omega)$ remains nearly unchanged. Already at very low frequencies (about 8 Hz) the viscous properties prevail over the elastic properties. This softening of the cells is also mirrored in the overall stiffness G_0 (Figure 64 A), where values of $G_0 = (76 \pm 7)$ Pa ($N = 49$) were found after 30 min of latrunculin A treatment compared to $G_0 = (189 \pm 16)$ Pa for the control cells. Additionally, the power-law coefficient α increases substantially from $\alpha = 0.27 \pm 0.003$ for control cells to $\alpha = 0.36 \pm 0.01$, demonstrating a more

liquid-like behaviour (Figure 64 B). The Newtonian viscosity η remains nearly unchanged during the drug treatment ($\approx 2 \text{ Pa} \cdot \text{s}$) (Figure 64 C). For a longer incubation time with the cytoskeletal drug only a slight reduction in the overall stiffness ($G_0 = (78 \pm 5) \text{ Pa}$ ($N = 65$)) could be observed and practically no change in the power law coefficient or the viscosity was observed (all data can be found in Table 18).

For epithelial cells with a reinforced cytoskeleton the storage modulus was slightly elevated compared to control cells. The loss modulus was considerably increased after 30 min of drug treatment. This leads to a strong frequency dependency of the loss tangent and a crossover of the storage and loss modulus at about 20 Hz. The overall stiffness after jasplakinolide treatment for 30 min was significantly increased ($G_0 = (234 \pm 58) \text{ Pa}$, control: $G_0 = (189 \pm 16) \text{ Pa}$) (Figure 64 A), whereas the power law coefficient was only slightly reduced ($\alpha = 0.25 \pm 0.01$, control: $\alpha = 0.27 \pm 0.003$; Figure 64 B). The Newtonian viscosity was notably increased to $\eta = (4.11 \pm 0.34) \text{ Pa} \cdot \text{s}$ (Figure 64 C). Additionally, the indentation depth was diminished by 400 nm to keep the set point of 500 pN, an indicative for stiffening of the probed material (data not shown). These findings suggest that epithelial cells after 30 min of jasplakinolide treatment stiffen their apical cortex by reinforcing the F-actin cytoskeleton. Interestingly, the effects on the frequency-dependent viscoelastic properties are practically restored to the initial values after drug incubation for 60 min. The overall stiffness dropped back to $G_0 = (82 \pm 26) \text{ Pa}$ ($N = 92$) and the viscosity was reduced again to $\eta = (1.65 \pm 0.15) \text{ Pa} \cdot \text{s}$ (Figure 64 A, C). The indentation depth of the cantilever at the same force was again approximately $1 \mu\text{m}$ (similar to control cells). Solely the power-law coefficient increased notably ($\alpha = 0.35 \pm 0.11$, Figure 64 B). In total a decrease of the zero frequency shear modulus upon disruption of the F-actin cytoskeleton and an increase upon reinforcement could be observed. The power law coefficient decreased for a reinforced F-actin cytoskeleton and increased upon dissolving the F-actin cytoskeleton. The Newtonian viscosity has mostly been unaltered with the exception of the jasplakinolide treatment after 30 min.

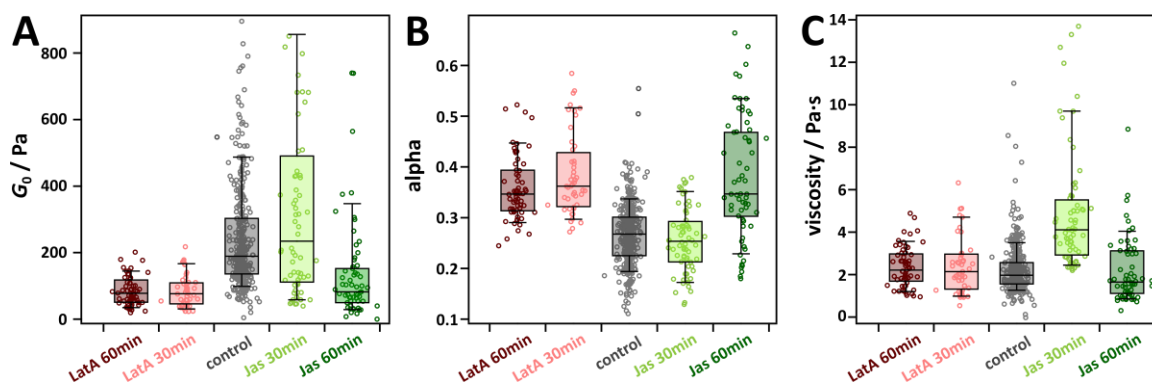


Figure 64: The effect of F-actin cytoskeleton manipulating drugs on viscoelastic parameters. Confluent layers of MDCKII cells were subjected to **latrunculin A** or **jasplakinolide** ($1 \mu\text{M}$) for 30 and 60 min, respectively. Data obtained from active atomic force microscopy based microrheology measurements (see 4.2.7.1) were fitted by the power law structural damping model (equation (41)). Resulting viscoelastic parameters are shown. **A:** Stiffness offset of the viscoelastic moduli G_0 ; **B:** Power law coefficient α ; **C:** Newtonian viscosity η . Box plots extend from the 25th to the 75th percentile, whiskers from the 10th to the 90th. Individual data points are plotted as circles, some outliers are not shown.

The viscoelastic properties of MDCK II cells measured in this context are in good agreement with previous measurements using the same cell line²⁸⁰. Furthermore, similar dependencies of the elastic modulus upon application of the two drugs were observed by Rotsch and Radmacher.³⁵⁶ They found a decreasing Young's modulus ($E_0 = 3 \cdot G_0$ for incompressible materials) for fibroblast cells treated with latrunculin A. However, they observed no clear reinforcement upon treatment with

jasplakinolide. Wakatsuki *et al.*³⁶⁷ found a general softening of cells exposed to latrunculin B by uniaxial stress-strain testing. In a comprehensive study comprising frequency viscoelastic measurements of various different cytoskeletal drugs, Laudadio *et al.* observed an even more pronounced decrease in the overall stiffness (G_0) upon latrunculin A administration (same concentration) than found by us⁶⁹. The reported change in the power law scaling of the shear modulus and the unchanged Newtonian viscosity upon latrunculin A treatment is in good accordance with our measurements. In general, an increased power law scaling of the shear modulus with frequency is associated with a less elastic behavior. In terms of active soft glassy rheology this can be interpreted as an increase in structural rearrangement²⁴⁶. However, in a quite recent study nearly no changes in the power law scaling and a rather low decrease in the overall stiffness upon latrunculin A treatment with about half of the concentration used here was found⁶⁸. When Fabry *et al.* induced a net depolymerisation of the F-actin cytoskeleton by the use of cytochalasin D they found a decrease in the overall stiffness and a rise in the power law scaling³⁸. Similar changes upon cytochalasin D treatment has also been observed by Pietuch *et al.*²⁴⁵. Rother (2014)³⁶⁸ found an increase in the power law coefficient of MDCKII cells upon treatment with cytochalasin D, which also has a depolymerizing effect on F-actin, accompanied by a decrease in the shear modulus at zero frequency. For jasplakinolide contradicting statements have been made with respect to its effect on the cytoskeleton ranging from reinforcement of the cytoskeleton, over no clear changes up to a decrease in absolute stiffness.^{356,357,360} We find a time dependent effect of jasplakinolide on the mechanical properties of MDCKII cells. The data presented here hint that the reinforcing effect of jasplakinolide might only occur in a short window of time. Afterwards, the cells possibly start to adjust and to regulate the changes in the cytoskeleton. These reported changes in the viscoelastic parameters upon cytoskeletal changes will be used for comparison in the next chapters.

Table 18: Viscoelastic parameters of MDCKII cells influenced by cytoskeletal drugs obtained by the PLSDM. Confluent layers of MDCKII cells were subjected to latrunculin A or jasplakinolide ($1\mu\text{M}$) for 30 and 60 min respectively. Fit parameters of the power law structural damping model (equation (41)) are reported: Shear modulus at zero frequency G_0 , power law coefficient α and Newtonian viscosity η (median \pm sem). *Data has been reported in the dissertation of Jan Rother (2014)³⁶⁸.

sample	G_0 / Pa	α	$\eta / \text{Pa} \cdot \text{s}$	N
control	189 ± 16	0.27 ± 0.003	1.97 ± 0.25	408
latrunculin A 30min	76 ± 7	0.36 ± 0.01	2.14 ± 0.19	49
latrunculin A 60min	78 ± 5	0.35 ± 0.01	2.21 ± 0.12	65
jasplakinolide 30min	234 ± 58	0.25 ± 0.01	4.11 ± 0.34	68
jasplakinolide 60min	82 ± 26	0.35 ± 0.01	1.65 ± 0.15	92
cytochalasin D	57 ± 14	0.32 ± 0.04	1.15 ± 0.11	*

5.2.2. Viscoelasticity of Kidney Epithelial Cells in Response to Matrix Elasticity

In this chapter the alterations in the viscoelastic properties measured on cells grown on substrates of elasticities ranging from 1 to 100 kPa will be investigated. Additionally, these results will be discussed in the context of cytoskeletal remodeling. The relation between substrate stiffness and mechanical properties of cells has often been reported.^{51,55,57} Here, the focus will be set to the frequency dependent viscoelastic properties, the apparent area compressibility and the cortical tension in order to provide a more complete picture.

Two exemplary frequency spectra of the viscoelastic moduli measured on cells grown on substrates with a Young's modulus of approximately 1 kPa and 30 kPa, respectively, are shown in Figure 65 A (for measured Young's moduli of the gels see chapter 4.2.1.2). Both, the storage and the loss modulus, are shifted towards higher values for cells grown on stiffer substrates. Fitting the shear modulus with the power law structural damping model gives access to the overall stiffness, the power law coefficient and the Newtonian viscosity, shown as box plots in Figure 65 B-D for four different substrate stiffnesses. Median values with standard error of mean are shown in Table 19. The overall stiffness and viscosity are markedly altered, while the alterations in the power law coefficient are moderate. The frequency at which the cells start to show predominantly viscous behavior (loss tangent $\delta > 1$) is not affected.

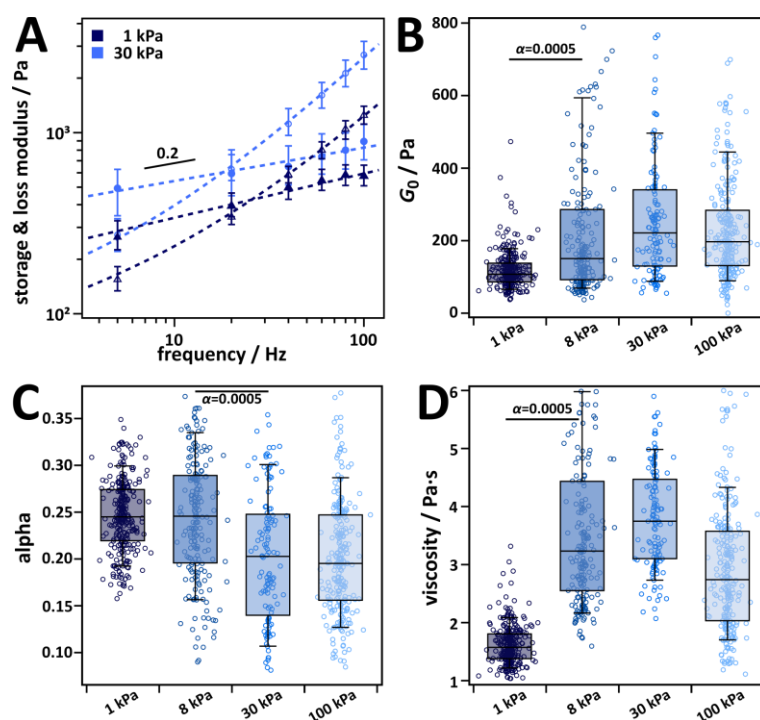


Figure 65: Viscoelastic properties of living MDCKII cells in dependency of substrate stiffness. MDCKII cells were cultured on substrates of different E-moduli: **1 kPa**, **8 kPa**, **30 kPa** and **100 kPa**. Data obtained from active atomic force microscopy based microrheology (see 4.2.7.1) were fitted by the power law structural damping model (equation (41)). **A:** Storage (closed symbols) and loss modulus (open symbols) of MDCKII cells cultured on on substrates of different elasticity: 1 kPa (●) and 30 kPa (▲) are shown. Data points: median value; Error bars: 25th and 75th percentile; Dashed lines: fit by the power law structural damping model. Solid line: power law scaling of 0.2. Resulting viscoelastic parameters from the PLSDM are shown in **B:** Stiffness offset of the viscoelastic moduli G_0 ; **C:** Power law coefficient α ; **D:** Newtonian viscosity η . Box plots extend from the 25th to the 75th percentile, whiskers from the 10th to the 90th. α indicates the confidence level of a Wilcoxon rank test. Individual data points are plotted as circles, some outliers are not shown. (Some of the data has been collected by Nico Gottschling during his internship (2014))

For cells grown on 100 kPa stiff polyacrylamide gels, similar viscoelastic properties were observed as found for cells grown on glass surfaces (see Table 19). Solely the power law coefficient is lower

than in previous measurements on glass. For softer substrates a clear dependency on the substrate elasticity can be observed in all three parameters. The shear modulus at zero frequency G_0 decreases for decreasing surface elasticity. Similarly, the power law coefficient α mirrors softer behavior of the cells than measured on substrates of higher elastic modulus. The Newtonian viscosity η is strongly altered which has been observed before for cytochalasin D treatment but not as pronounced for latrunculin A treatment.

Table 19: Viscoelastic parameters obtained by the PLSDM of MDCKII in dependency of substrate stiffness. MDCKII cells were cultured on substrates of different E -moduli: **1 kPa**, **8 kPa**, **30 kPa** and **100 kPa**. Fit parameters of the power law structural damping model (equation (41)) are reported: shear modulus at zero frequency G_0 , power law coefficient α and Newtonian viscosity η (median \pm sem). *Data reported by Rother *et al.*²⁸⁰. **Data reported by Rother (2014)³⁶⁸.

sample	G_0 / Pa	α	$\eta / \text{Pa} \cdot \text{s}$	N
1 kPa	107 \pm 3	0.25 \pm 0.002	1.57 \pm 0.02	277
8 kPa	150 \pm 18	0.25 \pm 0.005	3.23 \pm 0.12	198
30 kPa	221 \pm 16	0.20 \pm 0.007	3.75 \pm 0.08	129
100 kPa	197 \pm 11	0.20 \pm 0.004	2.74 \pm 0.09	251
glass	189 \pm 16	0.27 \pm 0.003	1.97 \pm 0.25	408
glass	188 \pm 21	0.25 \pm 0.02	1.9 \pm 0.1	*
porous (1.2 μm)	137 \pm 27	0.30 \pm 0.03	2.7 \pm 0.2	*
latA 60min	78 \pm 5	0.35 \pm 0.01	2.21 \pm 0.12	65
cytoD	57 \pm 14	0.32 \pm 0.04	1.15 \pm 0.11	**
blebbistatin	85 \pm 12	0.35 \pm 0.02	1.77 \pm 0.11	**

The described changes in the viscoelastic parameters obtained by the power law structural damping model can be interpreted in terms of reduced actomyosin contractility on soft substrates when viewed in conjunction with measurements where the F-actin cytoskeleton was impaired by either F-actin depolymerization or myosin II inhibition. As discussed in the previous chapter the overall stiffness and the power law coefficient are strongly affected when the F-actin cytoskeleton is dissolved, showing lower absolute values for the overall stiffness and an increased dependence of the shear modulus on the frequency (α) similar to the findings on soft substrates. Additionally, the power law coefficient has been shown to be dependent on the myosin induced contractility by others,^{75,241,368} exhibiting lower values for higher pre-stress in the cells. Upon blebbistatin treatment, which is an antagonist for non-muscular myosin II, Rother (2014)³⁶⁸ found an increased power law coefficient and a lowered overall stiffness of the cells. Furthermore, similar alterations in the viscoelastic properties have also been reported of cells grown on porous substrates with pore sizes of 1.2 μm diameter (see Table 19).²⁸⁰ Here, I observe reduced overall stiffnesses on 1 kPa and 8 kPa gels to only about half the value that was found on stiffer substrates. The effect on the power law coefficient is less pronounced, however, still noticeable. Viewed in conjunction with the previously described dependency of G_0 and α on the actomyosin cortex of living cells, these results suggest that the F-actin cytoskeleton is diminished on softer substrates. Indeed, no stress fibers could be observed in cells grown on 1 kPa stiff gels on the basal side of the cell (see Figure 66 B). A less pronounced F-actin cytoskeleton can be observed on gels with a Young's modulus of $E = 8 \text{ kPa}$ (see Figure 66 C), whereas distinct and highly ordered F-actin stress fibers could be observed on stiff gels (see Figure 66 D-E). Moreover, no stress fibers and altered growth (no monolayers) of MDCKII cells could be observed on 0.2 kPa gels. A loss of stress fibers for cells cultured on soft samples as well as distinct and ordered stress fibers for cells cultured on stiff samples has often been reported in literature,^{55,57,369,370} together with static adhesion complexes for cells cultured on stiff samples and more dynamic ones on soft samples.⁵⁵ Additionally, an increase in focal adhesion

area with increasing stiffness of substrate has been reported.^{53,370} This might imply that the alterations of the F-actin cytoskeleton found here for cells cultured on soft substrates are a result of weaker adhesion to the substrate.

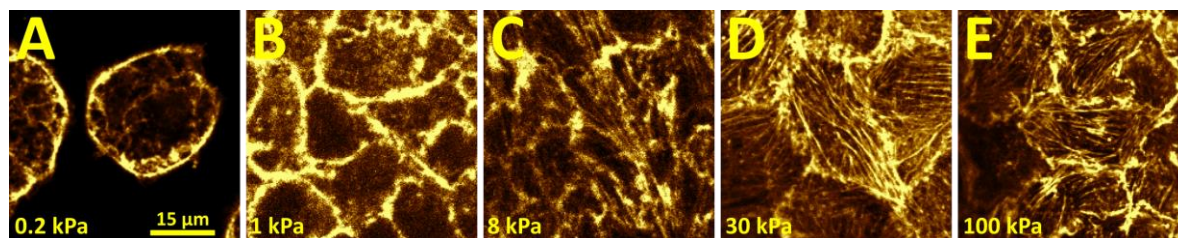


Figure 66: Confocal images of the F-actin cytoskeleton of MDCKII cells as a function of substrate elasticity. Labelling was performed using Alexa Fluor 546 Phalloidin. Young's moduli of gels: **A:** 0.2 kPa; **B:** 1 kPa; **C:** 8 kPa; **D:** 30 kPa; **E:** 100 kPa.

The general picture of this mechanosensitive process is the following: Cells which come into contact with soft substrates are not able to form stable adhesion complexes. No pinning-points for the contractile machinery are available and tension in the cell cortex cannot be built up or maintained. Thus, the spreading behavior is altered and cells maintain roundish and do not spread. In contrast, cells which come in contact with a stiff surface build up strong attachment sides, are able to spread, show highly ordered stress fibers and are able to build up a strong contractile actomyosin cortex. The role of focal adhesion kinase, vinculin and paxilin in mechano-sensing such as durotaxis is well documented.³⁷¹ Additionally, Trichet *et al.*⁵³ argue that rigidity sensing of cells is not only a molecular process. It is rather a large scale contractile mechanism, since single focal adhesions would only sense the local elasticity of micro-pillars but a dependency on the bending stiffness of the pillars is found rather than a dependency on the material property. The role of subsequent signaling processes has been portrayed in the introduction. Moreover, strong evidence of the role of non-muscle myosin II in rigidity sensing of cells has been presented by Engler *et al.*⁵² Others have found a relation of the speed of cell spreading to the surface elasticity³⁷². Moreover, an increased spreading area per cell is consistently found in literature for stiffer substrates.^{50,57,59,372} The role of cell-cell contacts in the maintenance of cellular tension has also been described by others.³⁷³ However, I do not see pronounced alterations in e-cadherin or ZO-1 distribution for cells cultured on substrates with different stiffness (see Figure 67). Along this line of arguments I put my results in the context contractility governed mechano-sensing during the process of cell spreading.

For further elucidation of the hypothesis, that the overall stiffness is altered due to an altered actomyosin based cortical tension, another force spectroscopy method was applied in order to assess the cortical tension of the cells (described in chapter 4.2.7.2). The results, notably the apparent area compressibility modulus $\tilde{\kappa}_A$, the overall tension T_0 and the membrane tension T_t , are summarized in Figure 68 (median \pm sem in Table 20). The cortical tension T_c is the difference between the overall tension and the membrane tension (see Table 20). For the apparent area compressibility modulus a dependency on the substrate stiffness is observed, with lower values for lower substrate stiffness. However, for the cortical tension and the membrane tension no dependency on the surface elasticity could be observed. This contradicts the before mentioned assumption that the alterations in the viscoelastic properties are caused by cortical tension. A tendency of the membrane tension towards lower values has been expected for cells cultured for softer gels, since a reduced membrane tension has been reported for cells, which were exposed to cytoskeletal drugs.^{168,374}

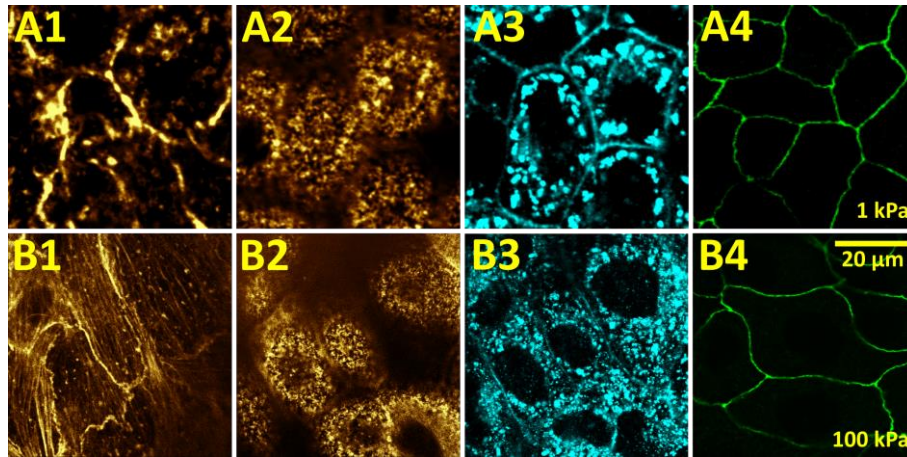


Figure 67: The F-actin cytoskeleton and cell-cell contacts of MDCKII cells as a function of substrate elasticity. Confocal images of important cytoskeletal proteins as a function of substrate elasticity are shown. Young's modulus of PAA gels: **A**: 1 kPa; **B**: 100 kPa. **A1&B1**: Fluorescently stained F-actin cytoskeleton, focus was set to the basal focal plane; **A2&B2**: Fluorescently stained F-actin cytoskeleton, focus was set to the apical focal plane; **A3&B3**: Fluorescently stained e-cadherin; **A4&B4**: Fluorescently stained ZO-1. A&B1-3 each show the same position on the sample, A&B4 are from a different samples. Labelling was performed as described in chapter 4.2.5.1 (Experiment performed by Franziska Ries (2016)).

More importantly, a dependence of the overall tension on the substrate stiffness was expected, since the cortical tension is the difference of the overall tension and the membrane tension and a change in the cortical tension has been assumed. A significant difference in the overall tension can be observed between cells grown on 1 kPa and either 2 kPa or 8 kPa stiff gels. Only a minor increase can be observed for 6 kPa stiff gels and no difference in the overall tension of cells seeded on 1 kPa or 100 kPa stiff gels can be observed. Here, the largest difference was expected. Others have found a two-fold decrease in the overall tension upon cytochalasin D¹⁶⁸ or latrunculin A³⁷⁴ treatment of MDCKII cells. Moreover, on porous substrates a decrease in the overall tension to 58 % compared to the tension of cells from the same cell line cultured on petri dishes was reported.²⁸⁰ Based on the observations made here about the changes in the F-actin cytoskeleton and the viscoelastic properties of the cells, a reduction of the overall tension for cells on softer substrates has been strongly expected.

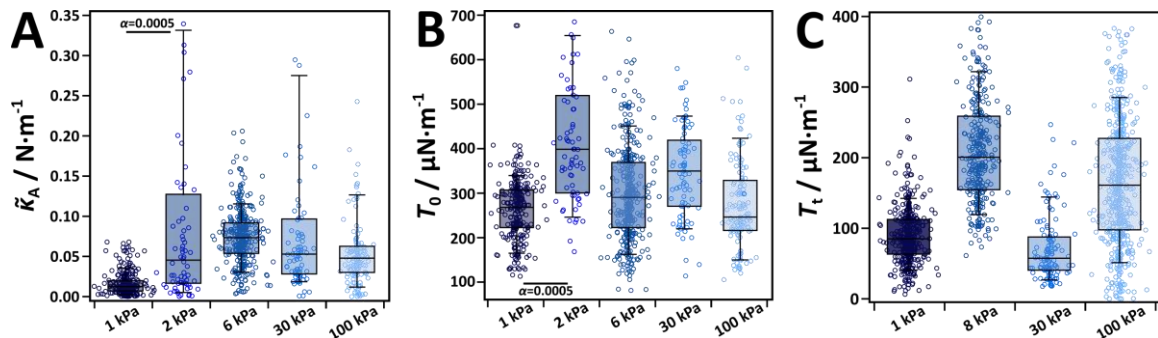


Figure 68: Apparent area compressibility modulus, over all tension and membrane tension of epithelial cells in dependency of substrate stiffness. MDCKII cells were cultured on substrates of different E -moduli: **1 kPa**, **8 kPa**, **30 kPa** and **100 kPa**. Data were obtained as described in chapter 4.2.7.2. **A**: Apparent area compressibility modulus $\tilde{\kappa}_A$; **B**: Overall tension T_0 (sum of cortical tension T_c and membrane tension T_t); **C**: Membrane tension T_t . Box plots extend from the 25th to the 75th percentile, whiskers from the 10th to the 90th. α indicates the confidence level of a Wilcoxon rank test. Individual data points are plotted as circles some outliers are not shown.

In general, the overall tension depends on many experimental factors. Usually the overall tension is determined by the first few hundred nanometers of the force indentation curve. Hence, an accurate determination of the contact point is crucial for the determination of the overall tension. Additionally, both the apparent area compressibility and the overall tension are calculated by the

liquid droplet model and depend on a good characterization of the geometry of the apical cell cap. The reported values were corrected for the average geometry. However, cell-to-cell variations might introduce inaccuracy in the data. The observed reduced area compressibility modulus for cells grown on soft substrates can be explained by an impaired F-actin cytoskeleton. Upon reduction of the F-actin cytoskeleton more excess membrane is available, which in turn leads to an increased apparent area compressibility modulus (see equation (64)).

Table 20: Apparent area compressibility modulus, over all tension and membrane tension of MDCKII cells in dependency of substrate stiffness. Cells were cultured on substrates of different E-moduli: 1 kPa, 2 kPa, 8 kPa, 30 kPa and 100 kPa. $\tilde{\kappa}_A$: Apparent area compressibility modulus; T_0 : Overall tension; T_t : Membrane tension (median \pm sem) and $T_c = T_0 - T_t$ cortical tension.

sample	$\tilde{\kappa}_A / \text{N} \cdot \text{m}^{-1}$	$T_0 / \text{mN} \cdot \text{m}^{-1}$	N	$T_t / \text{mN} \cdot \text{m}^{-1}$	N	$T_c / \text{mN} \cdot \text{m}^{-1}$
1 kPa	0.012 ± 0.001	0.27 ± 0.004	274	0.09 ± 0.002	393	0.18
2 kPa	0.045 ± 0.03	0.40 ± 0.02	72	n. a.	n. a.	n. a.
8 kPa	0.073 ± 0.002	0.29 ± 0.01	357	0.20 ± 0.01	320	0.09
30 kPa	0.053 ± 0.02	0.35 ± 0.01	81	0.06 ± 0.004	119	0.29
100 kPa	0.048 ± 0.01	0.25 ± 0.01	133	0.16 ± 0.01	513	0.09

Taken together, for most of the mechanical parameters a dependency on the substrate stiffness has been observed below 8 kPa. In literature changes in the cell stiffness together with a change in cell area were reported to occur at substrate stiffnesses around 1-20 kPa in many cell lines.^{50,57,59} Our findings agree with these observations. Consistently, lower stiffnesses and smaller areas per cell were reported for cells grown on softer substrates. Here, an increase of the cell size with increasing substrate stiffness is observed as well (see Table 21). When the substrate stiffness increased from about 1 kPa to 30 kPa, the area per cell also increased from 190 to 480 μm^2 . Thus the question arises whether the measured differences in the mechanical properties might be a pure effect of the altered cell size or if these changes are a result of altered spreading of cells and reorganization of the actomyosin cortex due to mechano-signaling. From the data presented so far it cannot be distinguished between these two possibilities. The relationship between substrate stiffness, cell size and mechanical properties will be subject of discussion in the next chapter.

Table 21: Effect of substrate stiffness on the shape of MDCKII epithelial cells. Averaged (N = number of cells) length, width and cap height (mean \pm std) extracted from contact AFM images in dependency of the E-modulus of the substrate. Cells were not fixated.

sample	length / μm	width / μm	height / μm	area / μm^2	N
1 kPa	18 ± 4	13 ± 3	1.4 ± 0.5	189 ± 63	37
8 kPa	23 ± 6	15 ± 5	1.3 ± 0.4	271 ± 110	28
30 kPa	30 ± 6	20 ± 2	1.3 ± 0.2	478 ± 109	12
100 kPa	26 ± 6	17 ± 4	1.9 ± 0.8	339 ± 112	16

5.2.3. Impact of Cell Size on the Viscoelastic Properties of Epithelial Cells

Data in this chapter has been measured by Franziska Ries (2016) within a laboratory internship during her supervised Bachelor studies.

As demonstrated in the previous chapter a correlation between cell size and the viscoelastic parameters was observed. In this chapter I aim to show that both, the cell size and the substrate elasticity have an impact on the viscoelasticity of MDCKII cells. The connection between cell size and mechanical properties is commonly studied in single cell assays, where cells are cultured on micro-fabricated pillars of defined shape and size.^{57,375,376} Here, I use a simple straight forward approach as a control for the study of cell mechanic as a function of substrate elasticity. Cells were seeded in densities of 750,000 c, 500,000 c and 250,000 c per 9.2 cm² (further called 750,000 c, 500,000 c and 250,000 c respectively) and the resulting cell size was determined from images recorded by atomic force microscopy in contact mode (see chapter 4.2.3). The determined cell dimensions are summarized in Table 22. Cells seeded in lower cell densities cover larger surface areas than cells seeded at intermediate densities. Cells seeded in even higher cell density showed smaller surface coverage per cell.

Table 22: Cell size as a function of seeding density. MDCKII cells were seeded in different densities (750,000, 500,000 and 250,000 cells per 9.2 cm²). Averaged (N = number of cells) length, width and cap height (mean \pm std) extracted from contact AFM images. Cells were not fixated.

seeding density / cells per 9.2 μm^2	length / μm	width / μm	height / μm	area / μm^2	N
750,000	21 \pm 4	14 \pm 3	0.8 \pm 0.3	231 \pm 66	42
500,000	22 \pm 3	15 \pm 2	0.6 \pm 0.2	260 \pm 49	37
250,000	35 \pm 6	22 \pm 4	1.0 \pm 0.3	604 \pm 151	22

In order to confirm cell viability and the formation of cell-cell interactions for all seeding densities at the specified culture conditions electric cell impedance sensing measurements were carried out. The resulting impedance is shown over time in Appendix 1 I. All cell samples reached confluency within 1 to 2 days. The starting time of a measurement was adjusted to these time points. On all samples cell-cell contacts were formed, reflected in the increase in barrier resistance (R_b , see Figure 69 A) and shown by fluorescence staining of e-cadherin and ZO-1 (see Appendix 1 II). All samples showed similar transepithelial resistance and γ , which is a measure for the constricted current flow beneath the cell. The parameter γ is inversely proportional to the cell-substrate distance. Hence, no major differences in the formed monolayers can be found in terms of cell-cell or cell-substrate interactions. Thus, changes in the cell mechanics can be attributed to changes in the cell size rather than other morphological changes.

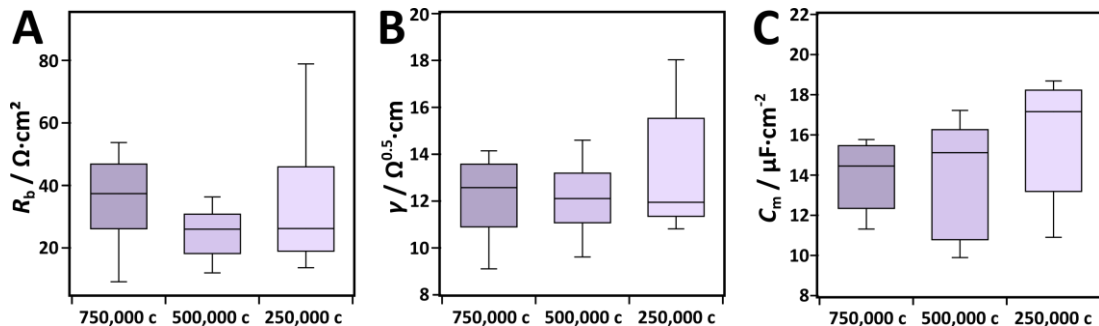


Figure 69: ECIS parameters for MDCKII cells in different seeding densities. The impedance was determined for different frequencies and fitted to a model of Lo and Ferrier (see chapter 4.2.6.3). Data was evaluated over the whole measuring time after formation of the monolayer. The resulting fit parameters are shown in box plots. Box plots extend from the 25th to the 75th percentile, whiskers from the 10th to the 90th. **A:** Transepithelial resistance R_b ; **B:** Parameter γ which is inversely proportional to the cell-substrate distance; **C:** Membrane capacitance C_m . Each boxplot contains at least $N = 2400$ data points.

In atomic force microscopy based microrheological experiments a dependency of all viscoelastic parameters on the cell seeding density was observed (see Figure 70 and Table 23). Compared to a cell density of 500,000 c per 9.2 cm² ($G_0 = (178 \pm 7)$ Pa) a higher overall stiffness ($G_0 = (256 \pm 5)$ Pa) was found for 250,000 cells cultured on the same area, while higher cell densities (750,000 c) resulted in a softening of the cells $G_0 = (126 \pm 6)$ Pa. Accordingly, the power law coefficient showed higher values for high cell density ($\alpha = 0.30 \pm 0.004$) and lower values for cells covering a larger area per cell ($\alpha = 0.21 \pm 0.001$). The fit parameter for the Newtonian viscosity of the cell showed a weak dependency on the cell density with a tendency towards higher values for lower cell density.

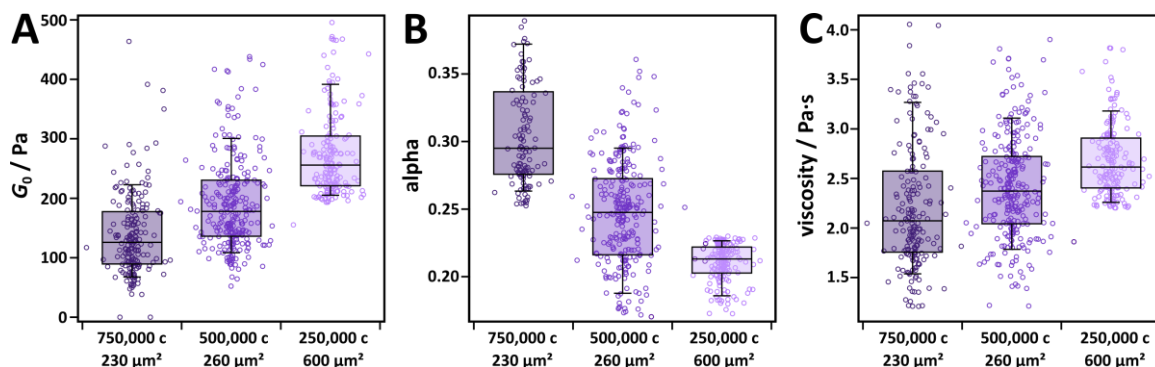


Figure 70: Cell size dependency of the viscoelastic parameters of living MDCKII cells. MDCKII cells were seeded in different densities (750,000, 500,000 and 250,000 cells per 9.2 cm²) to obtain cells of different cell sizes (see Table 22). Data obtained from active atomic force microscopy based microrheology (see 4.2.7.1) were fitted by the power law structural damping model (equation (41)). Resulting viscoelastic parameters are shown. **A:** Stiffness offset of the viscoelastic moduli G_0 ; **B:** Power law coefficient α ; **C:** Newtonian viscosity η . Box plots extend from the 25th to the 75th percentile, whiskers from the 10th to the 90th. Individual data points are plotted as circles, some outliers are not shown.

Table 23: Viscoelastic parameters obtained by the PLSDM of MDCKII cells in different seeding densities. Confluent layers of MDCKII cells were seeded in different densities (750,000, 500,000 and 250,000 cells per 9.2 cm²). Fit parameters of the power law structural damping model (equation (41)) are reported: shear modulus at zero frequency G_0 , power law coefficient α and Newtonian viscosity η (median \pm sem).

sample	G_0 / Pa	α	η / Pa · s	N
750,000 c	126 \pm 6	0.30 \pm 0.004	2.61 \pm 0.03	181
500,000 c	178 \pm 7	0.25 \pm 0.003	2.37 \pm 0.03	274
250,000 c	256 \pm 5	0.21 \pm 0.001	2.07 \pm 0.05	191

These changes in the viscoelastic parameters show similar dependencies as observed for cells cultured on substrates of different elasticities (*vide supra*). Thus, a causal connection between altered mechanical properties and changes in cell size on substrates of different elasticities are possible. Interestingly, no obvious differences in the stress fiber formation at the basal cell side could be observed for the different seeding densities (see Figure 71). This stays in contrast to cells grown on soft substrates where nearly no stress fibers could be observed (see Figure 66). Even on samples with 1,000,000 cells per 9.2 cm² distinct stress fibers could be observed. In literature alterations in the stress fiber development in dependency of the cell size have been reported^{377–379}, but for larger cell size changes than observed here. A strong dependency of cortical cell stiffness on the spreading area of cells has been reported for many cell lines in single cell measurements on micro-patterned surfaces.^{57,376,380} Consistently stiffer cells were reported for larger induced cell spreading areas, supporting the here presented findings.

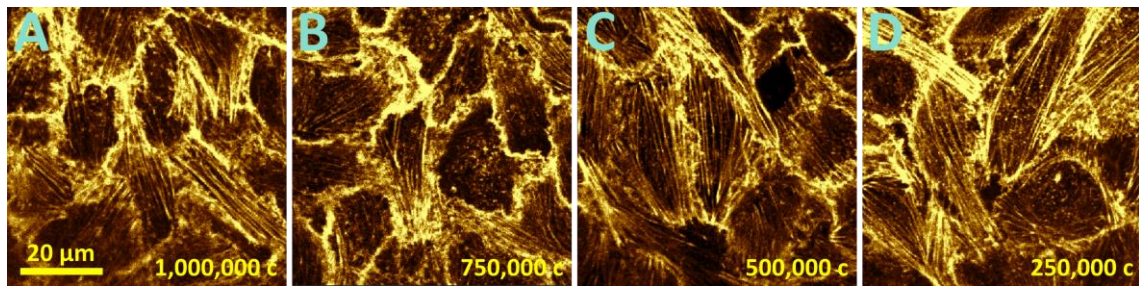


Figure 71: F-actin cytoskeleton organization at the basal side of MDCKII cells as a function of seeding density. Confocal images of the F-actin cytoskeleton of MDCKII cells as a function of different seeding density are shown (fluorescently labeled with Alexa Fluor 546 Phalloidin). **A:** 1,000,000 c; **B:** 750,000 c; **C:** 500,000 c; **D:** 250,000 c.

5.2.3.1. Influence of Cell Size on the Viscoelasticity of Cells Cultured on Substrates of Different Elasticities

Data within this chapter has been measured by Franziska Ries (2016) during her supervised Bachelor thesis.

As shown before the viscoelastic properties of cells are a function of both, the substrate elasticity and the cell size. Tee, Janmey and coworkers⁵⁷ already reported this bivalent dependency of the cortical stiffness of cells grown on elastic surfaces. In their study they reasoned that the cortical stiffness of cells grown on stiff substrates is dominated by cell size whereas cells grown on soft substrates are predominantly influenced by substrate elasticity.

Here, the viscoelastic parameters of cells cultured in different seeding densities and cells grown on substrates of different elasticities were plotted against the area of the respective cells. The area of the cell was determined from the height information of the force map. Since one force distance curve has a spatial resolution of $1.88 \mu\text{m} \cdot \text{s}^{-1}$ this analysis is somewhat limited but it is an easy tool to investigate the relationship between cell stiffness and actual area per cell. Exemplarily, the overall stiffness is shown in dependency of the area per cell (see Figure 72). The dependency of the other viscoelastic parameters on the area per cell is reported in the Appendix 1 III (Figure 79).

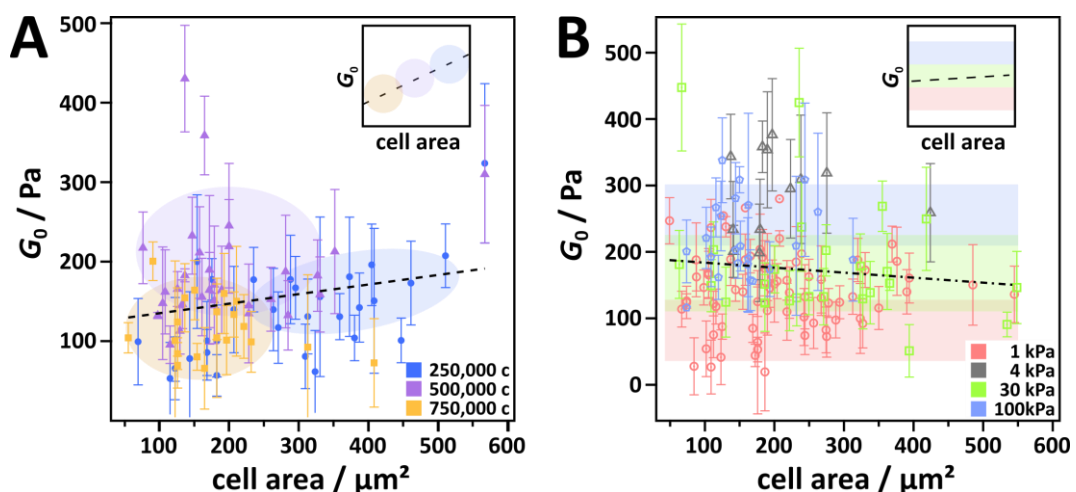


Figure 72: Cortical stiffness as a function of area per cell. The stiffness offset obtained from the PLSDM is shown in dependency of the area per cell. **A:** Cells grown on stiff glass substrates were seeded in different cell densities: 250,000 c (blue), 500,000 c (violet) and 750,000 c (orange). **B:** Cells grown on substrates of different elasticity: 1 kPa (red), 4 kPa (grey), 30 kPa (green) and 100 kPa (blue). Mean values (data points) and standard deviation (error bars) for all force distance curves that were evaluated for one single cell are plotted against the area which was obtained by the height map of the atomic force microscopy measurement. Dashed lines show a linear trend for all data. Insets represent the expected tendencies. (Data measured by Franziska Ries (2016))

For a dependency of the cell stiffness solely on the size of the cells a linear relationship between the area per cell and the stiffness of the cells is expected, with increasing shear modulus for an increasing cell size (see inset Figure 72 A). For samples where the cell size was controlled by different seeding densities of cells such a dependency was found (Figure 72 A). Here, a clustering of data points from low seeding densities at large areas per cell and an accumulation of data points at lower cell sizes for higher seeding densities were found as expected (indicated as colored shades in Figure 72). For samples where cells were cultured on substrates of different elasticities no increase in the shear modulus with increasing individual cell size was observed (Figure 72 B). Instead of clusters at different areas per cell, cells cultured on 1 kPa stiff gels showed a consistently lower overall stiffness than cells cultured on 30 kPa or 100 kPa stiff gels. The results found for cells grown on 4 kPa stiff gels do not follow this trend. Higher stiffnesses per cell were found. The results found here are backed by the aforementioned study of Tee, Janmey and coworkers⁵⁷. They suggest that the alterations in viscoelastic properties of cells are caused by the substrate elasticity rather than by the cell size. Hence, I picture that during the process of cell spreading the cells sense their environment and respond to the mechanical signal by altered spreading and reorganization of the F-actin cytoskeleton. As a result, cells occupy a smaller area and the actomyosin cortex is less developed.

5.2.4. Viscoelasticity of Mammary Gland Cells in Response to Matrix Elasticity

Data within this chapter has been measured by Christine Franke (2014) during her supervised Bachelor thesis.

The aim and idea of experiments presented in this chapter was to compare the changes in mechanotransduction between cells of different metastatic potential in response to substrate elasticity in a well-known breast cancer cell model.^{350–353,381} First, the MCF-10A cell line is studied. This cell line serves as a model for benign breast epithelial cells. Thus, changes in response to substrate stiffness are expected.

Figure 73 A shows the frequency dependent viscoelastic properties of MCF-10A cells in response to different substrate elasticities. For softer substrates (1 kPa) significantly lower viscoelastic moduli of cells are observed. Both, the storage and the loss modulus, decrease by a full order of magnitude (≈ 1000 Pa) for cells seeded on substrates with an elasticity of 1 kPa compared to 8 kPa. These tremendous changes are far more pronounced than observed for the MDCKII cell line (see 5.2.2). For comparison, only a two-fold decrease in magnitude of the shear modulus was found in MDCKII cells (≈ 100 Pa).^{iv}

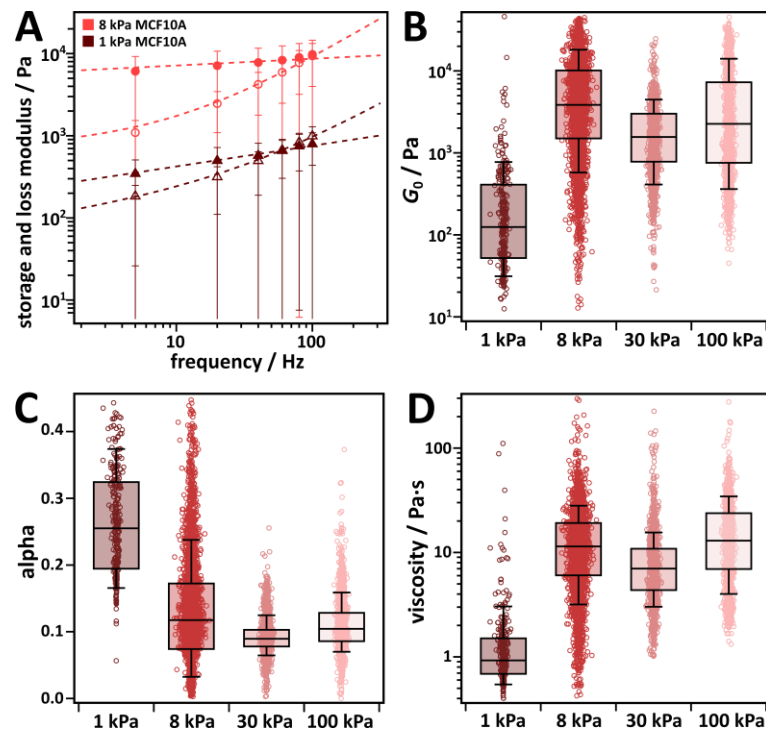


Figure 73: Viscoelastic properties of mammary gland cells in dependency of substrate stiffness. MCF-10A cells were cultured on substrates of different E -moduli: **1 kPa**, **8 kPa**, **30 kPa** and **100 kPa**. Data obtained from active atomic force microscopy based microrheology (see 4.2.7.1) were fitted by the power law structural damping model (equation (41)). **A:** Storage (solid symbols) and loss modulus (open symbols) of MCF-10A cells cultured on substrates of different elasticities are shown. Circles (\bullet): 8 kPa; Triangles (\blacktriangle): 1 kPa. Data points: median value; error bars: 25th and 75th percentile; Dashed lines: fit by the power law structural damping model. **B:** Stiffness offset of the viscoelastic moduli G_0 ; **C:** Power law coefficient α ; **D:** Newtonian viscosity η . Box plots extend from the 25th to the 75th percentile, whiskers from the 10th to the 90th. Individual data points are plotted as circles, some outliers are not shown.

^{iv} Note that for MCF-10A cells all data points of the force map were included. For MDCKII cells, only the center of the cells were analyzed. This was necessary because cell boundaries were not easy to determine. However, the effect of stiffer cell boundaries to the data from the much stiffer MCF-10A cell line is negligible and the data within this dataset (for 1 cell type) is consistently analyzed.

Similar to the MDCKII cell line the cross-over from the frequency regime, where the elastic contribution predominates, to the frequency regime, where the cells behave more fluid like, was not substantially shifted within one set of experiments. The MCF-10A cell line shows more solid like behavior ($G''/G' < 1$) up to higher frequencies compared to MDCKII cells. Consistent with this observation is that MCF-10A cells show a more pronounced elastic response compared to MDCKII cells and a lower power law coefficient for the scaling of the shear modulus with frequency. The viscoelastic parameters obtained from the power law structural damping model for all investigated substrate stiffnesses are shown in Figure 73 B-D. Values are reported in Table 24. For cells cultured on stiff substrates similar values (within the experimental uncertainty for these cells lines) were found as reported before in the working group²⁴⁴. Other working groups reported lower elastic moduli ($G \approx E/3 \approx 500$ Pa) for the MCF-10A cell line^{71,353}. However, sub-confluent cells were measured in their work. In all microrheological data obtained from MCF-10A cells on softer substrates a substantial variation in the parameters and moduli can be observed with a non-Gaussian distribution of the data points (Figure 73 B&D). A pronounced dependency on the substrate elasticity is reflected in all viscoelastic parameters similar to the changes observed for the MDCKII cell line: (1) the overall stiffness was substantially reduced, (2) the power law coefficient was significantly increased, (3) the Newtonian viscosity was strongly decreased and (4) less pronounced stress fibers were observed for cells seeded on very soft substrates (1 kPa & 0.2 kPa, Figure 74 A&B).

Table 24: Viscoelastic parameters obtained by the PLSDM of MCF-10A in dependency of substrate stiffness. Cells were cultured on substrates of different E-moduli: **1 kPa**, **8 kPa**, **30 kPa** and **100 kPa**. Fit parameters of the power law structural damping model (equation (41)) are reported: shear modulus at zero frequency G_0 , power law coefficient α and Newtonian viscosity η (median \pm sem). *Data measured on stiff glass substrates have already been published.²⁴⁴

sample	G_0 / Pa	α	η / Pa · s	N
MCF-10A 1 kPa	125 \pm 172	0.26 \pm 0.01	0.93 \pm 0.52	288
MCF-10A 8 kPa	3860 \pm 133	0.12 \pm 0.14	11.4 \pm 0.25	4074
MCF-10A 30 kPa	1560 \pm 130	0.09 \pm 0.001	7.00 \pm 1.26	2038
MCF-10A 100 kPa	2260 \pm 160	0.10 \pm 0.001	13.0 \pm 0.38	2046
MCF-10A glass	1370 \pm 70	0.10 \pm 0.01	5.30 \pm 0.10	*
MCF7 glass	250 \pm 20	0.25 \pm 0.02	3.44 \pm 0.10	*
MDA-MB-231 glass	690 \pm 60	0.22 \pm 0.01	8.69 \pm 0.21	*

The overall stiffness dropped to $G_0(1 \text{ kPa}) = (125 \pm 172) \text{ kPa}$ for MCF-10A cells grown on 1 kPa gels (compare $G_0(100 \text{ kPa}) = (2260 \pm 160) \text{ kPa}$), which is similar to the overall stiffness found for MDCKII cells, in which actin or myosin was depleted by cytochalasin D, latrunculin A or blebbistatin as well as MDCKII cells grown on soft (1 kPa) or porous (1.2 μm) substrates (*vide supra*). For these conditions similar power law coefficients were observed as found here for MCF-10A cells on 1 kPa stiff gels ($\alpha = 0.26 \pm 0.01$). Hence, a similar mechanotransduction process as described above might be plausible. However, in addition to the mechanical alterations strong morphological changes were observed when culturing the MCF-10A cell line on softer substrates (see Figure 75). On stiffer substrates (30 kPa or 100 kPa) monolayers of MCF-10A cells were observed. On 8 kPa stiff polyacrylamide gels occasionally cells growing on top of the lower cell layer were observed. Moreover, measurements showed strong variation between single measurements, which could be a result of locally different growth forms of the cells. On 1 kPa gels, only multi-layers or single cells were formed. At 0.2 kPa stiff gels spherical assemblies of cells were found. Here, cells were not spread but adhered to each other. These changes in morphology have also been reported by others and are indeed the natural occurrence in the soft mammary gland tissue (160 Pa).⁵⁹

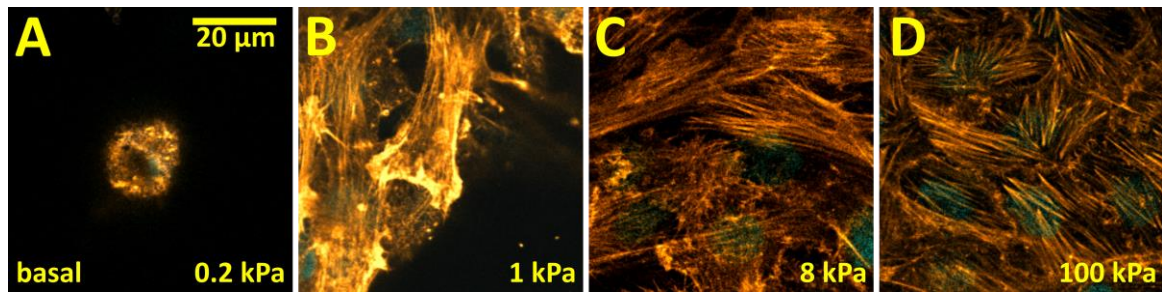


Figure 74: Cytoskeletal organization at the basal side of breast epithelial cells as a function of matrix elasticity. Confocal fluorescence images of the F-actin cytoskeleton (orange) at the basal side of MCF-10A cells cultured for 2-3 days on surfaces of different elasticity are shown. Matrix elasticity: **A:** 0.2 kPa; **B:** 1 kPa; **C:** 8 kPa; **D:** 100 kPa.

Due to these strong morphological differences comparative studies of the cell mechanics of malignant (MCF-7 & MDA-MB-231) and benign cells (MCF-10A) will not lead to unambiguous results. There are two reasons for this: First, I showed in the previous chapter that the measured viscoelastic parameters are dependent on the cell size. Second, cells growing in multi-layers show different properties compared to cells in direct contact with the substrate⁵⁵. Thus, I refrained from assessing the mechanical properties of MCF-7 and MDA-MB-231 cells on softer substrates. Previous results²⁴⁴ for measurements on MDA-MB-231 and MCF-7 cells grown on glass substrates are provided in Table 24. The morphology of MCF-10A cells is close to the 'malignant phenotype' as argued by Paszek *et al.*⁵⁹ However, substantial differences in the mechanical properties can be observed between MCF-10A cells grown and MDA-MB-231 cells on stiff substrates. With MDA-MB cells being softer as reported in many *in vitro* studies^{2,11,244,353,382–384} and *in vivo* studies.^{385,386} Agus *et al.*³⁵⁰ already showed that cell proliferation is a function of substrate stiffness for MCF-10A cells but less in MDA-MB cells. Additionally, they showed that the cell morphology of MDA-MB cells is not strongly dependent on the substrate elasticity. Accordingly, my expectation is that the contractility and thus the frequency dependent viscoelastic properties of MDA-MB cells are less dependent on substrate stiffness. This effect might be tested in the future in more defined essays such as single cell experiments where the cell size can be controlled by micro surface patterning^{57,375,376}. Traction force microscopy studies are another way to assess the contractility of single MDA-MB-231 cells.^{387,388} In a recent study³⁸⁸ on single MDA-MB-231 cells migrating through 3D collagen gels no difference in the contractility of the cells was found for different matrix stiffnesses. This could be a hint that the contractility of malignant cells is not altered by substrate stiffness. However, the authors stated that this might be a result of altered growth in the fibrous networks, also MDA-MB cells were not tested against a benign cell line.

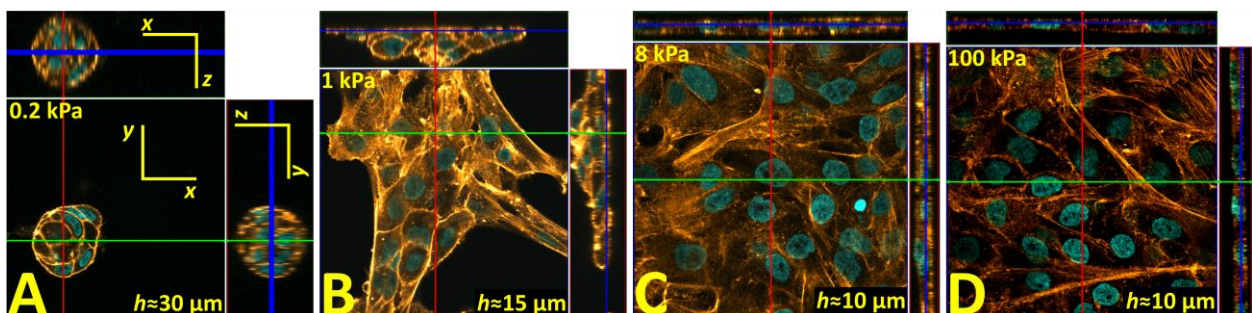


Figure 75: Morphology of breast epithelial cells in response to matrix elasticity. Orthogonal view of confocal fluorescence images of the F-actin cytoskeleton (orange) and the nuclei (turquoise) of MCF-10A cells cultured on surfaces of different elasticity for 2-3 days. Matrix elasticity: **A:** 0.2 kPa; **B:** 1 kPa; **C:** 8 kPa; **D:** 100 kPa. The dimension of each image section is $135 \times 135 \mu\text{m}^2$ in *x-y*-direction. Approximate height *h* of the cell assemblies is indicated in the lower right corner.

5.2.5. Conclusion

In this chapter the cell mechanics in response to surface stiffness have been studied. Two epithelial cell lines from different organs have been cultured on substrates of different elasticities ranging from 1 kPa to 100 kPa and their viscoelastic properties in response to the altered substrate elasticity has been measured.

First, the general changes of the viscoelastic properties upon dissolving or reinforcing the F-actin cytoskeleton were tested. The cytoskeletal drugs latrunculin A as well as jasplakinolide were used for this purpose. It was observed that depolymerization of F-actin, similarly to the inhibition of myosin II, leads to a decrease in the overall stiffness and to an increase in the power law coefficient obtained by a power law structural damping model fit to the measured frequency dependent shear modulus. Thus, these parameters are dependent on the actomyosin dependent tension in the cell. This was also proposed by others.²⁴¹ The Newtonian viscosity was not altered, with the exception of jasplakinolid treatment after 30 min. The here presented data and previously published data^{38,244} shows that this parameter is in general mostly dependent on the cell line.

Second, the influence of the substrate stiffness on the viscoelasticity of MDCKII and MCF-10A cells was tested. Similar to the cells where the F-actin cytoskeleton was impaired by drug treatment, cells grown on soft substrates (1 kPa) showed a lower overall stiffness and higher power law coefficients. In contrast to measurements on cells exposed to actin affecting drugs, the Newtonian viscosity of the cells was altered by the substrate stiffness. In correlation with the alterations in the mechanical properties of the cells, the F-actin cytoskeleton showed substantial rearrangement on softer substrates. A proposed dependency of the cortical tension on the substrate elasticity could not be confirmed by the here presented experiments. However, since all other mechanical parameters show the expected tendency, the measured overall tension might be influenced by other contributions. An overview of all changes in cell shape, F-actin cytoskeleton organization and mechanical parameters is provided in Figure 76.

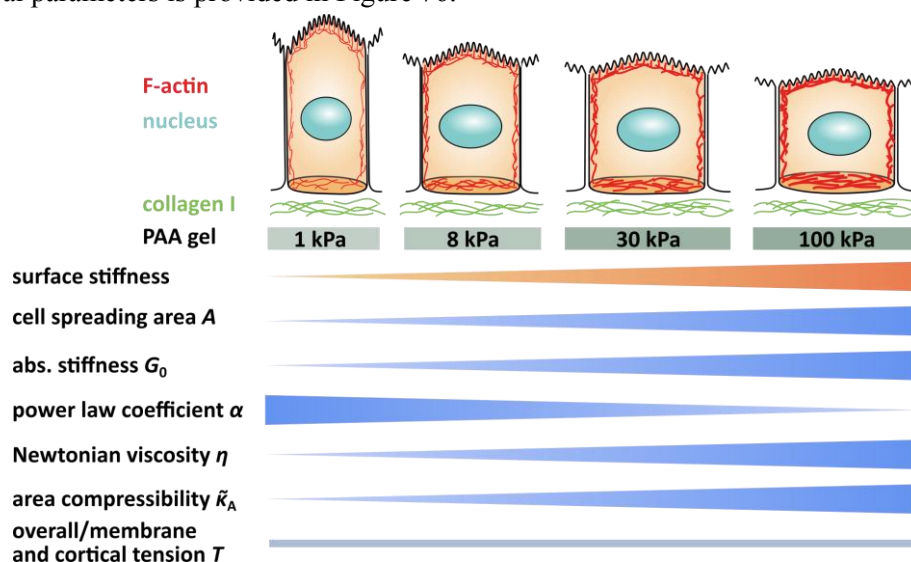


Figure 76: Overview of the effects of substrate stiffness on the average cellular shape and on the mechanical parameters observed here. **Top:** Scheme of the changes in cell morphology and organization of the cytoskeleton in response to surface stiffness. **Bottom:** Changes in the respective mechanical parameters and the cell spreading area are depicted by wedges.

Third, to illustrate the influence of cell size on the mechanical properties a series of measurements was performed where the cell size was altered by different cell seeding densities. These data suggested an additional dependency of all viscoelastic parameters on the cell size. Plotting the

overall stiffness against the individual cell size revealed a dependency of the cell stiffness on the cell size for the cells that were cultured in different densities. However, this tendency was not observed for cells cultured on substrates of different elasticity. Thus, it was argued that both effects, substrate elasticity as well as cell size, influence the viscoelastic properties but the mechanical properties on the elastic surfaces are mainly dominated by the mechano-sensing of the substrate properties.

The three here presented sets of experiments, when taken together, might suggest that an optimal tension exists. This is for two reasons: (1) the reinforcement of the cytoskeleton by jasplakinolide was time dependent. Only within the first 30 min of drug treatment a reinforcement of the cytoskeleton could be observed. An increase in the overall stiffness to 124 % of its original value could be observed during this time span. For longer exposure time to the drug the absolute stiffness dropped and the power law coefficient increased again. (2) For both cell lines the changes in the mechanical parameters leveled off to form a plateau at a substrate stiffnesses of about 5 kPa. For higher substrate stiffnesses no further increase in the tension dominated parameters or in the Newtonian viscosity was found even for cells cultured on glass substrates, which have a Young's modulus in the giga Pascal region (10^4 -fold increase). The absolute stiffness of the two cell lines investigated here, is entirely different: MCF-10A cells show a 12-fold higher stiffness on cells cultured on 100 kPa gels and a power law coefficient which was only half as high as found for MDCKII cells.

Similar mechanosensitive dependency on the substrate stiffness has been observed for both cell lines. They originate from different organs: MDCKII originate from the epithelium in the kidney which is about 2.2 kPa stiff and MCF-10A originate from the mammary gland which is among the softest tissues in the body (0.16 kPa).^{51,59} For MCF-10A cells a threshold substrate stiffness to an emerging plateau, where the mechanical parameters did not change as a function of surface elasticity, was reported at around 5 kPa in literature. Here we observed the strongest changes in mechanical properties between 1 and 8 kPa for MCF-10A. No trend for higher substrate stiffnesses could be observed. For MDCKII this threshold seemed to be slightly higher. For substrate stiffnesses higher than 30 kPa no changes in the area per cell or the mechanical parameters could be observed.

A comparison between the mechanics of benign and malign mammary gland cells as a function of substrate elasticity could not be carried out because the cell morphology of MCF-10A cells did show substantial changes in dependency of the substrate stiffness as argued above. For further studies another cell model, which does not show these strong morphological changes due to substrate elasticity should be used. Another possibility is to control the cell size in single cell measurements by micro-patterned surfaces or to study single cell traction force microscopy experiments to assess the cellular contractility of breast cancer cells (*vide supra*).

6. Summary

The overall aim of this study was to shed light on the determinants of cellular viscoelasticity. The connection between cytoskeletal organization and the mechanical properties of the cellular cortex were of key interest. To achieve this aim different cellular model systems were studied ranging from entangled actin networks, over minimal cortex model systems and apical cellular membrane patches to living cells. Active and passive microrheology measurements were carried out in order to answer two main research questions: (1) What is the impact of transient membrane linkage via ezrin on the frequency dependent viscoelastic properties of F-actin networks? (2) How is the viscoelasticity of epithelial monolayers altered by substrate elasticity?

One essential part of the work was the introduction of two passive (video particle tracking and optical tweezer based) and one active (optical tweezer based) microrheology method in the laboratory for the subsequent examination of minimal cortex model systems. Quantitative measurements on purely viscous samples could be performed with all techniques. Inconsistency between active and passive methods only occurred in the low frequency regime of the active microrheology measurements, which might be due to decreasing accuracy in the determination of the phase shift for low frequency oscillations ($<10^{-1}$ Hz).

Passive video particle tracking based microrheology measurements on thin minimal cortex model systems were established. So far viscoelastic measurements on minimal cortex model systems have only sparsely been reported in literature and to my knowledge no current microrheological data exists for a model system that mimics the physiological situation in the cortex as closely as the here studied PIP₂-ezrin interconnection between the model membrane and the F-actin network. Preliminary data obtained by the optical tweezer based techniques have also been shown.

For entangled F-actin networks the frequency dependent viscoelastic properties and important scaling behaviors similar to those reported in literature were found. However, the observations in the low frequency regime of the shear modulus differ considerably among literature. Our findings for this frequency regime conforms closely to theory but deviates from the majority of the reported measurements. The self-assembled minimal actin cortex, where the physiological interaction between PIP₂ and ezrin was used to anchor F-actin filaments to a solid-supported model membrane, showed a comparable thickness ($< 1 \mu\text{m}$) as found in living cells. Mesh sizes ranging from 500-1200 nm depending on the pinning-point (PIP₂) concentration in the model membrane were observed. A scaling of the mesh size with the pinning-point concentration of $\xi \propto P^{-0.9}$ was found. Using atomic force microscopy in quantitative imaging mode, it could be shown that about 64 % of the filaments in the model system have a diameter of $d \approx 8$ nm and are thus single filaments, while about 27 % have the diameter of a bundle of two filaments ($d \approx 16$ nm). Three distinct frequency regimes could be observed for the minimal actin cortex model system similar to

entangled F-actin networks in a frequency regime between $10^{-3} - 10^2$ Hz. Significant changes in the viscoelastic moduli could be observed. Notably a pronounced increase in the plateau modulus (>14-fold) upon F-actin attachment to a lipid membrane was observed. By variation of the PIP₂ density in the lipid bilayer a scaling behavior of the plateau modulus with the pinning-point density of $G_0 \propto P^{1.4}$ ($G_0 \propto \xi^{-1.5}$) was found, implying an affine behavior of the attached network. In the low frequency regime a broadened local maximum was found in the loss modulus, which was interpreted as two independent stress relaxation processes. Conclusive evidence for the assignment of the peaks could not yet be presented and measurements with complementary methods such as fluorescence recovery after photo bleaching (targeting ezrin and actin alternately) would be beneficial. By the here presented interpretation an apparent unbinding rate constant of $k_{\text{off}}^{\text{app}}(\text{PIP}_2 - \text{ezrin} - \text{actin}) = 0.054 \text{ s}^{-1}$ could be obtained using a semi-phenomenological model introduced by Bausch and coworkers to fit the data. A half-life of 13 s conforms well, with the assumption of a transient bond between F-actin, ezrin and PIP₂. This finding is supported by time lapsed images of the filaments that show network dynamics on this time scale. Additionally, an apparent unbinding activation energy of only $\approx 13 k_{\text{B}}T$ was observed. Two important influences that act on the bending dominated high frequency scaling of the shear modulus have been discussed. Increased hydrodynamic drag at a solid interface shifts the moduli in the high frequency regime. More importantly, the increased mass of the bead surrounding increases the moment of inertia and eventually acts on the storage modulus. A slightly elevated scaling with the frequency is found for the loss modulus. Measurements on a control sample, where the biopolymer network was attached via biotin and neutravidin were less conclusive but showed similar scaling of the plateau modulus. As expected significant differences could be observed in the low frequency regime. For model systems, such as the biotin-neutravidin model system, where the probability of re-binding for the F-actin-membrane cross-link is high, the model used for interpretation of the low frequency peak in the loss modulus is erroneous, since a first order decay kinetic is assumed. Further development of the model to include high re-binding rates and cooperativity would be preferable. The reported apparent unbinding rate constant for the biotin-neutravidin binding complex is thus to be taken with care. Also, the high frequency regime in this sample was disturbed by a noise signal. Here, the limit of video particle tracking for the study of stiffer samples became evident. Similar limitations were observed in the even stiffer apical cellular membrane patches. Solely an approximate plateau modulus of $G_0(\text{ACMP}) \approx 0.66 \text{ Pa}$ could be determined from the data. As expected this value is higher than found for minimal actin cortices ($G_0(\text{PIP}_2 \text{ 3 mol}\%) \approx 0.13 \text{ Pa}$) and substantially lower than for living cells ($G_0(\text{cell}) \approx 200 \text{ Pa}$), where myosin generated tension stiffens the cortex.

In the second part of this thesis the reorganization of the F-actin cytoskeleton and the changes in frequency dependent viscoelastic properties of living cells were studied in response to altered substrate elasticity. Polyacryamide gels with varying amounts of cross-links (Young's moduli: 1-100 kPa) coated with collagen I, were used as substrates. The alterations in the mechanical properties as a result of a mechanosensitive process was studied in two cell lines, which served as model systems for epithelial monolayers, kidney cells (MDCKII) and mammary gland cells (MCF-10A). Atomic force microscopy based active microrheology was used to measure the storage and loss modulus of living cells in a frequency regime ranging from 5 to 100 Hz. The data was fitted by the power law structural damping model and the resulting parameters were interpreted in terms of (active) soft glassy rheology. In both cell lines a dependency of the obtained parameters on the substrate elasticity was observed for substrates softer than 8 kPa. At the same time, strong changes in the organization of the F-actin cytoskeleton could be observed. All observed changes on the viscoelastic parameters (stiffness offset G_0 , power law coefficient α and Newtonian viscosity η)

indicated a softening and a less pronounced F-actin cytoskeleton on softer polyacrylamide gels. Above a threshold of substrate stiffness, no further changes in F-actin organization or mechanical properties could be observed. Two additional sets of experiments were performed, in order to identify the dependencies of the viscoelastic properties of living cells on the F-actin cytoskeleton and the cell size. First, the alterations in the viscoelastic parameters upon either reinforcement or destabilization of the cytoskeleton were examined using two cytoskeletal drugs, jasplakinolide and latrunculin A. Especially the power law coefficient and the overall stiffness showed strong dependency on the actin cytoskeleton similar to the changes in these parameters measured on cells cultured on soft substrates (1 kPa). A similar dependency was previously found for myosin II inhibition by others, supporting the assumption that these parameters are a function of actomyosin mediated tension. Second, the effect of cell size on the viscoelastic properties and the cytoskeleton organization was studied. A dependency of the parameters from the power law structural damping model on the area per cell could be shown. Since a dependency of the area per cell on the stiffness of the substrate was also observed, the question arose whether the observed changes in the mechanical properties of cells measured on soft substrates originate from the change of the cell size or if it was a result of integrin mediated changes in the organization of the F-actin cytoskeleton. Data in favor of the second hypothesis was presented, arguing that on soft samples the effect of substrate stiffness dominates. For MCF-10A cells however, the changes in cell morphology in response to substrate stiffness were far more pronounced. Here, the cells did not form monolayers on substrates below a substrate elasticity of 30 kPa. Multilayers and spherical structures were observed. Such strong alterations in the morphology lead to substantial changes in the force response, which might not necessarily be a function of the substrate. Thus, it was refrained from comparing these measurements to an additional malignant mammary gland cell line (MDA-MB-231). Furthermore, two findings supported the idea of a possible optimum of stiffness, or tension, in the cell: First, both cell lines studied here and most of the cell lines studied by other groups show no change in the absolute stiffness of the cell above a threshold of substrate stiffness. Second, the increased stiffness provoked by jasplakinolide could only be maintained for a short period of time before the F-actin cytoskeleton either ruptured or was de-regulated.

7. References

1. Fletcher, D. A.; Mullins, R. D. Cell mechanics and the cytoskeleton. *Nature* **463**, 485–492 (2010).
2. Suresh, S. Biomechanics and biophysics of cancer cells. *Acta Biomater.* **3**, 413–438 (2007).
3. Jonas, O.; Mierke, C. T. & Käs, J. A. Invasive cancer cell lines exhibit biomechanical properties that are distinct from their noninvasive counterparts. *Soft Matter* **7**, 11488 (2011).
4. Hall, A. The cytoskeleton and cancer. *Cancer Metast. Rev.* **28**, 5–14 (2009).
5. Glenister, F. K.; Coppel, R. L.; Cowman, A. F.; Mohandas, N. & Cooke, B. M. Contribution of parasite proteins to altered mechanical properties of malaria-infected red blood cells. *Blood* **99**, 1060–1063 (2002).
6. Suresh, S. Mechanical response of human red blood cells in health and disease. Some structure-property-function relationships. *J. Mater. Res.* **21**, 1871–1877 (2006).
7. Hosseini, S. M.; Feng, J. J. How malaria parasites reduce the deformability of infected red blood cells. *Biophys. J.* **103**, 1–10 (2012).
8. Nematbakhsh, Y.; Lim, C. T. Cell biomechanics and its applications in human disease diagnosis. *Acta Mech. Sinica* **31**, 268–273 (2015).
9. Otto, O. *et al.* Real-time deformability cytometry. On-the-fly cell mechanical phenotyping. *Nat. Methods* **12**, 199–202 (2015).
10. Xavier, M. *et al.* Mechanical phenotyping of primary human skeletal stem cells in heterogeneous populations by real-time deformability cytometry. *Integr. Biol.* **8**, 616–623 (2016).
11. Guck, J. *et al.* Optical deformability as an inherent cell marker for testing malignant transformation and metastatic competence. *Biophys. J.* **88**, 3689–3698 (2005).
12. Janmey, P. A.; Euteneuer, U.; Traub, P. & Schliwa, M. Viscoelastic Properties of Vimentin Compared with Other Filamentous Biopolymer Networks. *J. Cell Biol.* **113**, 155–160 (1991).

13. Blanchoin, L.; Boujemaa-Paterski, R.; Sykes, C. & Plastino, J. Actin dynamics, architecture, and mechanics in cell motility. *Physiol. Rev.* **94**, 235–263 (2014).
14. Mizuno, D.; Tardin, C.; Schmidt, C. F. & MacKintosh, F. C. Nonequilibrium Mechanics of Active Cytoskeletal Networks. *Science* **315**, 370–373 (2007).
15. Kollmannsberger, P.; Fabry, B. Active soft glassy rheology of adherent cells. *Soft Matter* **5**, 1771 (2009).
16. Turlier, H. *et al.* Equilibrium physics breakdown reveals the active nature of red blood cell flickering. *Nat. Phys.* **12**, 513–519 (2016).
17. Vicente-Manzanares, M.; Ma, X.; Adelstein, R. S. & Horwitz, A. R. Non-muscle myosin II takes centre stage in cell adhesion and migration. *Nat. Rev. Mol. Cell Bio.* **10**, 778–790 (2009).
18. Alvarado, J.; Sheinman, M.; Sharma, A.; MacKintosh, F. C. & Koenderink, G. H. Molecular motors robustly drive active gels to a critically connected state. *Nat. Phys.* **9**, 591–597 (2013).
19. Fehon, R. G.; McClatchey, A. I. & Bretscher, A. Organizing the cell cortex. The role of ERM proteins. *Nat. Rev. Mol. Cell Bio.* **11**, 276–287 (2010).
20. Chugh, P. *et al.* Actin cortex architecture regulates cell surface tension. *Nat. Cell Biol.* (2017).
21. Fritzsche, M.; Erlenkämper, C.; Moendarbary, E.; Charras, G. & Kruse, K. Actin kinetics shapes cortical network structure and mechanics. *Sci. Adv.* **2**, e1501337 (2016).
22. Morone, N. *et al.* Three-dimensional reconstruction of the membrane skeleton at the plasma membrane interface by electron tomography. *J. Cell Biol.* **174**, 851–862 (2006).
23. Braunger, J. A. *et al.* Phosphatidylinositol 4,5-bisphosphate alters the number of attachment sites between ezrin and actin filaments. A colloidal probe study. *J. Biol. Chem.* **289**, 9833–9843 (2014).
24. de La Cruz, E. M.; Gardel, M. L. Actin Mechanics and Fragmentation. *J. Biol. Chem.* **290**, 17137–17144 (2015).
25. Liu, J. *et al.* Microrheology probes length scale dependent rheology. *Phys. Rev. Lett.* **96**, 118104 (2006).
26. Mason, T. G.; Gisler, T.; Kroy, K.; Frey, E. & Weitz, D. A. Rheology of F-actin solutions determined from thermally driven tracer motion. *J. Rheol.* **44**, 917–928 (2000).
27. MacKintosh, F. C.; Käs, J. & Janmey, P. A. Elasticity of Semiflexible Biopolymer Networks. *Phys. Rev. Lett.* **24**, 4425–4428 (1995).

-
28. Hinner, B.; Tempel, M.; Sackmann, E.; Kroy, K. & Frey, E. Entanglement, Elasticity, and Viscous Relaxation of Actin Solutions. *Phys. Rev. Lett.* **81**, 2614–2617 (1998).
 29. Gardel, M. L.; Valentine, M. T.; Crocker, J. C.; Bausch, A. R. & Weitz, D. A. Microrheology of entangled F-actin solutions. *Phys. Rev. Lett.* **91**, 158302 (2003).
 30. Fritzsche, M.; Lewallea, A.; Duke, T.; Krusec, K. & Charras, G. Analysis of turnover dynamics of the submembranous actin cortex. *Mol. Biol. Cell*, 757–767 (2013).
 31. Marston, S. B. The rates of formation and dissociation of actin-myosin complexes. *Biochem. J.*, 453–460 (1982).
 32. Ferrer, J. M. *et al.* Measuring molecular rupture forces between single actin filaments and actin-binding proteins. *P. Natl. Acad. Sci. USA* **105**, 9221–9226 (2008).
 33. Fritzsche, M.; Thorogate, R. & Charras, G. Quantitative analysis of ezrin turnover dynamics in the actin cortex. *Biophys. J.* **106**, 343–353 (2014).
 34. Lieleg, O.; Claessens, M. M. A. E.; Luan, Y. & Bausch, A. R. Transient binding and dissipation in cross-linked actin networks. *Phys. Rev. Lett.* **101**, 108101 (2008).
 35. Lieleg, O.; Schmoller, K. M.; Claessens, M. M. A. E. & Bausch, A. R. Cytoskeletal polymer networks. Viscoelastic properties are determined by the microscopic interaction potential of cross-links. *Biophys. J.* **96**, 4725–4732 (2009).
 36. Broedersz, C. P. *et al.* Cross-link-governed dynamics of biopolymer networks. *Phys. Rev. Lett.* **105**, 238101 (2010).
 37. Wottawah, F. *et al.* Optical rheology of biological cells. *Phys. Rev. Lett.* **94**, 98103 (2005).
 38. Fabry, B. *et al.* Scaling the microrheology of living cells. *Phys. Rev. Lett.* **87**, 148102 (2001).
 39. Stossel, T. P. *et al.* Filamins as integrators of cell mechanics and signalling. *Nat. Rev. Mol. Cell Bio.*, 138–145 (2001).
 40. Aguilar-Cuenca, R.; Juanes-García, A. & Vicente-Manzanares, M. Myosin II in mechanotransduction. Master and commander of cell migration, morphogenesis, and cancer. *Cell. Mol. Life Sci.* **71**, 479–492 (2014).
 41. Luo, T. *et al.* Understanding the cooperative interaction between myosin II and actin cross-linkers mediated by actin filaments during mechanosensation. *Biophys. J.* **102**, 238–247 (2012).
 42. Luo, T.; Mohan, K.; Iglesias, P. A. & Robinson, D. N. Molecular mechanisms of cellular mechanosensing. *Nat. Mater.* **12**, 1064–1071 (2013).

43. Ehrlicher, A. J.; Nakamura, F.; Hartwig, J. H.; Weitz, D. A. & Stossel, T. P. Mechanical strain in actin networks regulates FilGAP and integrin binding to filamin A. *Nature* **478**, 260–263 (2011).
44. Schoen, I.; Pruitt, B. L. & Vogel, V. The Yin-Yang of Rigidity Sensing. How Forces and Mechanical Properties Regulate the Cellular Response to Materials. *Annu. Rev. Mater. Res.* **43**, 589–618 (2013).
45. Huveneers, S.; de Rooij, J. Mechanosensitive systems at the cadherin-F-actin interface. *J. Cell. Sci.* **126**, 403–413 (2013).
46. Moore, S. W.; Roca-Cusachs, P. & Sheetz, M. P. Stretchy proteins on stretchy substrates. The important elements of integrin-mediated rigidity sensing. *Dev. Cell.* **19**, 194–206 (2010).
47. Mitra, S. K.; Hanson, D. A. & Schlaepfer, D. D. Focal adhesion kinase. In command and control of cell motility. *Nat. Rev. Mol. Cell Bio.* **6**, 56–68 (2005).
48. Geiger, B.; Spatz, J. P. & Bershadsky, A. D. Environmental sensing through focal adhesions. *Nat. Rev. Mol. Cell Bio.* **10**, 21–33 (2009).
49. Choquet, D.; Felsenfeld, D. P. & Sheetz, M. P. Extracellular Matrix Rigidity Causes Strengthening of Integrin–Cytoskeleton Linkages. *Cell* **88**, 39–48 (1997).
50. Trappmann, B. *et al.* Extracellular-matrix tethering regulates stem-cell fate. *Nat. Mater.* **11**, 642–649 (2012).
51. Levental, I.; Georges, P. C. & Janmey, P. A. Soft biological materials and their impact on cell function. *Soft Matter* **3**, 299–306 (2007).
52. Engler, A. J.; Sen, S.; Sweeney, H. L. & Discher, D. E. Matrix elasticity directs stem cell lineage specification. *Cell* **126**, 677–689 (2006).
53. Trichet, L. *et al.* Evidence of a large-scale mechanosensing mechanism for cellular adaptation to substrate stiffness. *P. Natl. Acad. Sci. USA* **109**, 6933–6938 (2012).
54. Wang, N. *et al.* Mechanical behavior in living cells consistent with the tensegrity model. *P. Natl. Acad. Sci. USA* **98**, 7765–7770 (2001).
55. Discher, D. E.; Janmey, P. & Wang, Y.-L. Tissue cells feel and respond to the stiffness of their substrate. *Science* **310**, 1139–1143 (2005).
56. Ross, A. M.; Jiang, Z.; Bastmeyer, M. & Lahann, J. Physical Aspects of Cell Culture Substrates: Topography, Roughness, and Elasticity. *Small* **3**, 336–355 (2012).
57. Tee, S.-Y.; Fu, J.; Chen, C. S. & Janmey, P. A. Cell shape and substrate rigidity both regulate cell stiffness. *Biophys. J.* **100**, L25-7 (2011).

-
58. Hoess, A.; Thormann, A.; Friedmann, A. & Heilmann, A. Self-supporting nanoporous alumina membranes as substrates for hepatic cell cultures. *J. Biomed. Mater. Res. Part A*, 2230-2238 (2012).
 59. Paszek, M. J. *et al.* Tensional homeostasis and the malignant phenotype. *Cancer cell* **8**, 241–254 (2005).
 60. Pickup, M. W.; Mouw, J. K. & Weaver, V. M. The extracellular matrix modulates the hallmarks of cancer. *EMBO Rep.* **15**, 1243–1253 (2014).
 61. Tilghman, R. W. *et al.* Matrix rigidity regulates cancer cell growth and cellular phenotype. *PloS one* **5**, e12905 (2010).
 62. Jaalouk, D. E.; Lammerding, J. Mechanotransduction gone awry. *Nat. Rev. Mol. Cell Bio.* **10**, 63–73 (2009).
 63. Fritsch, A. *et al.* Are biomechanical changes necessary for tumour progression? *Nat. Phys.* **6**, 730–732 (2010).
 64. Ershov, D.; Stuart, M. C. & van der Gucht, J. Mechanical properties of reconstituted actin networks at an oil–water interface determined by microrheology. *Soft Matter* **8**, 5896–5903 (2012).
 65. Gardel, M. L. *et al.* Elastic behavior of cross-linked and bundled actin networks. *Science*, 1301–1305 (2004).
 66. Koenderink, G. H. *et al.* An active biopolymer network controlled by molecular motors. *P. Natl. Acad. Sci. USA* **106**, 15192–15197 (2009).
 67. Xu, J.; Palmer, A. & Wirtz, D. Rheology and microrheology of semiflexible polymer solutions: actin filament networks. *Macromolecules* **19**, 6486–6492 (1998).
 68. Rigato, A.; Miyagi, A.; Scheuring, S. & Rico, F. High-frequency microrheology reveals cytoskeleton dynamics in living cells. *Nat. Phys.* **87**, 148102 (2017).
 69. Laudadio, R. E. *et al.* Rat airway smooth muscle cell during actin modulation. Rheology and glassy dynamics. *Am. J. Physiol.-Cell Ph.* **289**, C1388-95 (2005).
 70. Cai, P. *et al.* Quantifying cell-to-cell variation in power-law rheology. *Biophys. J.* **105**, 1093–1102 (2013).
 71. Efremov, Y. M.; Wang, W.-H.; Hardy, S. D.; Geahlen, R. L. & Raman, A. Measuring nanoscale viscoelastic parameters of cells directly from AFM force-displacement curves. *Sci. Rep.* **7**, 1541 (2017).
 72. Hecht, F. M. *et al.* Imaging viscoelastic properties of live cells by AFM. Power-law rheology on the nanoscale. *Soft Matter* **11**, 4584–4591 (2015).
-

73. Deng, L. *et al.* Fast and slow dynamics of the cytoskeleton. *Nat. Mater.* **5**, 636–640 (2006).
74. Tharmann, R.; Claessens, M. M. A. E. & Bausch, A. R. Viscoelasticity of isotropically cross-linked actin networks. *Phys. Rev. Lett.* **98**, 88103 (2007).
75. Kollmannsberger, P.; Mierke, C. T. & Fabry, B. Nonlinear viscoelasticity of adherent cells is controlled by cytoskeletal tension. *Soft Matter* **7**, 3127–3132 (2011).
76. Alcaraz, J. *et al.* Microrheology of human lung epithelial cells measured by atomic force microscopy. *Biophys. J.* **84**, 2071–2079 (2003).
77. Chaudhuri, O.; Parekh, S. H. & Fletcher, D. A. Reversible stress softening of actin networks. *Nature* **445**, 295–298 (2007).
78. Tassieri, M.; Evans, R. M. L.; Warren, R. L.; Bailey, N. J. & Cooper, J. M. Microrheology with optical tweezers. Data analysis. *New J. Phys.* **14**, 115032 (2012).
79. de Gennes, P.-G. *Soft Matter. Nobel Lecture* (1991).
80. Chen, D. T.; Wen, Q.; Janmey, P. A.; Crocker, J. C. & Yodh, A. G. Rheology of Soft Materials. *Annu. Rev. Condens. Matter Phys.* **1**, 301–322 (2010).
81. Willenbacher, N. *et al.* Broad bandwidth optical and mechanical rheometry of wormlike micelle solutions. *Phys. Rev. Lett.* **99**, 68302 (2007).
82. Dreiss, C. A. Wormlike micelles. Where do we stand? Recent developments, linear rheology and scattering techniques. *Soft Matter* **3**, 956 (2007).
83. Raghavan, S. R.; Douglas, J. F. The conundrum of gel formation by molecular nanofibers, wormlike micelles, and filamentous proteins. Gelation without cross-links? *Soft Matter* **8**, 8539 (2012).
84. Cranford, S. W.; Tarakanova, A.; Pugno, N. M. & Buehler, M. J. Nonlinear material behaviour of spider silk yields robust webs. *Nature* **482**, 72–76 (2012).
85. Lai, S. K.; Wang, Y.-Y.; Cone, R.; Wirtz, D. & Hanes, J. Altering mucus rheology to "solidify" human mucus at the nanoscale. *PloS one* **4**, e4294 (2009).
86. Shayegan, M.; Forde, N. R. Microrheological characterization of collagen systems. From molecular solutions to fibrillar gels. *PloS one* **8**, e70590 (2013).
87. Zuidema, J. M.; Rivet, C. J.; Gilbert, R. J. & Morrison, F. A. A protocol for rheological characterization of hydrogels for tissue engineering strategies. *J. Biomed. Mater. Res. B* **102**, 1063–1073 (2014).
88. Harris, A. R. *et al.* Characterizing the mechanics of cultured cell monolayers. *P. Natl. Acad. Sci. USA* **109**, 16449–16454 (2012).

-
89. Backholm, M.; Schulman, R. D.; Ryu, W. S. & Dalnoki-Veress, K. Tangling of tethered swimmers. Interactions between two nematodes. *Phys. Rev. Lett.* **113**, 138101 (2014).
 90. Macosko, C. W. *Rheology: Principles, Measurements and Applications* (VCH Publishers, New York, 1994).
 91. Larson, R. G. *The Structure and Rheology of Complex Fluids* (Oxford University Press, New York, Oxford, 1999).
 92. Barnes, H.; Hutton, B. & Walters, K. *Introduction to Rheology* (Elsevier, Amsterdam, Lausanne, New York, Oxford, Shannon, Singapore, Tokio, 1989).
 93. Meschede, D. *Gerthsen Physik* (Springer, Berlin, Heidelberg, New York, Barcelona, Hongkong, London, Mailand, Paris, Tokio, 2002).
 94. Karam, H. J. Viscometers and their use. *Ind. Eng. Chem.* **55**, 38–43 (1963).
 95. Luan, Y.; Lieleg, O.; Wagner, B. & Bausch, A. R. Micro- and macrorheological properties of isotropically cross-linked actin networks. *Biophys. J.* **94**, 688–693 (2008).
 96. Buchanan, M.; Atakhorrami, M.; Palierne, J. F. & Schmidt, C. F. Comparing Macrorheology and One- and Two-Point Microrheology in Wormlike Micelle Solutions. *Macromolecules* **38**, 8840–8844 (2005).
 97. Apgar, J. *et al.* Multiple-Particle Tracking Measurements of Heterogeneities in Solutions of Actin Filaments and Actin Bundles. *Biophys. J.* **79**, 1095–1106 (2000).
 98. Fakhri, N. *et al.* High-resolution mapping of intracellular fluctuations using carbon nanotubes. *Science* **344**, 1031–1035 (2014).
 99. Käs, J. *et al.* F-actin, a model polymer for semiflexible chains in dilute, semidilute, and liquid crystalline solutions. *Biophys. J.* **70**, 609–625 (1996).
 100. Valentine, M. T. *et al.* Colloid surface chemistry critically affects multiple particle tracking measurements of biomaterials. *Biophys. J.* **86**, 4004–4014 (2004).
 101. Mason, T. G.; Weitz, D. A. Optical Measurements of Frequency-Dependent Linear Viscoelastic Moduli of Complex Fluids. *Phys. Rev. Lett.* **74**, 1250–1253 (1995).
 102. Squires, T. M.; Mason, T. G. Fluid Mechanics of Microrheology. *Annu. Rev. Fluid Mech.* **42**, 413–438 (2010).
 103. Dasgupta, B. R.; Tee, S.-Y.; Crocker, J. C.; Frisken, B. J. & Weitz, D. A. Microrheology of polyethylene oxide using diffusing wave spectroscopy and single scattering. *Phys. Rev. E* **65**, 51505 (2002).

104. Mason, T. G.; Ganesan, K.; van Zanten, J. H.; Wirtz, D. & Kuo, S. C. Particle Tracking Microrheology of Complex Fluids. *Phys. Rev. Lett.* **79**, 3282–3285 (1997).
105. Mason, T. G. Estimating the viscoelastic moduli of complex fluids using the generalized Stokes-Einstein equation. *Rheol. Acta* **39**, 371–378 (2000).
106. Wu, P.-H. *et al.* High-throughput ballistic injection nanorheology to measure cell mechanics. *Nat. Protoc.* **7**, 155–170 (2012).
107. Evans, R. M. L.; Tassieri, M.; Auhl, D. & Waigh, T. A. Direct conversion of rheological compliance measurements into storage and loss moduli. *Phys. Rev. E* **80**, 12501 (2009).
108. Broedersz, C. P.; MacKintosh, F. C. Modeling semiflexible polymer networks. *Rev. Mod. Phys.* **86**, 995–1036 (2014).
109. Pritchard, R. H.; Huang, Y. Y. S. & Terentjev, E. M. Mechanics of biological networks. From the cell cytoskeleton to connective tissue. *Soft Matter* **10**, 1864–1884 (2014).
110. Morse, D. C. Viscoelasticity of Concentrated Isotropic Solutions of Semiflexible Polymers. 1. Model and Stress Tensor. *Macromolecules* **31**, 7030–7043 (1998).
111. Morse, D. C. Viscoelasticity of Concentrated Isotropic Solutions of Semiflexible Polymers. 2. Linear Response. *Macromolecules* **31**, 7044–7067 (1998).
112. Plagge, J.; Fischer, A. & Heussinger, C. Viscoelasticity of reversibly crosslinked networks of semiflexible polymers. *Phys. Rev. E* **93**, 62502 (2016).
113. Gittes, F.; Mickey, B.; Nettleton, J. & Howard, J. Flexural Rigidity of Microtubules and Actin Filaments Measured from Thermal Fluctuations in Shape. *J. Cell Biol.* **4**, 923–934 (1993).
114. Ott, A.; Magnasco, M.; Simon, A. & Libchaber, A. Measurement of the persistence length of polymerized actin using fluorescence microscopy. *Phys. Rev. E* **48**, R1642-R1645 (1993).
115. Yanagida, T.; Nakase, M.; Nishiyama, K. & Oosawa, F. Direct observation of motion of single F-actin filaments in the presence of myosin. *Nature*, 58-60 (1984).
116. Berro, J.; Michelot, A.; Blanchoin, L.; Kovar, D. R. & Martiel, J.-L. Attachment conditions control actin filament buckling and the production of forces. *Biophys. J.* **92**, 2546–2558 (2007).
117. Palmer, A.; Mason, T. G.; Xu, J.; Kuo, S. C. & Wirtz, D. Diffusing Wave Spectroscopy Microrheology of Actin Filament Networks. *Biophys. J.* **76**, 1063–1071 (1999).
118. Suzuki, A.; Yamazaki, M. & Ito, T. Polymorphism of F-actin assembly. 1. A quantitative phase diagram of F-actin. *Biochemistry* **35**, 5238–5244 (1996).

-
119. Coppin, C. M.; Leavis, P. C. Quantitation of liquid-crystalline ordering in F-actin solutions. *Biophys. J.* **63**, 794–807 (1992).
120. Limozin, L.; Barmann, M. & Sackmann, E. On the organization of self-assembled actin networks in giant vesicles. *Eur. Phys. J. E* **10**, 319–330 (2003).
121. Isambert, H.; Maggs, A. C. Dynamics and Rheology of Actin Solutions. *Macromolecules* **29**, 1036–1040 (1996).
122. Gittes, F.; MacKintosh, F. C. Dynamic shear modulus of a semiflexible polymer network. *Phys. Rev. E* **58**, R1241-R1244 (1998).
123. Schnurr, B.; Gittes, F.; MacKintosh, F. C. & Schmidt, C. F. Determining Microscopic Viscoelasticity in Flexible and Semiflexible Polymer Networks from Thermal Fluctuations. *Macromolecules* **30**, 7781–7792 (1997).
124. Gittes, F.; Schnurr, B.; Olmsted, P. D.; MacKintosh, F. C. & Schmidt, C. F. Microscopic Viscoelasticity: Shear Moduli of Soft Materials Determined from Thermal Fluctuations. *Phys. Rev. Lett.* **17** (1997).
125. Schmidt, C. F.; Bärmann, M.; Isenberg, G. & Sackmann, E. Chain Dynamics, Mesh Size, and Diffusive Transport in Networks of Polymerized Actin. A Quasielastic Light Scattering and Microfluorescence Study. *Macromolecules*, 3638–3649 (1989).
126. Sackmann, E. *Modern Optics, Electronics, and High Precision Techniques in Cell Biology, chapter 11* (Springer, Berlin, Heidelberg, 1998).
127. Keller, M.; Tharmann, R.; Dichtl, M. A.; Bausch, A. R. & Sackmann, E. Slow filament dynamics and viscoelasticity in entangled and active actin networks. *Philos. T. Roy. A* **361**, 699–712 (2003).
128. Medalia, O. *et al.* Macromolecular Architecture in Eukaryotic Cells Visualized by Cryoelectron Tomography. *Science*, 1209-1213 (2002).
129. Tojkander, S.; Gateva, G. & Lappalainen, P. Actin stress fibers--assembly, dynamics and biological roles. *J. Cell. Sci.* **125**, 1855–1864 (2012).
130. Harris, A. R.; Daeden, A. & Charras, G. T. Formation of adherens junctions leads to the emergence of a tissue-level tension in epithelial monolayers. *J. Cell. Sci.* **127**, 2507–2517 (2014).
131. Clark, A. G.; Dierkes, K. & Paluch, E. K. Monitoring actin cortex thickness in live cells. *Biophys. J.* **105**, 570–580 (2013).
-

132. Clausen, M. P.; Colin-York, H.; Schneider, F.; Eggeling, C. & Fritzsche, M. Dissecting the actin cortex density and membrane-cortex distance in living cells by super-resolution microscopy. *J. Phys. D: Appl. Phys.* **50**, 64002 (2017).
133. Biro, M. *et al.* Cell cortex composition and homeostasis resolved by integrating proteomics and quantitative imaging. *Cytoskeleton* **70**, 741–754 (2013).
134. Lee, J. L.; Streuli, C. H. Integrins and epithelial cell polarity. *J. Cell. Sci.* **127**, 3217–3225 (2014).
135. Watanabe, T.; Hosoya, H. & Yonemura, S. Regulation of Myosin II Dynamics by Phosphorylation and Dephosphorylation of Its Light Chain in Epithelial Cells. *Mol. Biol. Cell* **18**, 605–616 (2007).
136. dos Remedios, C. G. *et al.* Actin binding proteins. Regulation of cytoskeletal microfilaments. *Physiol. Rev.* **83**, 433–473 (2003).
137. Grazi, E. What is the diameter of the actin filament? *FEBS Lett.* **405**, 249–252 (1997).
138. Holmes, K. C.; Popp, D.; Gebhard, W. & Kabsch, W. Atomic model of the actin filament. *Nature* **347**, 44–49 (1990).
139. Heuser, J. E. Procedure for freeze-drying molecules adsorbed to mica flakes. *J. Mol. Biol.* **169**, 155–195 (1983).
140. Winder, S. J.; Ayscough, K. R. Actin-binding proteins. *J. Cell. Sci.* **118**, 651–654 (2005).
141. Pollard, T. D.; Cooper, J. A. Actin, a Central Player in Cell Shape and Movement. *Science*, 1208-1212 (2009).
142. Janmey, P. A.; Stossel, T. P. Modulation of gelsolin function by phosphatidylinositol 4,5-bisphosphate. *Nature*, 362-364 (1987).
143. Sheetz, M. P. Cell control by membrane-cytoskeleton adhesion. *Nat. Rev. Mol. Cell Bio.* **2**, 392–396 (2001).
144. Yamada, K. M.; Pankov, R. & Cukierman, E. Dimensions and dynamics in integrin function. *Braz. J. Med. Biol. Res.* **36**, 959–966 (2003).
145. Roca-Cusachs, P.; Gauthier, N. C.; del Rio, A. & Sheetz, M. P. Clustering of $\alpha 5 \beta 1$ integrins determines adhesion strength whereas $\alpha v \beta 3$ and talin enable mechanotransduction. *P. Natl. Acad. Sci. USA*, 16245–16250 (2009).
146. Puklin-Faucher, E.; Sheetz, M. P. The mechanical integrin cycle. *J. Cell Sci.* **122**, 575 (2009).

-
147. Köster, D. V.; Mayor, S. Cortical actin and the plasma membrane. Inextricably intertwined. *Curr. Opin. Cell Biol.* **38**, 81–89 (2016).
148. Tsukita, S.; Yonemura, S. Cortical Actin Organization: Lessons from ERM (Ezrin/Radixin/Moesin) Proteins. *J. Biol. Chem.* **49**, 34507–34510 (1999).
149. Turunen, O.; Wahlström, T. & Vaheri, A. Ezrin Has a COOH-Terminal Actin-binding Site That Is Conserved in the Ezrin Protein Family. *J. Cell Biol.* **6**, 1445–1453 (1994).
150. Solinet, S. *et al.* The actin-binding ERM protein Moesin binds to and stabilizes microtubules at the cell cortex. *J. Cell Biol.* **202**, 251–260 (2013).
151. McClatchey, A. I. ERM proteins at a glance. *J. Cell Sci.* **127**, 3199–3204 (2014).
152. Saotome, I.; Curto, M. & McClatchey, A. I. Ezrin is essential for epithelial organization and villus morphogenesis in the developing intestine. *Dev. Cell.* **6**, 855–864 (2004).
153. Neisch, A. L.; Fehon, R. G. Ezrin, Radixin and Moesin. Key regulators of membrane-cortex interactions and signaling. *Curr. Opin. Cell Biol.* **23**, 377–382 (2011).
154. Charras, G. T.; Hu, C.-K.; Coughlin, M. & Mitchison, T. J. Reassembly of contractile actin cortex in cell blebs. *J. Cell Biol.* **175**, 477–490 (2006).
155. Ivetic, A.; Ridley, A. J. Ezrin/radixin/moesin proteins and Rho GTPase signalling in leucocytes. *Immunology* **112**, 165–176 (2004).
156. Phang, J. M. *et al.* Structural characterization suggests models for monomeric and dimeric forms of full-length ezrin. *Biochem. J.* **473**, 2763–2782 (2016).
157. van Meer, G.; Voelker, D. R. & Feigenson, G. W. Membrane lipids. Where they are and how they behave. *Nat. Rev. Mol. Cell Bio.* **9**, 112–124 (2008).
158. Zhang, L.; Mao, Y. S.; Janmey, P. A. & Yin, H. L. Phosphatidylinositol 4, 5 bisphosphate and the actin cytoskeleton. *Sub-Cell. Biochem.* **59**, 177–215 (2012).
159. Gary, R.; Bretscher, A. Ezrin self-association involves binding of an N-terminal domain to a normally masked C-terminal domain that includes the F-actin binding site. *Mol. Biol. Cell* **6**, 1061–1075 (1995).
160. Bretscher, A.; Reczek, D. & Berryman, M. Ezrin: a protein requiring conformational activation to link microfilaments to the plasma membrane in the assembly of cell surface structures. *J. Cell Sci.* **10**, 3011–3018 (1997).
161. Li, Q. *et al.* Self-masking in an intact ERM-merlin protein: an active role for the central α -helical domain. *J. Mol. Biol.* **365**, 1446–1459 (2007).

162. Roch, F. *et al.* Differential roles of PtdIns(4,5)P₂ and phosphorylation in moesin activation during *Drosophila* development. *J. Cell Sci.* **123**, 2058–2067 (2010).
163. Heiska, L. *et al.* Ezrin is key regulator of Src-induced malignant phenotype in three-dimensional environment. *Oncogene* **30**, 4953–4962 (2011).
164. Hunter, K. W. Ezrin, a key component in tumor metastasis. *Trends Mol. Med.* **10**, 201–204 (2004).
165. Hoskin, V. *et al.* Ezrin regulates focal adhesion and invadopodia dynamics by altering calpain activity to promote breast cancer cell invasion. *Mol. Biol. Cell* **26**, 3464–3479 (2015).
166. Li, J. *et al.* Prognostic Value of Ezrin in Various Cancers. A Systematic Review and Updated Meta-analysis. *Sci. Rep.* **5**, 17903 (2015).
167. Shin, H. K.; Ryu, B. J.; Choi, S.-W.; Kim, S. H. & Lee, K. Inactivation of Src-to-ezrin pathway. A possible mechanism in the ouabain-mediated inhibition of A549 cell migration. *BioMed Res. Int.* **2015**, 537136 (2015).
168. Pietuch, A.; Brückner, B. R.; Fine, T.; Mey, I. & Janshoff, A. Elastic properties of cells in the context of confluent cell monolayers. Impact of tension and surface area regulation. *Soft Matter* **9**, 11490 (2013).
169. Larson, S. M. *et al.* Cortical mechanics and meiosis II completion in mammalian oocytes are mediated by myosin-II and Ezrin-Radixin-Moesin (ERM) proteins. *Mol. Biol. Cell* **21**, 3182–3192 (2010).
170. Thomas, W. E.; Vogel, V. & Sokurenko, E. Biophysics of catch bonds. *Ann. Rev. Biophys.* **37**, 399–416 (2008).
171. Kholodenko, B. N. Cell-signalling dynamics in time and space. *Nat. Rev. Mol. Cell Bio.* **7**, 165–176 (2006).
172. Gowrishankar, K. *et al.* Active remodeling of cortical actin regulates spatiotemporal organization of cell surface molecules. *Cell* **149**, 1353–1367 (2012).
173. Bretscher, A.; Edwards, K. & Fehon, R. G. ERM proteins and merlin. Integrators at the cell cortex. *Nat. Rev. Mol. Cell Bio.* **3**, 586–599 (2002).
174. Vogel, S. K.; Schwille, P. Minimal systems to study membrane-cytoskeleton interactions. *Curr. Opin. Biotech.* **23**, 758–765 (2012).
175. Rivas, G.; Vogel, S. K. & Schwille, P. Reconstitution of cytoskeletal protein assemblies for large-scale membrane transformation. *Curr Opin. Chem. Biol.*, **22**: 18-26 (2014).
176. Strelnikova, N.; Herren, F.; Schoenenberger, C.-A. & Pfohl, T. Formation of Actin Networks in Microfluidic Concentration Gradients. *Front. Mater.* **3**, 2707 (2016).

-
177. Schnauß, J. *et al.* Motor-free force generation in biological systems. *diffusion-fundamentals.org* **23**, 1–15 (2015).
178. Huber, F.; Strehle, D.; Schnau, J. & Käs, J. Formation of regularly spaced networks as a general feature of actin bundle condensation by entropic forces. *New J. Phys.* **17**, 43029 (2015).
179. Xu, J. *et al.* Mechanical Properties of Actin Filament Networks Depend on Preparation, Polymerization Conditions, and Storage of Actin Monomers. *Biophys. J.* **74**, 2731–2740 (1998).
180. Lieleg, O.; Claessens, M. M. A. E. & Bausch, A. R. Structure and dynamics of cross-linked actin networks. *Soft Matter* **6**, 218–225 (2010).
181. Lee, H.; Ferrer, J. M.; Nakamura, F.; Lang, M. J. & Kamm, R. D. Passive and active microrheology for cross-linked F-actin networks in vitro. *Acta Biomater.* **6**, 1207–1218 (2010).
182. Wagner, B.; Tharmann, R.; Haase, I.; Fischer, M. & Bausch, A. R. Cytoskeletal polymer networks: The molecular structure of cross-linkers determines macroscopic properties. *P. Natl. Acad. Sci. USA* **38**, 13974–13978 (2005).
183. Frey, E.; Kroy, K. & Wilhelm, J. *Physics of Solutions and Networks of Semiflexible Macromolecules and the Control of Cell Function* (arXiv:9808022v1 [cond-mat.soft]).
184. Head, D. A.; Levine, A. J. & MacKintosh, F. C. Distinct regimes of elastic response and deformation modes of cross-linked cytoskeletal and semiflexible polymer networks. *Phys. Rev. E* **68**, 61907 (2003).
185. Lieleg, O.; Claessens, M. M. A. E.; Heussinger, C.; Frey, E. & Bausch, A. R. Mechanics of bundled semiflexible polymer networks. *Phys. Rev. Lett.* **99**, 88102 (2007).
186. Žagar, G.; Onck, P. R. & van der Giessen, E. Two fundamental mechanisms govern the stiffening of cross-linked networks. *Biophys. J.* **108**, 1470–1479 (2015).
187. Gurmessa, B.; Fitzpatrick, R.; Falzone, T. T. & Robertson-Anderson, R. M. Entanglement Density Tunes Microscale Nonlinear Response of Entangled Actin. *Macromolecules* **49**, 3948–3955 (2016).
188. Lee, H.; Ferrer, J. M.; Lang, M. J. & Kamm, R. D. Molecular origin of strain softening in cross-linked F-actin networks. *Phys. Rev. E* **82**, 11919 (2010).
189. Veigel, C.; Molloy, J. E.; Schmitz, S. & Kendrick-Jones, J. Load-dependent kinetics of force production by smooth muscle myosin measured with optical tweezers. *Nat. Cell Biol.* **5**, 980–986 (2003).
-

190. Maier, M. *et al.* A single charge in the actin binding domain of fascin can independently tune the linear and non-linear response of an actin bundle network. *Eur. Phys. J. E* **38**, 136 (2015).
191. Müller, K. W. *et al.* Rheology of semiflexible bundle networks with transient linkers. *Phys. Rev. Lett.* **112**, 238102 (2014).
192. Sijbesma, R. P. *et al.* Reversible Polymers Formed from Self-Complementary Monomers Using Quadruple Hydrogen Bonding. *Science* **28**, 1601-1604 (1997).
193. Narita, T.; Mayumi, K.; Ducouret, G. & Hébraud, P. Viscoelastic Properties of Poly(vinyl alcohol) Hydrogels Having Permanent and Transient Cross-Links Studied by Microrheology, Classical Rheometry, and Dynamic Light Scattering. *Macromolecules* **46**, 4174–4183 (2013).
194. Stam, S.; Alberts, J.; Gardel, M. L. & Munro, E. Isoforms Confer Characteristic Force Generation and Mechanosensation by Myosin II Filaments. *Biophys. J.* **108**, 1997–2006 (2015).
195. Kovács, M.; Wang, F.; Hu, A.; Zhang, Y. & Sellers, J. R. Functional divergence of human cytoplasmic myosin II. Kinetic characterization of the non-muscle IIA isoform. *J. Biol. Chem.* **278**, 38132–38140 (2003).
196. Wang, F. *et al.* Kinetic mechanism of non-muscle myosin IIB. Functional adaptations for tension generation and maintenance. *J. Biol. Chem.* **278**, 27439–27448 (2003).
197. Miyata, H.; Yasuda, R. & Kinosita, K. Strength and lifetime of the bond between actin and skeletal muscle α -actinin studied with an optical trapping technique. *Biochim. Biophys. Acta*, 83–88 (1996).
198. Goldmann, W. H.; Isenberg, G. Analysis of filamin and α -actinin binding to actin by the stopped flow method. *FEBS Lett.* **336**, 408–410 (1993).
199. Spiros, A.; Edelstein-Keshet, L. Testing a model for the dynamics of actin structures with biological parameter values. *B. Math. Biol.* **60**, 275–305 (1998).
200. Ward, S. M. V.; Weins, A.; Pollak, M. R. & Weitz, D. A. Dynamic viscoelasticity of actin cross-linked with wild-type and disease-causing mutant alpha-actinin-4. *Biophys. J.* **95**, 4915–4923 (2008).
201. Kuhlman, P. A.; Ellis, J.; Critchley, D. R. & Bagshaw, C. R. The kinetics of the interaction between the actin-binding domain of α -actinin and F-actin. *FEBS Lett.* **339**, 297–301 (1994).
202. Aratyn, Y. S.; Schaus, T. E.; Taylor, E. W. & Borisy, G. G. Intrinsic dynamic behavior of fascin in filopodia. *Mol. Biol. Cell* **18**, 3928–3940 (2007).

-
203. O'Connell, C. B.; Tyska, M. J. & Mooseker, M. S. Myosin at work: Motor adaptations for a variety of cellular functions. *Biochim. Biophys. Acta* **1773**, 615–630 (2007).
204. Finer, J. T.; Simmons, R. M. & Spudich, J. A. Single myosin molecule mechanics: piconewton forces and nanometre steps. *Nature*, 113–119 (1994).
205. Mizuno, D.; Head, D. A.; MacKintosh, F. C. & Schmidt, C. F. Active and Passive Microrheology in Equilibrium and Nonequilibrium Systems. *Macromolecules* **41**, 7194–7202 (2008).
206. Humphrey, D.; Duggan, C.; Saha, D.; Smith, D. & Käs, J. Active fluidization of polymer networks through molecular motors. *Nature* **416**, 413–416 (2002).
207. Yao, N. Y. *et al.* Nonlinear Viscoelasticity of Actin Transiently Cross-linked with Mutant α -Actinin-4. *J. Mol. Biol.* **411**, 1062–1071 (2011).
208. Gardel, M. L. *et al.* Stress-dependent elasticity of composite actin networks as a model for cell behavior. *Phys. Rev. Lett.* **96**, 88102 (2006).
209. Gardel, M. L. *et al.* Prestressed F-actin networks cross-linked by hinged filamins replicate mechanical properties of cells. *P. Natl. Acad. Sci. USA* **103**, 1762–1767 (2006).
210. Schmoller, K. M.; Lieleg, O. & Bausch, A. R. Structural and viscoelastic properties of actin/filamin networks. Cross-linked versus bundled networks. *Biophys. J.* **97**, 83–89 (2009).
211. Broedersz, C. P. *et al.* Measurement of nonlinear rheology of cross-linked biopolymer gels. *Soft Matter* **6**, 4120 (2010).
212. Vogel, S. K.; Heinemann, F.; Chwastek, G. & Schwille, P. The design of MACs (minimal actin cortices). *Cytoskeleton* **70**, 706–717 (2013).
213. Tanaka, M.; Sackmann, E. Polymer-supported membranes as models of the cell surface. *Nature* **437**, 656–663 (2005).
214. Barfoot, R. J. *et al.* Minimal F-actin cytoskeletal system for planar supported phospholipid bilayers. *Langmuir* **24**, 6827–6836 (2008).
215. Johnson, B. R. G.; Bushby, R. J.; Colyer, J. & Evans, S. D. Self-assembly of actin scaffolds at ponticulins-containing supported phospholipid bilayers. *Biophys. J.* **90**, L21–3 (2006).
216. Merkle, D.; Kahya, N. & Schwille, P. Reconstitution and anchoring of cytoskeleton inside giant unilamellar vesicles. *ChemBioChem* **9**, 2673–2681 (2008).
217. Murrell, M. P.; Gardel, M. L. F-actin buckling coordinates contractility and severing in a biomimetic actomyosin cortex. *P. Natl. Acad. Sci. USA* **109**, 20820–20825 (2012).
-

218. Köster, D. V. *et al.* Actomyosin dynamics drive local membrane component organization in an in vitro active composite layer. *P. Natl. Acad. Sci. USA* **113**, E1645-54 (2016).
219. Heinemann, F.; Vogel, S. K. & Schwille, P. Lateral membrane diffusion modulated by a minimal actin cortex. *Biophys. J.* **104**, 1465–1475 (2013).
220. Vogel, S. K.; Petrasek, Z.; Heinemann, F. & Schwille, P. Myosin motors fragment and compact membrane-bound actin filaments. *eLife*, 1–18 (2013).
221. Linsmeier, I. *et al.* Disordered actomyosin networks are sufficient to produce cooperative and telescopic contractility. *Nat. Commun.* **7**, 12615 (2016).
222. Murrell, M.; Gardel, M. L. Actomyosin sliding is attenuated in contractile biomimetic cortices. *Mol. Biol. Cell* **25**, 1845–1853 (2014).
223. Bosk, S.; Braunger, J. A.; Gerke, V. & Steinem, C. Activation of F-actin binding capacity of ezrin. Synergism of PIP₂ interaction and phosphorylation. *Biophys. J.* **100**, 1708–1717 (2011).
224. Kramer, C. Dissertation. Georg-August-Universität Göttingen, 2016.
225. Honigmann, A. *et al.* A lipid bound actin meshwork organizes liquid phase separation in model membranes. *eLife*, 1–16 (2014).
226. Reymann, A.-C. *et al.* Actin Network Architecture Can Determine Myosin Motor Activity. *Science* **336**, 1310–1314 (2012).
227. Schuppler, M.; Keber, F. C.; Kroger, M. & Bausch, A. R. Boundaries steer the contraction of active gels. *Nat. Commun.* **7**, 13120 (2016).
228. Noireaux, V. *et al.* Growing an Actin Gel on Spherical Surfaces. *Biophys. J.* **78**, 1643–1654 (2000).
229. Bussonnier, M. *et al.* Mechanical detection of a long-range actin network emanating from a biomimetic cortex. *Biophys. J.* **107**, 854–862 (2014).
230. Shah, E. A.; Keren, K. Symmetry breaking in reconstituted actin cortices. *eLife*, 1–15 (2014).
231. Häckl, W.; Bärmann, M. & Sackmann, E. Shape Changes of Self-Assembled Actin Bilayer Composite Membranes. *Phys. Rev. Lett.* **80**, 1786–1789 (1998).
232. Caorsi, V. *et al.* Cell-sized liposome doublets reveal active tension build-up driven by acto-myosin dynamics. *Soft Matter* **12**, 6223–6231 (2016).
233. Guevorkian, K.; Manzi, J.; Pontani, L.-L.; Brochard-Wyart, F. & Sykes, C. Mechanics of Biomimetic Liposomes Encapsulating an Actin Shell. *Biophys. J.* **109**, 2471–2479 (2015).

-
234. Keber, F. C. *et al.* Topology and dynamics of active nematic vesicles. *Science* **345**, 1135–1139 (2014).
235. Tsai, F.-C.; Koenderink, G. H. Shape control of lipid bilayer membranes by confined actin bundles. *Soft Matter* **11**, 8834–8847 (2015).
236. Loiseau, E. *et al.* Shape remodeling and blebbing of active cytoskeletal vesicles. *Sci. Adv.* **2**, e1500465 (2016).
237. Tan, T. H. *et al.* Self-organization of stress patterns drives state transitions in actin cortices (arXiv:1603.07600 [physics.bio-ph]).
238. Sawada, Y.; Sheetz, M. P. Force transduction by Triton cytoskeletons. *J. Cell Biol.* **156**, 609–615 (2002).
239. Nehls, S.; Janshoff, A. Elastic Properties of Pore-Spanning Apical Cell Membranes Derived from MDCK II Cells. *Biophys. J.* **113**, 1822–1830 (2017).
240. Lim, C. T.; Zhou, E. H. & Quek, S. T. Mechanical models for living cells--a review. *J. Biomech.* **39**, 195–216 (2006).
241. Kollmannsberger, P.; Fabry, B. Linear and Nonlinear Rheology of Living Cells. *Annu. Rev. Mater. Res.* **41**, 75–97 (2011).
242. Moeendarbary, E. *et al.* The cytoplasm of living cells behaves as a poroelastic material. *Nat. Mater.* **12**, 253–261 (2013).
243. Massiera, G.; van Citters, K. M.; Biancaniello, P. L. & Crocker, J. C. Mechanics of single cells. Rheology, time dependence, and fluctuations. *Biophys. J.* **93**, 3703–3713 (2007).
244. Rother, J.; Nöding, H.; Mey, I. & Janshoff, A. Atomic force microscopy-based microrheology reveals significant differences in the viscoelastic response between malign and benign cell lines. *Open Biol.* **4**, 140046 (2014).
245. Brückner, B. R.; Nöding, H. & Janshoff, A. Viscoelastic Properties of Confluent MDCK II Cells Obtained from Force Cycle Experiments. *Biophys. J.* **112**, 724–735 (2017).
246. Sollich, P.; Lequeux, F.; Hébraud, P. & Cates, M. E. Rheology of Soft Glassy Materials. *Phys. Rev. Lett.*, 2020–2023 (1997).
247. Mandadapu, K. K.; Govindjee, S. & Mofrad, M. R. K. On the cytoskeleton and soft glassy rheology. *J. Biomech.* **41**, 1467–1478 (2008).
248. Müller, K. W.; Cyron, C. J. & Wall, W. A. Computational analysis of morphologies and phase transitions of cross-linked, semi-flexible polymer networks. *Proc. R. Soc. A* **471**, 20150332 (2015).
-

249. Koltzsch, M.; Neumann, C.; König, S. & Gerke, V. Ca²⁺-dependent binding and activation of dormant ezrin by dimeric S100P. *Mol. Biol. Cell* **14**, 2372–2384 (2003).
250. Xu, T. *et al.* SOAX. A software for quantification of 3D biopolymer networks. *Sci. Rep.* **5**, 9081 (2015).
251. Xu, T.; Vavylonis, D. & Huang, X. 3D actin network centerline extraction with multiple active contours. *Med. Image Anal.* **18**, 272–284 (2014).
252. Molteni, M.; Magatti, D.; Cardinali, B.; Rocco, M. & Ferri, F. Fast two-dimensional bubble analysis of biopolymer filamentous networks pore size from confocal microscopy thin data stacks. *Biophys. J.* **104**, 1160–1169 (2013).
253. Münster, S.; Fabry, B. A simplified implementation of the bubble analysis of biopolymer network pores. *Biophys. J.* **104**, 2774–2775 (2013).
254. Nečas, D.; Klapetek, P. Gwyddion. An open-source software for SPM data analysis. *Open Phys.* **10** (2012).
255. Kilfoil, M. a. o. *2D feature finding and tracking algorithms & microrheology algorithms available at <http://people.umass.edu/kilfoil/tools.ph>*. MATLAB code (1999).
256. Tassieri, M. *et al.* Measuring storage and loss moduli using optical tweezers. Broadband microrheology. *Phys. Rev. E* **81**, 26308 (2010).
257. Preece, D. *et al.* Optical tweezers. Wideband microrheology. *J. Opt.* **13**, 44022 (2011).
258. Pommella, A. *et al.* Using optical tweezers for the characterization of polyelectrolyte solutions with very low viscoelasticity. *Langmuir* **29**, 9224–9230 (2013).
259. Tassieri, M. *et al.* Microrheology with optical tweezers. Measuring the relative viscosity of solutions 'at a glance'. *Sci. Rep.* **5**, 8831 (2015).
260. Sheetz, M. P. *Laser Tweezers in Cell Biology* (Academic Press, San Diego, 1998).
261. Tassieri, M. *MOT*. available at <https://sites.google.com/site/manliotassieri/labview-codes>. LabVIEW executable (Glasgow, 2015).
262. Mason, T. G.; Weitz, D. A. Optical measurements of frequency-dependent linear viscoelastic moduli of complex fluids. *Phys. Rev. Lett.* **74**, 1250–1253 (1995).
263. Pelham, R. J.; Wang, Y.-L. Cell locomotion and focal adhesions are regulated by substrate flexibility. *P. Natl. Acad. Sci. USA*, 13661–13665 (1997).
264. Jiao, Y.; Schaffer, T. E. Accurate height and volume measurements on soft samples with the atomic force microscope. *Langmuir* **20**, 10038–10045 (2004).

-
265. Hutter, J. L.; Bechhoefer, J. Calibration of atomic-force microscope tips. *Rev. Sci. Instrum.* **64**, 1868–1873 (1993).
266. Bilodeau, G. G. Regular Pyramid Punch Problem. *J. Appl. Mech.*, 519-523 (1992).
267. Hertz, H. Über die Berührung fester elastischer Körper. *J. Reine Angew. Math.* **1881**, 156–171.
268. Fine, T. Dissertation. Johannes Gutenberg-Universität Mainz, 2009.
269. Giaever, I.; Keese, C. R. A morphological biosensor for mammalian cells. *Nature* **366**, 591-592 (1993).
270. Wegener, J.; Keese, C. R. & Giaever, I. Electric cell-substrate impedance sensing (ECIS) as a noninvasive means to monitor the kinetics of cell spreading to artificial surfaces. *Exp. Cell Res.* **259**, 158–166 (2000).
271. Benson, K.; Cramer, S. & Galla, H.-J. Impedance-based cell monitoring: barrier properties and beyond. *Fluids Barriers CNS* **1**, 1 (2013).
272. Giaever, I.; Keese, C. R. Micromotion of mammalian cells measured electrically. *P. Natl. Acad. Sci. USA* **88**, 7896–7900 (1991).
273. Brückner, B. R.; Pietuch, A.; Nehls, S.; Rother, J. & Janshoff, A. Ezrin is a Major Regulator of Membrane Tension in Epithelial Cells. *Sci. Rep.* **5**, 14700 (2015).
274. Lo, C.-M.; Ferrier, J. Impedance analysis of fibroblastic cell layers measured by electric cell-substrate impedance sensing. *Phys. Rev. E* **57**, 6982–6987 (1998).
275. Shroff, S. G.; Saner, D. R. & Lal, R. Dynamic micromechanical properties of cultured rat atrial myocytes measured by atomic force microscopy. *Am. J. Physiol.-Cell Ph.* **269**, C286-C292 (1995).
276. Briscoe, B. J.; Sebastian, K. S. & Adams, M. J. The effect of indenter geometry on the elastic response to indentation. *J. Phys. D Appl. Phys.* **27**, 1156–1162 (1994).
277. Mahaffy, R. E.; Shih, C. K.; MacKintosh, F. C. & Käs, J. Scanning Probe-Based Frequency-Dependent Microrheology of Polymer Gels and Biological Cells. *Phys. Rev. Lett.* **85**, 880–883 (2000).
278. Alcaraz, J. *et al.* Correction of Microrheological Measurements of Soft Samples with Atomic Force Microscopy for the Hydrodynamic Drag on the Cantilever. *Langmuir* **18**, 716–721 (2002).
279. Butt, H.-J.; Cappella, B. & Kappl, M. Force measurements with the atomic force microscope: Technique, interpretation and applications. *Surf. Sci. Rep.* **59**, 1–152 (2005).
-

280. Rother, J. *et al.* Cytoskeleton remodelling of confluent epithelial cells cultured on porous substrates. *J. R. Soc. Interface* **12**, 20141057 (2015).
281. Sen, S.; Subramanian, S. & Discher, D. E. Indentation and Adhesive Probing of a Cell Membrane with AFM: Theoretical Model and Experiments. *Biophys. J.* **89**, 3203–3213 (2005).
282. Dai, J.; Sheetz, M. P. Membrane Tether Formation from Blebbing Cells. *Biophys. J.* **77**, 3363–3370 (1999).
283. de Gennes, P.-G. *Le Monde* (October, 23th 1991).
284. Pesen, D.; Hoh, J. H. Micromechanical architecture of the endothelial cell cortex. *Biophys. J.* **88**, 670–679 (2005).
285. Watanabe-Nakayama, T. *et al.* Direct detection of cellular adaptation to local cyclic stretching at the single cell level by atomic force microscopy. *Biophys. J.* **100**, 564–572 (2011).
286. Salbreux, G.; Charras, G. & Paluch, E. Actin cortex mechanics and cellular morphogenesis. *Trends Cell Biol.* **22**, 536–545 (2012).
287. Sens, P.; Plastino, J. Membrane tension and cytoskeleton organization in cell motility. *J. Phys.: Condens. Matter* **27**, 273103 (2015).
288. Murrell, M.; Oakes, P. W.; Lenz, M. & Gardel, M. L. Forcing cells into shape. The mechanics of actomyosin contractility. *Nat. Rev. Mol. Cell Bio.* **16**, 486–498 (2015).
289. Zhao, S.; Reichert, W. M. Influence of biotin lipid surface density and accessibility on avidin binding to the tip of an optical fiber sensor. *Langmuir* **8**, 2785–2791 (1992).
290. Shabardina, V. *et al.* Mode of Ezrin-Membrane Interaction as a Function of PIP2 Binding and Pseudophosphorylation. *Biophys. J.* **110**, 2710–2719 (2016).
291. McLaughlin, S.; Murray, D. Plasma membrane phosphoinositide organization by protein electrostatics. *Nature* **438**, 605–611 (2005).
292. Pearson, M. A.; Reczek, D.; Bretscher, A. & Karplus, P. Structure of the ERM Protein Moesin Reveals the FERM Domain Fold Masked by an Extended Actin Binding Tail Domain. *Cell* **101**, 259–270 (2000).
293. Parameswaran, N.; Matsui, K. & Gupta, N. Conformational switching in ezrin regulates morphological and cytoskeletal changes required for B cell chemotaxis. *J. Immunol.* **186**, 4088–4097 (2011).
294. Wayment, J. R.; Harris, J. M. Biotin-avidin binding kinetics measured by single-molecule imaging. *Anal. Chem.* **81**, 336–342 (2009).

-
295. Marttila, A. T. *et al.* Recombinant NeutraLite Avidin: a non-glycosylated, acidic mutant of chicken avidin that exhibits high affinity for biotin and low non-specific binding properties. *FEBS Lett.* **467**, 31–36 (2000).
296. Clasen, C.; Kavehpour, H. P. & McKinley, G. H. Bridging Tribology and Microrheology of Thin Films. *Appl. Rheol.* **20** (2010).
297. Schäfer, J. Master Thesis. Georg-August Universität, 2015.
298. Cole, R. W.; Jinadasa, T. & Brown, C. M. Measuring and interpreting point spread functions to determine confocal microscope resolution and ensure quality control. *Nat. Protoc.* **6**, 1929–1941 (2011).
299. Schmidt, C. F.; Baermann, M.; Isenberg, G. & Sackmann, E. Chain dynamics, mesh size, and diffusive transport in networks of polymerized actin. A quasielastic light scattering and microfluorescence study. *Macromolecules* **22**, 3638–3649 (1989).
300. Shin, J. H.; Gardel, M. L.; Mahadevan, L.; Matsudaira, P. & Weitz, D. A. Relating microstructure to rheology of a bundled and cross-linked F-actin network in vitro. *P. Natl. Acad. Sci. USA* **101**, 9636–9641 (2004).
301. Sackmann, E. in *Modern Optics, Electronics and High Precision Techniques in Cell Biology*, edited by G. Isenberg (Springer Berlin Heidelberg, Berlin, Heidelberg, 1998), pp. 211–257.
302. Lide, D. R. *CRC Handbook of Chemistry and Physics*. 2005th ed. (CRC Press, Boca Raton, 2005).
303. Glycerine Producers' Association (ed.). *Physical Properties of Glycerine and its Solutions* (New York, 1963).
304. Amblard, F.; Maggs, A. C.; Yurke, B.; Pargellis, A. N. & Leibler, S. Subdiffusion and Anomalous Local Viscoelasticity in Actin Networks. *Phys. Rev. Lett.* **77**, 4470–4473 (1996).
305. Hildebrandt, J. Comparison of mathematical models for cat lung and viscoelastic balloon derived by Laplace transform methods from pressure-volume data. *B. Math. Biophys.* **31**, 651–667 (1969).
306. Golde, T. *et al.* Fluorescent beads disintegrate actin networks. *Phys. Rev. E* **88** (2013).
307. Janmey, P. A. *et al.* Viscoelasticity of F-actin and F-actin/gelsolin complexes. *Biochemistry* **27**, 8218–8227 (1988).
308. Walder, R.; Levine, A. J. & Dennin, M. Rheology of two-dimensional F-actin networks associated with a lipid interface. *Phys. Rev. E* **77**, 11909 (2008).
-

309. Jung, L. S.; Nelson, K. E.; Stayton, P. S. & Campbell, C. T. Binding and Dissociation Kinetics of Wild-Type and Mutant Streptavidins on Mixed Biotin-Containing Alkylthiolate Monolayers. *Langmuir* **16**, 9421–9432 (2000).
310. Friddle, R. W.; Noy, A. & Yoreo, J. J. de. Interpreting the widespread nonlinear force spectra of intermolecular bonds. *P. Natl. Acad. Sci. USA* **109**, 13573–13578 (2012).
311. Guo, S.; Ray, C.; Kirkpatrick, A.; Lad, N. & Akhremitchev, B. B. Effects of multiple-bond ruptures on kinetic parameters extracted from force spectroscopy measurements. Revisiting biotin-streptavidin interactions. *Biophys. J.* **95**, 3964–3976 (2008).
312. Lee, C.-K.; Wang, Y.-M.; Huang, L.-S. & Lin, S. Atomic force microscopy. Determination of unbinding force, off rate and energy barrier for protein-ligand interaction. *Micron* **38**, 446–461 (2007).
313. Athappilly, F. K.; Hendrickson, W. A. Crystallographic analysis of the pH-dependent binding of iminobiotin by streptavidin. *Protein Sci.* **6**, 1338–1342 (1997).
314. Gyorgy, P.; Rose, C. S. The Liberation of Biotin from the Avidin-Biotin Complex (AB). *Exp. Biol. M.* **53**, 55–57 (2016).
315. Subramanian, N.; Subramanian, S.; Karande, A. A. & Adiga, P. R. A monoclonal antibody to avidin dissociates quaternary structure and curtails biotin binding to avidin and streptavidin. *Arch. Biochem. Biophys.* **344**, 281–288 (1997).
316. Morris, P. D.; Raney, K. D. DNA helicases displace streptavidin from biotin-labeled oligonucleotides. *Biochemistry* **38**, 5164–5171 (1999).
317. Merkel, R.; Nassoy, P.; Leung, A.; Ritchie, K. & Evans, E. Energy landscapes of receptor-ligand bonds explored with dynamic force spectroscopy. *Nature* **397**, 50–53 (1999).
318. Hane, F. T.; Attwood, S. J. & Leonenko, Z. Comparison of three competing dynamic force spectroscopy models to study binding forces of amyloid-beta (1-42). *Soft Matter* **10**, 1924–1930 (2014).
319. Kaur, P. *et al.* Antibody-unfolding and metastable-state binding in force spectroscopy and recognition imaging. *Biophys. J.* **100**, 243–250 (2011).
320. Cossio, P.; Hummer, G. & Szabo, A. On artifacts in single-molecule force spectroscopy. *P. Natl. Acad. Sci. USA* **112**, 14248–14253 (2015).
321. Obermayer, B.; Frey, E. Tension dynamics and viscoelasticity of extensible wormlike chains. *Phys. Rev. E* **80**, 40801 (2009).
322. Everaers, R.; Jülicher, F.; Ajdari, A. & Maggs, A. C. Dynamic Fluctuations of Semiflexible Filaments. *Phys. Rev. Lett.* **82**, 3717–3720 (1999).

-
323. Oddershede, L.; Grego, S.; Nørrelykke, S. F. & Berg-Sørensen, K. Optical Tweezer: Probing Biological Surfaces. *Probe Microscopy* **2**, 129–137 (2001).
324. Stout, A. L.; Webb, W. W. in *Laser Tweezers in Cell Biology*, edited by L. Wilson, P. T. Matsudaira & M. P. Sheetz (Elsevier 1998), pp. 99–116.
325. Yang, W. Y.; Gruebele, M. Folding at the speed limit. *Nature* **423**, 193–197 (2003).
326. Weiss, P. A. *The molecular control of cellular activity. chapter 2: From Cell to Molecule* (McGraw-Hill Co., New York, 1961).
327. Wozniak, M. A.; Chen, C. S. Mechanotransduction in development: a growing role for contractility. *Nat. Rev. Mol. Cell Bio.* **10**, 34–43 (2009).
328. Ingber, D. E. Cellular mechanotransduction. Putting all the pieces together again. *FASEB J.* **20**, 811–827 (2006).
329. Wang, N.; Tytell, J. D. & Ingber, D. E. Mechanotransduction at a distance: mechanically coupling the extracellular matrix with the nucleus. *Nat. Rev. Mol. Cell Bio.* **10**, 75–82 (2009).
330. Provenzano, P. P.; Keely, P. J. Mechanical signaling through the cytoskeleton regulates cell proliferation by coordinated focal adhesion and Rho GTPase signaling. *J. Cell Sci.* **124**, 1195–1205 (2011).
331. Frey, M. T.; Tsai, I. Y.; Russell, T. P.; Hanks, S. K. & Wang, Y.-L. Cellular Responses to Substrate Topography: Role of Myosin II and Focal Adhesion Kinase. *Biophys. J.* **90**, 3774–3782 (2006).
332. Chung, S. H.; Son, S. J. & Min, J. The nanostructure effect on the adhesion and growth rates of epithelial cells with well-defined nanoporous alumina substrates. *Nanotechnology* **21**, 1–7 (2010).
333. Karuri, N. W. *et al.* Biological length scale topography enhances cell- substratum adhesion of human corneal epithelial cells. *J. Cell Sci.* **15**, 3153-3164 (2004).
334. Huang, S.; Ingber, D. E. The structural and mechanical complexity of cell-growth control. *Nat. Cell Biol.* **1**, E131 - E138 (1999).
335. Albuschies, J.; Vogel, V. The role of filopodia in the recognition of nanotopographies. *Sci. Rep.* **3**, 1658 (2013).
336. Vogel, V.; Sheetz, M. Local force and geometry sensing regulate cell functions. *Nat. Rev. Mol. Cell Bio.* **7**, 265–275 (2006).
337. Liu, A. P.; Chaudhuri, O. & Parekh, S. H. New advances in probing cell-extracellular matrix interactions. *Integr. Biol.* **9**, 383–405 (2017).
-

338. Kumar, S. *et al.* Viscoelastic retraction of single living stress fibers and its impact on cell shape, cytoskeletal organization, and extracellular matrix mechanics. *Biophys. J.* **90**, 3762–3773 (2006).
339. Levental, K. R. *et al.* Matrix crosslinking forces tumor progression by enhancing integrin signaling. *Cell* **139**, 891–906 (2009).
340. Ng, M. R.; Brugge, J. S. A stiff blow from the stroma. Collagen crosslinking drives tumor progression. *Cancer cell* **16**, 455–457 (2009).
341. Ladoux, B.; Nicolas, A. Physically based principles of cell adhesion mechanosensitivity in tissues. *Rep. Prog. Phys.* **75**, 116601 (2012).
342. Harburger, D. S.; Calderwood, D. A. Integrin signalling at a glance. *J. Cell Sci.* **122**, 1472 (2009).
343. del Rio, A. *et al.* Stretching Single Talin Rod Molecules Activates Vinculin Binding. *Science* **323**, 638-641 (2009).
344. Huang, S.; Ingber, D. E. Cell tension, matrix mechanics, and cancer development. *Cancer cell* **8**, 175–176 (2005).
345. Alibert, C.; Goud, B. & Manneville, J.-B. Are cancer cells really softer than normal cells? *Biol. Cell* **109**, 167–189 (2017).
346. Sahai, E. Illuminating the metastatic process. *Nat. Rev. Cancer* **7**, 737–749 (2007).
347. Chen, Y.-C. *et al.* Single-cell Migration Chip for Chemotaxis-based Microfluidic Selection of Heterogeneous Cell Populations. *Sci. Rep.* **5**, 9980 (2015).
348. Wilson, K. *et al.* Mechanisms of leading edge protrusion in interstitial migration. *Nat. Commun.* **4**, 2896 (2013).
349. Wang, Y. *et al.* Quantitative analysis of the cell-surface roughness and viscoelasticity for breast cancer cells discrimination using atomic force microscopy. *Scanning* **38**, 558–563 (2016).
350. Agus, D. B. *et al.* A physical sciences network characterization of non-tumorigenic and metastatic cells. *Sci. Rep.* **3**, 1449 (2013).
351. Burdall, S. E.; Hanby, A. M.; Lansdown, M. R. J. & Speirs, V. Breast cancer cell lines. Friend or foe? *Breast Cancer Res.* **5**, 111 (2003).
352. Debnath, J.; Muthuswamy, S. K. & Brugge, J. S. Morphogenesis and oncogenesis of MCF-10A mammary epithelial acini grown in three-dimensional basement membrane cultures. *Methods* **30**, 256–268 (2003).

-
353. Li, Q. S.; Lee, G. Y. H.; Ong, C. N. & Lim, C. T. AFM indentation study of breast cancer cells. *Biochem. Biophys. Res. Co.* **374**, 609–613 (2008).
354. Pietuch, A.; Janshoff, A. Mechanics of spreading cells probed by atomic force microscopy. *Open Biol.* **3**, 130084 (2013).
355. Hoh, J. H.; Schoenenberger, C.-A. Surface morphology and mechanical properties of MDCK monolayers by atomic force microscopy. *J. Cell Sci.* **107**, 1105–1114 (1994).
356. Rotsch, C.; Radmacher, M. Drug-Induced Changes of Cytoskeletal Structure and Mechanics in Fibroblasts: An Atomic Force Microscopy Study. *Biophys. J.* **78**, 520–535 (2000).
357. Ayala, Y. A. *et al.* Effects of cytoskeletal drugs on actin cortex elasticity. *Exp. Cell Res.* **351**, 173–181 (2017).
358. Coué, M.; Brenner, S. L.; Spector, I. & Korn, E. D. Inhibition of actin polymerization by latrunculing A. *FEBS Lett.* **213**, 316–318 (1987).
359. Bubb, M. R.; Senderowicz, A. M. J.; Sausville, E. A.; Duncan, K. L. K. & Korn, E. D. Jasplakinolide, a Cytotoxic Natural Product, Induces Actin Polymerization and Competitively Inhibits the Binding of Phalloidin to F-actin. *J. Biol. Chem.* **259**, 14869–14871 (1994).
360. Bubb, M. R.; Spector, I.; Beyer, B. B. & Fosen, K. M. Effects of Jasplakinolide on the Kinetics of Actin Polymerization. *J. Biol. Chem.* **7**, 5163–5170 (2000).
361. Holzinger, A.; Meindl, U. Jasplakinolide, a novel actin targeting peptide, inhibits cell growth and induces actin filament polymerization in the green alga *Micrasterias*. *Cell Motil. Cytoskel.* **38**, 365–372 (1997).
362. Cai, S. *et al.* Effect of latrunculin-A on morphology and actin-associated adhesions of cultured human trabecular meshwork cells. *Mol. Vis.* **6**, 132–143 (2000).
363. Yarmola, E. G. *et al.* Actin-latrunculin A structure and function: differential modulation of actin-binding protein function by latrunculin A. *J. Biol. Chem.* **275**, 28120–28127 (2000).
364. Lázaro-Diéguéz, F. *et al.* Dynamics of an F-actin aggresome generated by the actin-stabilizing toxin jasplakinolide. *J. Cell Sci.* **121**, 1415–1425 (2008).
365. Spector, I.; Shochet, N. R.; Kashman, Y. & Groweiss, A. Latrunculins: Novel Marine Toxins That Disrupt Microfilament Organization in Cultured Cells. *Science* **4584**, 493-495 (1963).
366. Wilson, C. A. *et al.* Myosin II contributes to cell-scale actin network treadmilling through network disassembly. *Nature* **465**, 373–377 (2010).
-

367. Wakatsuki, T.; Schwab, B.; Thompson, N. C. & Elson, E. L. Effects of cytochalasin D and latrunculin B on mechanical properties of cells. *J. Cell. Sci.* **114**, 1025–1036 (2000).
368. Rother, J. H. Dissertation. Georg-August-Universität Göttingen, 2014.
369. Paluch, E. K. *et al.* Mechanotransduction. Use the force(s). *BMC Biol.* **13**, 47 (2015).
370. Gupta, M. *et al.* Adaptive rheology and ordering of cell cytoskeleton govern matrix rigidity sensing. *Nat. Commun.* **6**, 7525 (2015).
371. Plotnikov, S. V.; Pasapera, A. M.; Sabass, B. & Waterman, C. M. Force fluctuations within focal adhesions mediate ECM-rigidity sensing to guide directed cell migration. *Cell* **151**, 1513–1527 (2012).
372. Li, J.; Han, D. & Zhao, Y.-P. Kinetic behaviour of the cells touching substrate. The interfacial stiffness guides cell spreading. *Sci. Rep.* **4**, 3910 (2014).
373. Maruthamuthu, V.; Sabass, B.; Schwarz, U. S. & Gardel, M. L. Cell-ECM traction force modulates endogenous tension at cell-cell contacts. *P. Natl. Acad. Sci. USA* **108**, 4708–4713 (2011).
374. Brückner, B. R. Dissertation. Georg-August-Universität, 2016.
375. Rigato, A.; Rico, F.; Eghiaian, F.; Piel, M. & Scheuring, S. Atomic Force Microscopy Mechanical Mapping of Micropatterned Cells Shows Adhesion Geometry-Dependent Mechanical Response on Local and Global Scales. *ACS nano* **9**, 5846–5856 (2015).
376. Wang, X.; Hu, X.; Kawazoe, N.; Yang, Y. & Chen, G. Manipulating Cell Nanomechanics Using Micropatterns. *Adv. Funct. Mater.* **26**, 7634–7643 (2016).
377. Wang, X. *et al.* Influence of cell size on cellular uptake of gold nanoparticles. *Biomater. Sci.* **4**, 970–978 (2016).
378. Fitzpatrick, V. *et al.* Signal mingle. Micropatterns of BMP-2 and fibronectin on soft biopolymeric films regulate myoblast shape and SMAD signaling. *Sci. Rep.* **7**, 41479 (2017).
379. Tan, X.; Heureaux, J. & Liu, A. P. Cell spreading area regulates clathrin-coated pit dynamics on micropatterned substrate. *Integr. Biol.* **7**, 1033–1043 (2015).
380. Théry, M. Micropatterning as a tool to decipher cell morphogenesis and functions. *J. Cell Sci.* **123**, 4201–4213 (2010).
381. Cailleau, R.; Mackay, B.; Young, R. N. & Reeves Jr., W. J. Tissue Culture Studies on Pleural Effusions from Breast Carcinoma Patients. *Cancer Res.* **34**, 801–809 (1974).

-
382. Corbin, E. A.; Kong, F.; Lim, C. T.; King, W. P. & Bashir, R. Biophysical properties of human breast cancer cells measured using silicon MEMS resonators and atomic force microscopy. *Lab Chip* **15**, 839–847 (2015).
383. Ketene, A. N.; Schmelz, E. M.; Roberts, P. C. & Agah, M. The effects of cancer progression on the viscoelasticity of ovarian cell cytoskeleton structures. *Nanomedicine* **8**, 93–102 (2012).
384. Nikkhah, M.; Strobl, J. S.; Vita, R. de & Agah, M. The cytoskeletal organization of breast carcinoma and fibroblast cells inside three dimensional (3-D) isotropic silicon microstructures. *Biomaterials* **31**, 4552–4561 (2010).
385. Plodinec, M. *et al.* The nanomechanical signature of breast cancer. *Nat. Nanotechnol.* **7**, 757–765 (2012).
386. Cross, S. E.; Jin, Y.-S.; Rao, J. & Gimzewski, J. K. Nanomechanical analysis of cells from cancer patients. *Nat. Nanotechnol.* **2**, 780–783 (2007).
387. Koch, T. M.; Münster, S.; Bonakdar, N.; Butler, J. P. & Fabry, B. 3D Traction Forces in Cancer Cell Invasion. *PloS one* **7**, e33476 (2012).
388. Steinwachs, J. *et al.* Three-dimensional force microscopy of cells in biopolymer networks. *Nat. Methods* **13**, 171–176 (2016).

Appendix 1: Supplementary Data

I. Formation of Confluent Cell Layers as a Function of Seeding Density

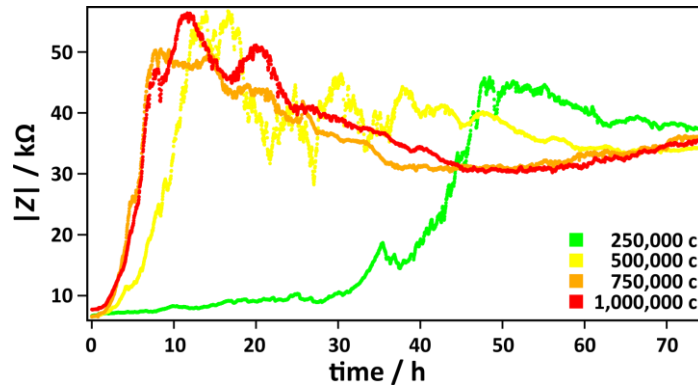


Figure 77: Formation of cell layers over time for different seeding densities. Impedance $|Z|$ over time at a frequency of 3360 Hz. MDCKII cells were seeded on an ECIS electrode (0.8 cm^2) with different seeding densities (see chapter 4.2.6.2) corresponding to: 250,000 c per 9.2 cm^2 (green), 500,000 c per 9.2 cm^2 (yellow), 750,000 c per 9.2 cm^2 (orange) and 1,000,000 c per 9.2 cm^2 (red). (Experiment performed by Franziska Ries (2016))

II. Cell-Cell Contacts as a Function of Seeding Density

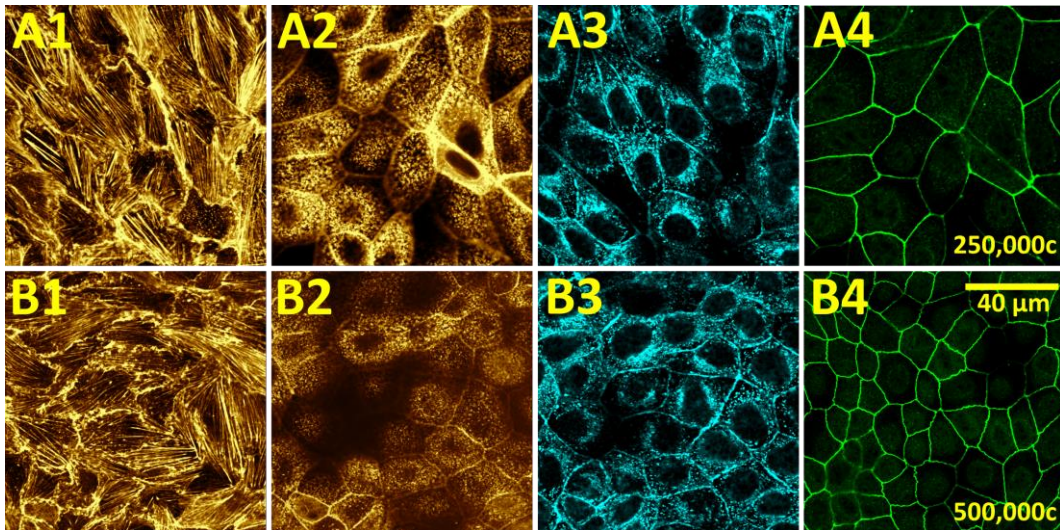


Figure 78: The F-actin cytoskeleton and cell-cell contacts of MDCKII cells as a function of seeding density. Confocal images of important cytoskeletal proteins as a function of different seeding density are shown. **A:** 250,000 c per 9.2 cm^2 ; **B:** 500,000 c per 9.2 cm^2 . **A1&B1:** Fluorescently stained F-actin cytoskeleton, focus was set to the basal focal plane; **A2&B2:** Fluorescently stained F-actin cytoskeleton, focus was set to the apical focal plane; **A3&B3:** Fluorescently stained e-cadherin; **A4&B4:** Fluorescently stained ZO-1. Cells were fixed after 2 days. Labelling was performed as described in chapter 4.2.5.1 (Experiment performed by Franziska Ries (2016))

III. Impact of Cell Size and Substrate Properties on the Viscoelastic Parameters obtained from PLSDM

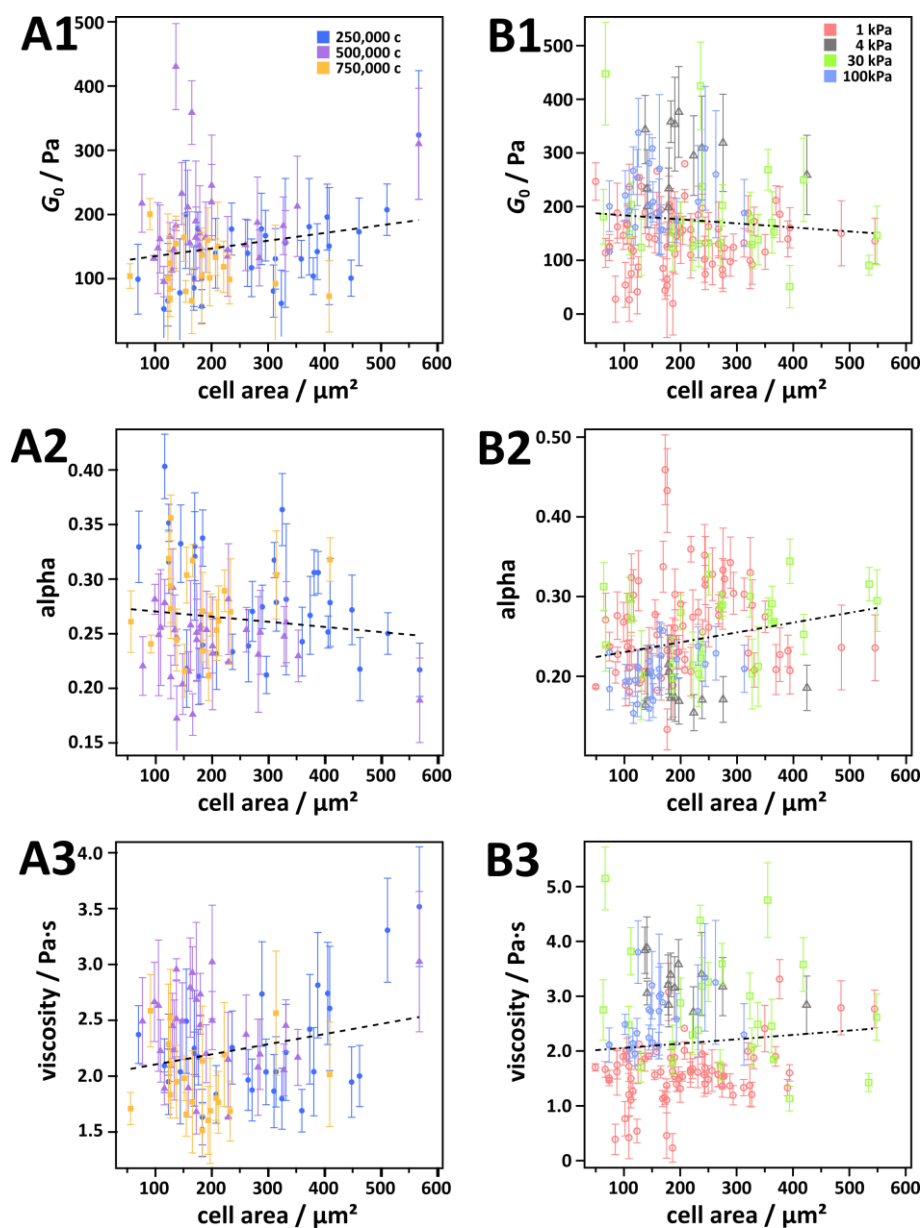


Figure 79: Correlation plot of the viscoelastic parameters obtained by the PLSDM on the cell size and substrate properties. A&B1: Stiffness offset in dependency of the area per cell. **A&B2:** Power law coefficient in dependency of the area per cell. **A&B3:** Newtonian viscosity in dependency of the area per cell. **A:** Cells grown on stiff glass substrates were seeded in different cell densities: 250,000 c (blue), 500,000 c (violet) and 750,000 c (orange). **B:** Cells grown on substrates of different elasticity: 1 kPa (red), 4 kPa (grey), 30 kPa (green) and 100 kPa (blue). Mean values (data points) and standard deviation (error bars) for all force distance curves that were evaluated for one single cell are plotted against the area which was obtained by the height map of the atomic force microscopy measurement. Dashed line shows a linear trend line for all data. (Data measured by Franziska Ries (2016))

IV. Table of Parameters Used to Model the Frequency Dependent Viscoelastic Properties

Table 25: Parameters used to model the frequency dependent viscoelastic properties using a semi-phenomenological model to describe binding kinetics in the low frequency regime. The storage and loss moduli of the respective frequency dependent viscoelastic properties presented in chapter 5.1.2.3 and 5.1.2.4, were fitted according to equation (69)+(70). Parameters: plateau modulus, G_0 ; number of the respective cross-link N_i ; unbinding rate constant of the respective cross-link, k_{off}^i and power law, p ; with $i=1$ for the entanglement kinetics and $i=2$ for the cross-linker kinetic or a different process as in the actin 36 μM sample. Parameters a - d are pre-factors as described in chapter 3.2.1. Due to the large number of parameters the fit parameters narrow boundaries had to be set for some parameters, assumptions had to be made in cases of supposedly overlapping peaks (***) and in some samples the high frequency regime did not contain enough data or could only partial be well fitted by the model (**).

	offset	low frequency 1				low frequency 2				high frequency		
sample	G_0 /Pa	$a_1 / \text{Pa} \cdot \text{s}^{-1}$	$c_1 / \text{Pa} \cdot \text{s}^{-1}$	N_1	$k_{\text{off}}^1 / \text{s}^{-1}$	$a_2 / \text{Pa} \cdot \text{s}^{-1}$	$c_2 / \text{Pa} \cdot \text{s}^{-1}$	N_2	$k_{\text{off}}^2 / \text{s}^{-1}$	$b / \text{Pa} \cdot \text{s}^{-p}$	$d / \text{Pa} \cdot \text{s}^{-p}$	p
actin 8-23 μM ; $N=5$	0.010	1.00e-7	1.00e-6	88	0.050	/	/	/	/	5.00e-3	1.02e-2	0.80***
actin 36 μM *; $N=3$	0.080	5.08e-6	3.29e-5	674	2.650	1.68e-5	1.25e-4	9	0.201	4.70e-3	1.84e-2	0.78
actin:gelsolin 750:1; $N=5$	0.036	3.43e-5	3.29e-5	23	0.877	/	/	/	/	3.70e-3	1.19e-2	0.72
actin:gelsolin 2500:1; $N=5$	0.052	8.24e-5	8.97e-4	4	0.272	/	/	/	/	2.11e-2	3.11e-2	0.71
PIP ₂ 3 mol% 2 μM ; $N=6$	0.133	1.00e-7	2.42e-5	100	0.400****	2.29e-6	1.45e-5	90	0.054	3.30e-3	1.43e-2	0.92***
PIP ₂ 3 mol% 5 μM ; $N=1$	0.092	5.00e-7	1.64e-5	52	0.165	9.00e-7	5.92e-6	63	0.027	3.3e-4	1.60e-2	0.89***
PIP ₂ 5 mol% 2 μM ; $N=9$	0.210	1.00e-7	2.68e-5	176	0.400****	2.55e-6	1.83e-5	112	0.054	3.00e-3	2e-2	0.92***
biotin 0.5 mol%; $N=1$	0.182	2.46e-6	2.11e-5	502	0.461	6.70e-7	5.21e-6	137	0.042	4.10e-3	1.12e-2	0.84***
biotin 3 mol%**; $N=2$	0.329	4.48e-6	3.20e-5	556	0.407	3.55e-7	2.49e-6	95	0.014	1.00e-3	1.00e-2	0.75***

* Note that for this dataset also frequency dependent moduli with only one maximum in the loss modulus were found (see discussion 5.1.2.3).

** Note that the high frequency regime above 1 Hz in the 'biotin 3 mol%' sample is affected by noise signal (see 5.1.2.6), which is why b , d and p were chosen so the resulting curve is similar to what is expected.

*** Note that in these cases the high frequency regime could not or only partially described by the model.

**** Note that this peak was assumed (and not fitted) in accordance with the 'biotin 3 mol%' sample for discussion see 5.1.2.4.

Appendix 2: List of Abbreviations, Symbols, Figures and Tables

List of Abbreviations and Symbols

abbrev./ symbol	explanation
A	input amplitude (AMR) or area, depending on context
a, b, c, d	parameters in the semi-phenomenological model from Bausch and co-workers
a. u.	arbitrary unit
$\hat{A}(f)$	power spectral density, Fourier transform of position autocorrelation function
$A(\tau)$	normalized position autocorrelation function
A_0	geometrical area in the liquid droplet model
ABP	actin binding proteins
ACMP	apical cellular membrane patches
ActA	actin assembly-inducing protein
A_{ex}	excess area in the liquid droplet model
ADP	adenosine diphosphate
AFM	atomic force microscopy
AMR	active microrheology
Arp2/3	arp2/3 complex with sub-units actin-related proteins ARP2 and ARP3
ATP	adenosine triphosphate
$b(h_0)$	hydrodynamic drag extrapolated to zero height (AMR AFM)
biotin	used as notation for the biotin-neutravidin-biotin model system
BSA	bovine serum albumin
c	concentration or cells depending on context
c_A	concentration of G-actin in [$\text{mg} \cdot \text{mL}^{-1}$]
C-ERMAD	ezrin-radixin-moesin association domain
CLSM	confocal LASER scanning microscopy
C_m	membrane capacitance in ECIS model
d	diameter
D	diffusion coefficient
$D(\omega)$	amplitude of response (in AMR)
DOPE	1,2-dioleoyl- <i>sn</i> -glycero-3-phosphoethanolamine
E	Young's modulus or elastic modulus
E_a	activation energy
ECIS	electric cell impedance sensing
ECM	extracellular matrix
ERK	extracellular signal-regulated kinases
ERM	ezrin, radixin, moesin family
F	force
f	frequency
FAK	focal adhesion kinase
FERM	four-point-one, ezrin-radixin-moesin
F_B	buckling force
f_c	corner frequency in power spectrum
f_R	random force from solvent molecules

F_t	tether force
G'	storage modulus
G''	loss modulus
G	shear modulus
G^*	complex shear modulus
G_0	plateau modulus, also absolute stiffness in the PLSDM (extrapolated to zero frequency) and plateau modulus in the semi-phenomenological model to describe transient cross-linker unbinding
GDA	glutaraldehyde
GSER	generalized Stokes Einstein relation
His	histidine
J	compliance
k	spring constant for Hooke's spring/ trap stiffness
K	correlation time in simulations
k_B	Boltzmann constant
K_{eq}	equilibrium constant
k_{off}	unbinding rate constant (also in the semi-phenomenological model to describe transient cross-linker unbinding)
k_{on}	binding rate constant
l	length
LASER	light amplification by stimulated emission of radiation
l_c	contour length
l_e	entanglement length
l_p	persistence length
m	mass
MAC	minimal actin cortex
MDCK II	Madin-Darby Canine Kidney epithelial cell line
MLCK	myosin light chain kinase
MR	microrheology
MSD or $\langle \Delta x^2(\tau) \rangle$	mean squared displacement
N	number of dimensions in MSD and GSER number of bonds in Bausch model
OT	optical tweezer
p	power law in the semi-phenomenological model to describe transient cross-linker unbinding
P	pinning-point density
PBS	phosphate buffered saline
PDB	protein data base
PIP ₂	phosphatidylinositol 4,5-bisphosphate also used as notation for the PIP ₂ -ezrin-actin model system
PLSDM	power law structural damping model
PMR	passive microrheology
POPC	1-palmitoyl-2-oleoylphosphatidylcholine
r	radius (mostly tracer particle radius)
R	ratio of cross-link concentration to G-actin concentration
R_b	trans epithelial resistance in ECIS model
RGD	amino acid sequence arginine, glycine and aspartic acid

ROCK	rho-associated protein kinase
s	Laplace frequency parameter
sem	standard error of mean
std	standard deviation
SUV	small unilamellar vesicles
t	time
t'	past time
T	temperature or tension depending on the context
T_0	overall tension in the liquid droplet model
T_c	cortical tension in the liquid droplet model
T_t	membrane tension in the liquid droplet model
v	velocity
VPT	video particle tracking
WASP	Wiskott–Aldrich Syndrome protein
x, y, z	x -, y - and z -position or direction
ZO	<i>zonula occludens</i> proteins
α	power law coefficient in different descriptions
α^*	complex response function
$\alpha(\omega)$	first order log derivative of polynomial fit function to MSD vs. time lag
$\alpha'(\omega)$	first order log derivative of polynomial fit function to G^* vs. frequency
$\beta(\omega)$	second order log derivative of polynomial fit function to MSD vs. time lag
$\beta'(\omega)$	second order log derivative of polynomial fit function to G^* vs. frequency
γ	ECIS parameter, reciprocal proportional to the square root of the cell-substrate distance
Γ	gamma function
δ	indentation depth or loss tangent depending on the context
$\delta(\omega)$	phase shift
ε	strain
ζ	memory function/ friction coefficient/ hydrodynamic drag coefficient
η	(solvent) viscosity, also parameter for the viscosity in PLSDM
η^*	complex viscosity
θ_{half}	half opening angle of a pyramidal cantilever tip
κ_A	area compressibility in the liquid droplet model
$\tilde{\kappa}_A$	apparent area compressibility in the liquid droplet model
κ_B	bending modulus
λ	wavelength (of motion)
ν	Poisson's ratio
ξ	mesh size
$\Pi(\tau)$	normalized mean squared displacement
ρ	material density (of particle)
σ	stress
τ	time lag
τ_{ent}	entanglement time
τ_{rep}	reptation time
$\varphi(\omega)$	phase shift
ω	angular frequency

List of Figures

- Figure 1: Scheme of mechanical model systems for cellular viscoelasticity investigated in the context of the here presented dissertation.** Top down approaches: 3D entangled F-actin networks and 2D F-actin networks transiently cross-linked to a solid supported membrane via the physiological cross-link ezrin. Top down approaches: functional apical membrane patches from epithelial cell cortices and living cells. 3
- Figure 2: Equivalent circuits and shear modulus of viscoelastic models.** **A:** Maxwell model. **B:** Kelvin-Voigt model. **C:** A more elaborate model capturing most of the rheological properties of F-actin networks. Solid lines: Storage modulus. Dotted lines: loss modulus. 6
- Figure 3: Phase diagrams of entangled F-actin filaments.** **A:** Dependency of the stiffness (G_0) on the concentration of G-actin. Isotropically entangled F-actin networks can be obtained at concentrations in the range of 5-50 μM G-actin (**green**). Below a concentration of 5 μM , solutions of polymers or loosely entangled networks are formed (**blue**). At higher concentrations anisotropic phases are forming (**red**). **B:** Stiffness (G_0) as a function of filament contour length, illustrating the phase transition from loosely entangled filaments to isotropically entangled filaments dependent on the filament contour length. Adapted from Palmer *et al.*¹¹⁷ and Hinner *et al.*²⁸ 11
- Figure 4: Schematic drawing of an entangled network (A) and respective length scales (B) of F-actin networks.** **A:** Green lines: Polymer contours. Most important parameters describing the polymer network are indicated. ξ : Average distance between filaments = mesh size. l_e : Average length between to entanglements = entanglement length. l_c : Average length of a polymer along its contour = contour length. l_p : Persistence length. d : diameter of the filament. Inset displays also the tube which is formed by the entanglements. The two basic movements of a polymer in a tube are indicated in red: high frequency bending movements and long time diffusion along tube (reptation). **B:** Important length scales in F-actin networks after Isambert and Maggs.¹²¹ 12
- Figure 5: Schematic illustration of the frequency dependent viscoelastic properties of F-actin networks.** **Red line:** Storage modulus G' . **Blue line:** Loss modulus G'' . **I:** High frequency bending modes. **II:** Plateau regime, which is dominated by entanglements. **III:** Low frequency regime, reptation movement of filaments. 13
- Figure 6: Overview of the architecture of the F-actin cytoskeleton on the basis of a scheme of a migrating cell (left) and a polarized epithelial cell in a confluent layer (right).** For detailed explanation see text (Figure partly designed after Blanchoin *et al.*¹³). 17
- Figure 7: Structure and activation of ezrin.** **A:** The different domains of ezrin. **Light blue:** FERM domain; **Yellow:** α -helical domain; **Red:** C-ERMAD with the F-actin binding site and the location of the threonine567 phosphorylation site. **B:** Cytosolic ezrin in a self-associated dormant state and in an activated state. Activation occurs upon PIP_2 binding and phosphorylation at threonine567. The homologous structure of moesin is shown (PDB 2I1J¹⁶¹). A crystal structure of the FERM domain of ezrin and it's complex with the C-terminal region can be found at PDB 4RM9 and has been discussed by Phang *et al.*¹⁵⁶ Inset: Simplified scheme of ezrin used throughout the document. **C:** Scheme of the role of ezrin in epithelial cells. 20
- Figure 8: Overview over the structural polymorphism in cross-linked F-actin networks.** Phase diagram depending on the cross-linker concentration, type of cross-link and cross-linker mass. **Green:** Phase was observed. **Red:** Phase was not observed. Reproduced from Bausch and coworkers.¹⁸⁰ 22
- Figure 9: Approximate phase transition and scaling behavior of the plateau modulus for cross-linked semi-flexible biopolymers.** **A:** Phase diagram depending on density of filaments ρ (compares to density of cross-links) and contour length l_c . Green dotted line shows a possible range of operation for the successive figures B+C. **B** and **C:** dependency of the plateau modulus (G_0) on relative cross-link concentration to G-actin R and G-actin concentration, cA . Color code throughout the graphic: **Blue:** solution; **Yellow:** nonaffine; **Pink:** affine entropic; **Violet:** affine enthalpic. Adapted from Head *et al.* (simulation)¹⁸⁴, Gardel *et al.* (study on scruin)⁶⁵ and Lieleg *et al.* (study on fascin and review)^{180,185} 22
- Figure 10: Stress stiffening of affine cross-linked networks.** **A:** F-actin/scruin; **B:** F-actin/rigor-HMM; **C:** F-actin/filamin. Reproduced from Zagar *et al.*¹⁸⁶ 23
- Figure 11: Scheme depicting the implications of transient actin binding proteins to F-actin networks.** **A:** Transient cross-links stabilize networks and provide stability under shear conditions. However, due to thermal activation transient cross-links eventually dissociate already at room temperature. **B:** This process leads to relaxation of the network, which determines the viscoelastic response (red: storage modulus, blue: loss modulus) on intermediate to low frequencies (highlighted in red). Adapted from Lieleg *et al.*³⁵ 24
- Figure 12: Three phases of active F-actin/myosin networks.** **A:** Phases of actively contracting F-actin/myosin networks shown as time overlays. Left: Local contraction; Middle: critically connected; Right: Global contraction. **B:** Proposed phase diagram in space of connectivity (=cross-linker concentration) and force (=motor protein concentration). Black dot denotes the marginal connectivity needed to produce contraction. Reproduced from Alvarado *et al.*¹⁸ 26
- Figure 13: Impact of myosin II on the frequency dependent viscoelastic response of F-actin networks.** **A:** Scheme of the myosin induced tension on F-actin filaments. Red: F-actin filaments; White: Myosin; Green arrows: force. Plus

and minus end of the filaments are marked to show the necessity of anti-parallel orientation for the power stroke. **B:** Imaginary part of the response function (α'') from active and passive measurements are shown for samples without myosin and with myosin (3.5 mM) after 2.5 h. **C:** Comparable spectrum as in B is shown for a sample containing myosin after 5 h. The non-equilibrium contribution is indicated by an arrow. Myosin activity acts on the frequency regime between 10^{-1} - 10^1 Hz. Reproduced from Mizuno, Schmidt *et al.*¹⁴..... 27

Figure 14: 2D minimal actin cortices. **A:** Schematic drawing of the preparation of quasi 2D minimal actin cortices on solid supported membranes or other substrates. Membrane bilayers are obtained from vesicle spreading. Pinning-points and cross-links provide membrane anchorage for pre-polymerized F-actin. **B:** Static membrane bound actomyosin model cortex reported by Gardel and coworkers.²¹⁷ Red: F-actin filaments; Green: Myosin micro-filaments. **C:** Contraction and restructuring of a 2D confined actomyosin network (methylcellulose) upon local myosin activation (inhibition of blebbistatin) on different length scales. **D:** Respective contractile velocities at the boundary reported by Gardel and coworkers.²²¹..... 29

Figure 15: Overview about the different 3D minimal actin cortex models. The interface of F-actin and membrane is of central importance (sketched in the box in the middle). Above: Structurally supported mono- or bilayers using microspheres or oil interfaces to determine the shape of the model system. Below: Liposome based strategies: either F-actin networks are bound to the outer (right) or inner (left) leaflet of the vesicles. 30

Figure 16: Frequency dependent viscoelastic properties of an actomyosin network bound to a lipid interface via streptavidin in a 3D oil in water approach. **A:** The scaling of the plateau modulus with the surface density of streptavidin is shown (w/o myosin). **B:** The storage (filled symbols) and the loss (open symbols) modulus of a membrane bound actomyosin network is shown in absence (**black**) and presence (**red**) of ATP. 30

Figure 17: Dendritic actin networks from *Xenopus laevis* egg extracts. **A:** The dendritic F-actin network (red) was polymerized between a surface and a cantilever. Atomic force microscopy based microrheology was performed. **B:** Linear viscoelastic measurements typical weak power law scaling with frequency and a rather high elastic modulus was found ($E@1\text{Hz} \approx 800$ Pa). **C:** Non-linear viscoelastic measurements. Interestingly, not only stress stiffening (yellow region) but also stress softening (green region) was found. **D:** Hypothesis for the underlying stress softening, induced buckling (green arrows) of short and highly cross-linked filaments, orthogonal to the direction of stress (red arrows) in the network lead to a softening in the direction of stress. Figures reproduced from Chaudhuri, Parekh and Fletcher.⁷⁷..... 32

Figure 18: Scaling behavior of living cells after Kollmannsberger and Fabry. **A-C:** Linear viscoelasticity. **A:** Weak power law scaling of the scaled elastic modulus with the frequency (0.1-0.5). **Blue:** Cells; **Violet:** Cell layers and tissue; **Red:** Actin networks cross-linked with different proteins. **B:** Scaling of the scaled elastic modulus with pre-stress. **C:** Scaling of the power law coefficient with pre-stress. **D:** Non-linear viscoelasticity, stress stiffening in dependency of externally applied stress. Reproduced from Kollmannsberger and Fabry.²⁴¹..... 34

Figure 19: F-actin networks at different concentrations. Confocal images (A-C) and epi-fluorescence image (D) of actin networks made from different G-actin concentrations. **A:** 23 μM ; **B:** 36 μM ; **C+D:** 40-46 μM . F-actin was stained with AlexaFluoPhalloidin488. Red structures in (C) are tracer particles (2 μm carboxylate)..... 37

Figure 20: Preparation and self-organization of membrane bound artificial model systems of the actin cortex. **A1-3:** Schematic representation of the preparation process of artificial model systems of the actin cortex. A solid supported lipid bilayer (**red**) containing receptor lipid (**yellow**) is incubated with the protein ezrin T567D (**blue**). Afterwards a pre-polymerized F-actin network (**green**) is attached to the bilayer. **B1-3:** fluorescence images confirm successfully spread lipid bilayer doped with TexasRed (**B1**) and attachment of the actin network doped with AlexaFluor488-phalloidin (**B2**) and overlay (**B3**). Scale bar: 10 μm . (parts of figure by Markus Schön)..... 38

Figure 21: F-actin filament network analysis. **A:** Confocal fluorescence images of F-actin filament networks were recorded. **B:** The images were enhanced in signal-to-noise ratio by using a fast Fourier transform filter. **C:** The open source software tool SOAX was used to detect filaments using multiple stretching open active contours.^{250,251} **D:** Local maxima in an Euclidian distance map between the computed filaments served as center points for circles inside a network pocket. **E:** Overlapping circles were compared to avoid multiple responses of one mesh. **F:** Solely the largest of the overlapping circles was taken as mesh size of one specific pocket. The method was described before.^{252,253} (Figure was gratefully received from Markus Schön)..... 40

Figure 22: Incorporation of the tracer particles in the F-actin filament network. Confocal fluorescence images of actin networks attached to a lipid membrane containing 3 mol% PIP₂ via ezrin are shown. Tracer particles: size $d = 2$ μm , non-fluorescent silica (Bangs Laboratories, Indiana, United States). **A:** xy -planes at three different z -positions, at the plane of the tracer particles ($z = 0$ μm), two planes below ($z = -1.44$ μm) and two planes above ($z = +1.44$ μm). **B:** An x - z -plane is shown. Non-fluorescent beads were used, the F-actin polymers organize around the silica surface. Estimated bead positions are marked with blue dotted lines. F-actin was fluorescently labeled with AlexaFluor488-phalloidin (Life Technologies, Carlsbad, USA)..... 41

Figure 23: Selection of trajectories. Raw data in the form of bead trajectories is shown. **A:** Trajectories in x - y -representation. **B:** x - and y -position as a function of time. **A+B1:** Trajectory without artefacts, no drift and similar variation in position over a long period of time. **A+B2:** Trajectory with minor artefacts, no drift and only a slight change in position variation. **A+B3:** Trajectory with a major artefact, bead is sticking to the surrounding cage. **A+B4:** Trajectory with a

major artefact, bead is moving on a circle. Flickering in the time course between the different positions can be observed. The bead is most likely not incorporated in the network but sits on top and performs a propeller-like movement. 42

Figure 24: Two example histograms of the y-position. **A:** Particle 1 from Figure 23 A&B1. **B:** Particle 3 from Figure 23 A&B3. 43

Figure 25: Overview Video Particle Tracking. **A:** Schematic representation of the method. Videos of at least 100,000 images were recorded on a sCMOS camera with a frame rate of about 50 fps and an exposure time of about 10 ms. **B:** Examples of trajectories of tracer particles in different viscoelastic media are displayed. Inset: Bead trajectory of a tracer particle in a 2D actin network coupled to a planar membrane via transient ezrin/PIP₂ linkage in comparison to the bead size. **C:** Mean squared displacement (**blue**) and respective locally fitted curve (**orange**). **D:** Viscoelastic moduli, the storage modulus (closed symbols) and the loss modulus (open symbols). **Blue:** Shear modulus of entangled F-actin networks. **Dotted grey line:** Theoretical loss modulus of water. 43

Figure 26: Schematic representation of the optical tweezer setup and beam bath. The NanoTracker 2 optical tweezer (JPK Instruments, Berlin, Germany) build on an inverted Zeiss microscope equipped with a 5 W 1064 nm LASER and a water immersion objective (63 x, C-Apochromat, NA = 1.2, Carl Zeiss, Jena, Germany). The LASER beam is split into two light paths. Trap 1 can be stirred by a piezo electric mirror, trap 2 by an acousto-optic deflector (AOD). Detection of the signal is carried out by quadrant photodiodes. 45

Figure 27: Overview of passive microrheology measurements by optical tweezer. **A:** Schematic representation of the setup. A tracer particle (red circle) is trapped in a polymer network (not shown). An optical trap of low trap stiffness (**blue**) records the particle movement. The motion of the tracer particle is recorded by a quadrant photodiode. **B:** Example of particle movement in *x*-direction of a tracer particle in a viscoelastic medium (raw signal). **C:** Example of normalized position autocorrelation function $A\tau$ (**orange**) of the tracer particle position. **D:** Example of normalized mean squared displacement $nMSD\tau$ (**green**) of the tracer particle position. **E:** Example of viscoelastic moduli, storage (**red**) and loss (**blue**). 45

Figure 28: Active microrheology measured by optical tweezer. **A:** Schematic representation of the setup. A tracer particle (red circle) is trapped in a polymer network (not shown), an optical trap of low trap stiffness (blue) records the particle movement, while another optical trap of higher trap stiffness (red) excites oscillatory movement of different frequencies and low amplitude ($2 \cdot A = 80 - 200$ nm, peak to peak). The motion of the tracer particle is recorded by a quadrant photodiode. **B:** Forces acting on the tracer particle (red circle). Harmonic potentials of the traps (trap 1 (red) & trap 2 (blue)). **C:** Detected signals at 80 Hz, response signal (blue) is damped in amplitude and phase shifted compared to the input signal (red). **D:** Exemplary spectrum of the viscoelastic moduli versus frequency. Red: Storage modulus; Blue: Loss modulus. 46

Figure 29: Overview optical tweezer calibration. **A:** Trap position calibration, trap 1 (**red**) and trap 2 (**green**) lie on top of each other. **B:** Example of a power spectra of both traps with respective fit (equation shown in B1). **B1:** Trap 1. **B2:** Trap 2. $A\omega$: Power spectral density (Fourier transform of the position autocorrelation); ζ : hydrodynamic drag coefficient; f_c : the corner frequency. 47

Figure 30: Evaluation of the model to simulate the motion of a tracer particle in a viscoelastic medium. Graphs display the mean squared displacement over time lag. **A:** Variation of the spring constant of the harmonic potential k . **B:** Variation of the diffusion coefficient D_{cage} of the cage. **C:** Variation of the correlation time K at which the time dependent memory function decays to $1/e$ of its original value. **D:** Variation of the temperature T . Other parameters were kept constant: mass $m = 1 \cdot 10^{-15}$ kg, time between two positions $\Delta t = 0.01$ s and total number of positions calculated $L = 100,000$ 49

Figure 31: Fluorescence staining of collagen I coated polyacrylamide gels. **A:** 8 kPa gel. **B:** 30 kPa Gel. Insets are deliberately produced defects to illustrate the difference between coated and uncoated locations. Collagen I was fluorescently labeled as described in 1.2.4 (Fluorescence images were produced during the Bachelor thesis of Franziska Ries (2016), Institute of Physical Chemistry, Georg-August-Universität, Göttingen, Germany). 50

Figure 32: determination of cell topography. AFM images (contact mode) of cells were evaluated. Two orthogonal diameters (length and width) and the height of each cell were obtained from the height profile of the contact images. Spreading area was calculated assuming an elliptic form. 53

Figure 33: Overview preparation of cellular patches with the sandwich-cleavage method. **A:** Schematic overview over the experimental procedure.¹⁶⁸ MDCK II cells are cultivated on a poly-D-lysine coated surface and exposed to osmotic pressure with ultrapure water before another poly-D-lysine coated surface was slightly pressed to the cell layer. When the substrate was taken off, apical cellular membrane patches could be identified on the surface of the second coverslip. **B1:** Epi fluorescence images of the plasma membrane of a cellular patch stained with CellMask Orange plasma membrane stain (Life Technologies GmbH, C10045, Eugene, Oregon, United States) on a porous substrate (fluXXion, Netherland; pore diameter 1.2 μ m, gold coated) substrate; **B2+B3:** Epi fluorescence images of F-actin staining of a cellular patch with AlexaFluoPhalloidin488 in different magnifications. (Images B1-B3 were gratefully received from Stefan Nehls) 53

Figure 34: Overview electric cell-substrate impedance sensing (ECIS). **A:** Schematic representation of the ECIS experiment. Attachment of cells and state of confluency of the cellular monolayer are observed by impedance measurements. AC current is applied through a $1\text{ M}\Omega$ resistor to obtain an approximately constant current source. The amplitude and phase of the voltage is measured by a lock-in amplifier (adapted from²⁷²). **B:** Schematic representation of the three parameters the measured complex impedance is a function of, the barrier resistance R_b , the membrane capacitance C_m and γ which is dependent on the distance between cell and substrate (adapted from <http://biophysics.com/ecismodel.php> (access 10.05.2017, 15:15)). **C:** Complex impedance over time at a frequency of 3360 Hz (**green**). Three stages can be distinguished. **I:** Empty electrode; **II:** Cell spreading on the electrode and cell proliferation; **III:** Cellular motion in the confluent monolayer. **D:** Complex impedance over frequency. **Blue:** Data (circles) and fit (line) for an empty electrode are shown. **Orange:** Data (triangles) and fit (line) for a confluent monolayer are shown. Inset: Equivalent circuit for a cell covered electrode. For description see text. 56

Figure 35: Measuring principle of the active microrheological measurement with AFM. **A:** Schematic representation of the measurement. A cantilever with a pyramidal tip was indented approximately $\delta 0 \approx 1\mu\text{m}$ into a cell before an oscillation protocol was performed to probe the viscoelastic properties of the cell. **B:** Measuring signal. **Above:** Amplitude diminution and phase shift between excitation and response signal (black and red curve respectively). **Below:** Deflection signal of the cantilever vs. time. Different regimes can be seen. **I:** Approach; **II:** Indentation; **III:** Creep; **IV:** Oscillation; **V:** Retraction. 58

Figure 36: Schematic overview of mechanical parameters, which can be probed by AFM force indentation experiments. **Left:** Relation of the cellular cortex components and the mechanical parameters probed by AFM indentation measurements. Microrheology measurements probe the viscoelasticity of the cellular cortex hence the F-actin cytoskeleton and its cross-links. Apparent area compressibility modulus dominated by the incompressibility of the lipid bilayer and the tension arising from either active contractility of the actin cytoskeleton or the interconnection of the membrane and the cytoskeleton. **Right:** Example of force distance curve measured on with an AFM. Regions are dominated by different mechanical properties of the cell. The trace of the contact regime is dominated by the overall tension and the area compressibility. The hysteresis between the trace and the retrace curve is a measure of the viscoelasticity of the cell. Sudden jumps in the retrace following a long plateau in force originate in the pulling of so called tethers. 59

Figure 37: Overview of the two different minimal actin cortex models. **A1:** Scheme of a minimal actin cortex using physiological combination of pinning-point and cross-link, PIP_2 -ezrin-T567D-actin. **B1:** The artificial combination of pinning-point and cross-link, biotinylated DOPE-neutravidin-biotinylated-actin. The two cross-links differ in binding ratio and binding affinity. **A2 & B2:** Confocal fluorescence images of the membrane F-actin composite. Membrane is shown in red (A2: membrane was doped with TexasRed; B2: membrane was doped with Atto390DOPE) and F-actin is shown in green (stained with low amounts of AlexaFluor 488 phalloidin). Bar is $5\mu\text{m}$. **C:** Orthogonal view of the network (x - z -direction). Total height of the image is $4\mu\text{m}$ (Figure adapted from Markus Schön). 63

Figure 38: Examples of confocal fluorescence images of F-actin bound to solid supported lipid membranes via the cross-linking protein ezrin T567D containing different molar ratios of PIP_2 . **A:** PIP_2 1 mol%; **B:** PIP_2 2 mol%; **C:** PIP_2 3 mol% and **D:** PIP_2 5 mol%. (Data obtained from Markus Schön). 64

Figure 39: Mesh size analysis of actin networks attached to a lipid membrane containing different pinning-point densities. **A:** A typical filament analysis for a network attached to a lipid membrane containing 3 mol% PIP_2 . Confocal fluorescence image (black and white image) with the multiple Stretching Open Active Contours (SOACs) algorithm of the software SOAX (see chapter 4.1.2).²⁵⁰ In **red** the identified filaments are shown. Meshes were identified by drawing circles originating in local maxima in an Euclidian distance map and subsequently removing all overlapping circles but the largest.²⁵³ The mesh size was interpreted as the diameter of these circles. In **green** the resulting meshes are depicted. **B:** Distribution of the mesh sizes ξ observed on samples with different pinning-point density in the lipid bilayer ranging from 1 mol% to 5 mol% PIP_2 in the solid supported membrane. Data is provided in form of box plots. Box plots extend from the 25th to the 75th percentile, whiskers from the 10th to the 90th. The number of analyzed meshes is provided on top of the graph. A Wilcoxon rank test indicated that the median of $\xi_{\text{PIP}_2\ 5\text{ mol}\%} = 641\text{ nm}$ ($M=33$) is significantly lower than the median of $\xi_{\text{PIP}_2\ 3\text{ mol}\%} = 1024\text{ nm}$ ($M=12$), $\alpha < 0.0005$, while a t -test was used to show that the median of $\xi_{\text{PIP}_2\ 3\text{ mol}\%}$ is significantly lower than the median of $\xi_{\text{PIP}_2\ 2\text{ mol}\%} = 1140\text{ nm}$ ($M=2$), $\alpha < 0.0005$, and that the median of $\xi_{\text{PIP}_2\ 2\text{ mol}\%}$ is significantly lower than the median of $\xi_{\text{PIP}_2\ 1\text{ mol}\%} = 1210\text{ nm}$ ($M=5$), $\alpha < 0.05$. M is the number of images analyzed, α is the confidence level. (Data by M. Schön). 65

Figure 40: Analysis of the actin filament diameter. Atomic force microscopy images of pre-polymerized F-actin filaments attached to a surface via poly-D-lysine were analyzed to determine the diameter (A1-2) and the diameter distribution (B1-2) of the pre-polymerized filaments. Both images (A1 and B1) were recorded in quantitative imaging mode to ensure high precision in z -direction. The height of the filaments was analyzed from line plots. **A:** The height of filaments (A2, **green**) and small bundles (A2, **red**) was determined. The green and red boxes (A1) mark the respective regions where the filament diameter was analyzed. Filament diameters of $d_{\text{filament}} = 7.9 \pm 2.4\text{ nm}$ (A2, green; $N=18$) and bundle diameters of $d_{\text{bundle}} = 19.1 \pm 2.6\text{ nm}$ (A2, red; $N=10$) could be determined. **B:** In an image with medium density of actin the distribution of filament diameters was analyzed. The distribution of the height of the actin fibers ($N=277$) is shown in a histogram (B2), the blue curve represents a Kernel probability density estimate. Peaks in the histogram are marked by black arrows. 67

Figure 41: Measured viscosity of liquids. The scaling of the loss modulus with the frequency for samples of different viscosity is shown. **A:** water and **B:** aqueous solutions of glycerol (1:1 (v/v)). Three different methods were employed. **▲:** Video particle tracking microrheology; **●:** Passive microrheology measured an optical tweezer. **■:** Active microrheology measured an optical tweezer. **Dotted lines:** expected scaling of the loss modulus with the frequency for different viscosities of the medium $\eta_{\text{water}} 20^\circ\text{C} = 1 \text{ mPa} \cdot \text{s}$ and $\eta_{\text{glycerol: water 1:1 v/v, } 20^\circ\text{C}} \approx 15 \text{ mPa} \cdot \text{s}$. Inset in **A** shows the mean squared displacement obtained from video particle tracking measurements (open triangles) and the theoretical curve progression for 22°C (dotted line). 69

Figure 42: Mean squared displacements of F-actin model systems. Shown is the time and ensemble averaged MSD of different samples. **A:** Physiological linker ezrin, which transiently links the membrane phospholipid PIP₂ and actin and **B:** Interaction *via* neutravidin, biotinylated lipids and biotinylated actin. **Blue:** Entangled actin network without connection to a membrane (8-23 μm , $N=5$). **Light green:** Actin attached to a lipid membrane via ezrin containing 3 mol% PIP₂ ($N=6$). **Dark green:** Actin attached to a lipid membrane containing 5 mol% PIP₂ via ezrin ($N=9$). **Dark red:** Actin attached to a lipid membrane containing 3 mol% biotinylated- DOPE via neutravidin (biotin 3 mol%, $N=2$). **Light red:** Actin attached to a lipid membrane containing 0.5 mol% biotinylated- DOPE via neutravidin (biotin 0.5 mol%, $N=1$). Red dotted line shows the theoretical MSD for water at 22°C and similar bead size. For better comparison some scaling behaviors are shown in the plot (straight black lines). 71

Figure 43: Frequency dependent viscoelastic properties of entangled F-actin networks of different concentrations. Shown are the storage modulus G' (filled symbols), the loss modulus G'' (open symbols) and a respective fit according to equation (69)+(70) (dashed line, for full set of parameters see Appendix IV).³⁴ **A:** Entangled F-actin network of concentration 8-23 μm (**dark blue**, $N=5$). **B:** F-actin networks at higher concentration without connection to a membrane (**light blue**, 36 μm , $N=3$). The data represents not all data collected for this concentration, other data showed a similar frequency dependency as in (A). **C:** The dependency of the plateau modulus G_0 on the G-actin concentration is shown. A power law fit to the data showed a scaling with the concentration as $G_0 \propto c 2.1 \pm 0.8$. Additionally, for comparison important scaling behaviors are shown in (A) + (C). (Data was partially collected in the Master thesis of Katharina Silbersdorff (2015)) 73

Figure 44: Frequency dependent viscoelastic properties of entangled F-actin networks adjusted to different polymer contour length by gelsolin. Shown are the storage modulus G' (filled symbols), the loss modulus G'' (open symbols) and a respective fit according to equation (69)+(70) (dashed line, for full set of parameters see Appendix 1 IV).³⁴ **A:** Entangled F-actin network consisting of actin filaments shortened by gelsolin (26 μm ; actin:gelsolin, 750:1; $N=5$). **B:** Entangled F-actin network consisting of actin filaments shortened by gelsolin (23 μm ; actin:gelsolin, 2500:1; $N=5$). **C:** The apparent unbinding rate constant $k_{\text{off}} = 2\pi \cdot f_{\text{rep}}$ from entangled F-actin networks as a function of the mean filament contour length, l_c . The length of the filaments can be estimated from the stoichiometric ratio of actin and gelsolin for the gelsolin containing samples.³⁰⁷ For the sample without gelsolin l_c was estimated from the reptation frequency.¹¹¹ Data was compared to a predicted scaling behavior (equation (34))¹¹¹ (green line) and fitted with a function $k_{\text{off}} l_c = a \cdot l_c - 3$ (black dashed line). (Data was partially collected in the Master thesis of Katharina Silbersdorff (2015) especially data in (A)) 77

Figure 45: Frequency dependent viscoelastic properties of quasi 2D actin networks coupled to a planar membrane via PIP₂-ezrin linkage. Shown are the storage modulus G' (filled symbols), the loss modulus G'' (open symbols) and a respective fit according to equation (69)+(70) (dashed line, for full set of parameters see Appendix 1 IV).³⁴ **A:** Actin attached to a lipid membrane containing 3 mol% PIP₂ mediated by ezrin, $N=6$. Three characteristic frequency regimes are marked: **(I)** Elastic regime at intermediate frequencies ($f \approx 0.01 - 10 \text{ Hz}$), **(II)** low frequency regime ($f \approx 0.001 - 0.01 \text{ Hz}$) and **(III)** high frequency regime ($f \approx 10 - 100 \text{ Hz}$). **B:** Actin attached to a lipid membrane containing 5 mol% PIP₂ mediated by ezrin, $N=9$. For comparison important scaling behaviors are shown in (A) + (B) (straight line). N is the number of averaged bead trajectories. 78

Figure 46: Frequency dependent viscoelastic properties of quasi 2D actin networks coupled to a planar membrane via neutravidin-biotin linkage. Shown are the storage modulus G' (filled symbols), the loss modulus G'' (open symbols) and a respective fit according to equation (54)(69)+(70) (dashed line, for full set of parameters see Appendix 1 IV).³⁴ **A:** Actin attached to a lipid membrane containing 0.5 mol% biotinylated DOPE via neutravidin, $N=1$. **B:** Actin attached to a lipid membrane containing 3 mol% biotinylated DOPE via neutravidin, $N=2$. For comparison important scaling behaviors are shown in (A) (straight line). N is the number of bead trajectories averaged. 79

Figure 47: Plateau modulus G_0 as a function pinning-point concentration and cross-linker. **Dark blue:** Entangled actin network (8-23 μm , median: 0.009 Pa), $N=8$. **Light green:** Actin attached to a lipid membrane containing 3 mol% PIP₂ via ezrin (median: 0.133 Pa), $N=6$. **Dark green:** Actin attached to a lipid membrane containing 5 mol% PIP₂ via ezrin (median: 0.276 Pa), $N=9$. **Pink:** Actin attached to a lipid membrane containing 0.5 mol% biotinylated DOPE via neutravidin (0.189 Pa), $N=1$. **Red:** Actin attached to a lipid membrane containing 3 mol% biotinylated DOPE via neutravidin (median: 0.324 Pa), $N=4$. A Wilcoxon rank test indicated that the median of $G_0(\text{PIP}_2 5 \text{ mol}\%) = 0.276 \text{ Pa}$ is significantly higher than the median of $G_0(\text{PIP}_2 3 \text{ mol}\%) = 0.133 \text{ Pa}$, with a confidence level of $\alpha < 0.3$, while the median of $G_0(\text{PIP}_2 3 \text{ mol}\%)$ is significantly higher than the median of $G_0(\text{actin } 8\text{-}23 \mu\text{m}) = 0.009 \text{ Pa}$, $\alpha < 0.005$. Box plots extend from the 25th to the 75th percentile, whiskers from the 10th to the 90th. Individual data points are plotted as circles. 79

Figure 48: Scaling behavior of the mesh size and the plateau modulus as a function of pinning-point density in the 'PIP₂' minimal actin cortex. A: Scaling of the plateau modulus G_0 with the pinning-point density P ($G_0 \propto P^{1.4}$). Inset shows the scaling of the plateau modulus G_0 with pinning-point density P ($G_0 \propto P^{0.3}$) for the 'biotin' sample. B: Scaling of the mesh size ξ with the pinning-point density P ($\xi \propto P^{-0.9}$). C: Scaling of the plateau modulus G_0 with the mesh size ξ ($G_0 \propto \xi^{-1.5}$). Median values are plotted. Dotted lines show the respective power law fit to the data points. ... 80

Figure 49: Unbinding rate constants k_{off} from microrheological measurements. Unbinding rate constant k_{off} obtained fitting the parameters of equation (69)+(70) to the viscoelastic spectra. **Dark blue:** Unbinding of entangled 3D actin networks 8-23 μM (mean \pm std: $0.037 \pm 0.028 \text{ s}^{-1}$, averaged: 0.05 s^{-1} , $N=5$). **Orange:** Unbinding of 3D actin network actin:gelsolin 750:1 ($0.475 \pm 0.440 \text{ s}^{-1}$, averaged: 0.877 s^{-1} , $N=5$). **Light blue:** First unbinding rate from the biotin samples, here attributed to the entanglement unbinding of quasi 2D actin network attached to lipid membranes ($0.468 \pm 0.091 \text{ s}^{-1}$, averaged: 0.41 s^{-1} , $N=2$). **Red:** Second unbinding rate from the biotin samples, here attributed to the dissociation of the binding complex biotinylated lipid-neutravidin-biotinylated actin ($0.028 \pm 0.020 \text{ s}^{-1}$, averaged: 0.014 s^{-1} , $N=2$). **Green:** Unbinding rate constant of the binding complex PIP₂-ezrin-actin ($0.067 \pm 0.032 \text{ s}^{-1}$, averaged: 0.054 s^{-1} , $N=15$). For the second underlying peak an unbinding rate constant of 0.4 s^{-1} , was assumed in accordance with the second peak in the biotin sample. Bar plot shows the respective mean values of single measurements; error bars represent the standard deviation; crosses depict k_{off} values from fit on shear modulus obtained from averaged MSD curves. (full set of parameters in Appendix 1 IV) 83

Figure 50: Time lapsed images of the F-actin network bound to a lipid membrane via ezrin. Confocal time lapsed images of F-actin filaments (green, AlexaFluorPhalloidin488 labeled) bound to a lipid membrane containing 3 mol% PIP₂ were recorded in time intervals of 1.6 s. A: Three images at $t = 0, 19.2$ and 38.4 s are shown. B: Inverted composite image of two images 45 s apart. **Green:** Positions that showed intensity at $t = 0$ s but not at $t = 45$ s. **Violet:** Positions that showed intensity at $t = 45$ s but not at $t = 0$ s. **Black:** positions no movement was observed. Scale bar is 5 μm . Similar to the image stacks shown in Figure 22 the green circles (or black in B) of diameter $d = 2 \mu\text{m}$ correspond with the bead position. 84

Figure 51: Two different effects acting on the high frequency scaling of F-actin networks bound to a lipid membrane. A: The impact of inertia on frequency spectra of viscoelastic properties. Calculated frequency dependent viscoelastic moduli, storage moduli (**red shades**) and loss moduli (**blue shades**) calculated by the above mentioned model. The radius r of the tracer particle was varied between 1-10 μm . **Grey dotted line:** theoretical loss modulus in pure water ($G''\omega = -i\omega\eta$, with $\eta = 0.981 \text{ mPa} \cdot \text{s}$). B: Calculated frequency dependent viscoelastic moduli, storage moduli (**red shades**) and loss moduli (**blue shades**). The solvent viscosity was set to values $\eta = 0.10, 0.32, 1.0, 3.2, 10 \text{ mPa} \cdot \text{s}$, respectively, in order to illustrate the impact of increased viscosity near surfaces on the measured viscoelastic moduli of solid supported actin cortex models. **Grey dotted lines:** theoretical loss modulus in pure solvent with different viscosities ($G''\omega = -i\omega\eta$). Frequency dependent moduli where calculated after equations (72) and (73) by a combined model.^{34,122,305} C: Measured loss modulus in water obtained by active microrheological measurements on an optical tweezer at different frequencies and heights above the sample surface (dots) (height was corrected for 0.5 μm) and the predicted dependency of the loss modulus with height and frequency (dashed lines). **Dark blue:** 40 Hz; **Light blue:** 60 Hz; **Green:** 80 Hz; **Orange:** 100 Hz; **Red:** 150 Hz. 86

Figure 52: Unbinding rate constant of the PIP₂-ezrin-actin complex in dependency of the temperature. The dependency of $k_{off\text{PIP}_2 - \text{ezrin} - \text{actin}}$ on the temperature (12, 27 and 36 $^{\circ}\text{C}$) obtained from video particle tracking measurements is shown in a typical Arrhenius plot. Data points are mean values ($N=5$); error bars are the respective standard deviation; the dotted line represents an Arrhenius fit. Fit results: activation energy $\Delta E_a = 31.3 \pm 12.4 \text{ kJ} \cdot \text{mol}^{-1} = 12.6 \cdot k_B T$ and pre-exponential factor $A = 1660 \pm 8299 \text{ s}^{-1}$. All unbinding rate constants were determined using equations (69)+(70)(see 4.1.3.4).³⁴ 88

Figure 53: Error analysis and propagation of error of the ensemble average of the mean squared displacement. The standard deviation of the ensemble average of the mean squared displacement (A) and its propagation of error to the storage and loss modulus (B) is shown as an example for the dataset of PIP₂ 5 mol% ($N=9$). A: ensemble and time averaged mean squared displacement (solid line) and standard deviation of the ensemble average (light green filled area) of the mean squared displacement. B: storage (red) and loss (blue) modulus (solid lines) and the respective propagated error (red and blue filled areas) from an error propagation of the standard deviation of the ensemble average. 90

Figure 54: Mean squared displacement and viscoelastic moduli resulting from simulated particle motions in a viscoelastic medium. The trace of the particle in a medium of varying viscoelastic properties was simulated ten times as described in chapter 4.1.4, afterwards the time and ensemble averaged mean squared displacement as well as the viscoelastic moduli were adjusted to resemble the experimental data. A: mean squared displacement (**green**) vs. time. B: storage (**red**) and loss modulus (**blue**) vs. frequency. **A+B 1:** simulated spectra similar to the experimental data of entangled F-actin (8-23 μM), $N = 10$. **A+B 2:** simulated spectra similar to the experimental data of actin attached to a lipid membrane containing 3 mol% PIP₂ mediated by ezrin, $N = 10$. **A+B 3:** simulated spectra similar to the experimental data of actin attached to a lipid membrane containing 5 mol% PIP₂ mediated by ezrin, $N = 10$. Dark solid line: mean value of the ensemble average. Light areas: standard deviation and error estimation by Gaussian error propagation (see equation (77)). Dotted lines: experimental data. Parameters for the simulation are listed in Table 17. 91

Figure 55: Influence of the bead size on the frequency dependent viscoelastic properties of minimal actin cortex models. Shown are the storage modulus G' (filled symbols), the loss modulus G'' (open symbols) and a respective fit

according to equation (69)+(70) (dashed line, for full set of parameters see Appendix 1 IV).³⁴ Actin attached to a lipid membrane containing 3 mol% PIP₂ mediated by ezrin measured with a tracer particle of a 2.5-fold larger radius ($r = 2.5 \mu\text{m}$), $N=1$, compared to the particle radius used in Figure 45. 93

Figure 56: Limitations of video particle tracking as a method to study artificial model cortices. Shown are the mean squared displacements (**A1-2**) and the respective viscoelastic moduli (**B1-2**) of a tracer particle embedded in an actin network. **A1** and **B1** show unfiltered data; **A2** and **B2** show the same data filtered with a notch filter. **Red:** Actin network attached to a lipid membrane containing 3 mol% biotinylated- DOPE via neutravidin. **Blue:** Entangled actin networks (8-23 μM) are shown for comparison. **Grey:** the mean squared displacement of stuck beads on a surface are shown. 93

Figure 57: Comparison of two methods to obtain the viscoelastic moduli from mean squared displacements. Mean squared displacements of the previously described model systems measured by video particle tracking were transformed to viscoelastic moduli by a direct conversion method introduced by Evans *et al.* (see chapter 2.2.2.1.2).¹⁰⁷ Storage (closed symbols) and loss modulus (open symbols) obtained by this method are shown. For comparison the moduli calculated after the method introduced by Dasgupta *et al.* (see chapter 2.2.2.1.2)¹⁰³ as shown in the previous chapter are displayed (dashed lines). **A:** Entangled 3D F-actin 8-23 μM ; **B:** PIP₂ 3 mol%; **C:** PIP₂ 5 mol%; **D:** Biotin 0.5 mol%; **E:** Biotin 3 mol%. 94

Figure 58: Comparison of three microrheology methods to measure the frequency dependent viscoelastic properties of cortex model systems. Large circles, ●: Active microrheology, optical tweezer. Crosses, x: Passive microrheology, optical tweezer. Dashed lines: Passive, video particle tracking based microrheology. **A: Entangled F-actin** (VPT: 8-23 μM , PMR OT: 15 μM , AMR OT: 36 μM); **B: PIP₂ 3 mol%**; **C: PIP₂ 5 mol%**. For better comparison the moduli where scaled by a factor so that the loss modulus in the high frequency regime agrees approximately throughout the methods. **D:** Trap (green) and bead movement (red) versus time are shown obtained from a force extension experiment of a bead on a PIP₂ 3 mol% sample. Sudden jumps in the bead movement correspond to a force of about 10 pN. 96

Figure 59: Artefacts in the low frequency regime of the loss modulus in active microrheology measurements. The loss modulus of water obtained by active optical tweezer based microrheology is shown. Error bars are the standard deviation. The spectrum is the same as in chapter 5.1.2.1, a broader frequency regime is shown. 97

Figure 60: Influence of solvent viscosity on the frequency dependent viscoelastic spectrum of the minimal actin cortex model system measured by active optical tweezer based microrheology. Storage modulus (G' , circles) and loss modulus (G'' , triangles). **A:** Spectrum of entangled F-actin (36 μM , blue), PIP₂ 2 mol% under normal buffer condition (green) and PIP₂ 2 mol% in aqueous solution of glycerol (same bead, pink). **B:** Spectrum of water (grey) and an aqueous solution of glycerol (red) are shown for comparison. Dashed line: Theoretical loss modulus of water. All data measured on the same day (despite the entangled F-actin sample) to minimize the error due to variation in trap calibration. All data measured with trap stiffness of $k_1 = 0.007 \mu\text{N} \cdot \text{m}^{-1}$ and $k_2 = 0.001 \mu\text{N} \cdot \text{m}^{-1}$, peak-to-peak amplitude was $A = 100 \text{ nm}$ 98

Figure 61: Frequency dependent viscoelastic properties of apical cellular membrane patches. **A:** Fluorescence image of an F-actin cortex attached to glass prepared by the sandwich-cleavage method (see chapter 4.2.4) and fluorescent beads (bright spherical spots, diameter 2 μm) used for video particle tracking based microrheology measurements. Inset: local actin cortex organization around a bead. **B:** Mean squared displacement of beads attached to apical cellular membrane patches (violet) is shown in comparison to the MSD that corresponds to setup noise (grey) and entangled F-actin networks (blue). **C:** Storage modulus G' (filled symbols) and loss modulus G'' (open symbols) of apical cellular membrane patches. Grey area marks the frequency regime that is disturbed by an artefact caused by a noise signal in samples, where the signal-to-noise ratio (the mean squared displacement) is not high enough. Inset: normalized peaks in the low frequency regime of apical cellular membrane patches (violet) and entangled F-actin networks (blue). Additionally a low frequency maximum of a sample with different band width is shown (green: PIP₂ 5 mol%). (Data has been collected in collaboration with Stefan Nehls). 99

Figure 62: Scheme of the integrin mediated mechanotransduction and its role in cancer. **A:** Structure and important proteins in focal contacts. **B:** Integrin signaling. Especially the Rho mediated tension generation in the actin cytoskeleton and its feedback loop on the stiffness of the extracellular matrix (ECM) leading to a positive feedback in cancer progression. **C:** Malignant transformation as a result of the tissue environment and the metastatic process. Cellular dislocation occurs via transportation in the blood vessels. Cellular flexibility is crucial for intravasation and extravasation. Modified from Mitra *et al.*⁴⁷, Paszek *et al.*⁵⁹ and Huang *et al.*³⁴⁴. 104

Figure 63: The effect of F-actin cytoskeleton manipulating drugs on the viscoelastic moduli. Confluent layers of MDCKII cells were subjected to latrunculin A (LatA) or jasplakinolide (Jas) (1 μM) for 30 min (**LatA & Jas**) and 60 min (**LatA & Jas**) respectively. Data obtained from active atomic force microscopy based microrheology measurements (see 4.2.7.1) (data points: median value; error bars: 25th and 75th percentile) were fitted by the power law structural damping model (equation (41), dashed lines). **A:** Storage modulus (●); **B:** Loss modulus (▲). Important power law scaling are indicated in the figures (solid lines). 105

Figure 64: The effect of F-actin cytoskeleton manipulating drugs on viscoelastic parameters. Confluent layers of MDCKII cells were subjected to **latrunculin A** or **jasplakinolide** (1 μM) for 30 and 60 min, respectively. Data obtained from active atomic force microscopy based microrheology measurements (see 4.2.7.1) were fitted by the power law

structural damping model (equation (41)). Resulting viscoelastic parameters are shown. **A:** Stiffness offset of the viscoelastic moduli G_0 ; **B:** Power law coefficient α ; **C:** Newtonian viscosity η . Box plots extend from the 25th to the 75th percentile, whiskers from the 10th to the 90th. Individual data points are plotted as circles, some outliers are not shown. 106

Figure 65: Viscoelastic properties of living MDCKII cells in dependency of substrate stiffness. MDCKII cells were cultured on substrates of different E-moduli: **1 kPa, 8 kPa, 30 kPa and 100 kPa**. Data obtained from active atomic force microscopy based microrheology (see 4.2.7.1) were fitted by the power law structural damping model (equation (41)). **A:** Storage (closed symbols) and loss modulus (open symbols) of MDCKII cells cultured on on substrates of different elasticity: 1 kPa (●) and 30 kPa (▲) are shown. Data points: median value; Error bars: 25th and 75th percentile; Dashed lines: fit by the power law structural damping model. Solid line: power law scaling of 0.2. Resulting viscoelastic parameters from the PLSDM are shown in **B:** Stiffness offset of the viscoelastic moduli G_0 ; **C:** Power law coefficient α ; **D:** Newtonian viscosity η . Box plots extend from the 25th to the 75th percentile, whiskers from the 10th to the 90th. α indicates the confidence level of a Wilcoxon rank test. Individual data points are plotted as circles, some outliers are not shown. (Some of the data has been collected by Nico Gottschling during his internship (2014)) 108

Figure 66: Confocal images of the F-actin cytoskeleton of MDCKII cells as a function of substrate elasticity. Labelling was performed using Alexa Fluor 546 Phalloidin. Young's moduli of gels: **A:** 0.2 kPa; **B:** 1 kPa; **C:** 8 kPa; **D:** 30 kPa; **E:** 100 kPa..... 110

Figure 67: The F-actin cytoskeleton and cell-cell contacts of MDCKII cells as a function of substrate elasticity. Confocal images of important cytoskeletal proteins as a function of substrate elasticity are shown. Young's modulus of PAA gels: **A:** 1 kPa; **B:** 100 kPa. **A1&B1:** Fluorescently stained F-actin cytoskeleton, focus was set to the basal focal plane; **A2&B2:** Fluorescently stained F-actin cytoskeleton, focus was set to the apical focal plane; **A3&B3:** Fluorescently stained e-cadherin; **A4&B4:** Fluorescently stained ZO-1. A&B1-3 each show the same position on the sample, A&B4 are from a different samples. Labelling was performed as described in chapter 4.2.5.1 (Experiment performed by Franziska Ries (2016)). 111

Figure 68: Apparent area compressibility modulus, over all tension and membrane tension of epithelial cells in dependency of substrate stiffness. MDCKII cells were cultured on substrates of different E -moduli: **1 kPa, 8 kPa, 30 kPa and 100 kPa**. Data were obtained as described in chapter 4.2.7.2. **A:** Apparent area compressibility modulus κ_A ; **B:** Overall tension T_0 (sum of cortical tension T_c and membrane tension T_t); **C:** Membrane tension T_t . Box plots extend from the 25th to the 75th percentile, whiskers from the 10th to the 90th. α indicates the confidence level of a Wilcoxon rank test. Individual data points are plotted as circles some outliers are not shown. 111

Figure 69: ECIS parameters for MDCKII cells in different seeding densities. The impedance was determined for different frequencies and fitted to a model of Lo and Ferrier (see chapter 4.2.6.3). Data was evaluated over the whole measuring time after formation of the monolayer. The resulting fit parameters are shown in box plots. Box plots extend from the 25th to the 75th percentile, whiskers from the 10th to the 90th. **A:** Transepithelial resistance R_b ; **B:** Parameter γ which is inversely proportional to the cell-substrate distance; **C:** Membrane capacitance C_m . Each boxplot contains at least $N = 2400$ data points..... 113

Figure 70: Cell size dependency of the viscoelastic parameters of living MDCKII cells. MDCKII cells were seeded in different densities (750,000, 500,000 and 250,000 cells per 9.2 cm²) to obtain cells of different cell sizes (see Table 22). Data obtained from active atomic force microscopy based microrheology (see 4.2.7.1) were fitted by the power law structural damping model (equation (41)). Resulting viscoelastic parameters are shown. **A:** Stiffness offset of the viscoelastic moduli G_0 ; **B:** Power law coefficient α ; **C:** Newtonian viscosity η . Box plots extend from the 25th to the 75th percentile, whiskers from the 10th to the 90th. Individual data points are plotted as circles, some outliers are not shown. 114

Figure 71: F-actin cytoskeleton organization at the basal side of MDCKII cells as a function of seeding density. Confocal images of the F-actin cytoskeleton of MDCKII cells as a function of different seeding density are shown (fluorescently labeled with Alexa Fluor 546 Phalloidin). **A:** 1,000,000 c; **B:** 750,000 c; **C:** 500,000 c; **D:** 250,000 c. 115

Figure 72: Cortical stiffness as a function of area per cell. The stiffness offset obtained from the PLSDM is shown in dependency of the area per cell. **A:** Cells grown on stiff glass substrates were seeded in different cell densities: 250,000 c (**blue**), 500,000 c (**violet**) and 750,000 c (**orange**). **B:** Cells grown on substrates of different elasticity: 1 kPa (**red**), 4 kPa (**grey**), 30 kPa (**green**) and 100 kPa (**blue**). Mean values (data points) and standard deviation (error bars) for all force distance curves that were evaluated for one single cell are plotted against the area which was obtained by the height map of the atomic force microscopy measurement. Dashed lines show a linear trend for all data. Insets represent the expected tendencies. (Data measured by Franziska Ries (2016)) 115

Figure 73: Viscoelastic properties of mammary gland cells in dependency of substrate stiffness. MCF-10A cells were cultured on substrates of different E -moduli: **1 kPa, 8 kPa, 30 kPa and 100 kPa**. Data obtained from active atomic force microscopy based microrheology (see 4.2.7.1) were fitted by the power law structural damping model (equation (41)). **A:** Storage (solid symbols) and loss modulus (open symbols) of MCF-10A cells cultured on substrates of different elasticities are shown. Circles (●): 8 kPa; Triangles (▲): 1 kPa. Data points: median value; error bars: 25th and 75th percentile; Dashed lines: fit by the power law structural damping model. **B:** Stiffness offset of the viscoelastic moduli G_0 ;

C: Power law coefficient α ; D: Newtonian viscosity η . Box plots extend from the 25th to the 75th percentile, whiskers from the 10th to the 90th. Individual data points are plotted as circles, some outliers are not shown. 117

Figure 74: Cytoskeletal organization at the basal side of breast epithelial cells as a function of matrix elasticity. Confocal fluorescence images of the F-actin cytoskeleton (**orange**) at the basal side of MCF-10A cells cultured for 2-3 days on surfaces of different elasticity are shown. Matrix elasticity: **A:** 0.2 kPa; **B:** 1 kPa; **C:** 8 kPa; **D:** 100 kPa. 119

Figure 75: Morphology of breast epithelial cells in response to matrix elasticity. Orthogonal view of confocal fluorescence images of the F-actin cytoskeleton (**orange**) and the nuclei (**turquoise**) of MCF-10A cells cultured on surfaces of different elasticity for 2-3 days. Matrix elasticity: **A:** 0.2 kPa; **B:** 1 kPa; **C:** 8 kPa; **D:** 100 kPa. The dimension of each image section is 135x135 μm^2 in *x-y*-direction. Approximate height *h* of the cell assemblies is indicated in the lower right corner. 119

Figure 76: Overview of the effects of substrate stiffness on the average cellular shape and on the mechanical parameters observed here. **Top:** Scheme of the changes in cell morphology and organization of the cytoskeleton in response to surface stiffness. **Bottom:** Changes in the respective mechanical parameters and the cell spreading area are depicted by wedges. 120

Figure 77: Formation of cell layers over time for different seeding densities. Impedance *Z* over time at a frequency of 3360 Hz. MDCKII cells were seeded on an ECIS electrode (0.8 cm^2) with different seeding densities (see chapter 4.2.6.2) corresponding to: 250,000 c per 9,2 cm^2 (**green**), 500,000 c per 9,2 cm^2 (**yellow**), 750,000 c per 9,2 cm^2 (**orange**) and 1,000,000 c per 9,2 cm^2 (**red**). (Experiment performed by Franziska Ries (2016)) a

Figure 78: The F-actin cytoskeleton and cell-cell contacts of MDCKII cells as a function of seeding density. Confocal images of important cytoskeletal proteins as a function of different seeding density are shown. **A:** 250,000 c per 9.2 cm^2 ; **B:** 500,000 c per 9.2 cm^2 . **A1&B1:** Fluorescently stained F-actin cytoskeleton, focus was set to the basal focal plane; **A2&B2:** Fluorescently stained F-actin cytoskeleton, focus was set to the apical focal plane; **A3&B3:** Fluorescently stained e-cadherin; **A4&B4:** Fluorescently stained ZO-1. Cells were fixed after 2 days. Labelling was performed as described in chapter 4.2.5.1 (Experiment performed by Franziska Ries (2016)) a

Figure 79: Correlation plot of the viscoelastic parameters obtained by the PLSDM on the cell size and substrate properties. **A&B1:** Stiffness offset in dependency of the area per cell. **A&B2:** Power law coefficient in dependency of the area per cell. **A&B3:** Newtonian viscosity in dependency of the area per cell. **A:** Cells grown on stiff glass substrates were seeded in different cell densities: 250,000 c (**blue**), 500,000 c (**violet**) and 750,000 c (**orange**). **B:** Cells grown on substrates of different elasticity: 1 kPa (**red**), 4 kPa (**grey**), 30 kPa (**green**) and 100 kPa (**blue**). Mean values (data points) and standard deviation (error bars) for all force distance curves that were evaluated for one single cell are plotted against the area which was obtained by the height map of the atomic force microscopy measurement. Dashed line shows a linear trend line for all data. (Data measured by Franziska Ries (2016)) b

List of Tables

Table 1: Overview of microrheology methods and their measuring ranges.	7
Table 2: Reported reptation times τ_{rep} for F-actin filaments in entangled networks.	15
Table 3: Transient F-actin binding proteins and their respective unbinding rate constant k_{off} from F-actin.	25
Table 4: Overview of lipid film compositions used in this study.	35
Table 5: Overview of spreading buffer composition.	36
Table 6: Overview over beads used in this study.	36
Table 7: Buffer compositions for preparation of pre-polymerized F-actin filaments used in this study.	37
Table 8: Overview over the protein buffers used in this study. All buffers were used at pH 7.4.	38
Table 9: Volume ratio of acrylamide (AA) and bis-acrylamide (bis-AA) in stock solutions and the resulting <i>E</i> -modulus (mean \pm std) after polymerization measured by atomic force microscopy. (Measured <i>E</i> -moduli were partially produced during the Bachelor thesis of Franziska Ries (2016) and Christine Franke (2014), Institute of Physical Chemistry, Georg-August-Universität, Göttingen, Germany).	51
Table 10: Cell lines used in this study.	51
Table 11: Composition of the cell culture media for the different cell lines used in this study.	52
Table 12: List of ingredients of the cell culture media.	52

Table 13: Composition of the different buffers used in this study for fluorescence staining. The globular protein bovine serum albumin and the nonionic surfactant Triton X-100 were purchased at Sigma Aldrich, St. Louis, Missouri, United States. Buffers were sterile filtered after preparation and used under sterile conditions. 54

Table 14: Overview of fluorescence markers used in the cell studies. 55

Table 15: Seeding densities of cells in ECIS experiments used in this study. 56

Table 16: Dynamic viscosities measured by different microrheology methods. Passive microrheology methods (PMR) and active microrheology methods (AMR), by video particle tracking and by optical tweezer (OT). The dynamic viscosities were obtained by a fit ($G''\omega = -i\omega\eta$) to the data shown in Figure 41. 69

Table 17: Parameters used to simulate particle traces by equation (58) in media with similar properties as found in experiments. k is the trap stiffness of the harmonic potential of the cage, D_{cage} is the diffusion coefficient of the cage and K is the correlation time at which the time dependent memory function ζ_{Maxwell} decays to half of its original value. 91

Table 18: Viscoelastic parameters of MDCKII cells influenced by cytoskeletal drugs obtained by the PLSDM. Confluent layers of MDCKII cells were subjected to latrunculin A or jasplakinolide ($1\mu\text{M}$) for 30 and 60 min respectively. Fit parameters of the power law structural damping model (equation (41)) are reported: Shear modulus at zero frequency G_0 , power law coefficient α and Newtonian viscosity η (median \pm sem). *Data has been reported in the dissertation of Jan Rother (2014)³⁶⁸. 107

Table 19: Viscoelastic parameters obtained by the PLSDM of MDCKII in dependency of substrate stiffness. MDCKII cells were cultured on substrates of different E -moduli: **1 kPa, 8 kPa, 30 kPa and 100 kPa**. Fit parameters of the power law structural damping model (equation (41)) are reported: shear modulus at zero frequency G_0 , power law coefficient α and Newtonian viscosity η (median \pm sem). *Data reported by Rother *et al.*²⁸⁰. **Data reported by Rother (2014)³⁶⁸. 109

Table 20: Apparent area compressibility modulus, over all tension and membrane tension of MDCKII cells in dependency of substrate stiffness. Cells were cultured on substrates of different E -moduli: 1 kPa, 2 kPa, 8 kPa, 30 kPa and 100 kPa. κ_A : Apparent area compressibility modulus; T_0 : Overall tension; T_t : Membrane tension (median \pm sem) and $T_c = T_0 - T_t$ cortical tension. 112

Table 21: Effect of substrate stiffness on the shape of MDCKII epithelial cells. Averaged (N = number of cells) length, width and cap height (mean \pm std) extracted from contact AFM images in dependency of the E -modulus of the substrate. Cells were not fixated. 112

Table 22: Cell size as a function of seeding density. MDCKII cells were seeded in different densities (750,000, 500,000 and 250,000 cells per 9.2 cm^2). Averaged (N = number of cells) length, width and cap height (mean \pm std) extracted from contact AFM images. Cells were not fixated. 113

Table 23: Viscoelastic parameters obtained by the PLSDM of MDCKII cells in different seeding densities. Confluent layers of MDCKII cells were seeded in different densities (750,000, 500,000 and 250,000 cells per 9.2 cm^2). Fit parameters of the power law structural damping model (equation (41)) are reported: shear modulus at zero frequency G_0 , power law coefficient α and Newtonian viscosity η (median \pm sem). 114

Table 24: Viscoelastic parameters obtained by the PLSDM of MCF-10A in dependency of substrate stiffness. Cells were cultured on substrates of different E -moduli: **1 kPa, 8 kPa, 30 kPa and 100 kPa**. Fit parameters of the power law structural damping model (equation (41)) are reported: shear modulus at zero frequency G_0 , power law coefficient α and Newtonian viscosity η (median \pm sem). *Data measured on stiff glass substrates have already been published.²⁴⁴ 118

Table 25: Parameters used to model the frequency dependent viscoelastic properties using a semi-phenomenological model to describe binding kinetics in the low frequency regime. The storage and loss moduli of the respective frequency dependent viscoelastic properties presented in chapter 5.1.2.3 and 5.1.2.4, were fitted according to equation (69)+(70). Parameters: plateau modulus, G_0 ; number of the respective cross-link N_i ; unbinding rate constant of the respective cross-link, $k_{\text{off}i}$ and power law, p ; with $i=1$ for the entanglement kinetics and $i=2$ for the cross-linker kinetic or a different process as in the actin $36\mu\text{M}$ sample. Parameters a - d are pre-factors as described in chapter 3.2.1. Due to the large number of parameters the fit parameters narrow boundaries had to be set for some parameters, assumptions had to be made in cases of supposedly overlapping peaks (***) and in some samples the high frequency regime did not contain enough data or could only partial be well fitted by the model (***) c

Appendix 3: *Curriculum Vitae*

Personal Information

Name: Nöding, Helen
E-Mail: helen.noeding@chemie.uni-goettingen.de
helenoeding@gmx.de
Date of Birth: 21.02.1988 in Heidelberg

Tertiary Education

PhD PhD thesis in the field of biophysical chemistry in Professor Andreas Janshoff's group, *Georg-August-University* in Göttingen/Germany. Program: *Göttingen Graduate School for Neurosciences, Biophysics, and Molecular Biosciences* (GGNB) program *Physics of Biological and Complex Systems*. Doctoral thesis project:
Active and Passive Microrheology of F-Actin Membrane Composites – From Minimal Cortex Model Systems to Living Cells

Master of Science Master (Sc.) Chemistry, Georg-August-University Göttingen. Master's thesis in the field of biophysical chemistry in Professor Andreas Janshoff's group, *Georg-August-University* Göttingen/Germany. Master thesis project:
Mikrorheologische Untersuchung der Zellmechanik in Abhängigkeit externer Stimuli

Bachelor of Science Bachelor (Sc.) Chemistry, Georg-August-University Göttingen, Bachelor's thesis in the field of bioinorganic chemistry in Professor Peter Faller's group, *Laboratoire de Chimie de Coordination* (CNRS) in Toulouse/France. Bachelor thesis project:
Interaction of ligands with copper amyloid- β complexes

Secondary Education

1998-2007 *Bundespräsident-Theodor-Heuss-Gymnasium* in Homberg (Efze)
23/06/2007 German qualification for university entrance (Abitur).

Awards

02/2014 - 01/2017 Scholarship holder of the *Deutsche Telekom Stiftung*
01/2008 - 05/2013 Scholarship holder of the *German National Academic Foundation (Studienstiftung des deutschen Volkes)*

International Experience

04/2010 - 07/2010 Research project in France: Laboratory internship at the *Laboratoire de Chimie de Coordination* (CNRS) in Toulouse in Professor Faller's group
01/2012 - 06/2012 Study visit to the United Kingdom: Studies at the *University of Bangor* (Wales) within the ERASMUS program of the European Union

Research Internships

12/2009 - 03/2010 Research Project in Professor Franc Meyer's groups at the Institute for Inorganic Chemistry at the Georg-August-University in Göttingen

Publications

Nöding, H.; Schön, M.; Reiner mann, C.; Dörrer, N.; Küschner, A.; Geil, B.; Mey, I.; Heussinger, C.; Janshoff, A.; Steinem, C. (2018) Rheology of Membrane-Attached Minimal Actin Cortices. *J. Phys. Chem. B* 122, 4537–4545

Brückner, B.R.; Nöding, H.; Janshoff, A. (2017) Viscoelastic Properties of Confluent MDCK II Cells Obtained from Force Cycle Experiments. *Biophys. J.* 112, 724-735.

Rother, J.; Büchsen schütz-Göbeler, M.; Nöding, H.; Steltenkamp, S.; Samwer, K.; Janshoff, A. (2015) Cytoskeleton remodelling of confluent epithelial cells cultured on porous substrates. *J. R. Soc. Interface* 12, 20141057.

Rother, J.; Nöding, H.; Mey, I.; Janshoff, A. (2014) AFM-based microrheology reveals significant differences in the viscoelastic response between malign and benign cell lines. *Open Biol.* 4: 140046.

Selected Talks

22/02/16 -25/02/16 International Symposium "Biological Dynamics from Microscopic to Mesoscopic Scales", Grimma, Germany:
Self-organization and mechanics of actomyosin networks attached to artificial and cellular plasma membranes

Selected Poster Presentations

07/09/16 - 10/09/16 EMBO Symposium "Actin in Action: From Molecules to Cellular Functions", Heidelberg, Germany:
Self-organization and mechanics of actomyosin networks attached to artificial and cellular plasma membranes

22/02/16 -25/02/16 International Symposium "Biological Dynamics from Microscopic to Mesoscopic Scales", Grimma, Germany:
Self-organization and mechanics of actomyosin networks attached to artificial and cellular plasma membranes

30/08/15 - 04/09/15 EMBO Conference "Physics of Cells: From Molecules to Systems (PhysCell 2015)", Kloster Banz/ Bad Staffelstein, Germany:
Mechanics and self-organization of actin cortices attached to cellular plasma membranes

14/09/14 - 17/09/14 Annual Meeting of the German Biophysical Society, Lübeck, Germany:
Active and Passive Microrheology of Living Cells and Model Systems

17/03/14 - 19/03/14 Euro AFM Forum, Göttingen, Germany:
Cell Mechanics in the Context of Cell-Surface Interaction

Other Languages

English C1 level according to the *Common European Framework of Reference for Languages* (CEFR) "Fluency in both written and spoken"

French C1 level according to the *Common European Framework of Reference for Languages* (CEFR) "Fluency in both written and spoken"

Appendix 4: Acknowledgments

An erster Stelle möchte ich Prof. Andreas Janshoff für Seine Betreuung und das spannende Thema dieser Arbeit danken, das stete Interesse am Fortgang der Projekte, die hilfreichen Diskussionen und Anregungen, aber auch die Möglichkeit mich recht frei und eigenständig in diesem Projekt zu entwickeln.

Des Weiteren danke ich Dr. Florian Rehfeldt für die Übernahme der Zweitkorrektur und Prof. Jörg Enderlein sowie Dr. Florian Rehfeldt für die gute Betreuung im Thesis Committee. Prof. Sarah Köster, Prof. Silvio Rizzoli und Prof. Michael Meinecke möchte ich für Ihre Bereitschaft danken meine Prüfung als *Examination Board* Mitglieder mitzugestalten.

Prof. Burkhard Geil möchte ich für die Theoriearbeit an meinem Projekt, viele hilfreiche Diskussionen und die Python Skripte zur Simulation von Partikel Trajektorien danken. Prof. Claudia Steinem möchte ich für die gute Kooperation und hilfreiche Diskussionen danken.

Der Deutsche Telekom Stiftung möchte ich für die finanzielle Unterstützung meiner Doktorarbeit, für die interessant gestalteten Stipendiaten Treffen, für spannende Seminare, und Einblicke in mögliche spätere Berufsfelder danken. Allen aktiven Stipendiatinnen und Stipendiaten möchte ich für das gute und kollegiale Gruppenklima und die Offenheit in den Diskussionen danken.

Der Deutschen Forschungsgemeinschaft speziell dem SFB937 möchte ich für die Finanzierung des Projektes A17 und viele interessante wissenschaftliche Treffen danken.

Für ein spannendes und ausgewogenes Programm zur Fortbildung möchte ich meinem Promotionsprogramm "Göttingen Graduate School for Neurosciences, Biophysics, and Molecular Biosciences" (GGNB) danken. Dem Büro vom Unterprogramm "Physics of Biological and Complex Systems" möchte ich für die gute und reibungslose Betreuung während der Promotion danken.

Für das intensive und nette Mentoring möchte ich mich sehr bei Herrn Dr. Volker Krüger von B.Braun Melsungen AG bedanken. Vielen Dank, dass Sie mir viele Einblicke in die Arbeitswelt verschafft haben!

Bei Dr. Ingo Mey möchte ich mich für den vielseitigen technischen Input, der mir gerade in den Anfangszeiten vieles leichter gemacht hat, bedanken. Vielen Dank auch für die gemeinsame Fehlersuche vor dem Gerät. Vor allem aber auch für Dein Gespür, wann Menschen Unterstützung brauchen und wann man sie besser einfach mal machen lässt und für Dein Interesse und Deine Bereitschaft über die Arbeitswelt und Zukunftspläne zu sprechen.

Markus, Dir danke ich für die langjährige sehr gute Kooperation, für deine kollegiale, zuverlässige und ausdauernde Arbeit und für die gegenseitige Motivation, wenn die Präparation oder die Messung mal wieder nicht geklappt haben! Ich hoffe, du hast auch die nächsten Monate weiter Spaß an diesem Thema. Auch den weiteren Kooperationspartnern Basti, Kerstin und Stefan möchte ich für die gute Zusammenarbeit danken.

Basti und Jan, euch beiden herzlichen Dank für das Korrektur lesen meiner Arbeit! Vielen Dank für die Zeit und Mühe, die ihr euch gemacht habt!

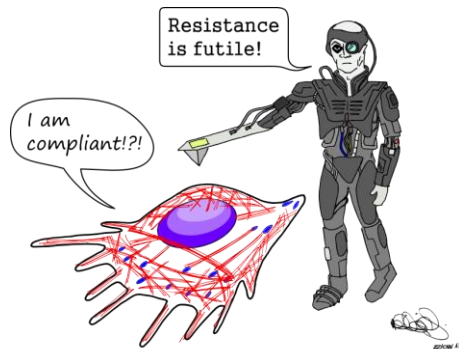
Chrisi, Nico, Kathi, und Franzi, das Arbeiten mit Euch hat mir Spaß gemacht. Euch, "meinen Studenten", möchte ich dafür danken, dass wir gegenseitig gelernt haben, wie man das Betreuer-Student-Verhältnis am besten gestaltet und natürlich auch für die Ergebnisse, die ihr erzielt habt und die in diese Arbeit eingeflossen sind. Ich wünsche euch allen viel Erfolg!

Liebe Petra, vielen Dank für jegliche Unterstützung bei der Einstellung, wenn wir Arbeitskreisaktivitäten geplant haben, ich Paper brauchte und wenn ich Probleme mit falschen Dienstreiseanträgen hatte.

Angela und Anja möchte ich für das Betreiben der Zellkultur bedanken und dafür, dass Ihr mir trotzdem noch Zellen gemacht habt, auch wenn ich sie schon viel zu spät aufgeschrieben habe.

Lieber Arbeitskreis, die gemeinsame Zeit mit euch habe ich sehr genossen. Danke nicht nur für die ca. 900 Mensa-Essen mit regem Austausch zu politischen, wissenschaftlichen und persönlichen Themen. Sondern vor allem auch für die Filmabende, die AK Ausflüge und das gemeinsame essen gehen in der Stadt. Nicht zu

vergessen die vielen "schlechten" Witze, die uns immer wieder erheitert haben. Auch möchte ich mich für die gute Atmosphäre und die gegenseitigen wissenschaftlichen Ratschläge und Unterstützungen bedanken.



Liebe Janseaten und Krussis, hier noch ein schlechter Witz, den ich mir lange für euch aufgehoben habe. In Erinnerung an die gemeinsamen Star Trek Film-Abende und viele AFM Messungen.

Liebe Freunde, vielen Dank, für das gemeinsame "Kopf frei kriegen" beim Klettern, Spielen, Wandern, auf Klettersteigen, Schneewanderungen, Radtouren, gemeinsamen Urlauben, Hochzeiten und anderen schönen Anlässen zu denen wir uns in den letzten Jahren getroffen haben. Und riesigen Dank für jeden Anruf, spontanen Besuch und unerwartete Einladung, wenn ich mich mal wieder Monatelang in meiner Arbeit vergraben habe. Und dafür, dass wir uns trotz großer Distanzen und wenig Zeit noch alle gut kennen.

Sarah, Hazem, Pascal und Martin möchte ich für das gemeinschaftliche Organisieren der ersten Herbstakademie der Deutsche Telekom Stiftung 2014 danken. Viel wichtiger noch für die Freundschaften, die daraus gewachsen sind und für die anschließenden Besuche untereinander. Auch, wenn wir nie wieder vollständig sein werden, hoffe ich, dass wir uns wiedersehen.

Meinem ehemaligen Chemie Lehrer Herrn Hüttl möchte ich dafür danken, dass er sich immer sehr darum bemüht hat den Unterricht für uns spannend zu gestalten und uns dazu gebracht hat, uns das chemische Wissen eigenständig aus Experimenten abzuleiten, ein wesentliches Denkmuster der Chemie, was mir viel gebracht hat.

Liebe Kollegen aus der Trinkwassergruppe vom THW Göttingen. Euch möchte ich dafür bedanken, dass ihr mich mindestens alle 4 Wochen komplett aus dem Wissenschaftsbetrieb rausgeholt und mir damit den nötigen Ausgleich gegeben habt.

Liebe Familie an euch geht ein besonders großer Dank! Vor allem für die große Unterstützung und, dass ihr mir den Rücken frei gehalten habt, wenn ihr konntet, die unzähligen Postkarten, die Musik zum Schreiben und die beiden großen Versorgungspakete in der Schreibzeit. Vielen Dank, dass ihr euch für meine Arbeit interessiert und zumindest für den Versuch zu verstehen, was ich eigentlich genau mache =). Danke, für alle schönen Feste, Geburtstagswochenenden und jedes Wochenende, das wir auf dem Balkon in der Sonne gegessen oder mit Terry einen langen Spaziergang gemacht haben und, ja, auch für das ein oder andere Foto...

Liebe Renate und lieber Lex, euch Danke ich für euer großes Interesse an meinem Werdegang und dass ihr mich jederzeit unterstützt und in meinem Tun bestätigt habt. Lex, dir danke ich besonders dafür, dass du bis jetzt jede meiner Abschlussarbeiten gelesen hast und dein Interesse in Diskussionen bekundet hast.

Jan für dich gilt die Summe aller vorher gegangenen Danksagungen und noch viel mehr. Niemand hat diese Zeit so nah mitbekommen wie Du, konnte damit so gut umgehen, hatte immer nochmal einen kleinen Lacher parat und hatte so ungemein viel Verständnis dafür. Vielen Dank für einfach Alles!
